DEPARTAMENTO DE ASTROFISICA

Universidad de La Laguna

DIPARTIMENTO DI ASTRONOMIA

Università degli Studi di Padova

Estructura y dinámica de las regiones centrales de galaxias con disco

Struttura e dinamica delle regioni centrali di galassie a disco

Structure and dynamics of the central regions of disk galaxies

Memoria que presenta
D. Jairo Méndez Abreu
para optar al grado de
Doctor en Ciencias Físicas.

julio de 2008

Examination date: July, 2008
Thesis supervisor: José Alfonso López Aguerri
Thesis supervisor: Enrico Maria Corsini

Some of the material included in this document has been already published in *MNRAS, A&A, ApJ.*

A mi madre

Acknowledgments

Durante estos cuatro años de doctorado, además de realizar mi sueño de llegar a ser un astrónomo profesional, mi vida a cambiado radicalmente. He pasado por los mejores y por los peores momentos de mi vida, pero de todo esto lo mejor que me ha pasado es conocer y convivir con la gente que ha estado a mi lado durante todo este tiempo.

En primer lugar, quiero agradecer a mis dos supervisores, Alfonso Aguerri y Enrico Maria Corsini, que me han dado la oportunidad de realizar esta tesis y que me han enseñado lo que quiere decir hacer ciencia y como hacer de esta algo más que un trabajo. A Alfonso por haber conseguido siempre motivarme, incluso cuando nos tocaba borrarlo todo y comenzar desde cero de nuevo, con sus ganas de sacar adelante el trabajo y su capacidad para inventarse nuevos proyectos. Ad Enrico, per essere stato più che un semplice relatore in questi quattro anni, per la tua infinita disponibilità pure nei momenti più incasinati, per la pazienzia nel correggere il mio povero inglese (e italiano) e per avermi insegnato ad essere preciso nel lavoro. Me considero muy afortunado de haber realizado esta tesis con ustedes.

Inoltre, devo ringraziare a tutto il gruppo di "galassisti" del dipartimento di astronomia della università di Padova. Al Prof. Bertola per avermi concesso di realizzare questa tesi all'interno del suo gruppo, ad Alessandro Pizzella per essere un continuo appoggio in questi anni, ad Elena dB., a Lodo, ad Andrea, ad Elena T., a Stefano, a Mary, insomma, a tutti quelli che hanno fatto parte del gruppo e hanno lasciato in me il suo segno.

No, non mi sono dimenticato, ma è d'obbligo un ringraziamento speciale per le altre due persone del gruppo. Loro sanno che sono più che semplici colleghi, che hanno lasciato in me un segno molto profondo. A Lorenzo, il mio primo appoggio in un paese ancora sconosciuto per me, per la cena più triste del mondo, per l'indimenticabile vento del nord e per tante altre cose che tu sai. Ad Alessandra, arrivata tardi al secondo piano, per essersi fatta "sentire"

non solo come colonna sonora del piano ma per aver reso i pomeriggi davanti alla mura di Padova più divertenti.

A tutte le persone che hanno fatto parte della mia vita padovana, a quelli che mi aiutarono ad adattarmi all'inizio e a quelli che mi hanno fatto sentire in Italia come a casa. Ad Aldo por sacarme de paseo en los primeros momentos, ad Anna per il suo *fare la finta tonta*, grazie per volermi bene nonostante tutto, ad Antonio per tante cose, troppe per dirle qua, ti aspetto a Tenerife, ad Avik per essere sempre disponibile, a Benedetta e Lucia, le nuove canarie, a Carlo per i cazzeggi al secondo piano, a Demetrio per essere così senza censure, ad Elena per sopportarmi come compagno di appartamento, ad Irene per la sua festa di laurea, a Jesús por traernos el *pan de cada dia* y por su dueto con Fayna, a Nacho por haber invertido bien el dinero de la Reina de Inglaterra, a Nancy por ser mi compañera de fatigas, tanto en la vida en Italia como en el doctorado, a Simona per le serate latine, insomma a tutti i padovani e non solo che hanno lasciato in me il loro segno, Carmelo, Claudio, Francesca, Jacopo A., Jacopo Fa., Jacopo Fr., Jasna, Maria, Mattia, Nicola, Pippo, Simonetta, Valentina G., Valentina V. e sopratutto al MERCOLEDÌ SPRITZ!!!.

Tampoco me puedo olvidar de la gente que ha estado conmigo desde antes de empezar este doctorado y que todavía me siguen aguantando. A Rubén y Teo, los que fuimos, somos y seremos siempre los mejores. Al resto de miembros del tercer corralín que me dejaron un sitio de infiltrado durante mis estancias en Tenerife, Adri, Juan, Ricardo. Juan gracias por no hacerme volver a casa en condiciones, digamos que difíciles. Adri esta tesis no estaría depositada sin ti. Ricardo buena suerte en el futuro, viejo. A mis dos canarias preferidas que aunque nos vemos menos, no por eso nos queremos menos a Montse y Ethel. A los que se buscaron la vida fuera de Tenerife como yo. A Luis, escribe ya el cómic de tu vida. Al Charly, lo siento tio, pero no se escribir en árabe. A Omaira, menos mal que sólo te doctoras una vez. Al Norbert, Rebe, Dario, Miguel, George. Todos ustedes han tenido algo que ver con que haya podido llegar hasta aquí.

Se c'è una persona che non può mancare in queste righe, quella sei tu, Mile. La persona con cui ho condiviso questi quattro anni, con cui ho vissuto tutti i momenti, sia belli che brutti, di questi anni. Probabilmente il motivo per il cui non ho mollato tutto agli inizi e da cui ho imparato quasi tutto quello che so sull'italiano, l'Italia e molte altre cose. La persona che mi ha regalato tutto il suo amore in questi anni senza chiedere mai niente in cambio. Senza di te non sarei arrivato fin qua e non starei scrivendo queste parole. GRAZIE per essere sempre lì.

Finalmente esta tesis se la dedico a mi familia, ustedes han sido siempre mi pilar principal, habeis estado siempre a mi lado apoyándome en cada decisión,

en cada nueva aventura, en cada viaje, ustedes son mi equilibrio. A mi padre, por estar siempre ahí, sin hacer ruido, pero velando siempre por nosotros, a Noe por ser el elemento comunicativo de la familia, a David porque sin tu apoyo no habría llegado hasta aquí, a Sergio y Nieves los mejores cuñados que habría podido imaginar, a Aday que ha devuelto la alegría a esta familia. A mi madre, esta tesis va por ti, por haberme enseñado que en la vida hay que luchar siempre por las personas que se quieren y no hay que rendirse nunca ante las dificultades. Te quiero.

Y, a todos los que en estos años han pasado por mi vida, que por mi pobre memoria y porque son muchos no los puedo citar aquí, gracias.

Jairo Méndez Abreu

Resumen

El objetivo fundamental de esta tesis es el estudio de la estructura de las regiones centrales de galaxias con disco, con particular atención al estudio de los bulbos y de las barras, y a los procesos de formación y evolución de estas componentes. Con esta finalidad, han sido analizadas las propiedades estructurales y fotométricas de los bulbos y de las barras, así como sus características cinemáticas y sus poblaciones estelares, en diferentes muestras de galaxias cercanas.

La primera parte de la tesis se basa principalmente en la estructura, cinemática y poblaciones estelares de los bulbos.

En esta parte presentamos un nuevo código de ajuste (GASP2D) para realizar la descomposición fotométrica bidimensional de la distribución de brillo superficial de galaxias con disco. GASP2D asume un perfil de Sérsic para el bulbo y un perfil exponencial para el disco. Las dos componentes poseen isofotas elípticas y concéntricas con elipticidades y ángulos de posición constantes, pero diferentes para cada componente.

Los parámetros estructurales de una muestra de 148 galaxias S0-Sb limitada en magnitud se obtuvieron aplicando GASP2D a las imágenes en banda J proporcionadas por el Two Micron All Sky Survey (2MASS). En este estudio encontramos que los bulbos más grandes son más luminosos y poseen un perfil de brillo más concentrado que el de bulbos más pequeos. Además, estos bulbos se encuentran en discos mayores. Este acoplamiento entre los parámetros estructurales de los bulbos y de los discos ha sido interpretado como una indicación de la formación de los bulbos por evolución secular del disco. Sin embargo, los bulbos en estudio también siguen el mismo plano fundamental, relación Faber-Jackson y plano fotométrico de las galaxias elípticas, lo que sugiere un escenario de formación común dominado por procesos disipativos. Como conclusión, estos resultados nos indican que el análisis de las relaciones de escala no es suficiente para distinguir entre bulbos formados por un colapso disipativo,

por fusiones/interacciones o por evolución secular.

Posteriormente se calculó la función de distribución de probabilidad (PDF) de la elipticidad ecuatorial de los bulbos a partir de la distribución de elipticidades observadas y de la diferencia de ángulos de posición entre el bulbo y el disco. Aproximadamente el 80% de los bulbos en galaxias no barradas lenticulares y espirales tempranas son elipsoides triaxiales. Su relación entre ejes media en el plano ecuatorial es $\langle B/A \rangle = 0.85$ y su PDF no depende significativamente de la morfología, concentración de la luz o luminosidad. Estos resultados no cambian con la presencia de barras nucleares y deben ser tenidos en cuenta por los escenarios de formación de los bulbos.

Los datos fotométricos y espectroscópicos de una muestra de 14 galaxias de cúmulo fueron analizados para estudiar sus propiedades fotométricas y sus poblaciones estelares. Los parámetros estructurales de las galaxias se obtuvieron usando GASP2D sobre las imágenes disponibles en banda R. La cinemática estelar así como la intensidad de las lineas de H_β, Mg, and Fe se midieron usando espectros obtenidos a lo largo del eje mayor de las galaxias. Esto nos ha permitido derivar sus valores de edad, metalicidad y relación α/Fe. Tres clases de bulbos fueron identificados: bulbos jóvenes ($\sim$ 2 Ga) con formación estelar en acto, bulbos de edad intermedia (4-8 Ga) con metalicidad solar y bulbos viejos ($\sim$ 10 Ga) con alta metalicidad. La mayoría de los bulbos presentan relaciones α/Fe solares, no tienen gradientes de edad y presentan un gradiente negativo de metalicidad. Este último favorece un escenario de formación por colapso disipativo, sin embargo, esto implicaría también un gradiente negativo de la relación α/Fe que no se observa. El bulbo de NGC 1292 es el candidato más fiable a ser un pseudobulbo de nuestra muestra. Sus propiedades estructurales son parecidas a las de un disco y su población estelar es consistente con un lento crecimiento dentro de un escenario de evolución secular.

Seis galaxias con un disco estelar de bajo brillo superficial y cuatro con un disco estelar de alto brillo superficial fueron también observadas tanto fotométricamente como espectroscópicamente. Los parámetros estructurales se obtuvieron usando GASP2D. La cinemática estelar y del gas ionizado fue medida a lo largo de los ejes mayor y menor en la mitad de las galaxias, mientras que en la otra mitad sólo a lo largo de dos ejes diagonales. Las medidas cinemáticas se extienden hasta un nivel de brillo superficial $\mu_R \approx 24$ mag arcsec^{-2}, alcanzando en todos los casos la parte plana de la curva de rotación. La cinemática estelar resultó ser más regular y simétrica que la cinemática del gas ionizado, la cual a menudo muestra la presencia de movimientos no circulares, fuera de plano o desordenados. Esto implica que el gas ionizado no es un buen trazador de la velocidad circular en la región central de galaxias LSB, con lo que puede llevar a errores a la hora de calcular la dis-

tribución de masa.

La segunda parte de la tesis se basa principalmente en la estructura, cinemática y frecuencia de las barras en galaxias cercanas.

La fracción de galaxias barradas y sus propiedades se estudiaron en una muestra de $\sim$ 3000 galaxias extraídas del Sloan Digital Sky Survey (SDSS). Estas galaxias representan una muestra limitada en volumen con todas las galaxias situadas en el intervalo de redshift $0.01 < z < 0.04$, más brillantes de $M_{\rm r} = -20$ y con una inclinación i <60°. La fracción de galaxias barradas (45%) se determinó usando dos metodos: ajuste de elipses y análisis de Fourier. Los dos métodos fueron comparados y calibrados con simulaciones de galaxias barradas y no barradas con propiedades parecidas a las observadas. En este estudio encontramos que el 32% de las galaxias S0, el 55% de las espirales de tipo temprano y el 52% de las espirales de tipo tardío son galaxias barradas. Las barras en galaxias S0 son más débiles que las encontradas en tipos morfológicos mas tardíos, además encontramos una correlación entre la longitud de la barra y el tamaño de esta, barras más grandes se encuentran en galaxias con discos mayores. Sin embargo, ni la intensidad de la barra ni su longitud correlan con la densidad local de galaxias, esto sugiere que el entorno local no tiene un papel decisivo en la formación de las barras. Por el contrario, las propiedades internas de las galaxias si determinan las propiedades de las barras. De esta manera, galaxias con una alta concentración central de la luz (galaxias SO) albergan menos barras y estas son más débiles que en tipos mas tardíos.

El código de ajuste GASP2D se mejoró para tener en cuenta la presencia de las barras en galaxias con disco. La distribucion de brillo superficial de la barra puede ser descrita con un perfil plano, elíptico o de Ferrers y viene aadido al modelo del bulbo y del disco. Las isofotas de la barra se construyeron en un sistema de elipses generalizadas, donde se permite que las isofotas no sean elipses perfectas. Estas elipses poseen elipticidades y ángulos de posición constantes y son concéntricas a las del bulbo y del disco. La capacidad de GASP2D v2.0 de recuperar correctamente los parámetros estructurales de las galaxias se comprobó usando galaxias con parámetros conocidos a priori. Además, su potencial se ha comprobado analizando imágenes extraídas del archivo del SDSS.

El estudio sobre la presencia de bulbos tipo *boxy/peanut* (B/P) se realizó gracias a la medida de la cinemática estelar. Observando tres galaxias vista de cara, NGC 98, NGC 600, y NGC 1703, ha sido posible confirmar, por primera vez, la predicción que los bulbos B/P pueden ser identificados en galaxias con baja inclinación. Esto se realizado verificando la presencia de un doble mínimo en el perfil, a lo largo del eje major de la barra, del momento de orden cuatro de Gauss-Hermite, h_4, que describe la distribución de velocidades a lo largo de la línea de vista (LOSVD). En NGC 98, la presencia del doble mínimo es clara a

lo largo el eje mayor de la barra. Por el contrario, en NGC 600 que es también una galaxia barrada, pero no posee un bulbo significativo, no encontramos esta caracteristica cinemática. En el caso de NGC 1703, que es una galaxia de control no barrada, tampoco encontramos, como esperábamos, evidencias de la presencia de un bulbo B/P. También se ha comprobado que la LOSVD es más ancha en la posición del mínimo de h_4 en NGC 98. Este método más directo evita problemas asociados a la medida de la LOSVD y de h_4.

Las conclusiones de la tesis se pueden resumir en tres puntos: (1) Las relaciones de escala, usadas normalmente para el estudio de las galaxias, no pueden ser usadas en solitario para distinguir entre los posibles escenarios de formación propuestos hasta ahora ya que diferentes escenarios son capaces de reproducir las mismas relaciones. Sin embargo, la medida de las propiedades intrínsecas representa un paso adelante en este campo y fija nuevos límites que deben ser reproducidos por las simulaciones. (2) Las propiedades cinemáticas y de las poblaciones estelares de los bulbos son fundamentales e imponen fuertes límites a la formación de los bulbos. Esta información, combinada con las propiedades estructurales de las galaxias puede ayudar a obtener una visión más general de los bulbos necesaria para desvelar su mecanismo de formación. (3) La conexión entre los bulbos y las barras es fundamental para entender la formación de las dos componentes. La posibilidad de identificar bulbos B/P en galaxias con baja inclinación permitirá estudiar la frecuencia de estas estructuras y aclarar finalmente cual es su conexión con las barras.

Riassunto

Questa tesi è dedicata allo studio della struttura delle regioni centrali delle galassie a disco, con particolare attenzione agli sferoidi e alle barre e con lo scopo di far luce sui loro processi di formazione ed evoluzione. A questo fine sono state analizzate sia le proprietà fotometriche e cinematiche che le caratteristiche delle popolazioni stellari di un ampio campione di galassie vicine.

La struttura, la cinematica e le popolazioni stellari degli sferoidi sono studiate nella prima parte della tesi, che si apre con la presentazione di un nuovo codice per la decomposizione fotometrica bidimensione della distribuzione di brillanza superficiale delle galassie a disco. Questo codice, denominato GASP2D, adotta un profilo radiale di brillanza superficiale che segue la legge di Sérsic per gli sferoidi e un profilo radiale esponenziale per i dischi. Entrambe le componenti hanno isofote ellittiche e concentriche con una ellitticità e un angolo di posizione costanti. Le due componenti possono avere angoli di posizioni diversi. Il codice è concepito per tener conto degli effetti osservativi e strumentali delle immagini da analizzare.

Con GASP2D sono state analizzate le immagini in banda J estratte dall'archivio Two Micron All Sky Survey (2MASS) per un campione di 148 galassie di tipo morfologico da S0 a Sb. Si è trovato che gli sferoidi più grandi sono più luminosi e più concentrati di quelli più piccoli. Essi risiedono nei dischi di maggiori dimensioni. Questo accoppiamento tra i parametri strutturali degli sferoidi e dei dischi è stato interpretato come l'indicazione della formazione degli sferoidi a seguito di fenomeni di evoluzione secolare dei dischi. Tuttavia, gli sferoidi studiati seguono le stesse relazioni scala misurate per le galassie ellittiche, suggerendo un comune scenario di formazione dominato da processi dissipativi. Si è quindi concluso che l'analisi delle relazioni di scala non è sufficiente per discriminare se gli sferoidi si siano formati per collasso dissipativo, per fenomeni di accrescimento e interazione o per evoluzione secolare.

Successivamente è stata derivata la funzione di distribuzione delle proba-

bilità (PDF) dell'ellitticità equatoriale degli sferoidi a partire dalle ellitticità osservate e dalla differenza degli angoli di posizione di sferoidi e dischi. Circa l'80% degli sferoidi delle galassie a disco non barrate dei primi tipi morfologici sono ellissoidi triassiali. Il loro rapporto assiale medio sul piano equatoriale è $\langle B/A \rangle = 0.85$ e la PDF non dipende significativamente dalla morfologia, dalla concentrazione e dalla luminosità. Questi risultati non cambiano in presenza di barre nucleari e devono essere presi in considerazione da qualsiasi scenario di formazione degli sferoidi venga proposto.

Per un campione di 14 galassie a disco di ammasso sono stati ottenuti dati sia fotometrici che spettroscopici. I parametri strutturali delle galassie sono stati misurati analizzando con GASP2D le loro immagini in banda R. La cinematica stellare e gli indici Hβ, Mg e Fe sono stati misurati dagli spettri ottenuti lungo gli assi maggiori delle galassie. Questo ha permesso di derivare i valori delle loro età, metallicità e dei rapporti α/Fe. Sono state così identificate tre tipologie di sferoidi: quelli giovani ($\sim$ 2 Gyr) in cui la formazione stellare è ancora attiva, quelli di età intermedia (4-8 Gyr) di metallicità solare e quelli vecchi ($\sim$ 10 Gyr) di alta metallicità. La maggior parte di essi ha un rapporto α/Fe di tipo solare, non mostra gradienti di età ed è caratterizzata da un gradiente negativo di metallicità. Quest'ultimo si spiega ammettendo uno scenario di formazione per collasso dissipativo, che però implicherebbe anche un gradiente negativo di α/Fe, che invece non viene misurato. Tra le galassie del campione è NGC 1292 quella che più probabilmente ospita uno sferoide, con caratteristiche strutturali assimilabili ad un disco e una popolazione stellare con proprietà compatibili con una lenta formazione per evoluzione secolare.

Sei galassie con un disco stellare di bassa brillanza superficiale e quattro galassie con un disco stellare di alta brillanza superficiale sono state osservate sia fotometricamente che spettroscopicamente. I parametri strutturali sono stati derivati con GASP2D e la cinematica di gas e stelle è stata misurata sugli assi maggiori e minori o sugli assi intermedi delle galassie. Le misure cinematiche si estendono fino a livelli di brillanza superficiale di $\mu_R \approx 24$ mag arcsec^{-2}, raggiungento il tratto piatto della curva di rotazione. La cinematica delle stelle è risultata più regolare di quella del gas, che invece è caratterizzato da moti non circolari, disordinati o fuori dal piano galattico. La velocità del gas ionizzato non è dunque un buon tracciante della velocità circolare soprattutto al centro delle galassie con conseguenze sulla corretta derivazione della distribuzione di massa.

La seconda parte della tesi tratta della struttura, cinematica e frequenza delle barre nelle galassie vicine.

La frazione di galassie barrate è stata derivata in un campione di $\sim$ 3000 galassie estratte dalla Sloan Digital Sky Survey (SDSS). Si tratta di un campi-

one definito entro un volume che raccoglie tutte le galassie non interagenti con un redshift di $0.01 < z < 0.04$, più brillanti di $M_{\rm r} = -20$ e con una inclinazione i <60° La frazione di galassie barrate (45%) è stata determinata con due metodi basati sull'analisi delle isofote e su quella di Fourier. Entrambi i metodi sono stati messi alla prova e calibrati con l'analisi di alcune migliaia di immagini di galassie artificiali con proprietà simili a quelle osservate. Si è trovato che il 32% delle galassie S0, il 55% delle spirali dei primi tipi e il 52% delle spirali di tipo avanzato ospitano una barra. Ma la forza e la lunghezza delle barre non correlano con la densità locale di galassie suggerendo che l'ambiente non ha avuto un peso rilevante nella formazione delle barre. Al contrario le proprietà delle barre sono legate a quelle della galassia ospite. In particolare risulta che le barre delle S0 sono meno frequenti e più deboli di quelle delle spirali e le barre più lunghe si trovano nelle galassie con i dischi più grandi.

Il codice di decomposizione fotometrica GASP2D è stato aggiornato per poter analizzare la distribuzione di luce delle galassie barrate. Il modello fotometrico prevede la possibilità di includere una barra con un profilo di brillanza superficiale piatto, alla Ferrers o ellittico in aggiunta allo sferoide e al disco. Le isofote della barra hanno ellitticità costante sono concentriche a quelle dello sferoide e del disco ma possono deviare dalla perfetta forma ellittica e avere un diverso angolo di posizione. L'efficacia del nuovo codice è stata verificata con immagini di galassie barrate di cui i parametri strutturali erano già noti e le sue potenzialità sono state rivelate con l'analisi di immagini estratte dall'archivo della SDSS.

Lo studio degli sferoidi di tipo *boxy/peanut* (B/P) è stato condotto grazie alla misura della loro cinematica stellare. Osservando le galassie NGC 98, NGC 600 e NGC 1703 è stato possibile provare per la prima volta la predizione teorica secondo cui la struttura B/P può essere rivelata anche in galassie viste di faccia. Questo si è fatto verificando la presenza di due minimi simmetrici situati in prossimità della fine della barra nel profilo radiale del coeffieciente di Gauss-Hermite h_4 della distribuzione di velocità lungo la linea di vista (LOSVD). I minimi sono stati osservati in NGC 98, una galassia barrata dotato un cospicuo sferoide, ma non in NGC 600 e NGC 1703. La prima è una galassia barrata senza sferoide, la seconda è una galassia non barrata. Si è anche visto che LOSVD è più larga in corrispondenza dei minimi di h_4, il che offre un ulteriore metodo di misura, meno sensibile alla scelta della parametrizzazione della LOSVD e alla degenerazione tra dispersione di velocità e h_4.

Le conclusioni della tesi possono essere schematizzate in tre punti: (1) le relazioni di scala solitamente usate per studiare le galassie non bastano da sole a discriminare i diversi scenari di formazione degli sferoidi, che devono anche tener conto dei vincoli posti dalla misura dei parametri strutturali delle diverse

componenti che costituiscono una galassia; (2) le proprietà delle popolazioni stellari (età, metallicità e rapporto α/Fe) sono essenziali e complementari ai dati strutturali fotometrici e cinematici quando si tratta di svelare il meccanismo che ha guidato la formazione di uno sferoide; (3) la connessione tra sferoide e barra è cruciale per comprendere la formazione e l'evoluzione di entrambe queste due componenti. La possibilità di individuare sferoidi di tipo B/P anche in galassie di bassa inclinazione permetterà proprio di derivare la frequenza di queste strutture e chiarire finalmente quale sia il loro legame reciproco.

Abstract

In this thesis, we focus on the structural components observed in the central regions of disk galaxies, namely bulges and bars. We aim to better understand the formation and evolution scenarios which could lead to the bulges and bars observed in the nearby universe. This study was performed from an observational point of view, by analyzing either the structural and photometric properties of bulges and bars, their kinematics, and stellar population characteristics.

The first part of the thesis is mainly focussed on the structure, photometry and stellar populations of bulges.

We present a new fitting algorithm (GASP2D) to perform two-dimensional photometric decomposition of the galaxy surface-brightness distribution. We adopted a Sérsic and an exponential profile to describe the surface-brightness distribution of the bulge and disk, respectively. Both components are characterized by elliptical and concentric isophotes with constant (but possibly different) ellipticity and position angles.

The structural parameters of the bulges and disks of a magnitude-limited sample of 148 S0-Sb galaxies were derived from the Two Micron All Sky Survey (2MASS) $J-$band images by means of GASP2D. We found that the surface-brightness radial profiles of larger bulges are more centrally peaked than those of the smaller bulges. Larger bulges have a lower effective surface-brightness and higher absolute luminosities. They reside in larger disks, as revealed by the correlation between central velocity dispersion and disk scale-length. This reveals a strong coupling between bulges and disks. This has been interpreted as an indication of the formation of bulges via the secular evolution of their host disks. However, the bulges of the sample galaxies follow the same fundamental plane, Faber-Jackson, and photometric plane relationships as those found for elliptical galaxies, supporting the idea that bulges and ellipticals formed in the same way. These results indicate that the scaling relations alone are not enough to clearly distinguish between bulges formed by early dissipative

collapse, merging or secular evolution.

The probability distribution function (PDF) of the equatorial ellipticity of the bulges was derived from the distribution of the observed ellipticities of bulges and misalignments between bulges and disks. About 80% of bulges in unbarred lenticular and early-to-intermediate spiral galaxies are not oblate but triaxial ellipsoids. Their mean axial ratio in the equatorial plane is $\langle B/A \rangle = 0.85$. Their PDF is not significantly dependent on morphology, light concentration or luminosity. The scenarios proposed until now in which bulges have assembled from mergers and/or have grown over long times through disk secular evolution have to be tested against this derived PDF of bulge intrinsic ellipticities.

Photometry and long-slit spectroscopy are presented for 14 cluster disk galaxies. The structural parameters of the galaxies are derived from the $R-$band images by means of GASP2D. The rotation curves, velocity dispersion profiles and H_β, Mg, and Fe line-strengths are measured from the spectra obtained along the major-axis of galaxies. Correlations between the central values of Mg_2, $\langle Fe \rangle$, H_β, and σ are found. Three classes of bulges are identified. The youngest bulges ($\sim$ 2 Gyr) with ongoing star formation, intermediate-age bulges (4-8 Gyr) have solar metallicity, and old bulges ($\sim$ 10 Gyr) have high metallicity. Most of the sample bulges display solar α/Fe ratio, no gradient in age, and a negative gradient of metallicity. This metallicity radial profile favors a scenario with bulge formation via dissipative collapse. This implies strong inside-out formation that should give rise to a negative gradient in the [α/Fe] ratio too. But, no gradient is measured in the [α/Fe] radial profiles for all the galaxies, except for NGC 1366. The bulge of NGC 1292 is the most reliable pseudobulge of our sample. The properties of its stellar population are consistent with a slow buildup within a scenario of secular evolution.

Photometry and long-slit spectroscopy are presented for a sample of 6 galaxies with a low surface-brightness (LSB) stellar disk and for 4 galaxies with a high surface-brightness disk. The characterizing parameters of the bulge and disk components were derived by means of GASP2D. The stellar and ionized-gas kinematics were measured along the major and minor-axis in half of the sample galaxies, whereas the other half was observed only along two diagonal axes. Spectra along two diagonal axes were obtained also for one of the objects with major and minor-axis spectra. The kinematic measurements extend in the disk region out to a surface-brightness level $\mu_R \approx 24$ mag arcsec^{-2}, reaching in all cases the flat part of the rotation curve. The stellar kinematics turns out to be more regular and symmetric than the ionized-gas kinematics, which often shows the presence of non-circular, off-plane, and non-ordered motions. This raises the question about the reliability of the use of the ionized gas as the tracer of the circular velocity in the modeling of the mass distribution, in

particular in the central regions of LSB galaxies.

The second part of the thesis is mainly focussed on the structure, photometry, and frequency of bars in nearby galaxies.

The fraction of barred disk galaxies and their properties was studied in a sample of $\sim$ 3000 galaxies from the Sloan Digital Sky Survey (SDSS). This represents a volume limited sample with all non-interacting galaxies located in the redshift range $0.01 < z < 0.04$, brighter than $M_{\rm r} = -20$, and with i <60°. The bar fraction was determined by two methods: ellipse fitting and Fourier analysis. Both methods were tested and calibrated with extensive simulations of barred and non-barred galaxies similar to the observed ones. The fraction of barred galaxies in our sample turned out to be 45%. We split the sample into different morphological types, finding that 32% of S0s, 55% of early-type spirals, and 52% of late-type spirals, are barred galaxies. Neither the bar strength nor the bar length correlates with the local galaxy density, indicating that local environment does not play an important role in bar formation and evolution. In contrast, internal galaxy properties (such as the central light concentration and disk size) determine bar properties. Thus, galaxies with high central light concentrations (i.e., the S0 galaxies) have fewer and weaker bars than late-type ones and the larger bars reside in larger galaxies.

A new version of the fitting algorithm GASP2D was developed to perform two-dimensional photometric decomposition of galaxy surface-brightness distributions taking into account the presence of bars. We adopted a Sérsic and an exponential profile to describe the surface-brightness distribution of the bulge and disk, respectively. The bar surface-brightness distribution can be described by either flat, elliptical or Ferrers profiles. The bulge and the disk are characterized by elliptical and concentric isophotes with constant (but possibly different) ellipticity and position angles. On the contrary, the bar component is built on a frame of generalized ellipses, where boxy and disky shapes are allowed. These ellipses have constant ellipticity and are concentric to those of the other components. We demonstrate the ability of GASP2D v2.0 to recover the correct photometric structural parameters for the bulge, disk and bar components. In addition, we confirm the capacity of the code to work efficiently with the data from the SDSS.

We presented the results of high resolution absorption-line spectroscopy of 3 face-on galaxies, NGC 98, NGC 600, and NGC 1703 with the aim of searching for box/peanut (B/P)-shaped bulges. These observations tested and confirmed, for the first time the prediction that face-on B/P-shaped bulges can be recognized by two minima in the profile along the bar's major axis of the fourth Gauss-Hermite moment h_4 of the line-of-sight velocity distribution (LOSVD). In NGC 98, a clear double minimum in h_4 is present along the

major axis of the bar and before the end of the bar, as predicted. In contrast, in NGC 600, which is also a barred galaxy but lacks a substantial bulge, we did not find any significant kinematic signature for a B/P-shaped bulge. In NGC 1703, which is an unbarred control galaxy, we found no evidence of a B/P bulge. We also show directly that the LOSVD is broader at the location of the h_4 minimum in NGC 98 than elsewhere. This more direct method avoids possible artifacts associated with the degeneracy between the measurement of line-of-sight velocity dispersion and h_4.

The conclusions of this thesis can be summarized in three main points: (1) The typical scaling relations for galaxies cannot be used alone to distinguish between the different formation scenarios proposed until now since different models are able nowadays to reproduce these relations. Measuring the intrinsic structural properties represents an useful step forward in this field and sets new constraints that should be reproduce by numerical simulations for galaxy formation; (2) the kinematic and stellar population properties of bulges give strong additional constraints needed to unveil their formation mechanism; (3) the link between bulges and bars appears to be fundamental to understand the formation of both components. The existence of boxy/peanut bulges and their relation with bars can be now investigated by a new kinematic diagnostic that can be applied in face-on galaxies. This result opens a new line of research which will help to give a more general scheme of bulge/bar formation and evolution.

Contents

List of Tables

List of Figures

1

Introduction

The formation and evolution of galaxies is nowadays one of the foremost questions in astronomy. The complexity of the dynamical processes which involves the principal components of the universe, namely dark matter, gas and stars is still not well understood.

Since galaxies span a wide range of morphologies, luminosities, masses, and sizes, the first studies of their properties were based on a taxonomic subdivision according to their visual properties. In 1936, Edwin Hubble introduced the "Tuning Fork" scheme for the classification of galaxies (see Fig. 1.1). In this first study, Hubble suggested that galaxies evolved from the left-hand to the right end of this sequence. This speculation is now discredited , but galaxies that lie at the left-hand end of the sequence are still called early-type galaxies, while those toward the right-hand end are referred to as late-type galaxies. One of the main qualitative criteria used by Hubble was the ratio between the luminosity of the spheroidal component and the total luminosity of the galaxy (B/T). On the left hand of the Hubble diagram are placed those galaxies without a disk, therefore with $B/T \sim 1$, and which appear to be smooth and structureless. They were called elliptical galaxies due to the shape of their isophotes and they were organized as a function of their flattening. The more flattened ellipticals were positioned on the left side of the diagram. After the elliptical galaxies, Hubble's diagram bifurcates into two branches, the "normal" and the "barred" galaxies. These two types are mainly characterized by the presence of a stellar disk, and are usually called spiral galaxies due to the presence of star-forming spiral arms in their disks. A "normal" spiral galaxy contains also a central brightness condensation (the bulge or the spheroidal component) sim-

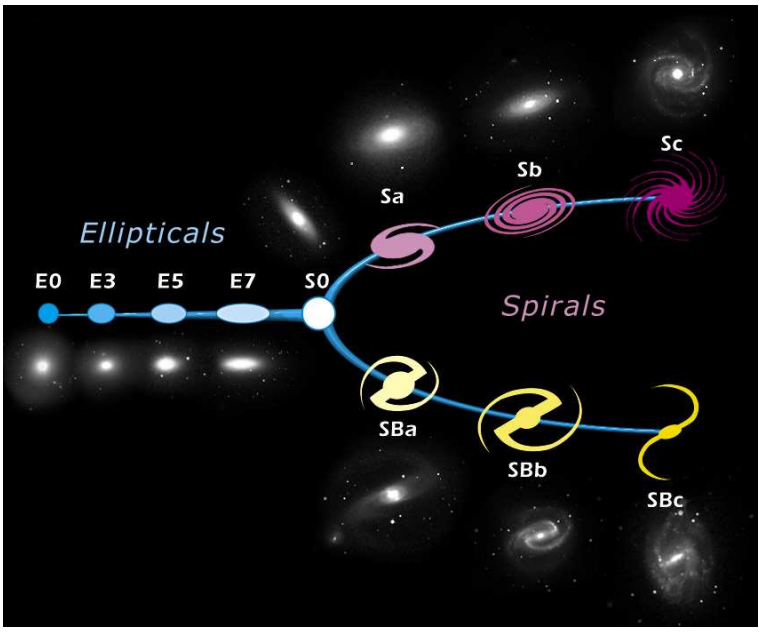

FIGURE 1.1— Hubble's galaxy classification scheme.

ilar to an elliptical galaxy. A barred spiral contains, interior to the spiral arms, a prominent stellar structure with a bar shape. This bar often contains dark lanes produced by the absorption of the light by dust. The B/T ratio of spiral galaxies has been a matter of debate in recent years. In the work of Simien & de Vaucouleurs (1986), they show a good correlation between the B/T ratio and the Hubble morphological type for spiral galaxies, with a B/T ranging from about 0.5 to $\sim$0 for early- and late-type spirals, respectively. However, a recent study by Laurikainen et al. (2007) has pointed out that the contribution of the spheroidal component is actually smaller, ranging from $B/T \sim 0.25$ to $\sim$0, and that this difference is probably due to the more sophisticated decomposition algorithm, including the bar component, used in this latter work. Lenticular galaxies were placed in the transition between these two broad morphological types. Lenticular galaxies differ from ellipticals by the presence of a stellar disk. However, unlike the disk of spiral galaxies those of lenticular galaxies have no spiral structure and are not actively forming stars..

1.1 Properties of stellar disks

The radial surface-brightness profiles of galaxy stellar disks are usually assumed to be exponential in nature, though it is by no means obvious that a galaxy disk

should have an exponential profile. One of the more successful early attempts to show that an exponential disk could form naturally was by Yoshii & Larsen (1989). They found that an exponential disk forms if the time scales for viscosity and the star formation are comparable (see, for recent studies, Ferguson & Clark 2001; Slyz et al. 2002). Although early attempts to derive exponential disks from first principles in cosmological simulations yielded disks with an excess of brightness in the inner profiles (Navarro & White 1994), more recent experiments in which star formation was included in the simulations have been more successful (Robertson et al. 2004; Governato et al. 2007).

Freeman (1970) pointed out that not all disks are simple exponentials. In particular, he identified two basic types of disk profiles: Type I, in which the disk show a simple exponential form; and Type II, where the outer part of the disk shows a purely exponential fall-off, but where the inner part of the profile falls below the inward projection of the outer exponential. Another feature which is sometimes taken to be a general property of disks is that of a truncation of the stellar population at large radii, typically 2-4 exponential scale-lengths (van der Kruit 1979; van der Kruit & Searle 1981a; van der Kruit & Searle 1981b; Pohlen et al. 2004). They were inferred primarily from the major-axis profiles of edge-on, late-type spirals. More recently, Pohlen et al. (2002) used deep images of three face-on spirals to show that the truncation actually takes the form of a change in slope, from the shallow exponential of the main disk to a steeper exponential at larger radii. From this perspective, truncations can be seen as another form of Freeman's Type II profile, with breaks at fainter surface-brightness levels than was typical of Freeman's original sample.

Evidence for a third general class of disk profiles has been presented by Erwin et al. (2005) for early-type disks and by Hunter & Elmegreen (2005) and Pohlen & Trujillo (2006) for late-type disks; an earlier identification of this phenomenon in extreme late-type spirals is that of Matthews & Gallagher (1997). In this class, called Type III (or "antitruncation") by Erwin et al. (2005), the inner profile is a relatively steep exponential, which gives way to a shallower surface- brightness profile (which may or may not be exponential itself) beyond the break radius. This profile is thus something like the inverse of a Type II profile, bending up instead of down beyond the break radius. Elmegreen & Hunter (2006) showed that something like a Type III profile could result from star formation if the initial gas disk has the right (ad-hoc) radial density profile; more recently, Younger et al. (2007) argued that minor mergers can produce Type III profiles.

1.2 The central regions of disk galaxies

Throughout this thesis, I will refer to the central regions of disk galaxies considering only the bulge and the bar components. However, it is worth remembering that central regions of disk galaxies, specially the most inner regions, are rich of different substructures. In the recent years, the Hubble Space Telescope has opened a new window on this issue allowing the scientist to zoom into the central regions of disk galaxies. Among the new discovered structures we can point out the following: *nuclear stellar disks*, they are characterized by a smaller scale-length and higher central surface-brightness with respect to the large kiloparsec scale disks typical of lenticular and spiral galaxies. Nuclear stellar disks were first discovered in ellipticals and S0 galaxies (Scorza & Bender 1995; Seifert & Scorza 1996). Up to now the smallest disks we know have scale-lengths of a few tens of parsecs, and they have been identified in the nuclei of a handful of early-type disk galaxies (Burkhead 1986; Kormendy 1988; Burkhead 1991; Emsellem et al. 1994; Lauer et al. 1995; Emsellem et al. 1996; van den Bosch et al. 1998; Scorza & van den Bosch 1998; Pizzella et al. 2002). *Nuclear clusters*, they are common structures in late Hubble types (Carollo et al. 1998), usually these nuclei appear pointlike in the HST images. However, many are marginally resolved with half-light radii $0\farcs1$-$0\farcs2$, corresponding to linear scales from a few up to 20 pc (Carollo et al. 1997; Böker et al. 2002). *Nuclear bars*, these inner or nuclear bars were first discovered as optical isophote twists in the central regions of barred galaxies (e.g., de Vaucouleurs 1974; Sandage & Brucato 1979; Kormendy 1982) and interpreted as triaxial bulges of barred galaxies. Later on, ground-based studies at higher resolution have revealed more galaxies with nuclear bars, lying inside large galactic bars (Wozniak et al. 1995; Laine et al. 2002; Erwin 2004). The study of these inner components is beyond the scope of this thesis.

1.3 Properties of bulges

About 25% of the stellar luminosity in the universe is contained in the bulges of spiral galaxies (e.g., Persic & Salucci 1992; Fukugita et al. 1998). Understanding their formation is therefore a necessary step in understanding galaxy formation in general. However, defining what is a bulge is not a straightforward task. Some people define a bulge as the protuberance that swells out of the central part of a disk seen edge-on, other authors state that bulges are ellipticals that happen to have a prominent disk around them. However, the most used and maybe the most operative definition is to consider a bulge as the extra light in the central region of the disk, above the exponential profile. This definition overcomes problems with galaxy inclination and assumes that

disks are symmetric and thin structures with a radial luminosity distribution well described by an exponential profile.

From the morphological point of view, the first ground based datasets consider that the radial surface-brightness of bulges follow reasonably well a $r^{1/4}$ profile (de Vaucouleurs 1948). Later results, using the more general Sérsic profile (Sérsic 1968), showed evidence of a continuum in the shape of bulges, changing from the deVaucouleurs profile for early-type galaxies to an exponential profile as we move toward later type galaxies (Andredakis et al. 1995). High spatial-resolution observations indicate that bulges do not follow the $r^{1/4}$ law after all, and that the high n values obtained from ground-based observations are the result of nuclear point sources blending with the bulge light due to seeing (Balcells et al. 2003). Therefore, early-type bulges form a continuum with the late-type bulges in terms of the shapes of the surface-brightness profiles.

The kinematics of a galactic bulge is somewhat harder to measure than that of an elliptical galaxy: light from the surrounding disk contaminates the observable properties of the bulge, and obscuration due to the dust further complicates the analysis. The observation of the bulge of a disk galaxy that lies reasonably close to face-on allows us to measure its central velocity dispersion with little contamination from the disk. Combining such kinematic measurements with the bulge structural properties suggests that these systems lie on the same fundamental plane as ellipticals. One solution to the problem of the disk contamination is to observe edge-on systems, the surface-brightness of the disk drops rapidly with distance from the galactic plane, so we see fairly pure bulge kinematics in regions away from the major-axis of an edge-on galaxy. Kinematic maps derived from the observations of edge-on galaxies reveal that bulge kinematics vary smoothly with distance from the galaxies' central plane. Consequently, some estimates can be made about the bulge kinematics along the major-axis by extrapolating off-axis observations down to the plane of the galaxy. Such analysis has shown that rotational velocities are, on average, higher for bulges than for elliptical galaxies with similar luminosities (Davies & Illingworth 1983; Kormendy & Illingworth 1982). The (v/σ) diagram is a very powerful tool to characterize the nature of galactic bulges. Kormendy & Illingworth (1982) showed that bulges fall close to the oblate rotators i.e., the isotropic objects flattened by their own rotation. Kormendy & Illingworth (1982) and Davies et al. (1983) showed that bulges have the same kinematic behaviour as intermediate mass ellipticals. The bulges for which kinematics was available at that time were all large bulges of early-type spirals. Later, Kormendy (1982) could add other bulges to the diagram. He found that some of them had a larger (v/σ) than expected for an isotropic rotator, showing a more disk-like kinematics. In recent years, the picture is becoming clearer. Many

galaxies have been discovered in which a thin, rotating disk is dominating the light in the very inner parts, accompanied by a local minimum in the velocity dispersion. The first observed cases of central velocity dispersion minima date back to the late 80s and early 90s (e.g., Bottema 1989, 1993). Several others were found from long-slit data (Emsellem et al. 2001; Márquez et al. 2003). SAURON observations showed that 13 out of 24 Sa and Sab galaxies are characterized by a central local minimum in the velocity dispersion (Falcón-Barroso et al. 2006). These σ-drops are probably due to central disks that formed from gas falling into the central regions through a secular evolution process.

From the stellar populations point of view, spectroscopic studies of the metallicity and age of the central parts of bulges were pioneered by Bica (1988). During the following years, clear evidence was provided for a central metallicity luminosity (Z/L) relation. Several studies underlined the similarities between ellipticals and bulges (Jablonka et al. 1996; Idiart et al. 1996), both with respect to the slope of the Z/L relation and to the similar apparent α/Fe element overabundances (relative to solar abundance ratios) in the two types of systems. The Hubble type of the parent galaxy appeared to have little influence on the stellar population properties of the bulge, which instead scaled mainly with central velocity dispersion and bulge luminosity (Jablonka et al. 1996). A few years later, possible distinctions were suggested between bulge properties of late-type spirals and those of early-type spirals (Falcón-Barroso et al. 2002; Proctor & Sansom 2002). As pointed out by Thomas & Davies (2006) however, these apparent differences seem to disappear when the appropriate range of central velocity dispersion is considered. It is also true that the homogeneity of the samples and their sizes have an impact on the conclusions. Substantial progress would be possible with spatially resolved spectroscopy of bulges, so that radial gradients of their stellar population can be measured. Unfortunately, investigations of such radial gradients using large surveys have so far addressed only early-type galaxies i.e., elliptical and lenticular galaxies, with only very modest and rare excursions into later type galaxies (Sansom et al. 1994; Ganda et al. 2006; Moorthy & Holtzman 2006). For late-type bulges (type Sbc and later) most of our information comes from HST studies (e.g., Böker et al. 2002, 2003; Carollo et al. 2002). We know that late-type spirals have nuclear clusters that are more prominent than the ones in early-type spirals. Colors indicate that the central regions are full of dust and young stars. Given the fact that these bulges are very small compared to their disks, it is hard to establish whether these young stars and dust are situated in the disk or in the bulge. In our own Milky Way one is able to de-contaminate the bulge from the disk using e.g. proper motions. In this way Zoccali et al. (2003) find that the Galactic bulge is old, around 12-13 Gyr in age.

1.3.1 Formation theories for bulges

In the last years, it has become usual to consider that bulges in disk galaxies can be divided schematically into at least three different types (Athanassoula 2005). These three types are characterized by different formation histories and show different observational properties. However, it is worth noting that we live in an universe in transition, where the dominant processes (see Fig. 1.2) which drive the galactic evolution are changing as a function of the cosmic epoch (Kormendy & Kennicutt 2004). This implies that different kind of bulges and different evolutionary processes can coexist in the same galaxy (Athanassoula 2005). Rapid processes that happen in discrete events are giving way to slow, ongoing processes. Specifically, the processes leading to some kinds of bulges are bar driven. Therefore, a fundamental key to study the formation of bulges is the study of the formation and evolution of bars and their link with the bulges in the central regions of disk galaxies.

Classical bulges

They are formed by gravitational collapse (Eggen et al. 1962; Sandage 1990; Gilmore & Wyse 1998; Merlin & Chiosi 2006) or by hierarchical merging of small objects (Kauffmann 1996; Baugh et al. 1996; Cole et al. 2000). The formation process of these bulges might occur in a short period of time before the formation of the galaxy disk (Steinmetz & Muller 1995; Samland & Gerhard 2003; Sommer-Larsen et al. 2003). However, numerical simulations have demonstrated that it is also possible to built up a classical bulge by acreeting small substructures even after the disk is already settled (Aguerri et al. 2001b; Fu et al. 2003; Eliche-Moral et al. 2006).

This kind of bulges might share important characteristics with elliptical galaxies, i.e., they should present a luminosity profile well described by a Sérsic law with high n index (Scannapieco & Tissera 2003; Tissera et al. 2006). Their kinematic properties are well described by dynamical models of rotationally flattened oblate spheroids with little or no anisotropy, and should be formed by type II stellar population (see Fig. 1.3). From an observational point of view, several authors have associated this scenario wit the bulges of early-type galaxies. These bulges present mainly an $r^{1/4}$ profile (Andredakis et al. 1995; Möllenhoff & Heidt 2001), kinematics mainly dominated by random motions (Kormendy & Illingworth 1982; Davies & Illingworth 1983; Cappellari et al. 2006) and formed the bulk of their stellar populations between redshift 3 and 5 ($\sim$ 12 Gyr) on a short time-scale (Wyse et al. 1997; Mehlert et al. 2003; Thomas et al. 2005).

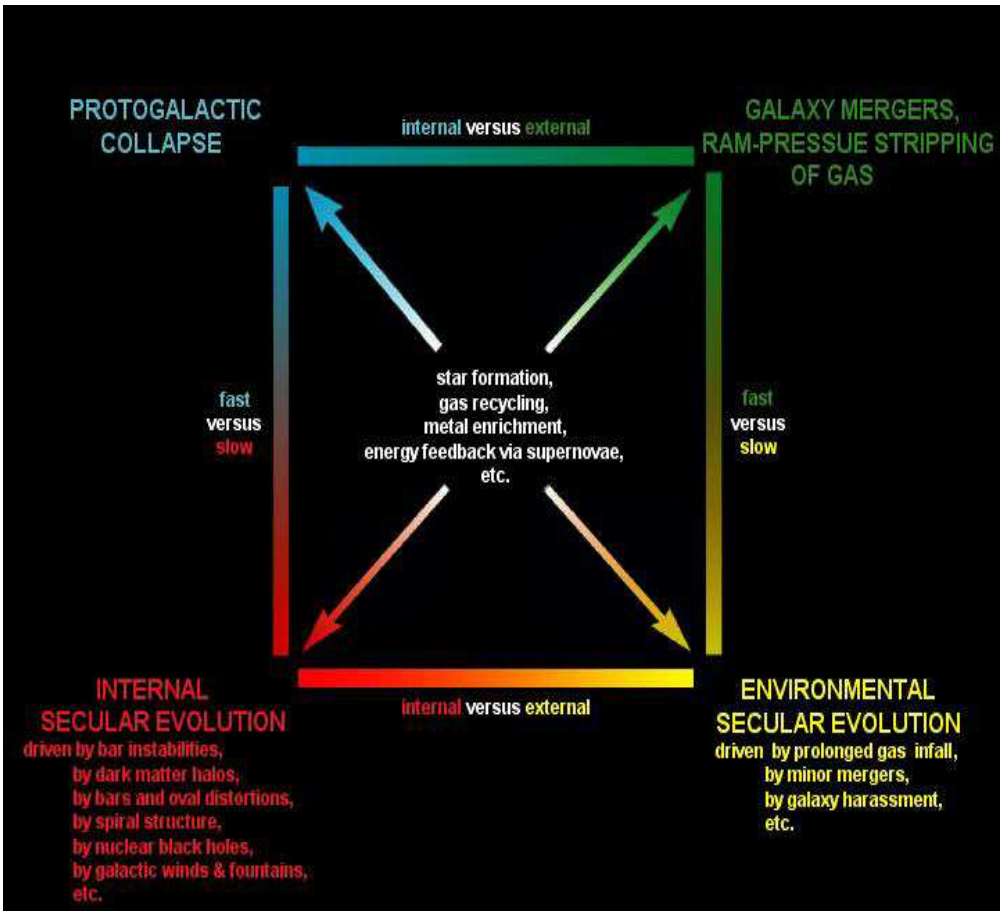

FIGURE 1.2— Morphological box diagram taken from Kormendy & Kennicutt (2004) . Processes are divided vertically into fast (top) and slow (bottom). Fast evolution happens on a free-fall timescale, $t_{\rm dyn} \sim (G\rho)^{-1/2}$, where ρ is the density of the object produced and G is the gravitational constant. Slow means many galaxy rotation periods. Processes are divided horizontally into ones that happen purely internally in one galaxy (left) and ones that are driven by environmental effects such as galaxy interactions (right). The processes at the center are common to all types of galaxy evolution.

Boxy/peanut (B/P) bulges

These objects are believed to be formed by the natural evolution of barred galaxies and have been observed during the past (Burbidge & Burbidge 1959; Jarvis 1986). After the bar formation, some of the bar particles acquire vertical motions whose amplitudes grow with time (Raha et al. 1991; Debattista et al. 2004; Martínez-Valpuesta et al. 2006). For this reason, when viewed edge-on,

FIGURE 1.3— Sombrero (M104) galaxy. A Sa galaxy hosting a classical bulge [NASA and The Hubble Heritage Team (STScI/AURA)].

they show a characteristic B/P shape (see Fig. 1.4 and Fig. 1.5). Objects formed in this way should present morphological, photometric and kinematic characteristics similar to the bars predicted in N-body simulations, while the stellar population must be similar to the internal disk, at least out to a radius comparable to the B/P feature. In addition, it has been noted that the fraction of B/P in edge-on galaxies is $\sim 45\%$ (Lütticke et al. 2000) which is consistent with the fraction of galaxies containing bars $\sim 70\%$ (Knapen et al. 2000; Eskridge et al. 2000) once the arbitrary position of the bar is taken into account. This is consistent with the theory explained above that B/P structures form part of the bar even if little is known observationally about them.

In edge-on disk galaxies, direct confirmation of the relation between B/P bulges and bars comes from kinematic measurements of ionized-gas emission and stellar absorption lines. The kinematics show the behavior expected of barred spirals viewed edge-on. This has been demonstrated by the observations of Kuijken & Merrifield (1995), Vega-Beltrán et al. (1997), Merrifiel & Kuijken (1999), Bureau & Freeman (1997, 1999) and Chung & Bureau (2004), and by the modeling of Athanassoula & Bureau (1999) and Bureau & Athanassoula (1999, 2005). Recently, Bureau et al. (2006) have demonstrated the presence of B/P bulges in edge-on galaxies using only photometric data.

FIGURE 1.4— Edge-on view of NGC 4565. A typical Sb galaxy hosting a boxy bulge [Bruce Hugo, Leslie Gaul, and Adam Block (KPNO Visitor Program)].

However, in galaxies with low inclination, this feature is masked by the projection of the B/P onto the disk plane. This makes it impossible to compare the basic properties of these bulges and bars with those of face-on galaxies. Debattista et al. (2005) proposed a new kinematic diagnostic to detect B/P bulges in face-on galaxies, namely a double minimum in the fourth-order Gauss-Hermite parameterization of the line-of-sight velocity distribution (LOSVD) along the major-axis of the bar. These minima occur because at the location of the B/P shape, the vertical density distribution of stars become flat. In face-on systems the viewing geometry is well constrained and bars can be fully characterized. If we can also recognize peanuts in them, then we obtain an important new perspective on the relation of peanuts and bars. For example, this permits study of the relative sizes of bars and peanuts. Moreover, it becomes possible to measure accurately the pattern speed of the bar (Debattista 2003) and therefore to test for resonances and compare with theoretical predictions. It would also allow determination of the fraction of barred galaxies with peanuts, which may be different from the fraction of peanuts with bars. And finally the ability to detect peanuts face-on opens the possibility of exploring bulge formation mechanisms.

FIGURE 1.5— Hickson Compact Group 87. Galaxy 87a at the bottom of the image hosts the typical X-shaped peanut bulge [NASA and The Hubble Heritage Team (STScI/AURA)].

Disk-like bulges

They are usually called pseudobulges (Kormendy & Kennicutt 2004). These bulges might be formed due to secular processes inside the galaxy, which are intimately related with the bar. In a first hypothesis, the gas is driven inward, due to the forces exerted by the bar, forming an inner disk or ring. When the inner component becomes massive enough, it starts to form stars and it is observed as a pseudobulge (Athanassoula 1992; Wada & Habe 1992; Heller & Shlosman 1994). In a second hypothesis, the accumulation of material in the galaxy center, if it becomes too massive, can even destroy the bar. Therefore, the pseudobulge is a mix of bar and inner component material (Hasan et al. 1993; Bournaud & Combes 2002; Shen & Sellwood 2004). Bulges formed in this scenario should show a flattened structure, follow an exponential luminosity profile, rotate as fast as disks, and host a young stellar population (see Fig. 1.6). These properties have been observed mainly in bulges of late-type spiral galaxies. Bulges of these Hubble types are better represented by an exponential profile (Andredakis & Sanders 1994; Courteau et al. 1996; de Jong 1996;

FIGURE 1.6— NGC 3370 galaxy. A Sc galaxy hosting a disk-like bulge [NASA and The Hubble Heritage Team (STScI/AURA)].

MacArthur et al. 2003), the kinematics of their stars is mainly dominated by rotation (Kormendy 1993; Kormendy et al. 2002), and present a stellar population younger than early-type bulges (Trager et al. 1999; Goudfrooij et al. 1999; Thomas & Davies 2006). However, disk-like bulges have been also identified in early-type galaxies (Erwin et al. 2004).

1.4 Properties of bars

On the other hand, stellar bars are quasi-elliptical structures which are present in most of the disks of spiral galaxies (Marinova & Jogee 2007; Menéndez-Delmestre et al. 2007). This is also true at high redshift, since the bar fraction is constant out to redshift $z \sim 1$ (Marinova & Jogee 2007). Therefore, the study of bar properties is fully related to the study of bulges and a compulsory issue in studying the central regions of disk galaxies.

In addition, stellar bars have been recognized as the most important internal factor in redistributing the angular momentum of the baryonic and dark matter components of disk galaxies (Weinberg 1985; Debattista & Sellwood 1998; Athanassoula & Misiriotis 2002; Berentzen et al. 2006). Bars drive gas efficiently from the outer disk to the central few hundred parsecs and are observed to feed central starbursts in local galaxies (Elmegreen 1994; Jogee et al.

2005). In several galaxies, bar-driven gas inflows appear intimately related to the formation of disky bulges (Kormendy & Kennicutt 2004)

Bars are fully characterized by three parameters: Two of them photometric (size and strength) and the other dynamical (pattern speed). Intuitively, the easiest parameter to be measured should be the bar radius. However, there are several problems associated with this measurement which are mainly related to the difficulties in determining the true shape of bars. Athanassoula et al. (1990) showed that good fits to the bar isophotes can be obtained with generalized ellipses, which are elliptical curves either boxy or disky as a function of an extra parameter c (see Chapter 8). Several methods have been developed in the literature for obtaining the length of the bars (see Erwin 2005 for an observational review and Michel-Dansac & Wozniak 2006 for measurement on simulated galaxies) obtaining differences in the measurement as big as 35%.

With respect to the bar strength, in de Vaucouleurs' morphological classification, the bars are divided into strong and weak bars based on visual inspection of how prominent the bar looks in the optical images. Nowadays, bars are generally characterized as strong when they are long and massive, and also when they have large ellipticities (Aguerri 1999; Whyte et al. 2002) or the tangential forces induced by bars are large (Buta & Block 2001). Like the bar radius, the bar strength has been historically measured by different approximations. The most used method is the so-called Q_g parameter defined by Buta & Block (2001), which represents the maximum value of the ratio of the tangential force to the mean axisymmetric radial force in a barred galaxy.

The key dynamical parameter of a stellar bar is its pattern speed $\Omega_{\rm p}$, that is, the angular velocity with which its figure rotates. Bar pattern speeds are most usefully parameterized by the distance-independent ratio $\mathcal{R} = R_{\rm cr}/a_{\rm bar}$, where $R_{\rm cr}$ and $a_{\rm bar}$ are the corotation radius and the bar semi-major axis, respectively. Bars that end near corotation ($1 \leq \mathcal{R} \leq 1.4$) are termed fast, while shorter bars ($\mathcal{R} > 1.4$) are said to be slow. Several observational methods have been proposed in the literature to measure the bar pattern speed, among others: looking for minima in the star formation outside the bar regions (Cepa & Beckman 1990); variation of colors out from the bar region (Aguerri et al. 2000); hydrodynamical simulations (Laine et al. 1998; Aguerri et al. 2001a; Weiner et al. 2001), variation of the Fourier $m = 2$-phase (Puerari & Dottori 1997; Aguerri et al. 1998). However, the best observational method is the Tremaine-Weinberg method (Tremaine & Weinberg 1984). This method measures $\Omega_{\rm p}$ directly from kinematic observations of a tracer which satisfies the continuity equation. This is a good approximation for the stars in gas-poor early-type disk galaxies. The Tremaine-Weinberg method has been applied to a small, but growing, sample of high surface-brightness disk galaxies; all these measurements

have found fast bars (Debattista et al. 2002; Aguerri et al. 2003; Debattista & Williams 2004; Corsini et al. 2003, 2007). Even if, in principle, gas is not a good tracer since does not satisfy the continuity equation, Fathi et al. (2007) demonstrate how excellent linear fits and therefore clear pattern speed can be obtained using integral field spectroscopy of H_α-emmiting gas.

1.5 Aims and outline of this thesis

In this thesis, we focus on the structural components observed in the central regions of disk galaxies, namely bulges and bars. We aim to better understand the formation and evolution scenarios which could lead to the bulges and bars observed in the nearby universe. This study was performed from an observational point of view. We analyzed either the structural and photometric properties of bulges and bars, and their kinematic and stellar population characteristics. In this way, we planned to obtain a more complete description of the physical processes involved in the galactic centers. As we have shown above, much progress in this field has been achieved in the last years, but a lot of questions still remain unanswered. How and when did bulges and disks form?. What is their intrinsic shape?. Is the formation of bulges and bars intimately linked?. What the connection of B/P with bulges and bars?. This thesis was organized in two main blocks. From chapters 2 to 6, we focus mainly on the structure, photometry and stellar populations of bulges, we will show our new code designed to perform two-dimensional photometric decomposition (GASP2D) and its application to different fields of galactic astronomy. From chapters 7 to 10, we study the principal characteristics of bars, their frequency in the nearby universe, their photometric properties and their relation to the B/P structure. The detailed structure of this thesis is as follows:

Chapter 2. We present a new fitting algorithm (GASP2D) to perform two-dimensional photometric decomposition of the galaxy surface-brightness distribution. We adopted a Sérsic and an exponential profile to describe the surface-brightness distribution of the bulge and disk, respectively. Both components are characterized by elliptical and concentric isophotes with constant (but possibly different) ellipticity and position angles. The GASP2D technical implementation, the minimization algorithm, and the seeing treatment are described in detail in this chapter.

Chapter 3. The structural parameters of the bulges and disks of a magnitude-limited sample of 148 S0-Sb galaxies were derived from 2MASS $J-$band images. We used GASP2D, our new code for two-dimensional photometric decomposition. We found that the surface-brightness radial profiles of larger bulges are more centrally peaked than those of the smaller bulges. Larger bulges have a

lower effective surface-brightness and higher absolute luminosities. They reside in larger disks, as revealed by the correlation between central velocity dispersion and disk scale-length. This reveals a strong coupling between bulges and disks. This has been interpreted as an indication of the formation of bulges via the secular evolution of their host disks. However, the bulges of the sample galaxies follow the same fundamental plane, Faber-Jackson, and photometric plane relationships as those found for elliptical galaxies, supporting the idea that bulges and ellipticals formed in the same way. These results indicate that the scaling relations alone are not enough to clearly distinguish between bulges formed by early dissipative collapse, merging or secular evolution.

Chapter 4. The probability distribution function of the equatorial ellipticity of the bulges was derived from the distribution of the observed ellipticities of bulges and misalignments between bulges and disks. About 80% of bulges in unbarred lenticular and early-to-intermediate spiral galaxies are not oblate but triaxial ellipsoids. Their mean axial ratio in the equatorial plane is $\langle B/A \rangle = 0.85$. Their probability distribution function is not significantly dependent on morphology, light concentration or luminosity. Montecarlo simulations using mock galaxies have demonstrated how the possible presence of nuclear bars does not influence these results. The scenarios proposed until now in which bulges have assembled from mergers and/or have grown over long times through disk secular evolution have to be tested against this derived distribution of bulge intrinsic ellipticities.

Chapter 5. Photometry and long-slit spectroscopy are presented for 14 S0 and spiral galaxies of the Fornax, Eridanus, and Pegasus clusters, and NGC 7582 group. The structural parameters of the galaxies are derived from the $R-$band images by performing a two-dimensional photometric decomposition of the surface-brightness distribution. The rotation curves, velocity dispersion profiles and H_β, Mg, and Fe line-strengths are measured from the spectra obtained along the major-axis of galaxies. Correlations between the central values of Mg_2, $\langle Fe \rangle$, H_β, and σ are found. Three classes of bulges are identified. The youngest bulges ($\sim$ 2 Gyr) with ongoing star formation, intermediate-age bulges (4-8 Gyr) have solar metallicity, and old bulges ($\sim$ 10 Gyr) have high metallicity. Most of the sample bulges display solar α/Fe ratio, no gradient in age, and a negative gradient of metallicity. This metallicity radial profile favors a scenario with bulge formation via dissipative collapse. This implies strong inside-out formation that should give rise to a negative gradient in the [α/Fe]ratio too. But, no gradient is measured in the [α/Fe] radial profiles for all the galaxies, except for NGC 1366. The bulge of NGC 1292 is the most reliable pseudobulge of our sample. The properties of its stellar population are consistent with a slow buildup within a scenario of secular evolution.

Chapter 6. Photometry and long-slit spectroscopy are presented for a sample of 6 galaxies with a low surface-brightness stellar disk and for 4 galaxies with a high surface-brightness disk. The characterizing parameters of the bulge and disk components were derived by means of a two-dimensional photometric decomposition of the images of the sample galaxies. The stellar and ionized-gas kinematics were measured along the major and minor-axis in half of the sample galaxies, whereas the other half was observed only along two diagonal axes. Spectra along two diagonal axes were obtained also for one of the objects with major and minor-axis spectra. The kinematic measurements extend in the disk region out to a surface-brightness level $\mu_R \approx 24$ mag arcsec^{-2}, reaching in all cases the flat part of the rotation curve. The stellar kinematics turns out to be more regular and symmetric than the ionized-gas kinematics, which often shows the presence of non-circular, off-plane, and non-ordered motions. This raises the question about the reliability of the use of the ionized gas as the tracer of the circular velocity in the modeling of the mass distribution, in particular in the central regions of low surface-brightness galaxies.

Chapter 7. The fraction of barred disk galaxies and their properties was studied in a sample of $\sim$ 3000 galaxies from SDSS fifth data release (SDSS-DR5). This represents a volume limited sample with all galaxies located in the redshift range $0.01 < z < 0.04$, brighter than $M_{\rm r} = -20$, and with i <60°. Galaxies with signs of interactions were excluded from the sample. The bar fraction was determined by two methods: ellipse fitting and Fourier analysis. Both methods were tested and calibrated with extensive simulations of barred and non-barred galaxies similar to the observed ones. The fraction of barred galaxies in our sample turned out to be 45%. We split the sample into different morphological types, finding that 32% of S0s, 55% of early-type spirals, and 52% of late-type spirals, are barred galaxies. Bars in S0 galaxies were weaker than those in the galaxies of later morphological types. We also found a correlation between the bar length and galaxy size, larger bars being located in larger galaxies. Neither the bar strength nor the bar length correlates with the local galaxy density, indicating that local environment does not play an important role in bar formation and evolution. In contrast, internal galaxy properties (such as the central light concentration) determine bar properties. Thus, galaxies with high central light concentrations (i.e., the S0 galaxies) have fewer and weaker bars than late-type ones.

Chapter 8. In this chapter, a new version of the fitting algorithm GASP2D was developed to perform two-dimensional photometric decomposition of galaxy surface-brightness distributions taking into account the presence of bars. We adopted a Sérsic and an exponential profile to describe the surface-brightness distribution of the bulge and disk, respectively. The bar surface-brightness

distribution can be described by either flat, elliptical or Ferrers profiles. The bulge and the disk are characterized by elliptical and concentric isophotes with constant (but possibly different) ellipticity and position angles. On the contrary, the bar component is built on a frame of generalized ellipses, where boxy and disky shapes are allowed. These ellipses have constant ellipticity and are concentric to those of the other components. We demostrate the ability of GASP2D v2.0 to recover the correct photometric structural parameters for the bulge, disk and bar components. In addition, we confirm the capacity of the code to work efficiently with the data from the Sloan Digital Sky Survey.

Chapter 9. In this chapter, We presented the results of high resolution absorption-line spectroscopy of 3 face-on galaxies, NGC 98, NGC 600, and NGC 1703 with the aim of searching for box/peanut (B/P)-shaped bulges. These observations tested and confirmed, for the first time the prediction that face-on B/P-shaped bulges can be recognized by two minima in the profile along the bar's major axis of the fourth Gauss-Hermite moment h_4 of the line-of-sight velocity distribution (LOSVD). In NGC 98, a clear double minimum in h_4 is present along the major axis of the bar and before the end of the bar, as predicted. In contrast, in NGC 600, which is also a barred galaxy but lacks a substantial bulge, we did not find any significant kinematic signature for a B/P-shaped bulge. In NGC 1703, which is an unbarred control galaxy, we found no evidence of a B/P bulge. We also show directly that the LOSVD is broader at the location of the h_4 minimum in NGC 98 than elsewhere. This more direct method avoids possible artifacts associated with the degeneracy between the measurement of line-of-sight velocity dispersion and h_4.

Chapter 10. The conclusions obtained in this thesis are reviewed in this chapter. In addition, future research lines opened up by the research presented in the thesis are discussed and analyzed.

Bibliography

Aguerri, J. A. L. 1999, A&A, 351, 43
Aguerri, J. A. L., Beckman, J. E., & Prieto, M. 1998, AJ, 116, 2136
Aguerri, J. A. L., Muñoz-Tuñón, C., Varela, A. M., & Prieto, M. 2000, A&A, 361, 841
Aguerri, J. A. L., Hunter, J. H., Prieto, M., et al. 2001a, A&A, 373, 786
Aguerri, J. A. L., Balcells, M., & Peletier, R. F. 2001b, A&A, 367, 428
Aguerri, J. A. L., Debattista, V. P., & Corsini, E. M. 2003, MNRAS, 338, 465
Andredakis, Y. C., & Sanders, R. H. 1994, MNRAS, 267, 283
Andredakis, Y. C., Peletier, R. F., & Balcells, M. 1995, MNRAS, 275, 874
Athanassoula, E. 1992, MNRAS, 259, 345
Athanassoula, E., & Misiriotis, A. 2002, MNRAS, 330, 35
Athanassoula, E. 2005, MNRAS, 358, 1477
Athanassoula, E., & Bureau, M. 1999, ApJ, 522, 699

Athanassoula, E., Morin, S., Wozniak, H., et al. 1990, MNRAS, 245, 130
Balcells, M., Graham, A. W., Domínguez-Palmero, L., & Peletier, R. F. 2003, ApJ, 582, L79
Baugh, C. M., Cole, S., & Frenk, C. S. 1996, MNRAS, 283, 1361
Berentzen, I., Shlosman, I., & Jogee, S. 2006, ApJ, 637, 582
Bica, E. 1988, A&A, 195, 76
Bournaud, F., & Combes, F. 2002, A&A, 392, 83
Böker, T., Laine, S., van der Marel, R. P., et al. 2002, AJ, 123, 1389
Böker, T., Stanek, R., & van der Marel, R. P. 2003, AJ, 125, 1073
Bottema, R. 1989, A&A, 221, 236
Bottema, R. 1993, A&A, 275, 16
Burbidge, E. M., & Burbidge, G. R. 1959, ApJ, 130, 20
Bureau, M., & Athanassoula, E. 1999, ApJ, 522, 686
Bureau, M., & Athanassoula, E. 2005, ApJ, 626, 159
Bureau, M., & Freeman, K. C. 1997, PASA, 14, 146
Bureau, M., & Freeman, K. C. 1999, AJ, 118, 126
Bureau, M., Aronica, G., Athanassoula, E., et al. 2006, MNRAS, 370, 753
Burkhead, M. S. 1986, AJ, 91, 777
Burkhead, M. S. 1991, AJ, 102, 893
Buta, R., & Block, D. L. 2001, ApJ, 550, 243
Cappellari, M., Bacon, R., Bureau, M., et al. 2006, MNRAS, 366, 1126
Carollo, C. M., Stiavelli, M., de Zeeuw, P. T., & Mack, J. 1997, AJ, 114, 2366
Carollo, C. M., Stiavelli, M., & Mack, J. 1998, AJ, 116, 68
Carollo, C. M., Stiavelli, M., Seigar, M., de Zeeuw, P. T., & Dejonghe, H. 2002, AJ, 123, 159
Cepa, J., & Beckman, J. E. 1990, ApJ, 349, 497
Chung, A., & Bureau, M. 2004, AJ, 127, 3192
Cole, S., Lacey, C. G., Baugh, C. M., & Frenk, C. S. 2000, MNRAS, 319, 168
Corsini, E. M., Debattista, V. P., & Aguerri, J. A. L. 2003, ApJ, 599, L29
Corsini, E. M., Aguerri, J. A. L., Debattista, V. P., et al. 2007, ApJ, 659, L121
Courteau, S., de Jong, R. S., & Broeils, A. H. 1996, ApJ, 457, L73
Davies, R. L., & Illingworth, G. 1983, ApJ, 266, 516
Davies, R. L., Efstathiou, G., Fall, S. M., Illingworth, G., & Schechter, P. L. 1983, ApJ, 266, 41
Debattista, V. P. 2003, MNRAS, 342, 1194
Debattista, V. P., & Sellwood, J. A. 1998, ApJ, 493, L5
Debattista, V. P., & Williams, T. B. 2004, ApJ, 605, 714
Debattista, V. P., Corsini, E. M., & Aguerri, J. A. L. 2002, MNRAS, 332, 65
Debattista, V. P., Carollo, C. M., Mayer, L., & Moore, B. 2004, ApJ, 604, L93
Debattista, V. P., Carollo, C. M., Mayer, L., & Moore, B. 2005, ApJ, 628, 678
de Grijs, R., Kregel, M., & Wesson, K. H. 2001, MNRAS, 324, 1074
de Jong, R. S. 1996, A&AS, 118, 557
de Vaucouleurs, G. 1948, Annales d'Astrophysique, 11, 247
de Vaucouleurs, G., de Vaucouleurs, A., & Pence, W. 1974, ApJ, 194, L119
Eggen, O. J., Lynden-Bell, D., & Sandage, A. R. 1962, ApJ, 136, 748
Eliche-Moral, M. C., Balcells, M., Aguerri, J. A. L., & González-García, A. C. 2006, A&A, 457, 91
Elmegreen, B. G. 1994, ApJ, 425, L73
Elmegreen, B. G., & Hunter, D. A. 2006, ApJ, 636, 712

Emsellem, E., Monnet, G., Bacon, R., & Nieto, J.-L. 1994, A&A, 285, 739
Emsellem, E., Bacon, R., Monnet, G., & Poulain, P. 1996, A&A, 312, 777
Emsellem, E., Greusard, D., Combes, F., et al. 2001, A&A, 368, 52
Erwin, P. 2004, A&A, 415, 941
Erwin, P. 2005, MNRAS, 364, 283
Erwin, P., Beckman, J. E., & Vega-Beltran, J.-C. 2004, Penetrating Bars Through Masks of Cosmic Dust, eds. D. L. Block, I. Puerari, K. C. Freeman, R. Groess, and E. K. Block (Kluwer Academic Publishers,Dordrecht) 319, 775
Erwin, P., Beckman, J. E., & Pohlen, M. 2005, ApJ, 626, L81
Eskridge, P. B., Frogel, J. A., Pogge, R. W., et al. 2000, AJ, 119, 536
Falcón-Barroso, J., Peletier, R. F., & Balcells, M. 2002, MNRAS, 335, 741
Falcón-Barroso, J., Bacon, R., Bureau, M., et al. 2006, MNRAS, 369, 529
Fathi, K., Toonen, S., Falcón-Barroso, J., et al. 2007, ApJ, 667, L137
Ferguson, A. M. N., & Clarke, C. J. 2001, MNRAS, 325, 781
Freeman, K. C. 1970, ApJ, 160, 811
Fu, Y. N., Huang, J. H., & Deng, Z. G. 2003, MNRAS, 339, 442
Fukugita, M., Hogan, C. J., & Peebles, P. J. E. 1998, ApJ, 503, 518
Ganda, K., Falcón-Barroso, J., Peletier, R. F., et al. 2006, MNRAS, 367, 46
Gilmore, G., & Wyse, R. F. G. 1998, AJ, 116, 748
Goudfrooij, P., Gorgas, J., & Jablonka, P. 1999, Ap&SS, 269, 109
Governato, F., Willman, B., Mayer, L., et al. 2007, MNRAS, 374, 1479
Hasan, H., Pfenniger, D., & Norman, C. 1993, ApJ, 409, 91
Heller, C. H., & Shlosman, I. 1994, ApJ, 424, 84
Hubble, E. P. 1936, The realm of Nebulae (Yale University Press, New Haven)
Hunter, D. A., & Elmegreen, B. G. 2005, ApJS, 162, 49
Idiart, T. P., de Freitas Pacheco, J. A., & Costa, R. D. D. 1996, AJ, 112, 2541
Jablonka, P., Martin, P., & Arimoto, N. 1996, AJ, 112, 1415
Jarvis, B. J. 1986, AJ, 91, 65
Jogee, S., Scoville, N., & Kenney, J. D. P. 2005, ApJ, 630, 837
Kauffmann, G. 1996, MNRAS, 281, 487
Knapen, J. H., Shlosman, I., & Peletier, R. F. 2000, ApJ, 529, 93
Kormendy, J. 1982, ApJ, 257, 75
Kormendy, J. 1988, ApJ, 335, 40
Kormendy, J. 1993, Galactic Bulges, ed. H. DeJonghe and H. J. Habing (Kluwer Academic Publishers, Dordrecht), 153, 209
Kormendy, J., & Illingworth, G. 1982, ApJ, 256, 460
Kormendy, J., & Kennicutt, R. C. 2004, ARA&A, 42, 603
Kormendy, J., Bender, R., & Bower, G. 2002, The Dynamics, Structure & History of Galaxies: A Workshop in Honour of Professor Ken Freeman, ed. G.S. Da Costa and H. Jerjen (ASP, San Francisco), 273, 29
Kuijken, K., & Merrifield, M. R. 1995, ApJ, 443, L13
Laine, S., Shlosman, I., & Heller, C. H. 1998, MNRAS, 297, 1052
Laine, S., Shlosman, I., Knapen, J. H., & Peletier, R. F. 2002, ApJ, 567, 97
Lauer, T. R., Ajhar, E. A., Byun, Y.-I., et al. 1995, AJ, 110, 2622
Laurikainen, E., Salo, H., Buta, R., & Knapen, J. H. 2007, MNRAS, 381, 401
Lütticke, R., Dettmar, R.-J., & Pohlen, M. 2000, A&AS, 145, 405
MacArthur, L. A., Courteau, S., & Holtzman, J. A. 2003, ApJ, 582, 689
Marinova, I., & Jogee, S. 2007, ApJ, 659, 1176
Márquez, I., Masegosa, J., Durret, F., et al. 2003, A&A, 409, 459

Martínez-Valpuesta, I., Shlosman, I., & Heller, C. 2006, ApJ, 637, 214
Matthews, L. D., & Gallagher, J. S. 1997, AJ, 114, 1899
Mehlert, D., Thomas, D., Saglia, R. P., Bender, R., & Wegner, G. 2003, A&A, 407, 423
Menéndez-Delmestre, K., Sheth, K., Schinnerer, E., Jarrett, T. H., & Scoville, N. Z. 2007, ApJ, 657, 790
Merrifield, M. R., & Kuijken, K. 1999, A&A, 345, L47
Merlin, E., & Chiosi, C. 2006, A&A, 457, 437
Michel-Dansac, L., & Wozniak, H. 2006, A&A, 452, 97
Möllenhoff, C., & Heidt, J. 2001, A&A, 368, 16
Moorthy, B. K., & Holtzman, J. A. 2006, MNRAS, 371, 583
Navarro, J. F. & White, S. D. M. 1994, MNRAS, 267, 401
Persic, M., & Salucci, P. 1992, MNRAS, 258, 14P
Pizzella, A., Corsini, E. M., Morelli, L., et al. 2002, ApJ, 573, 131
Pohlen, M., & Trujillo, I. 2006, A&A, 454, 759
Pohlen, M., Dettmar, R.-J., Lütticke, R., & Aronica, G. 2002, A&A, 392, 807
Pohlen, M., Beckman, J. E., Hüttemeister, S., et al. 2004, Penetrating Bars through Masks of Cosmic Dust: The Hubble Tuning Fork Strikes a New Note, ed. D. L. Block, I. Puerari, K. C. Freeman, R. Groess, & E. K. Block (Springer, Dordrecht), 731
Proctor, R. N., & Sansom, A. E. 2002, MNRAS, 333, 517
Puerari, I., & Dottori, H. 1997, ApJ, 476, L73
Raha, N., Sellwood, J. A., James, R. A., & Kahn, F. D. 1991, Nature, 352, 411
Robertson, B., Yoshida, N., Springel, V., & Hernquist, L. 2004, ApJ, 606, 32
Samland, M., & Gerhard, O. E. 2003, A&A, 399, 961
Sandage, A. 1990, JRASC, 84, 70
Sandage, A., & Brucato, R. 1979, AJ, 84, 472
Sansom, A. E., Peace, G., & Dodd, M. 1994, MNRAS, 271, 39
Scannapieco, C., & Tissera, P. B. 2003, MNRAS, 338, 880
Scorza, C., & Bender, R. 1995, A&A, 293, 20
Scorza, C., & van den Bosch, F. C. 1998, MNRAS, 300, 469
Seifert, W., & Scorza, C. 1996, A&A, 310, 75
Sérsic, J. L. 1968, Atlas de galaxias australes (Observatorio Astronómico, Cordoba)
Shen, J., & Sellwood, J. A. 2004, ApJ, 604, 614
Simien, F., & de Vaucouleurs, G. 1986, ApJ, 302, 564
Slyz, A. D., Devriendt, J. E. G., Silk, J., & Burkert, A. 2002, MNRAS, 333, 894
Sommer-Larsen, J., Götz, M., & Portinari, L. 2003, ApJ, 596, 47
Steinmetz, M., & Muller, E. 1995, MNRAS, 276, 549
Thomas, D., & Davies, R. L. 2006, MNRAS, 366, 510
Thomas, D., Maraston, C., Bender, R., & Mendes de Oliveira, C. 2005, ApJ, 621, 673
Tissera, P. B., Smith Castelli, A. V., & Scannapieco, C. 2006, A&A, 455, 135
Trager, S. C., Dalcanton, J. J., & Weiner, B. J. 1999, The formation of galactic bulges, ed. C.M. Carollo, H.C. Ferguson, R.F.G. Wyse. (New York, Cambridge University Press), 42
Tremaine, S., & Weinberg, M. D. 1984, ApJ, 282, L5
van den Bosch, F. C., Jaffe, W., & van der Marel, R. P. 1998, MNRAS, 293, 343
van der Kruit, P. C., 1979, A&AS, 38, 15
van der Kruit, P. C., & Searle, L., 1981a, A&A, 95, 105

van der Kruit, P. C., & Searle, L., 1981b, A&A, 95, 116
Vega Beltrán, J. C., Corsini, E. M., Pizzella, A., & Bertola, F. 1997, A&A, 324, 485
Wada, K., & Habe, A. 1992, MNRAS, 258, 82
Weinberg, M. D. 1985, MNRAS, 213, 451
Weiner, B. J., Sellwood, J. A., & Williams, T. B. 2001, ApJ, 546, 931
Whyte, L. F., Abraham, R. G., Merrifield, M. R., et al. 2002, MNRAS, 336, 1281
Wozniak, H., Friedli, D., Martinet, L., Martin, P., & Bratschi, P. 1995, A&AS, 111, 115
Wyse, R. F. G., Gilmore, G., & Franx, M. 1997, ARA&A, 35, 637
Yoshii, Y., & Sommer-Larsen, J. 1989, MNRAS, 236, 779
Younger, J. D., Cox, T. J., Seth, A. C., & Hernquist, L. 2007, ApJ, 670, 269
Zoccali, M., Renzini, A., Ortolani, S., et al. 2003, A&A, 399, 931

2

GASP2D: A new two-dimensional photometric decomposition code

We present a new fitting algorithm (GASP2D) to perform two-dimensional photometric decomposition of the galaxy surface-brightness distribution. We adopted a Sérsic and an exponential profile to describe the surface-brightness distribution of the bulge and disk, respectively. Both components are characterized by elliptical and concentric isophotes with constant (but possibly different) ellipticity and position angles. The GASP2D technical implementation, the minimization algorithm, and the seeing treatment are described in detail in this chapter.

2.1 Introduction

In order to go beyond the subjective nature of visual classifications of galaxies, different objective classification schemes based on the measurements of quantitative parameters have been proposed. These quantitative methods have two major advantages over visual classifications: They are reproducible, and the biases can be understood and carefully characterized through simulations. Moreover, the use of quantitative morphology allows us to recover reliable information about the galaxy structural parameters which play a fundamental role in understanding the evolution and origin of galaxies. The most challenging photometric algorithm developed until now in the literature will be described from a historical perspective in the following.

2.1.1 One-dimensional photometric decompositions

Freeman's method

Freeman (1970) introduced a method to obtain the parameters which describe the luminosity distribution of an exponential disk. It was called, the *marking the disk* method. It consists in determining the region where the galaxy surface-brightness profile is dominated by the disk luminosity. In magnitude units, the central surface-brightness of the disk and its scale-length can be determined by a linear fit. This method established the starting point for the following decomposition methods even though it is not a robust method due to the ambiguous selection of the disk-dominated region.

Kormendy's method

Kormendy (1977) introduced a method to iteratively fit the surface-brightness distribution of the bulge and disk. Since the luminosity of the bulge can not be neglected even at large radii, Kormendy (1977) proposed to fit first the disk component with a single exponential profile. After subtracting this component to the total surface-brightness profile of the galaxy, a new linear fit assuming a $r^{1/4}$ for the bulge profile was made. Finally, the bulge contribution was subtracted again from the total luminosity profile in an iterative process. The weakness of the method is shown because the different structural parameters obtained when starting the iteration by fitting first the bulge or disk component.

To solve this ambiguity, Kormendy (1977) introduced a new method to fit both components at the same time using a non-linear least-squares method. Nowadays, this idea is still in use when dealing with photometric decompositions including more than one component.

Boroson's method

The method introduced by Boroson (1981) is a step forward because it allowed the derivation of the galaxy inclination and bulge ellipticity from a one-dimensional decomposition.

It is based on the extraction of the surface-brightness profile along axes with different position angles, all of them decomposed as if they are independent. The central surface-brightness of the disk and spheroid are assumed to be the same for all the profiles. Their values are determined by using the different cuts independently. If θ and θ_0 are the position angles of the profile and galaxy major-axis, respectively, the scale-lengths of the bulge and disk can be calculated as

$$r_{\rm e}(\theta) = \left[\frac{\cos^2(\theta-\theta_0)}{r^2_{\rm e,maj}} + \frac{\sin^2(\theta-\theta_0)}{r^2_{\rm e,min}}\right]^{-1/2} \tag{2.1}$$

$$h(\theta) = \left[\frac{\cos^2(\theta-\theta_0)}{h^2_{\rm maj}} + \frac{\sin^2(\theta-\theta_0)}{h^2_{\rm min}}\right]^{-1/2} \tag{2.2}$$

where $r_{\rm e,maj}$, $h_{\rm maj}$, $r_{\rm e,min}$, $h_{\rm min}$ are the scale-length of the bulge and disk, respectively, along the major and minor-axis of the corresponding ellipse. In this way, the bulge axis ratio is given by $(b/a)_{\rm bulge} = (r_{\rm e,min}/r_{\rm e,maj})$ and the galaxy inclination is $i = \arccos(h_{\rm min}/h_{\rm maj})$.

2.1.2 Two-dimensional photometric decompositions

Conventional bulge-disk decompositions based on elliptically averaged surface-brightness profiles usually do not take into account the intrinsic shapes (Prieto et al. 2001) or the position angle (Trujillo et al. 2001c) of the bulge and disk components. This can produce systematic errors in the results (Byun & Freeman 1995).

For this reason a number of two-dimensional parametric decomposition techniques have been developed in the last years. As an example, we may point out the algorithms developed by Scorza & Bender (1990), Simard (1998, GIM2D), Peng et al. (2002, GALFIT), Cappellari (2002, MGE), de Souza et al. (2004, BUDDA) and Pignatelli et al. (2006, GASPHOT). These methods were developed to solve different problems of galaxy decomposition, when fitting the two-dimensional galaxy surface-brightness distribution. They use different functions to parameterize the galaxy components and different minimization routines to perform the fit.

Scorza-Bender's method

Scorza & Bender (1990) developed this method which works by creating a model image of the disk, using an exponential profile. Then, this image is subtracted from the real galaxy image obtaining an image which represents the bulge contribution to the total luminosity. The search for the best-fit disk is done by comparing the bulge isophotes with perfect ellipses, (i.e., searching for bulge ellipses with Fourier coefficients near to zero).

Multi-Gaussian Expansion

The original idea of the MGE (Multi-Gaussian Expansion) method was developed by Bendinelli (1991). Later on, the method has been improved by several authors (Monnet et al. 1992; Emsellem et al. 1999; Cappellari 2002).

The algorithm works by expanding the galaxy surface-brightness distribution in a series of Gaussians given by

$$\sum(R,\theta) = \sum_{j=1}^{N} \frac{L_j}{2\pi\sigma_j^2 q_j} exp\left\{-\frac{1}{2\sigma_j^2}\left(x_j^2 + \frac{y_j^2}{q_j^2}\right)\right\}, \tag{2.3}$$

with

$$x_j = R\sin(\theta - \psi_j), \tag{2.4}$$

$$y_j = R\cos(\theta - \psi_j), \tag{2.5}$$

where (R,θ) are the polar coordinates in the sky plane and N is the number of Gaussians. The j-th Gaussian has total luminosity L_j, axis ratio given by $0 \leq q_j \leq 1$, dispersion along the major-axis σ_j, and position angle ψ_j. Once we have the formalism, the technical problem is just to perform the non-linear fit of Eq. 2.3 to the real galaxy surface-brightness distribution.

Multi-component non-linear fits

These methods fit simultaneously the parametric surface-brightness distribution chosen for describing every galaxy component (bulge, disk, bar) to the real galaxy image. They use different functions to parameterize the galaxy components and different minimization routines to perform the fit. The most used minimization algorithms are Simulated Annealing or Levenberg-Marquardt methods.

Simulated Annealing: This method looks for the best fit by generating random solutions in parameter space. If one solution is better than another, then this is settled as "best" solution and the algorithm starts the search again from this solution. On the other hand, if the solution obtained is worse, it is not discarded automatically and the method gives it a probabilistic opportunity to be the best solution. This method is used in the code GIMP2D (Simard 1998)

Levenberg-Marquardt: This method, which will be described in detail in Sect. 2.4, is based on the information given by the function gradient to probe the local structure of the space parameter and find the best solution more quickly. This method is used in several photometric decomposition codes such as GALFIT (Peng et al. 2002), BUDDA (de Souza et al. 2004), and GASPHOT (Pignatelli et al. 2006).

In this Chapter, we present the first version of the new decomposition algorithm named GASP2D (GAlaxy Surface Photometry 2 Dimensional decomposition). The code is similar to GIM2D and GASPHOT in minimizing the interaction with the user. It works in automatically to be more efficient when

dealing with a large number of galaxies. Like GALFIT and BUDDA, it adopts a Levenberg-Marquardt algorithm to fit the two-dimensional surface-brightness distribution of the galaxy. This reduces the computating time needed to obtain robust and reliable estimates of the galaxy structural parameters. The Chapter is organized as follows: the description of the galaxy light distribution modeled by GASP2D is given in Sect. 2.2. The merit function and the weights used to perform the fit are described in Sect. 2.3. The minimization routine adopted to find the best-fit model is presented in Sect. 2.4. The procedure adopted to correct for seeing effects is discussed in Sect. 2.5. The technical procedure followed by the code is described in Sect. 2.6. The code time performance is presented in Sect. 2.7. Finally, conclusions are given in Sect. 2.8. In Chapter 8 we will show an improved version of GASP2D where a bar component is also included in the model.

2.2 Photometric model

We assumed the galaxy surface-brightness distribution to be the sum of the contribution of a bulge and disk component. It is worth noting that inward extrapolation of the disk into the central bulge may have no physical basis. It only provides a convenient description of the light distributions that may be otherwise dynamically decoupled. In addition, in this Chapter the definition of a bulge is purely photometric, considering as a bulge the extra light that stands out above the extrapolation of the disk profile to the inner galaxy regions. Both the bulge and the disk are characterized by elliptical and concentric isophotes with constant (but possibly different) ellipticity and position angles.

Let (x, y, z) be Cartesian coordinates with the origin at the galaxy center, the $x-$axis parallel to the direction of right ascension and pointing westward, the $y-$axis parallel to the direction of declination and pointing northward, and the $z-$axis along the line-of-sight and pointing toward the observer. The plane of the sky is the (x, y) plane.

We adopted the Sérsic law (Sérsic 1968) to describe the surface-brightness of the bulge component. The Sérsic law has been extensively used in the literature for modeling the surface-brightness profiles of galaxies. For instance, it has been used to model the surface-brightness of elliptical galaxies (Capaccioli 1987; Graham & Guzmán 2003), bulges of early- and late-type galaxies (Andredakis et al. 1995; Moriondo et al. 1998; Khosroshahi et al. 2000; Graham 2001; Prieto et al. 2001; Aguerri et al. 2004; Möllenhoff 2004), the low surface-brightness host galaxy of blue compact galaxies (Caon et al. 2005; Papaderos et al. 1996; Amorín et al. 2007) and dwarf elliptical galaxies (Binggeli & Jerjen 1998; Aguerri et al. 2005; Graham & Guzmán 2003). It is given by

$$I_{\rm b}(x,y) = I_{\rm e} 10^{-b_n\left[(r_{\rm b}/r_{\rm e})^{1/n}-1\right]}, \tag{2.6}$$

where $r_{\rm e}$, $I_{\rm e}$, and n are the effective (or half-light) radius, the intensity at $r_{\rm e}$, and a shape parameter describing the curvature of the surface-brightness profile, respectively. A profile with $n = 4$ corresponds to the $r_{\rm b}^{1/4}$ model (de Vaucouleurs 1948) that was traditionally used to describe bright elliptical galaxies, a profile with $n = 1$ corresponds to an exponential model. The value of b_n is coupled to n so that half of the total luminosity of the bulge is within $r_{\rm e}$ and can be approximated as $b_n = 0.868\,n - 0.142$ (Caon, Capaccioli, & D'Onofrio 1993). Bulge isophotes are ellipses centered on (x_0, y_0) with constant position angle $\mathrm{PA_b}$ and constant ellipticity $\epsilon_{\rm b} = 1 - q_{\rm b}$. The radius $r_{\rm b}$ is given by

$$\begin{aligned} r_{\rm b} \;=\; & \Big[(-(x-x_0)\sin\mathrm{PA_b} + (y-y_0)\cos\mathrm{PA_b})^2 + \\ & - ((x-x_0)\cos\mathrm{PA_b} + (y-y_0)\sin\mathrm{PA_b})^2/q_{\rm b}^2\Big]^{1/2}. \end{aligned} \tag{2.7}$$

We adopted the exponential law (Freeman 1970) to describe the surface-brightness of the disk component

$$I_{\rm d}(x,y) = I_0\, e^{-r_{\rm d}/h}, \tag{2.8}$$

where I_0 and h are the central intensity and scale-length of the disk, respectively. Disk isophotes are ellipses centered at (x_0, y_0) with constant position angle $\mathrm{PA_d}$ and constant ellipticity $\epsilon_{\rm d} = 1 - q_{\rm d}$. The constant ellipticity of the disk defines its inclination, which is given by $i = \arccos(q_{\rm d})$. The radius $r_{\rm d}$ is given by

$$\begin{aligned} r_{\rm d} \;=\; & \Big[(-(x-x_0)\sin\mathrm{PA_d} + (y-y_0)\cos\mathrm{PA_d})^2 + \\ & - ((x-x_0)\cos\mathrm{PA_d} + (y-y_0)\sin\mathrm{PA_d})^2/q_d^2\Big]^{1/2}. \end{aligned} \tag{2.9}$$

Of potential relevance to the study of galaxy structure is the relative light fraction contributed by the bulge and disk. This can be expressed in terms of a bulge-to-disk luminosity ratio, B/D, derived by integrating the bulge and disk luminosity profiles to infinity. For a face-on Sérsic profile the total extrapolated luminosity is given by

$$L_{\rm b} = \int_0^\infty I_{\rm b}(r) 2\pi r dr = 2\pi I_{\rm e} r_{\rm e}^2 n e^{b_n} \frac{\Gamma(2n)}{b_n^{2n}}, \tag{2.10}$$

where $\Gamma(2n)$ is the complete gamma function (Abramowitz & Stengun 1964). For a face-on exponential disk

$$L_{\rm d} = \int_0^\infty I_{\rm d}(r) 2\pi r dr = 2\pi I_0 h^2. \tag{2.11}$$

Therefore, the resulting bulge-to-disk ratio is given by

$$\frac{B}{D} = \frac{I_{\rm e} n e^{b_n} \Gamma(2n)}{b_n^{2n}} \left(\frac{r_{\rm e}}{h}\right)^2. \tag{2.12}$$

In some cases, to quantify the prominence of the bulge with respect to the disk, we may be interested in the fraction of light that comes from the bulge out to a given radius. The luminosity enclosed by the Sérsic profile at any radius can be calculated as

$$L_{\rm b}(r) = \int_0^r I_{\rm b}(r) 2\pi r dr = 2\pi I_{\rm e} r_{\rm e}^2 n e^{b_n} \frac{\gamma\left(2n, b_n \left(\frac{r}{r_{\rm e}}\right)^{1/n}\right)}{b_n^{2n}}, \tag{2.13}$$

where $\gamma\left(2n, b_n \left(\frac{r}{r_{\rm e}}\right)^{1/n}\right)$ is the incomplete gamma function (Abramowitz & Stengun 1964).

At this point, it is worth noting an important caveat about GASP2D, which does not fit the sky surface-brightness. In fitting a galaxy, the outer wings of the galaxy could be coupled to the sky value (i.e., the sky surface-brightness can compensate a lack of light at large radii in the intrinsic galaxy profile leading to wrong results). This is particularly true for the disk parameters. However, we decided that an accurate subtraction of the sky surface-brightness has to be performed by the user before using GASP2D. In addition, systematic errors in the structural parameters due to wrong sky subtraction can be assessed by simulations with artificial galaxies as shown in Sect. 3.3.

2.3 Merit function and weights

To derive the coordinates (x_0, y_0) of the galaxy center, the photometric parameters of the bulge ($I_{\rm e}$, $r_{\rm e}$, n, PA$_{\rm b}$, and $q_{\rm b}$) and disk (I_0, h, PA$_{\rm d}$, and $q_{\rm d}$) we fitted iteratively a model of the raw intensity $I_{\rm m}(x, y)$=$I_{\rm b}(x, y)$+$I_{\rm d}(x, y)$ to the observations using a non-linear least-squares minimization method. GASP2D minimizes the χ^2 residual between the data image and the model, adjusting all free parameters simultaneously. This is done by using the robust Levenberg-Marquardt method (Press et al. 1996) implemented by Moré et al. (1980),

where the computation was done using the MPFIT algorithm implemented by C. B. Markwardt in the IDL environment[1].

For each pixel (x, y), the observed galaxy photon counts $I_{\rm g}(x, y)$ are compared with those predicted from the model $I_{\rm m}(x, y)$. Therefore the χ^2 to be minimized can be written as

$$\chi^2 = \frac{1}{N_{\rm dof}} \sum_{x=1}^{N} \sum_{y=1}^{M} \frac{[\, I_{\rm m}\,(x,\, y) - I_{\rm g}\,(x,\, y)\,]^2}{\sigma^2}, \tag{2.14}$$

where $N_{\rm dof}$ is the number of degrees of freedom, x and y ranging over the whole $N \times M$ pixel image and σ is weight function.

An important point to consider here is the weight function used to calculate the χ^2. Some authors claim that is better to assign to each pixel an uncertainty given by the Poissonian noise (e.g., Wadadekar et al. 1999; Peng et al. 2002; MacArthur et al. 2003), while others adopt a constant weight to obtain better results (e.g., Mollenhoff & Heidt 2001; de Souza et al. 2004).

In the case of Poissonian noise, each pixel is weighted according to the variance of its total observed photon counts due to the contribution of both galaxy and sky, and determined assuming photon noise limitation by taking into account for the detector readout noise (RON). The χ^2 in this case is given by

$$\chi^2 = \frac{1}{N_{\rm dof}} \sum_{x=1}^{N} \sum_{y=1}^{M} \frac{[\, I_{\rm m}\,(x,\, y) - I_{\rm g}\,(x,\, y)\,]^2}{I_{\rm g}\,(x,\, y) + I_{\rm s}\,(x,\, y) + {\rm RON}^2}. \tag{2.15}$$

Both possibilities, constant and Poissonian weights, were implemented in GASP2D.

2.4 MPFIT fitting algorithm

The χ^2 topology for galaxy fitting is complex. It has many local minima (degeneracies), because the parameter space is large (11 parameters for a bulge-disk decomposition). A fitting method such as the Metropolis algorithm (Metropolis et al. 1953; Saha & Williams 1994) is in principle preferable since it was designed to search for the optimal parameter values in this complicated topology. However, no algorithm can guarantee the convergence on the global minimum in such acomplicated topology, and this kind of method is CPU time intensive and therefore not efficient when dealing with a large number of galaxies. Therefore, a Levenberg-Marquardt algorithm (MPFIT), which is indeed very

[1]The updated version of this code is available on http://cow.physics.wisc.edu/ craigm/idl/idl.html

less time consuming, was preferred for GASP2D. In addition, the MPFIT implementation of the Levenberg-Marquardt algorithm allows the user to keep constant or impose boundary constraints on any parameter during the fitting process, avoiding time loss in searching for non-meaningful solutions.

Let us explain how MPFIT works. The Levenberg-Marquardt algorithm combines the best features of the gradient search with a quasi-Newton method. The gradient descent search is the simplest and most intuitive technique to find minima in a function. In this scheme all the parameters x are incremented simultaneously, with relative magnitudes adjusted so that the resulting direction in the parameter space is along the gradient. This situation can be improved by using the curvature as well as the gradient information, namely second derivatives. Expanding the function f (in our case the χ^2), using a Taylor series around the current state (x_0), we get

$$f(x) = f(x_0) + f'(x_0)\,(x - x_0) + \frac{1}{2} f''(x_0)\,(x - x_0)^2, \tag{2.16}$$

Where $f'(x)$ is the gradient vector of the function f at x, and $f''(x)$ is the Hessian matrix of second derivatives of f at x. The vector x is the set of function parameters, not the measured data vector. The minimum of f, $f(x_m)$ can be found using Newton's method, and the following linear equation

$$f''(x_0)(x_m - x_0) = -f'(x_0). \tag{2.17}$$

If we can find the inverse matrix for $f''(x_0)$ then the equation is solved for the step vector from the current position x_0 to the new projected minimum $(x_m - x_0)$. Here the problem has been linearized (i.e., the gradient information is known to first order). $f''(x_0)$ is a symmetric $n \times n$ matrix, and should be positive definite. The main advantage of this technique is its rapid convergence. However, the rate of convergence is sensitive to the starting location. The Levenberg-Marquardt technique is a variation on this theme. It adds an additional diagonal term to the equation which may aid the convergence properties

$$(f''(x_0) + \nu I)\,(x_m - x_0) = -f'(x_0), \tag{2.18}$$

where I is the identity matrix. When ν is large, the overall matrix is diagonally dominant, and the iterations follow the steepest descent. When ν is small, the iterations are quadratically convergent. In principle, if $f''(x_0)$ and $f'(x_0)$ are known then $(x_m - x_0)$ can be determined. However, the Hessian matrix is often difficult or impossible to compute. The gradient $f'(x_0)$ may be easier to compute, if only by finite difference techniques. So called quasi-Newton

techniques attempt to estimate successively $f''(x_0)$ by building up the gradient information as the iterations proceed. In the least-squares problem there are further simplifications which assist in solving Eq. 2.17. If the function f to be minimized is a sum of squares $f = \sum(h_i^2)$ where h_i is the i^{th} residual of m residuals as described above. This can be substituted back into Eq. 2.17 after computing the derivatives

$$f' = 2\sum(h_i h_i') \tag{2.19}$$

$$f'' = 2\sum(h_i' h_j') + 2\sum(h_i h_i''). \tag{2.20}$$

If one assumes that the parameters are already close enough to a minimum, then one typically finds that the second term in f'' is negligible (or, in any case, is too difficult to compute). Thus, Eq. 2.17 can be solved, at least approximately, using only the gradient information. In matrix notation, the combination of Eq. 2.17 and 2.20 becomes:

$$h_T'\, h'\, dx = -h_T'\, h, \tag{2.21}$$

where h is the residual vector (length m), h_T is its transpose, h' is the Jacobian matrix (dimensions $n \times m$), and dx is $(x_m - x_0)$. The user function supplies the residual vector h, and in some cases h' when it is not found by finite differences. Even if dx is not the best absolute step to take, it does provide a good estimate of the best direction, so often a line minimization will occur along the dx vector direction. The method of solution employed by MPFIT is to form the $Q\,R$ factorization of h', where Q is an orthogonal matrix such that $Q_T\, Q = I$, and R is upper right triangular. Using $h' = Q\,R$ and the orthogonality of Q, Eq. 2.21 becomes

$$(R_T\, Q_T)(Q\, R)\, dx = -(R_T\, Q_T)\, h \tag{2.22}$$

$$R_T\, R\, dx = -R_T\, Q_T\, h \tag{2.23}$$

$$R\, dx = -Q_T\, h, \tag{2.24}$$

where the last statement follows because R is upper triangular. Here, R, Q_T, and h are known so this is a matter of solving for dx.

2.5 Seeing effects

The ground-based images are affected by seeing, which scatters the light of the objects and produces a loss of spatial resolution. This is particularly critical in

the central regions of galaxies, where the slope of the radial surface-brightness profile is steeper. Since the bulge contribution dominates the surface-brightness distribution at small radii, seeing mostly affects bulge structural parameters. Seeing effects on the scale parameters of a Sérsic surface-brightness profile have been extensively discussed by Trujillo et al. (2001a,b).

GASP2D accepts three kinds of point spread functions (PSFs): A two-dimensional Gaussian PSF, a two-dimensional Moffat PSF or a user-supplied PSF. GASP2D automatically normalizes the total flux in all input PSFs to ensure the flux conservation in the convolution process. The two-dimensional Gaussian and Moffat are generated by GASP2D with the seeing full width half maximum (FWHM) specified by the user in the GASP2D input parameter file. The Gaussian PSF is written as

$$\mathrm{PSF}_{\mathrm{gauss}}(r) = \frac{1}{2\sigma^2\pi} e^{-\frac{r^2}{2\sigma^2}}, \tag{2.25}$$

where σ is the standard deviation, and is related to the FWHM in the following way FWHM=$2\sqrt{2\ln(2)}\sigma$.

The Moffat function is written as

$$\mathrm{PSF}_{\mathrm{moffat}}(r) = \frac{\beta-1}{\pi\alpha^2}\left(1+\left(\frac{r}{\alpha}\right)^2\right)^{-\beta}, \tag{2.26}$$

where the parameters α and β define the profile shape and are related to the FWHM in the following way FWHM=$2\alpha\sqrt{2^{1/\beta}-1}$. The Gaussian and Moffat functions differ mainly in the outer wings of the profile, indeed, when $\beta \to \infty$ the Moffat function becomes a Gaussian.

GASP2D deals with the effects of seeing in the model galaxy light by convolving, during each iteration of the fitting algorithm, the model image with the adopted PSF. This is done before comparing with the real galaxy to calculate the χ^2 value. This process is very time consuming, since the convolution must be evaluated many times before achieving the convergence of the fit. GASP2D can address this issue in two different ways: by using the Fourier transform or by solving directly the convolution integrals. The former is the most widely used method in literature, as far as photometric decomposition codes are concerned. Its main advantage resides in being computationally fast, since the Fast Fourier Transform (Press et al. 1996, FFT) algorithm can be used. This reduces the computational time by a factor $N^2/N\log_2(N)$ in comparison with purely numerical integration methods, where N is the number of pixels. However, as a drawback the Fourier transform has problems when there are strong changes in the spatial scale of the galaxy profile. The inner parts of the galaxy

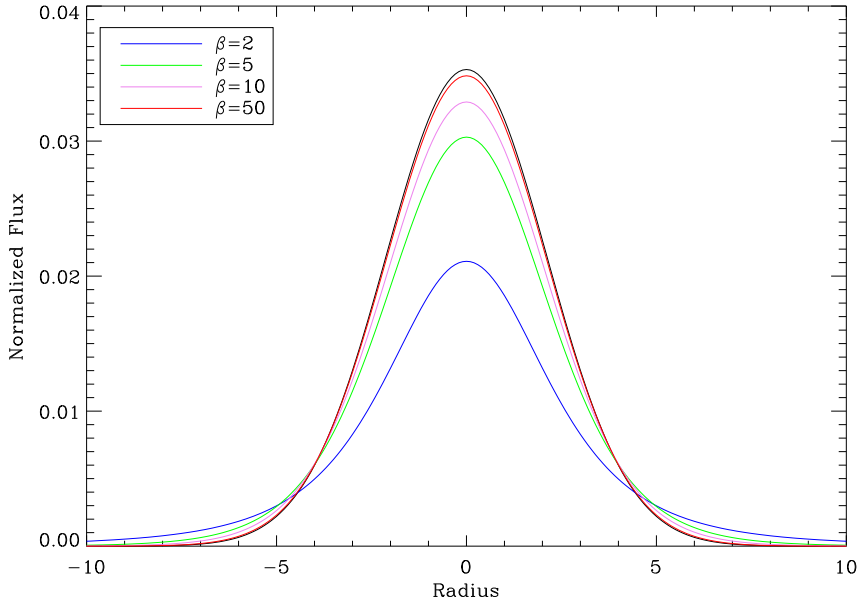

FIGURE 2.1— Comparison among a Gaussian PSF (black line) and different Moffat PSFs (blue, green, violet and red lines). All the PSFs use the same FWHM. For the Moffat PSFs, different colors represent different values of the β shape parameter (see Eq. 2.26).

profiles are steep, and this demands a very accurate measurement of the high frequencies in the Fourier domain. Consequently, flatter distributions are obtained as a result of a convolution using FFT with respect to the traditional methods of integration in the real domain.

An alternative way to deal with the seeing problem is to deconvolve the image. This process has the benefit that the observed image needs only to be deconvolved once and does not depend on the model for the intrinsic image. Several authors, (e.g. Lauer et al. 1995) show that galaxy images with high signal-to-noise (S/N) in the center can be accurately deconvolved using the Lucy-Richardson algorithm (Richardson 1972; Lucy 1974). The drawback of this method is that the deconvolution does not work properly for low S/N or undersampled images, amplifying Poisson and pixelation noise. GASP2D uses convolution, but it can be turned off by the user if deconvolution was performed previously.

2.6 Technical procedure of the fit

Since the fitting algorithm is based on a χ^2 minimization, it is important to adopt initial trials for the free parameters as close as possible to their true values. This should ensure that the iteration procedure does not just stop on a local minimum of the χ^2 distribution. With this aim GASP2D proceeds through a set of steps.

SExtractor. The photometric package SExtractor (Bertin & Arnouts 1996) is used to measure position, magnitude and ellipticity of all the sources (e.g., foreground and background stars or companion galaxies as well as bad pixels) in the images. Then all these sources, except for the galaxy under study, are masked using elliptical masks out to the radius that encloses 99% of the light of the source. If any of the mask overlap with another nearby galaxy whose light extends out to the center of the galaxy studied, GASP2D recreates the mask allowing the center of the target galaxy to be non masked, and puts a flag in the output file with the structural parameters.

ELLIPSE. To derive the elliptically-averaged radial profiles of the surface-brightness, ellipticity, and position angle of the galaxy, GASP2D fits ellipses to the galaxy isophotes with the ELLIPSE task in IRAF[2]. After masking the spurious sources using the parameters provided by SExtractor, ellipses centered on the position of the galaxy center are fitted. The coordinates of the galaxy center are adopted as initial trials for (x_0, y_0) in the two-dimensional fit but left as free parameters of the model. This step can be performed either interactively or automatically. If the interactive method is chosen, then the user can create new masks in the standard ELLIPSE way, that will be added to the SExtractor masks when the two-dimensional fit is performed.

Trial estimates of the structural parameters. Some of the trial values for the structural parameters of the galaxies are derived by performing a standard one-dimensional decomposition technique similar to that adopted by several authors (e.g., Kormendy 1977; Prieto et al. 2001). GASP2D begins by fitting an exponential law to the radial surface-brightness profile extracted with ELLIPSE at large radii, where the light distribution of the galaxy is expected to be dominated by the disk contribution. The central surface-brightness and scale-length of the fitted exponential profile are adopted as initial trials for I_0 and h, respectively. The fitted profile is extrapolated to small radii and then subtracted from the observed radial surface-brightness profile. The residual radial surface-brightness profile iss assumed to be a first estimate of the light distribution of the bulge. A Sérsic law is then fitted by assuming the bulge shape parameter to

[2]IRAF is distributed by NOAO, which is operated by AURA Inc., under contract with the National Science Foundation.

be $0.5, 1, 1.5, ..., 6$. The bulge effective radius, effective surface-brightness, and shape parameter which (together with the disk parameters) give the best fit to the radial surface-brightness profile are adopted as initial trials for $r_{\rm e}$, $I_{\rm e}$, and n respectively.

The initial trials for ellipticity and position angle of disk and bulge are also obtained from the ELLIPSE ellipticity and position angle profiles, respectively. The values for $q_{\rm d}$ and $\rm PA_d$ are found by averaging the values in the outermost portion of the radial profiles of ellipticity and position angle. The initial trials for $q_{\rm b}$ and $\rm PA_b$ are estimated by interpolating at $r_{\rm e}$ the radial profiles of the ellipticity and position angle, respectively.

Two-dimensional fit. The initial guesses for the structural parameters calculated before are then adopted to initialize the non-linear least-squares fit to the galaxy image, where all the parameters, including n, aree allowed to vary. A convergent model is reached when the χ^2 is a minimum and the relative change of the χ^2 between the iterations is less than 10^{-7}. From this first set of structural parameters, a model of the galaxy surface-brightness distribution is built. This is convolved with the adopted PSF and subtracted from the observed image to obtain a residual image. In order to ensure the minimum in the χ^2-space found in this first iteration, we perform two further iterations. In these iterations all the pixels and/or regions of the residual image with values greater or less than a fixed threshold, controlled by the user, are rejected. Those regions are masked out and the fit is repeated assuming as initial trials for the free parameters the values obtained in the previous iteration. These kind of masks are useful when galaxies have prominent structures other than a bulge and a disk (e.g., spiral arms and dust lanes) which can affect to the fitted parameters when solving the problem automatically. We found that after three iterations the algorithm converges and the parameters do not change.

Outputs. GASP2D produces an output file with all the best-fitted free parameters for every galaxy, plus the reduced χ^2 of the fit and the ratio B/D. In addition, GASP2D provides the user three FITS images: the best model fitted to the galaxy, the residuals obtained from the best model, and the masks used during the fitting process. Some examples of the code outputs are shown in Fig. 2.2 and 2.3.

2.7 Time performances

Due to our implementation of the algorithm to perform the decomposition, the computational time depends on three main issues: 1) the method used to compute the convolution of the model image with the PSF, 2) the number of parameters (components) to fit and 3) the size of the fitted image.

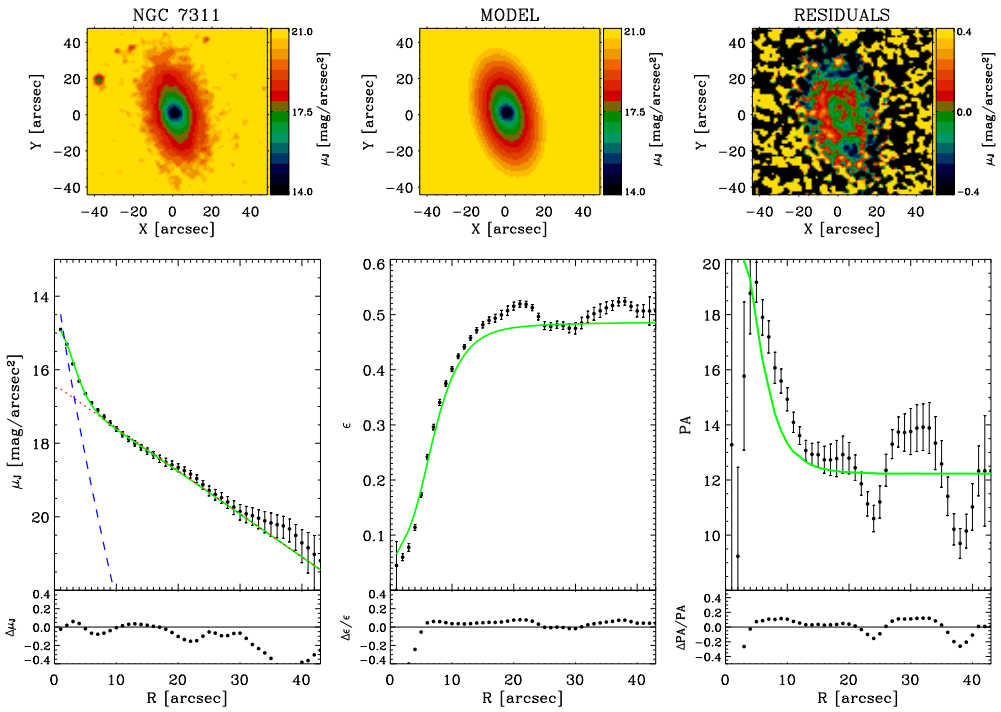

FIGURE 2.2— Example of the outputs given by GASP2D. A spiral galaxy from the sample described in detail in Chapter 3. We show in the upper panels (from left to right): the original galaxy image, the best GASP2D fit, and the residuals (observed-modeled) in magnitude units. The surface-brightness range of each image is indicated at the right of the panel. In the lower panels (from left to right): Ellipse-averaged radial profile of the surface-brightness, ellipticity and position angle in the observed (black dots with error-bars) and modeled image (green line). The dashed blue line and the dotted red line represent the intrinsic surface-brightness contribution of the bulge and disk, respectively. The difference between the ellipse-averaged radial profiles from the observed and modeled images is also shown.

We used a typical desk computer, namely an Intel Celeron 2.8 GHz computer with 256 Mbyte of memory. The time needed to reach the convergence of the fit for a typical galaxy in a frame of 200 × 200 pixels, using two components (i.e., 11 free parameters), and performing the convolution using the FFT method is 1-2 minutes. This time is almost linear with the image size since for an image frame of 400 × 400 pixels the typical computer time needed is 5-7 minutes. However, if the fit is performed by solving the convolution integrals the time involved fitting a 200 × 200 pixels image is 4-5 minutes, 3 times more than using FFT convolution. A more complete sample of experiments is shown in

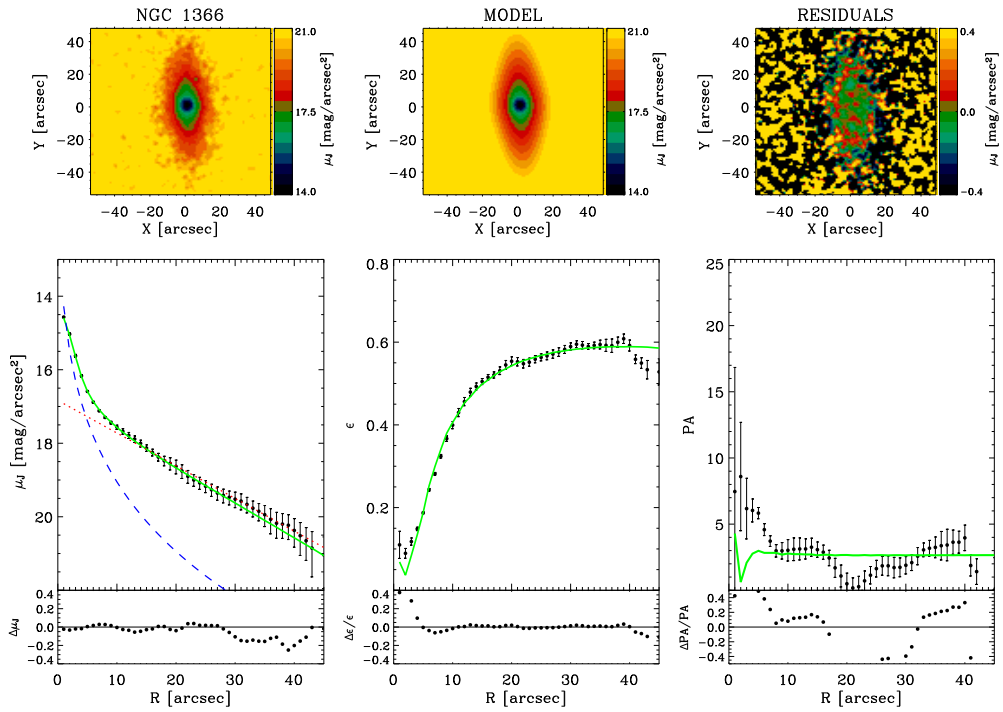

FIGURE 2.3— As in Fig. 2.2 but for a lenticular galaxy from the sample described in detail in Chapter 3.

Tab. 2.1.

These time estimates take into account the overall time needed to fit a galaxy, from the run of the SExtractor package until the final two-dimensional fit. Since GASP2D does not need initial conditions, this constitutes the whole time the user spends fitting a galaxy.

2.8 Conclusions

We have presented a new fitting algorithm (GASP2D) to perform two-dimensional photometric decomposition of galaxy images. The surface-brightness distribution of the galaxy was assumed to be the sum of the contribution of a Sérsic bulge and an exponential disk.

GASP2D is optimized to deal with large image samples, and it adopts a robust Levenberg-Marquardt fitting algorithm in order to obtain reliable estimates of the galaxy structural parameters. In Chapters 3, 5 and 6, we will

TABLE 2.1— Computational times required for two-dimensional galaxy modeling

Image Size (pixels × pixels) (1)	Functions (2)	Convolution Method (3)	Time (minutes) (4)
200 × 200	Sérsic	FFT	< 1
		INT	2-3
	Sérsic+exp.	FFT	1-2
		INT	4-5
400 × 400	Sérsic	FFT	3-4
		INT	10-12
	Sérsic+exp.	FFT	5-7
		INT	12-14
800 × 800	Sérsic	FFT	12-13
		INT	30-35
	Sérsic+exp.	FFT	20-25
		INT	45-50

NOTE. The columns show the following: (1) size of the galaxy image to be fitted; (2) parametric functions used in the fit; (3) method used to perform the convolution: FFT=fast Fourier transform; INT=numerical convolution integrals; (4) time used by GASP2D to perform the fit, the interval corresponds to different tests with different galaxies.

apply this code to different astrophysical problems, testing it with simulations and previous results from the literature, and demonstrating its robustness and versatility.

Bibliography

Abramowitz, M., & Stengun, I. 1964, Handbook of Mathematical Functions (Dover, New York)

Aguerri, J. A. L., Iglesias-Paramo, J., Vilchez, J. M., & Muñoz-Tuñón, C. 2004, AJ, 127, 1344

Aguerri, J. A. L., Iglesias-Páramo, J., Vílchez, J. M., Muñoz-Tuñón, C., & Sánchez-Janssen, R. 2005, AJ, 130, 475

Amorín, R. O., Muñoz-Tuñón, C., Aguerri, J. A. L., Cairós, L. M., & Caon, N. 2007, A&A, 467, 541

Andredakis, Y. C., Peletier, R. F., & Balcells, M. 1995, MNRAS, 275, 874

Bendinelli, O. 1991, ApJ, 366, 599

Bertin, E., & Arnouts, S. 1996, A&AS, 117, 393

Binggeli, B., & Jerjen, H. 1998, A&A, 333, 17

Boroson, T. 1981, ApJS, 46, 177

Byun, Y. I., & Freeman, K. C. 1995, ApJ, 448, 563

Caon, N., Capaccioli, M., & D'Onofrio, M. 1993, MNRAS, 265, 1013
Caon, N., Cairós, L. M., Aguerri, J. A. L., & Muñoz-Tuñón, C. 2005, ApJS, 157, 218
Capaccioli, M. 1987, Structure and Dynamics of Elliptical Galaxies, ed. T. de Zeeuw (Reidel Publishing Co., Dordrecht) 127, 47
Cappellari, M. 2002, MNRAS, 333, 400
de Souza, R. E., Gadotti, D. & dos Anjos, S. 2004, ApJS, 153, 411
de Vaucouleurs, G. 1948, Annales d'Astrophysique, 11, 247
Emsellem, E., Dejonghe, H., & Bacon, R. 1999, MNRAS, 303, 495
Freeman, K. C. 1970, ApJ, 160, 811
Graham, A. W. 2001, AJ, 121, 820
Graham, A. W., & Guzmán, R. 2003, AJ, 125, 2936
Khosroshahi, H. G., Wadadekar, Y., & Kembhavi, A. 2000, ApJ, 533, 162
Kormendy, J. 1977, ApJ, 217, 406
Lauer, T. R., Ajhar, E. A., Byun, Y.-I., et al. 1995, AJ, 110, 2622
Lucy, L. B. 1974, AJ, 79, 745
MacArthur, L. A., Courteau, S., & Holtzman, J. A. 2003, ApJ, 582, 689
Metropolis, N., Rosenbluth, A. W., Rosenbluth, M. N., Teller, A. H., & Teller, E. 1953, Journal of Chemical Physics, 21, 1087
Möllenhoff, C. 2004, A&A, 415, 63
Möllenhoff, C., & Heidt, J. 2001, A&A, 368, 16
Monnet, G., Bacon, R., & Emsellem, E. 1992, A&A, 253, 366
Moré, J. J., Garbow, B. S., & Hillstrom, K. E. 1980, User guide for MINPACK-1, Argonne National Laboratory Report ANL-80-74
Moriondo, G., Giovanardi, C., & Hunt, L. K. 1998, A&AS, 130, 81
Papaderos, P., Loose, H.-H., Thuan, T. X., & Fricke, K. J. 1996, A&AS, 120, 207
Peng, C. Y., Ho, L. C., Impey, C. D., & Rix, H. 2002, AJ, 124, 266
Pignatelli, E., Fasano, G., & Cassata, P. 2006, A&A,446, 373
Press, W. H., Teukolsky, S. A., Vetterling, W. T., & Flannery, B. P. 1996, Numerical Recipes in Fortran 77: The Art of Scientific Computing (Cambridge University Press, Cambridge)
Prieto, M., Aguerri, J. A. L., Varela, A. M., & Muñoz-Tuñón, C. 2001, A&A, 367, 405
Richardson, W. H. 1972, Journal of the Optical Society of America, 62, 55
Saha, P., & Williams, T. B. 1994, AJ, 107, 1295
Scorza, C., & Bender, R. 1990, A&A, 235, 49
Sérsic, J. L. 1968, Atlas de galaxias australes (Observatorio Astronómico, Cordoba)
Simard, L. 1998, Astronomical Data Analysis Software Systems VII, ed. R. Albrecht, R. N. Hook, & H. A. Bushouse (ASP, San Francisco), 108
Trujillo, I., Aguerri, J. A. L., Cepa, J., & Gutiérrez, C. M. 2001a, MNRAS, 328, 977
Trujillo, I., Aguerri, J. A. L., Cepa, J., & Gutiérrez, C. M. 2001b, MNRAS, 321, 269
Trujillo, I., Aguerri, J. A. L., Gutiérrez, C. M., & Cepa, J. 2001c, AJ, 122, 38
Wadadekar, Y., Robbason, B., & Kembhavi, A. 1999, AJ, 117, 1219

3

Structure of disk galaxies: NIR global scaling relations

Based on J. Méndez-Abreu, J. A. L Aguerri, E. M. Corsini and E. Simonneau, 2008, A&A, 478, 353

The structural parameters of the bulges and disks of a magnitude-limited sample of 148 S0-Sb galaxies were derived from 2MASS $J-$band images. We used GASP2D, our new code for two-dimensional photometric decomposition (Méndez-Abreu et al. 2008). We found that the surface-brightness radial profiles of larger bulges are more centrally peaked than those of the smaller bulges. Larger bulges have a lower effective surface-brightness and higher absolute luminosities. They reside in larger disks, as revealed by the correlation between central velocity dispersion and disk scale-length. This reveals a strong coupling between bulges and disks. This has been interpreted as an indication of the formation of bulges via secular evolution of their host disks. However, the bulges of the sample galaxies follow the same fundamental plane, Faber-Jackson, and photometric plane relationships found for elliptical galaxies, supporting the idea that bulges and ellipticals formed in the same way. These results indicate that the scaling relations alone are not enough to clearly distinguish between bulges formed by early dissipative collapse, merging or secular evolution.

3.1 Introduction

Global scaling relations provide useful diagnostics for the structure of disk galaxies. From the detailed analysis of the correlations between the parameters of galaxies, derived from the photometric decomposition of their structural

components, a lot of information about formation and evolution of galaxies can be extracted.

Historically, the sample of de Jong & van der Kruit (1994) provided a useful reference for intermediate- to late-type field disk galaxies. These scaling relations were analyzed by de Jong (1996) and Courteau et al. (1996), their bulge-disk photometric decompositions were performed assuming two exponential profiles for the bulge and disk components. Graham (2001) and MacArthur et al. (2003) performed more recent studies of intermediate- to late-type spirals, using a Sérsic profile for the bulge. Hunt et al. (2003) have also analyzed bulge and disk scaling relations from a sample of disk galaxies in the Perseus-Pisces supercluster; their sample comprises mostly Sb and Sc spirals. At the other end of the Hubble sequence, S0 galaxies are often discussed together with ellipticals, but are rarely compared to spiral galaxies. More recently, Balcells et al. (2007) presented a complementary paper to the ones above. They sampled early- to intermediate-type, disk galaxies, ranging from S0 to Sbc.

The parameters used for the scaling relations, derived from near infrared (NIR) images, are less affected by dust extinction than those derived from optical images. Furthermore, mass-to-light (M/L) variations with population, age, and metallicity are small in the NIR, yielding small differences between the photometric scale-lengths and the stellar-mass scales of the galaxies. In this Chapter we present the largest sample of galaxies to date decomposed into a bulge and disk component using a fully two-dimensional code (see Chapter 2) and NIR images.

The Chapter is organized as follows: the selection criteria of our sample galaxies is described in Sect. 3.2. The application of GASP2D to simulated galaxies in order to retrieve meaningful errors in the structural parameters of the bulge and disk is presented in Sect. 3.3. The structural parameters derived for the sample galaxies are shown in Sect. 3.3.1. The correlations between the structural parameters of the sample galaxies are discussed in Sect. 3.4. Finally, conclusions are given in Sect. 3.5.

3.2 Sample selection and data acquisition

Our objective was to select a well-defined and complete sample of nearby, unbarred disk galaxies to study in a systematic way the photometric properties of their structural components. Since our sample galaxies do not host bars, they constitute a good test for our new bulge-disk decomposition algorithm. We will compare our results with previous published ones. Since these properties are strongly dependent on the dominant stellar population at the observed wavelength, it is preferable to consider NIR images to map the mass-carrying

evolved stars and avoid contamination due to dust and bright young stars (e.g., Möllenhoff & Heidt 2001, hereafter MH01). The complete sample is drawn from the Extended Source Catalogue (Jarrett et al. 2000, XSC) of the Two Micron All Sky Survey (Skrutskie et al. 2006, 2MASS). Our sample consists of galaxies that meet the following requirements: (1) Hubble type classification from S0 to Sb ($-3 \leq \mathrm{HT} \leq 3$; de Vaucouleurs et al. 1991, hereafter RC3) to ensure that bulges are fully resolved in 2MASS images; (2) unbarred classification in RC3; (3) total $J-$band magnitude $J_T < 10$ mag (2MASS/XSC); (4) inclination $i < 65°$ (RC3); (5) Galactic latitude $\mid b_G \mid > 30°$ (RC3) to minimize both Galactic extinction and contamination due to Galactic foreground stars.

We ended up with a sample of 184 unbarred galaxies. We retrieved their 2MASS $J-$band images from the NASA/IPAC Infrared Science Archive. The galaxy images were reduced and flux calibrated with the standard 2MASS extended source processor GALWORKS (Jarrett et al. 2000). Images have a typical field of view of few arc-minutes and a spatial scale of $1''$ pixel^{-1}. They were obtained with an average seeing FWHM$\sim 3\farcs1$ as measured by fitting a circular two-dimensional Gaussian to the field stars.

After a visual inspection of the images, we realized that some of the sample galaxies were not suitable for our study. We rejected paired and interacting objects as well as those galaxies that resulted in being barred after performing the photometric decomposition (see Sect. 3.3.1). Therefore, the final sample presented in this paper contains 148 galaxies (90 lenticular and 58 early-type spiral galaxies). A compilation of their main properties is given in Table 3.2. Figure 3.1 shows the distribution of the sample galaxies over the Hubble types. The lenticular galaxies are predominant over the spirals due to our magnitude selection, which favors red galaxies. Moreover, we show the distribution of radial velocities of the sample galaxies with respect to the 3K background. The mean radial velocity is 2000 km s^{-1} (corresponding to a distance of 27 Mpc assuming $H_0 = 75$ km s^{-1} Mpc^{-1}), but we include galaxies as far as 8500 km s^{-1} (113 Mpc) because the sample is magnitude limited.

Tonry et al. (2001) derived the distance of 30 galaxies of our sample from the measurement of their surface-brightness fluctuations. The difference between the distances obtained from radial velocities and those derived from surface-brightness fluctuations was calculated for all these galaxies. The standard deviation of the distance differences is 5 Mpc and it was assumed as being a typical distance error. For the 4 common galaxies in the Virgo cluster it is 2 Mpc.

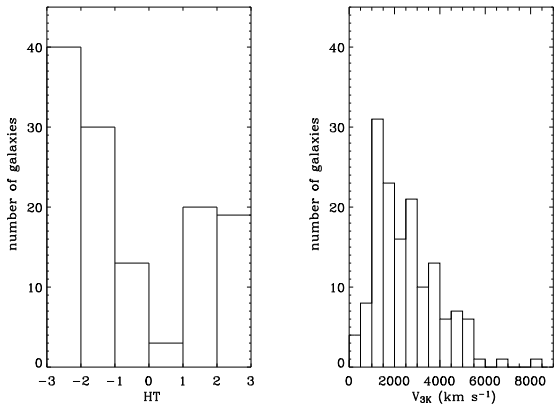

FIGURE 3.1— Distribution of the sample galaxies over the Hubble types (left panel) and radial velocities with respect to the 3K background (right panel).

3.3 Test on simulated galaxies

To test the reliability and accuracy of our two-dimensional technique for bulge-disk decomposition, we carried out extensive simulations on a large set of artificial disk galaxies. We generated 1000 images of galaxies with a Sérsic bulge and an exponential disk. The central surface-brightness, scale-length, and apparent axial ratios of the bulge and disk of the artificial galaxies were randomly chosen in the range of values observed in the $J-$band by MH01 for a sample of 40 bright spiral galaxies. The adopted ranges were

$$1 \leq r_{\rm e} \leq 3 \text{ kpc} \qquad 0.4 \leq q_{\rm b} \leq 0.9 \qquad 0.5 \leq n \leq 6 \tag{3.1}$$

for the bulge parameters, and

$$2 \leq h \leq 5 \text{ kpc} \qquad 0.4 \leq q_{\rm d} \leq 0.9 \tag{3.2}$$

for the disk parameters. The parameters of the artificial galaxies also have to satisfy the following conditions

$$q_{\rm d} < q_{\rm b} \qquad 0 < B/T < 0.8 \qquad 8 < J_T < 12 \text{ mag.} \tag{3.3}$$

All the simulated galaxies were assumed to be at a distance of 30 Mpc. This is the average distance of the galaxies of our sample and it corresponds to a scale of 145 pc arcsec^{-1}. The pixel scale used was 1 arcsec pixel^{-1}, and the CCD gain and RON were 8 e$^-$ ADU^{-1} and 40 e$^-$, respectively, in order to mimic the instrumental setup of the 2MASS data. Finally, a background level

TABLE 3.1— Relative errors on the photometric parameters of the bulge and disk calculated for different galaxy magnitudes by means of Monte Carlo simulations.

		$8 < J_T \leq 9$			$9 < J_T \leq 10$			$10 < J_T \leq 11$			$11 < J_T \leq 12$		
Par.	Run	#	Mean	St.Dev.	#	Mean	St.Dev.	#	Mean	St.Dev.	#	Mean	St.Dev.
(1)	(2)	(3)	(4)	(5)	(6)	(7)	(8)	(9)	(10)	(11)	(12)	(13)	(14)
I_e	1	226	$-1 \cdot 10^{-3}$	0.02	217	$-8 \cdot 10^{-3}$	0.04	238	$-1 \cdot 10^{-2}$	0.06	206	$-4 \cdot 10^{-2}$	0.14
	2	223	$1 \cdot 10^{-2}$	0.08	211	$1 \cdot 10^{-1}$	0.09	235	$9 \cdot 10^{-2}$	0.10	205	$2 \cdot 10^{-2}$	0.16
	3	225	$-1 \cdot 10^{-2}$	0.09	214	$-1 \cdot 10^{-1}$	0.09	231	$-8 \cdot 10^{-2}$	0.10	208	$-6 \cdot 10^{-2}$	0.15
	4	212	$-6 \cdot 10^{-2}$	0.08	206	$-7 \cdot 10^{-2}$	0.10	220	$-6 \cdot 10^{-2}$	0.11	180	$-3 \cdot 10^{-2}$	0.15
r_e	1	226	$1 \cdot 10^{-3}$	0.02	217	$7 \cdot 10^{-3}$	0.03	238	$1 \cdot 10^{-2}$	0.06	206	$6 \cdot 10^{-2}$	0.13
	2	223	$-7 \cdot 10^{-2}$	0.08	211	$-9 \cdot 10^{-2}$	0.08	235	$-7 \cdot 10^{-2}$	0.09	205	$-2 \cdot 10^{-2}$	0.14
	3	225	$7 \cdot 10^{-2}$	0.06	214	$9 \cdot 10^{-2}$	0.07	231	$1 \cdot 10^{-1}$	0.09	208	$1 \cdot 10^{-1}$	0.13
	4	212	$7 \cdot 10^{-2}$	0.09	206	$8 \cdot 10^{-2}$	0.10	220	$1 \cdot 10^{-1}$	0.11	180	$8 \cdot 10^{-2}$	0.14
n	1	226	$2 \cdot 10^{-3}$	0.02	217	$4 \cdot 10^{-3}$	0.02	238	$4 \cdot 10^{-3}$	0.04	206	$4 \cdot 10^{-2}$	0.09
	2	223	$-5 \cdot 10^{-2}$	0.05	211	$-6 \cdot 10^{-2}$	0.05	235	$-7 \cdot 10^{-2}$	0.07	205	$-3 \cdot 10^{-2}$	0.12
	3	225	$5 \cdot 10^{-2}$	0.04	214	$6 \cdot 10^{-2}$	0.05	231	$7 \cdot 10^{-2}$	0.07	208	$1 \cdot 10^{-1}$	0.11
	4	212	$1 \cdot 10^{-1}$	0.08	206	$1 \cdot 10^{-1}$	0.08	220	$1 \cdot 10^{-1}$	0.09	180	$1 \cdot 10^{-1}$	0.15
I_0	1	226	$-3 \cdot 10^{-3}$	0.03	217	$-6 \cdot 10^{-3}$	0.03	238	$-8 \cdot 10^{-3}$	0.05	206	$-3 \cdot 10^{-2}$	0.14
	2	223	$1 \cdot 10^{-2}$	0.05	211	$1 \cdot 10^{-2}$	0.05	235	$3 \cdot 10^{-2}$	0.07	205	$2 \cdot 10^{-3}$	0.13
	3	225	$-2 \cdot 10^{-2}$	0.05	214	$-3 \cdot 10^{-2}$	0.05	231	$-3 \cdot 10^{-2}$	0.05	208	$-3 \cdot 10^{-2}$	0.07
	4	212	$-7 \cdot 10^{-2}$	0.10	206	$-9 \cdot 10^{-2}$	0.10	220	$-9 \cdot 10^{-2}$	0.11	180	$-1 \cdot 10^{-1}$	0.12
h	1	226	$2 \cdot 10^{-3}$	0.02	217	$9 \cdot 10^{-3}$	0.03	238	$9 \cdot 10^{-3}$	0.04	206	$4 \cdot 10^{-2}$	0.10
	2	223	$3 \cdot 10^{-3}$	0.02	211	$5 \cdot 10^{-3}$	0.03	235	$6 \cdot 10^{-3}$	0.05	205	$2 \cdot 10^{-2}$	0.11
	3	225	$3 \cdot 10^{-3}$	0.02	214	$8 \cdot 10^{-3}$	0.03	231	$1 \cdot 10^{-2}$	0.05	208	$6 \cdot 10^{-2}$	0.10
	4	212	$8 \cdot 10^{-2}$	0.09	206	$8 \cdot 10^{-2}$	0.08	220	$9 \cdot 10^{-2}$	0.10	180	$1 \cdot 10^{-1}$	0.11
q_b	1	226	$-1 \cdot 10^{-3}$	0.01	217	$-4 \cdot 10^{-3}$	0.02	238	$-2 \cdot 10^{-3}$	0.03	206	$1 \cdot 10^{-2}$	0.06
	2	223	$3 \cdot 10^{-3}$	0.01	211	$3 \cdot 10^{-3}$	0.01	235	$3 \cdot 10^{-3}$	0.02	205	$1 \cdot 10^{-2}$	0.06
	3	225	$-5 \cdot 10^{-3}$	0.01	214	$-7 \cdot 10^{-3}$	0.02	231	$-5 \cdot 10^{-3}$	0.03	208	$-5 \cdot 10^{-3}$	0.06
	4	212	$1 \cdot 10^{-2}$	0.10	206	$4 \cdot 10^{-2}$	0.12	220	$4 \cdot 10^{-2}$	0.12	180	$6 \cdot 10^{-2}$	0.13
q_d	1	226	$-1 \cdot 10^{-3}$	0.01	217	$-8 \cdot 10^{-3}$	0.04	238	$-3 \cdot 10^{-3}$	0.03	206	$-3 \cdot 10^{-2}$	0.09
	2	223	$8 \cdot 10^{-3}$	0.02	211	$8 \cdot 10^{-3}$	0.04	235	$2 \cdot 10^{-2}$	0.04	205	$2 \cdot 10^{-2}$	0.11
	3	225	$-1 \cdot 10^{-2}$	0.02	214	$-2 \cdot 10^{-2}$	0.03	231	$-2 \cdot 10^{-2}$	0.04	208	$-5 \cdot 10^{-2}$	0.10
	4	212	$-8 \cdot 10^{-2}$	0.08	206	$-7 \cdot 10^{-2}$	0.08	220	$-9 \cdot 10^{-2}$	0.09	180	$-1 \cdot 10^{-1}$	0.10
PA_b	1	226	$1 \cdot 10^{-4}$	0.01	217	$1 \cdot 10^{-3}$	0.02	238	$-2 \cdot 10^{-3}$	0.02	206	$-4 \cdot 10^{-3}$	0.06
	2	223	$-1 \cdot 10^{-3}$	0.02	211	$-1 \cdot 10^{-3}$	0.02	235	$-2 \cdot 10^{-3}$	0.03	205	$3 \cdot 10^{-3}$	0.05
	3	225	$1 \cdot 10^{-3}$	0.01	214	$3 \cdot 10^{-3}$	0.02	231	$-3 \cdot 10^{-3}$	0.03	208	$-1 \cdot 10^{-3}$	0.06
	4	212	$-1 \cdot 10^{-2}$	0.10	206	$-2 \cdot 10^{-2}$	0.10	220	$-3 \cdot 10^{-2}$	0.10	180	$-1 \cdot 10^{-2}$	0.12
PA_d	1	226	$-3 \cdot 10^{-3}$	0.02	217	$-3 \cdot 10^{-4}$	0.02	238	$-2 \cdot 10^{-3}$	0.02	206	$5 \cdot 10^{-3}$	0.07
	2	223	$-1 \cdot 10^{-3}$	0.04	211	$-1 \cdot 10^{-3}$	0.02	235	$1 \cdot 10^{-3}$	0.04	205	$6 \cdot 10^{-3}$	0.08
	3	225	$2 \cdot 10^{-3}$	0.04	214	$-2 \cdot 10^{-3}$	0.04	231	$-2 \cdot 10^{-3}$	0.04	208	$5 \cdot 10^{-3}$	0.08
	4	212	$8 \cdot 10^{-3}$	0.08	206	$3 \cdot 10^{-3}$	0.08	220	$4 \cdot 10^{-3}$	0.08	180	$2 \cdot 10^{-2}$	0.11

NOTE. The columns show the following: (1) photometric parameter; (2) run of the Monte Carlo simulation. Artificial galaxies are analyzed by assuming the correct values of PSF FWHM and sky level (Run 1), correct sky level and a PSF FWHM 2% larger than the true value (Run 2), correct sky level and a PSF FWHM 2% smaller than the true value(Run 3). Artificial galaxies are built by assuming the correct PSF FWHM and a sky level 1% larger than the true value (Run 4); (3, 6, 9, 12) number of artificial galaxies in the magnitude bin; (4, 7, 10, 13) mean of the relative errors; (5, 8, 11, 14) standard deviation of the relative errors.

and photon noise were added to the resulting images to yield a signal-to-noise ratio similar to that of the available 2MASS images.

The two-dimensional parametric decomposition was applied to analyze the images of the artificial galaxies as if they were real. Errors on the fitted param-

eters were estimated by comparing the input $p_{\rm i}$ and output $p_{\rm o}$ values. Relative errors $(1 - p_{\rm i}/p_{\rm o})$ were assumed to be normally distributed, with mean and standard deviation corresponding to the systematic and typical error on the relevant parameter, respectively.

The results of the simulations are given in Table 3.1. In Run 1 we built the artificial galaxies by assuming the correct values of PSF FWHM and sky level, so only errors due to the Poisson noise are studied. The mean relative errors on the fitted parameters are smaller than 0.01 (absolute value) and their standard deviations are smaller than 0.02 (absolute value) for all galaxies with $J_T < 10$ mag, proving the reliability of our derived structural parameters. Relative errors increase for fainter galaxies, which are not included in our sample.

Systematic errors given by wrong estimates of PSF and sky level are the most significant contributors to the error budget. To understand how a typical error in the measurement of the PSF FWHM affects our results, we analyzed the artificial galaxies by adopting the correct sky level and a PSF FWHM that was 2% larger (Run 2) or smaller (Run 3) than the true values. As expected (Sect. 2.5), the parameters of the surface-brightness profiles show larger errors for the bulge than for the disk. We recovered larger values for the Sérsic parameters ($\rm r_{\it e}$, n) when the PSF FWHM is overestimated, and lower values when it is underestimated. Relative errors are correlated with the values of effective radius and shape parameter of the bulge but not with the magnitude of the galaxy. In Run 4 we built the artificial galaxies by adopting the correct PSF FWHM and a sky level that was 1% larger than the actual one. For brighter galaxies an incorrect sky subtraction mostly affects the parameters of the disk surface-brightness profile. For fainter galaxies, the large relative errors on the bulge parameters are due to their coupling with the disk parameters. This is consistent with the results of similar tests performed by Byun & Freeman (1995).

3.3.1 Results on real galaxies and comparison with previous studies

The parameters derived for the structural components of the sample galaxies are collected in Table 3.2. All the listed values are corrected for seeing smearing and galaxy inclination. Surface-brightnesses were calibrated by adopting, for the 2MASS images, the flux zero point given in the image headers (Jarrett et al. 2000).

The comparison of the structural parameters obtained for the same galaxy by different authors is often not straightforward on account of possible differences in the observed bandpass, parameterization of the surface-brightness distribution, and fitting method.

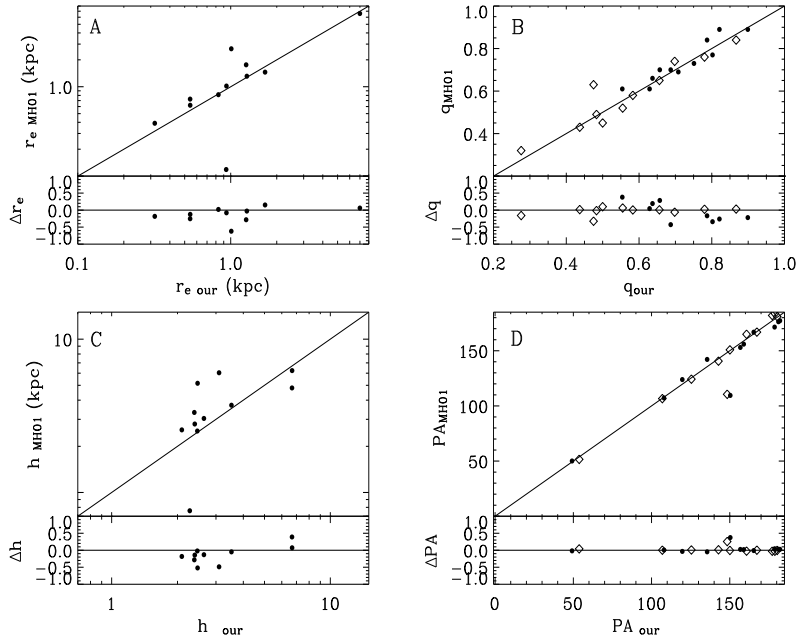

FIGURE 3.2— Comparison between the structural parameters measured in this work and by MH01. (A) Bulge effective radius, (B) axis ratios, (C) disk scale-length and (D) position angles. Filled dots and open diamonds in (B) and (D) correspond to values measured for bulges and disks, respectively. Residuals $\Delta r_{\rm e}$, Δq, Δh and ΔPA are defined as $1 - r_{\rm e,MH01}/r_{\rm e,our}$, $1 - {\rm q_{MH01}/q_{our}}$, $1 - {\rm h_{MH01}/h_{our}}$ and $1 - {\rm PA_{MH01}/PA_{our}}$, respectively.

MH01 already studied 11 of our sample galaxies (NGC 772, NGC 2775, NGC 2841, NGC 2985, NGC 3169, NGC 3626, NGC 3675, NGC 3898, NGC 4450, NGC 4501 and NGC 4826). They performed a two-dimensional parametric decomposition of the $J-$band surface-brightness distribution. They considered ellipticities and position angles of both the bulge and disk as free parameters. Therefore, we considered their results as the most suitable to be compared with ours. The structural parameters we measured are consistent with those given by MH01 for all the common galaxies but NGC 4826. We argue that they strongly underestimated the scale-length of its disk (and consequently obtained a wrong estimate of the other parameters) because of the small field of view ($3' \times 3'$) of their image. In Fig. 3.2 we show the comparison between our structural parameters ($r_{\rm e}$, h, q and PA) of the bulge and disk and those measured by MH01.

Table 3.2: Main properties and structural bulge and disk parameters of the galaxies in the sample.

Galaxy	Type	J_T	V_{3K}	D	σ_0	μ_e	r_e	n	q_b	PA_b	μ_0	h	q_d	PA_d
		(mag)	(km/s)	(Mpc)	(km/s)	(mag/"^{2})	(")			(°)	(mag/"^{2})	(")		(°)
(1)	(2)	(3)	(4)	(5)	(6)	(7)	(8)	(9)	(10)	(11)	(12)	(13)	(14)	(15)
ESO443-024	SA(s)0$^-$	9.48	5397	72.0	273	17.90	8.7	2.83	0.64	169.9	17.99	13.8	0.90	146.0
ESO507-025	SA0$^-$	9.27	3602	48.0	260	16.97	5.5	2.08	0.68	95.6	17.49	13.4	0.78	87.8
ESO445-002	SA0$^-$	9.46	4528	60.4	-	17.04	3.9	1.80	0.93	84.5	18.27	18.9	0.71	102.4
IC0750	Sab: sp	9.25	935	17.0*	116	18.24	10.2	1.57	0.22	42.7	16.81	11.1	0.40	36.5
IC2035	S0 pec	9.81	1408	16.5*	109	16.30	2.8	4.13	0.70	35.0	16.13	5.5	0.71	91.6
IC3152	SA0$^-$	9.99	3600	48.0	161	17.80	5.1	3.06	0.94	62.6	17.67	9.2	0.83	43.6
IC4310	S0 pec	9.81	2714	36.2	-	17.90	3.7	2.10	0.77	64.3	18.01	14.2	0.40	72.5
IC4991	SA(r)0° pec	9.45	5624	75.0	-	17.79	6.0	1.59	0.79	136.5	18.10	17.2	0.73	121.2
IC5063	SA(s)0$^+$:	9.70	3183	42.4	161	16.77	3.2	1.46	0.67	118.9	17.01	9.8	0.85	117.0
IC5267	SA(s)0/a	8.29	1484	19.8	-	16.74	5.1	1.69	0.93	144.9	17.35	21.3	0.79	142.2
MCG-02-33-017	(R)SA(r)0$^+$ pec	9.69	4247	56.6	-	17.47	4.8	2.34	0.90	24.1	18.04	15.2	0.95	39.9
NGC50	S0$^-$ pec	9.65	5156	68.7	-	17.44	5.3	2.48	0.64	164.1	17.96	13.8	0.68	161.9
NGC80	SA0$^-$:	9.92	5409	72.1	260	16.62	2.3	1.56	0.89	34.8	17.40	9.9	0.86	0.2
NGC148	S0°:sp	9.99	1253	18.4*	-	19.28	8.5	4.21	0.61	89.7	19.46	16.0	0.24	88.9
NGC254	(R)SA(r)0$^+$:	9.61	1358	17.1*	-	16.60	2.5	1.69	0.82	131.8	17.87	14.5	0.50	131.8
NGC383	SA0$^-$	9.49	4804	64.0	278	17.02	5.2	1.34	0.87	143.5	18.18	17.4	0.89	163.1
NGC467	SA(s)0° pec	9.97	5146	68.6	247	18.99	9.9	2.96	0.97	46.3	18.83	15.8	0.80	140.5
NGC470	SA(rs)b	9.76	2063	30.5*	122	16.40	2.2	0.92	0.54	154.3	18.21	16.6	0.59	163.2
NGC488	SA(r)b	7.91	1959	29.3*	199	16.80	4.9	1.51	0.91	0.7	17.54	29.3	0.75	7.0
NGC524	SA(rs)0$^+$	8.13	2126	32.1*	252	17.35	9.6	2.52	0.94	22.7	17.07	19.2	0.92	76.7
NGC615	SA(rs)b	9.51	1568	23.1*	-	17.33	2.8	2.23	0.75	161.7	17.84	15.1	0.32	161.2
NGC665	(R)S0° ?	9.85	5162	68.8	189	17.26	3.8	1.12	0.93	34.8	17.96	12.8	0.56	116.2
NGC772	SA(s)b	8.17	2166	32.6*	128	20.83	44.2	4.93	0.80	119.6	18.78	42.3	0.70	125.4
NGC883	SA(s)0$^-$:	9.85	5189	69.2	311	16.65	3.5	1.65	0.80	69.6	17.35	9.5	0.93	63.9
NGC897	SA(rs)a	9.71	4582	61.1	-	17.86	4.1	3.37	0.75	23.3	17.85	13.4	0.67	28.5
NGC1024	(R')SA(r)ab	9.75	3304	44.1	172	16.73	3.7	0.93	0.51	164.2	17.84	13.6	0.49	144.3
NGC1045	SA0$^-$ pec	9.82	4404	58.7	-	17.71	6.2	3.25	0.62	58.5	18.07	11.8	0.69	58.8
NGC1070	Sb	9.64	3864	51.5	-	18.81	13.9	2.03	0.81	6.6	19.24	16.8	0.79	179.0
NGC1107	S0	9.51	3225	43.0	251	17.45	5.2	1.81	0.57	143.2	17.93	15.1	0.53	137.0
NGC1200	SA(s)0$^-$	9.57	3866	51.5	-	17.34	4.6	1.96	0.84	44.7	18.24	17.5	0.82	94.2
NGC1201	SA(r)0°:	8.55	1524	20.2*	167	17.64	7.5	2.77	0.74	13.0	18.53	28.7	0.43	8.5
NGC1351	SA0- pec	9.60	1426	16.9*	137	17.66	5.9	3.22	0.62	140.8	18.27	15.2	0.59	142.4
NGC1357	SA(s)ab	9.29	1882	24.7*	124	17.03	5.8	1.86	0.94	141.1	17.55	22.7	0.75	144.3
NGC1366	S0°	9.91	1195	11.6*	120	17.93	3.5	5.32	0.81	3.5	18.12	12.2	0.31	2.6
NGC1400	SAO$^-$	8.75	418	5.0*	255	17.00	7.4	2.95	0.88	27.2	17.89	17.8	0.87	56.3
NGC1411	SA(r)0$^-$:	9.02	890	11.2*	-	16.48	4.3	2.69	0.85	16.8	17.86	17.9	0.73	12.8
NGC1425	SA(s)b	9.13	1406	17.4*	-	18.67	5.1	3.28	0.77	125.7	18.25	21.2	0.45	131.8
NGC1482	SA0$^+$ pec sp	9.72	1757	19.6*	-	16.42	4.8	1.02	0.40	106.3	17.95	12.4	0.56	105.6
NGC1527	SA(r)0$^-$:	8.55	1006	11.0*	165	17.70	6.4	2.49	0.79	83.0	18.01	24.7	0.39	78.3
NGC1546	SA0$^+$	9.08	1131	13.4*	-	18.03	14.7	1.04	0.32	148.6	18.02	17.8	0.61	145.4
NGC1550	SA(s)0$^-$:	9.78	3598	48.0	336	16.73	4.3	2.15	0.79	34.1	17.91	12.1	0.96	26.2
NGC1553	SA(r)0°	7.18	1098	13.4*	177	16.18	5.9	1.63	0.67	158.1	16.31	23.4	0.63	151.3

Table 3.2: continued.

Galaxy	Type	J_T	V_{3K}	D	σ_0	μ_e	r_e	n	q_b	PA_b	μ_0	h	q_d	PA_d
		(mag)	(km/s)	(Mpc)	(km/s)	(mag/"^{2})	(")			(°)	(mag/"^{2})	(")		(°)
(1)	(2)	(3)	(4)	(5)	(6)	(7)	(8)	(9)	(10)	(11)	(12)	(13)	(14)	(15)
NGC1947	S0$^-$ pec	8.43	1262	12.1∗	134	18.21	12.8	2.68	0.91	49.7	17.26	17.2	0.95	4.3
NGC1956	SA(s)a	9.77	4881	65.1	-	18.46	3.9	2.33	0.86	69.2	18.09	15.2	0.46	67.4
NGC2460	SA(s)a	9.48	1532	23.6∗	-	18.32	7.9	2.63	0.79	5.6	17.31	11.0	0.68	38.9
NGC2629	SA(r)0°:	9.81	3762	50.2	298	16.74	3.9	2.46	0.68	93.3	17.85	10.3	0.71	98.9
NGC2639	(R)SA(r)a:	9.39	3376	45.0	198	19.01	6.2	5.35	0.69	130.7	16.73	9.9	0.49	135.5
NGC2768	S0	7.93	1525	23.7∗	182	19.27	19.8	2.80	0.66	96.8	18.79	42.4	0.36	93.2
NGC2775	SA(r)ab	7.92	1654	17.0∗	176	18.06	12.4	3.06	0.90	158.9	17.58	30.0	0.78	160.7
NGC2841	SA(r)b:	7.01	805	12.2∗	205	19.44	28.4	3.91	0.66	156.8	19.37	113.1	0.28	150.1
NGC2911	SA(s)0: pec	9.61	3529	47.0	234	18.85	10.2	3.94	0.78	145.2	19.33	23.7	0.69	120.9
NGC2985	(R')SA(rs)ab	8.31	1386	22.4∗	140	17.94	13.2	2.92	0.82	178.4	18.22	25.8	0.87	1.5
NGC3031	SA(s)ab	4.76	46	1.4 ∗	161	16.64	39.8	3.69	0.70	143.7	16.01	78.6	0.66	157.6
NGC3065	SA(r)0°	9.97	993	31.3∗	160	16.89	3.9	2.86	0.97	111.4	18.89	16.4	0.92	139.4
NGC3169	SA(s)a pec	8.25	1581	19.7∗	165	16.92	8.7	2.45	0.69	49.2	18.23	27.7	0.66	53.7
NGC3230	S0	9.82	3141	41.9	-	18.03	4.2	2.65	0.79	137.0	18.02	14.1	0.40	116.5
NGC3245	SA(r)0°:	8.79	1649	22.2∗	210	15.97	3.3	1.71	0.65	176.5	17.44	17.6	0.52	177.2
NGC3277	SA(r)ab	9.83	1707	25.0∗	205	18.23	7.5	3.54	0.86	10.6	18.17	12.5	0.81	38.6
NGC3497	SA(s)0°:	9.65	4055	54.1	270	17.47	4.8	2.67	0.76	54.8	17.94	14.3	0.64	53.0
NGC3593	SA(s)0/a	8.41	970	5.5 ∗	54	17.67	11.0	1.18	0.40	89.4	18.53	33.1	0.38	89.2
NGC3607	SA(s)0°:	7.61	1282	19.9∗	223	16.42	8.1	1.86	0.76	124.2	17.21	21.5	0.88	124.4
NGC3619	(R)SA(s)0$^+$:	9.57	1703	27.9∗	-	16.31	2.8	2.04	0.90	50.4	17.77	13.3	0.82	47.5
NGC3626	(R)SA(rs)0$^+$	9.10	1803	26.3∗	-	15.64	2.5	1.98	0.63	165.3	17.59	16.4	0.58	167.3
NGC3665	SA(s)0°	8.62	2324	32.4∗	184	17.05	6.3	1.93	0.75	24.5	17.20	17.1	0.78	28.2
NGC3675	SA(s)b	7.84	1003	12.8∗	106	17.87	8.7	2.26	0.55	2.0	18.00	39.7	0.44	0.3
NGC3801	S0/a	9.87	3653	48.7	182	18.53	5.7	2.18	0.86	125.9	18.33	16.0	0.51	119.2
NGC3813	SA(rs)b:	9.81	1729	26.4∗	-	20.61	8.9	1.82	0.78	151.4	18.27	20.5	0.36	81.4
NGC3898	SA(s)ab	8.58	1340	21.9∗	207	18.13	11.9	3.75	0.64	107.9	19.07	29.2	0.50	106.9
NGC3900	SA(r)0$^+$	9.62	2101	29.4∗	144	18.46	5.1	3.81	0.90	167.7	18.10	16.4	0.55	1.5
NGC3998	SA(r)0°	8.33	1207	21.6∗	305	15.20	3.8	1.59	0.82	133.5	16.97	16.3	0.81	135.2
NGC4036	S0$^-$	8.47	1482	24.6∗	181	18.83	8.9	4.01	0.80	69.7	17.42	20.0	0.32	81.4
NGC4087	SA0$^-$:	9.85	3657	48.8	215	18.38	7.3	4.20	0.89	36.1	18.57	13.3	0.73	39.1
NGC4138	SA(r)0$^+$	9.12	1105	17.0∗	140	16.11	2.4	0.93	0.73	151.0	16.99	13.9	0.61	151.0
NGC4150	SA(r)0°	9.92	492	9.7∗	85	16.51	2.8	2.21	0.80	143.9	17.82	13.6	0.61	148.1
NGC4223	SA(s)0$^+$:	9.99	2574	34.3	-	19.82	11.3	4.52	0.54	123.1	18.94	19.2	0.53	131.5
NGC4224	SA(s)a: sp	9.49	2934	35.1∗	-	18.73	6.1	3.49	0.69	56.3	18.35	19.4	0.42	54.8
NGC4233	S0°	9.71	2723	35.1∗	220	18.08	4.7	1.62	0.86	22.1	19.49	20.5	0.25	178.3
NGC4270	S0	9.95	2725	35.1∗	154	18.59	3.7	3.67	0.86	111.9	17.74	12.1	0.40	106.0
NGC4281	S0$^+$:sp	8.89	3072	35.1∗	280	17.28	4.9	2.92	0.58	83.8	17.72	18.2	0.41	86.6
NGC4324	SA(r)0$^+$	9.42	1999	35.1∗	98	17.80	3.9	3.31	0.83	68.0	17.52	13.3	0.47	51.2
NGC4350	SA0	8.76	1565	16.8∗	180	18.87	8.1	6.00	0.68	30.4	17.16	14.2	0.24	27.7
NGC4369	(R)SA(rs)a	9.78	1289	21.6∗	-	17.68	6.1	1.47	0.57	159.6	17.93	14.0	0.87	83.8
NGC4377	SA0$^-$	9.73	1694	16.8∗	144	15.59	2.5	1.34	0.78	158.8	17.16	10.1	0.86	175.3
NGC4378	(R)SA(s)a	9.42	2888	35.1∗	198	18.01	7.2	3.83	0.84	164.7	17.58	11.8	0.79	162.2
NGC4379	S0$^-$ pec	9.65	1390	16.8∗	108	17.49	6.6	2.32	0.73	94.8	17.85	12.5	0.86	85.5
NGC4380	SA(rs)b:	9.22	1300	16.8∗	62	18.81	6.0	1.50	0.60	157.7	19.12	35.3	0.55	156.1
NGC4382	SA(s)0$^-$ pec	7.06	1070	16.8∗	179	18.06	18.7	3.39	0.79	36.8	18.01	53.4	0.66	10.9

Table 3.2: continued.

Galaxy	Type	J_T	V_{3K}	D	σ_0	μ_e	r_e	n	q_b	PA_b	μ_0	h	q_d	PA_d
		(mag)	(km/s)	(Mpc)	(km/s)	(mag/"^{2})	(")			(°)	(mag/"^{2})	(")		(°)
(1)	(2)	(3)	(4)	(5)	(6)	(7)	(8)	(9)	(10)	(11)	(12)	(13)	(14)	(15)
NGC4429	SA(r)0$^+$	7.73	1459	16.8∗	192	18.01	10.7	2.05	0.68	90.3	18.24	43.5	0.38	98.3
NGC4438	SA(s)0/a pec	8.25	395	16.8 ∗	-	17.45	6.0	2.69	0.80	33.8	16.95	17.3	0.47	19.3
NGC4450	SA(s)ab	7.94	2271	16.8∗	129	17.75	6.7	3.08	0.79	1.1	17.74	29.4	0.56	178.8
NGC4459	SA(r)0$^+$	8.10	1542	16.8∗	171	18.05	14.5	3.38	0.89	94.2	18.48	28.7	0.66	109.0
NGC4492	SA(s)a	9.87	2101	16.8 ∗	-	19.73	10.7	4.80	0.91	169.1	18.64	17.7	0.83	52.9
NGC4501	SA(rs)b	7.21	2602	16.8 ∗	161	18.43	11.5	3.45	0.71	135.5	17.55	43.3	0.48	142.8
NGC4528	S0°:	9.87	1692	22.6	117	17.63	3.7	3.03	0.85	75.8	17.25	9.1	0.48	4.8
NGC4578	SA(r)0°:	9.34	2616	16.8∗	120	19.05	14.2	3.66	0.73	31.3	20.15	36.4	0.61	34.5
NGC4639	SA(rs)b	9.65	1300	16.8 ∗	87	18.03	7.7	1.73	0.69	159.9	18.53	18.3	0.87	78.7
NGC4698	SA(s)ab	8.40	1328	16.8 ∗	133	19.12	13.8	4.07	0.82	74.8	18.48	33.0	0.48	166.2
NGC4736	(R)SA(r)ab	6.03	531	4.3∗	104	15.55	11.4	1.81	0.90	17.9	16.87	40.4	0.67	96.0
NGC4750	(R)SA(rs)ab	9.04	1683	26.1∗	-	16.76	2.1	2.32	0.83	53.7	16.76	12.9	0.77	128.0
NGC4772	SA(s)a	9.16	1366	16.3∗	-	19.34	12.3	3.68	0.91	47.5	18.95	21.0	0.50	150.9
NGC4789	SA0:	9.99	8497	113.3	270	16.86	2.4	1.41	0.79	2.4	17.64	9.6	0.69	174.0
NGC4800	SA(rs)b	9.28	984	15.2∗	99	17.29	4.1	1.97	0.81	50.1	16.98	12.3	0.69	21.1
NGC4802	SA(r)0	9.36	1339	17.8	-	17.16	2.2	1.62	0.85	27.9	16.93	10.9	0.71	11.1
NGC4814	SA(s)b	9.99	2658	39.3∗	-	17.29	1.7	1.01	0.73	102.3	17.11	9.9	0.68	115.0
NGC4825	SA0$^-$	9.47	4776	63.7	-	17.55	6.1	1.30	0.69	142.5	17.86	15.5	0.68	136.0
NGC4826	(R)SA(rs)ab	6.27	702	4.1∗	91	18.09	47.0	3.60	0.75	150.3	17.68	114.5	0.47	148.3
NGC5087	SA0:	8.80	2121	27.8∗	283	16.48	6.3	2.54	0.52	10.8	17.19	13.3	0.65	13.6
NGC5273	SA(s)0°	9.50	1320	21.3∗	66	17.24	3.2	2.43	0.84	1.5	18.06	18.30	0.87	6.7
NGC5292	(R')SA(rs)ab	9.62	4729	63.0	-	17.09	3.6	1.51	0.65	51.3	17.82	15.1	0.81	49.3
NGC5313	Sb	9.80	2732	37.8∗	-	16.15	1.5	0.62	0.72	33.2	17.42	12.6	0.51	45.8
NGC5326	SAa:	9.80	2712	37.8∗	165	18.17	9.1	1.65	0.53	133.4	18.93	22.3	0.60	133.0
NGC5440	Sa	9.83	3890	51.9	-	17.53	3.4	1.95	0.70	41.7	18.42	15.7	0.36	46.1
NGC5485	SA0 pec	9.32	2074	32.8∗	159	18.18	8.9	2.27	0.85	0.9	17.93	15.3	0.78	173.4
NGC5533	SA(rs)ab	9.75	4051	54.0	-	17.70	5.1	2.34	0.66	23.6	18.03	14.1	0.64	26.3
NGC5614	SA(r)ab pec	9.50	4073	54.3	-	17.60	6.1	3.41	0.94	47.2	17.84	12.8	0.88	149.3
NGC5631	SA(s)0°	9.39	2075	32.7∗	168	17.29	6.1	3.61	0.82	125.4	17.55	11.6	0.94	157.7
NGC5687	S0$^-$	9.89	2192	34.4∗	190	18.25	7.5	2.31	0.66	103.7	19.72	27.1	0.54	96.9
NGC5838	SA0$^-$	8.48	1555	28.5∗	266	17.38	6.2	2.01	0.82	44.9	18.65	30.6	0.34	42.8
NGC6278	S0	9.96	2786	37.1	150	16.83	3.1	2.35	0.66	109.7	18.08	12.6	0.53	131.4
NGC6340	SA(s)0/a	9.25	1169	22.0∗	144	17.17	4.3	3.17	0.95	121.5	17.59	16.0	0.97	64.6
NGC6851	S0	9.69	2913	38.8	224	17.31	5.9	3.13	0.69	167.4	17.81	10.9	0.73	156.7
NGC6861	SA(s)0$^-$:	8.66	2636	35.5∗	-	16.67	9.1	2.11	0.53	142.4	18.01	17.8	0.70	133.8
NGC6890	SA(rs)ab	9.99	2323	31.8∗	-	18.69	5.4	3.80	0.55	24.8	17.18	9.8	0.70	162.3
NGC6893	SA(s)°	8.95	2996	39.9	-	16.86	5.6	1.85	0.72	2.1	18.74	26.4	0.57	10.9
NGC6920	SA(rs)0°:	9.39	2762	36.8	-	16.54	3.9	2.46	0.82	140.4	17.59	13.1	0.84	130.2
NGC7007	SA0$^-$:	9.91	2801	37.3∗	125	16.78	3.1	1.86	0.81	133.0	17.80	11.7	0.60	1.7
NGC7020	(R)SA(r)0$^+$	9.77	2987	37.8∗	-	17.52	2.8	2.56	0.89	160.6	18.20	15.3	0.40	163.9
NGC7049	SA(s)0	8.14	2051	27.6∗	240	16.92	8.4	2.17	0.74	59.9	17.04	18.1	0.76	55.8
NGC7083	SA(s)bc	9.37	2999	38.7∗	71	18.19	3.6	1.34	0.95	16.1	17.88	18.6	0.56	7.9
NGC7096	SA(s)a	9.84	2847	36.7∗	248	18.95	12.5	4.05	0.90	124.8	18.58	10.8	0.82	101.3
NGC7135	SA0$^-$ pec	9.72	1799	34.7∗	-	18.84	8.1	4.69	0.74	6.6	18.90	21.1	0.64	48.8
NGC7166	SA0$^-$	9.47	2233	30.2∗	-	16.12	2.7	1.70	0.67	9.9	17.73	13.5	0.47	13.2
NGC7172	Sa pec	9.44	2315	33.9∗	179	17.35	3.3	1.16	0.82	80.3	17.56	15.5	0.52	95.8

Table 3.2: continued.

Galaxy	Type	J_T	V_{3K}	D	σ_0	μ_e	r_e	n	q_b	PA_b	μ_0	h	q_d	PA_d
		(mag)	(km/s)	(Mpc)	(km/s)	(mag/"^{2})	(")			(°)	(mag/"^{2})	(")		(°)
(1)	(2)	(3)	(4)	(5)	(6)	(7)	(8)	(9)	(10)	(11)	(12)	(13)	(14)	(15)
NGC7192	SA0$^-$:	9.37	2794	31.6∗	179	18.08	10.0	2.91	0.96	8.5	18.38	16.5	0.96	137.0
NGC7302	SA(s)0$^-$:	9.99	2221	33.7∗	-	16.31	2.2	1.35	0.86	88.0	17.66	11.0	0.61	99.0
NGC7311	Sab	9.96	4185	55.8	-	16.11	1.8	1.26	0.82	25.8	17.14	9.3	0.51	12.2
NGC7377	SA(s)0$^+$	9.08	3036	40.5	144	17.93	7.7	1.78	0.84	105.6	18.22	21.6	0.78	102.8
NGC7550	SA0$^-$	9.93	4789	63.8	234	18.68	9.2	3.40	0.97	179.5	18.30	12.1	0.86	146.8
NGC7585	(R')SA(s)0$^+$ pec	9.36	3104	41.4	219	17.74	6.9	3.33	0.69	106.4	17.70	15.1	0.82	106.4
NGC7600	S0$^-$ sp	9.82	3086	41.1	210	17.96	5.9	2.75	0.97	175.0	17.89	11.7	0.90	150.1
NGC7606	SA(s)b	8.62	1881	28.9∗	147	17.45	2.8	1.02	0.63	147.2	18.22	31.9	0.41	145.1
NGC7625	SA(rs)a pec	9.90	1272	23.0∗	-	17.77	4.3	0.89	0.59	58.1	16.91	9.0	0.74	32.0
NGC7702	(R)SA(r)0$^+$	9.92	3062	40.8	-	16.64	2.6	1.02	0.61	99.8	17.82	12.9	0.53	114.8
NGC7711	S0	9.99	3705	49.4	180	18.62	5.7	3.30	0.75	93.0	19.37	19.1	0.33	9 1.7
NGC7722	S0/a	9.88	3673	49.0	165	17.26	4.3	1.52	0.61	144.8	17.37	10.5	0.85	139.8
NGC7742	SA(r)b	9.60	1294	22.2∗	95	15.66	1.4	3.10	0.91	12.6	16.24	7.5	0.98	180.0
NGC7769	(R)SA(rs)b	9.90	3877	51.6	-	18.43	6.6	3.82	0.60	11.6	17.59	12.1	0.87	100.4
UGC12591	S0/a	9.99	6615	88.2	288	16.78	3.7	1.51	0.43	59.2	17.77	11.3	0.51	58.2

NOTE. The columns show the following: (1) galaxy name; (2) morphological classification from de Vaucouleurs et al. (1991, hereafter RC3); (3) total observed J-band magnitude from the 2MASS all-sky extended source catalogue (XSC); (4) radial velocity with respect to the CMB radiation from Lyon Extragalactic Database (hereafter LEDA); (5) distances obtained as V_{3K}/H_0 with H_0=75 km s^{-1}Mpc^{-1}, distances marked with an asterisk have been taken from Tully (1988); (6) central velocity dispersion from LEDA; (7) effective surface-brightness of the bulge; (8) effective radius of the bulge; (9) shape parameter of the bulge; (10) axis ratio of the bulge; (11) position angle of the bulge; (12) central surface-brightness of the disk; (13) scale-length of the disk; (14) axis ratio of the disk; (15) position angle of the disk.

3.4 Correlations between structural parameters

The study of correlations between the structural parameters of bulges and disks of our sample galaxies will help us to both cross check our results with those available in literature and identify and rule out peculiar bulges from any further analysis.

3.4.1 Bulge parameters

We did not find any correlations between the bulge parameters and Hubble type. Neither the effective radius (Fig. 3.3A), effective surface-brightness (Fig. 3.3B) nor the n shape parameter (Fig. 3.3C) show a statistically significant Pearson correlation coefficient (r).

From NIR observations of spiral galaxies, Andredakis et al. (1995) found that bulges of early-type spirals are characterized by $n \approx 4$ (i.e., they have a de Vaucouleurs radial surface-brightness profile), while the bulges of late-type spirals are characterized by $n \approx 1$ (i.e., they have an exponential radial surface-brightness profile). This early result was confirmed in various studies (e.g., de Jong et al. 1996; Khosroshahi et al. 2000; MacArthur et al. 2003; Möllenhoff & Heidt 2001; Möllenhoff 2004; Hunt et al. 2004). We argue that our data does not show such a correlation due to the smaller range of Hubble types covered by our sample (S0–Sb) with respect to the cited works, where it is mostly evident for Hubble types later than Sb.

The n shape parameter increases with effective radius. Larger bulges have a surface-brightness radial profile that is more centrally peaked than that of the smaller bulges (Fig. 3.3D). We obtained

$$\log n = 0.38(\pm 0.02) + 0.18(\pm 0.05)\ \log r_{\rm e} \qquad (r = 0.28). \tag{3.4}$$

The effective surface-brightness is dependent on the effective radius. Larger bulges have a lower effective surface-brightness (Fig. 3.3E). We found a linear regression

$$\log \mu_{\rm e} = 17.74(\pm 0.07) + 1.7(\pm 0.2)\ \log r_{\rm e} \qquad (r = 0.55). \tag{3.5}$$

This is in agreement, within the errors, with the correlation by MH01. If we use the mean surface-brightness inside one effective radius instead of the effective surface-brightness this relation becomes the so-called Kormendy relation, already known for bulges and elliptical galaxies (Kormendy 1977).

Finally, the absolute luminosity of the bulge is correlated with the effective radius. Larger bulges are more luminous (Fig. 3.3F). This result in

$$M_{\rm b} = -21.93(\pm0.06) - 3.4(\pm0.2)\ \log r_{\rm e} \qquad (r = -0.80), \tag{3.6}$$

where $M_{\rm b}$ is the $J-$band magnitude of the bulge. A similar result was obtained by MH01 for a smaller sample of disk galaxies spanning a larger range of Hubble types.

Bulges and elliptical galaxies follow a tight relation, the fundamental plane (FP), defined by the effective radius, mean surface-brightness within effective radius, and central velocity dispersion of the galaxy (Djorgovski & Davis 1987; Dressler et al. 1987). Therefore, we derived the FP for the bulges of our sample galaxies. The measurements of the central stellar velocity dispersion for a subsample of 98 galaxies were available in the literature and were retrieved from the on line HyperLeda catalog (Paturel et al. 2003). The velocity dispersions given by the catalogue are corrected to a circular aperture of radius of 0.595 $\rm h^{-1}$ kpc, which is equivalent to an angular diameter of $3\farcs4$ at the distance of Coma, following the prescription by Jorgensen et al. (1995). The aperture-corrected velocity dispersions are given in Table 3.2. The coefficients describing the FP

$$\log r_{\rm e} = 1.08(\pm0.09)\log\sigma_0 + 0.25(\pm0.02)\langle\mu_{\rm e}\rangle - 6.61(\pm0.40), \tag{3.7}$$

were derived by minimizing the square root of the residuals along the $\log r_{\rm e}$ axis. Errors given for every coefficient were calculated by performing a bootstrap analysis with 1000 iterations. No statistically significant difference was observed when only bulges of lenticular or early-to-intermediate spiral galaxies were considered. The dispersion around this relation is $\sigma = 0.11$ dex and was measured as the rms scatter in the residuals of $\log r_{\rm e}$. The observational error on the FP is 0.066 dex and includes the measurement errors in $\log r_{\rm e}$ (0.055 dex), $\log\sigma_0$ (0.029 dex), and $\langle\mu_{\rm e}\rangle$ (0.021 mag arcsec^{-2}). Errors in $\log r_{\rm e}$ and $\langle\mu_{\rm e}\rangle$ are not independent (Kormendy 1977). Compared with the dispersion around the relation, this gives an intrinsic scatter of 0.088 dex. Figure 3.4 shows an edge-on view of the FP. Our coefficients and those by Falcón-Barroso et al. (2002) are consistent within the errors, although they analyzed $K-$band data. Unfortunately, we have not found in the literature the coefficient of the FP in the $J-$band for a direct comparison (Bernardi et al. 2003).

One of the projections of the FP is the so-called Faber-Jackson (FJ) relation, which relates the luminosity of elliptical galaxies and bulges to their central velocity dispersion (Faber & Jackson 1976). We derived the $J-$band FJ relation for the bulge subsample obtaining

$$\log\sigma_0 = 0.1(\pm0.2) - 0.10(\pm0.01)M_{\rm b} \qquad (r = -0.71). \tag{3.8}$$

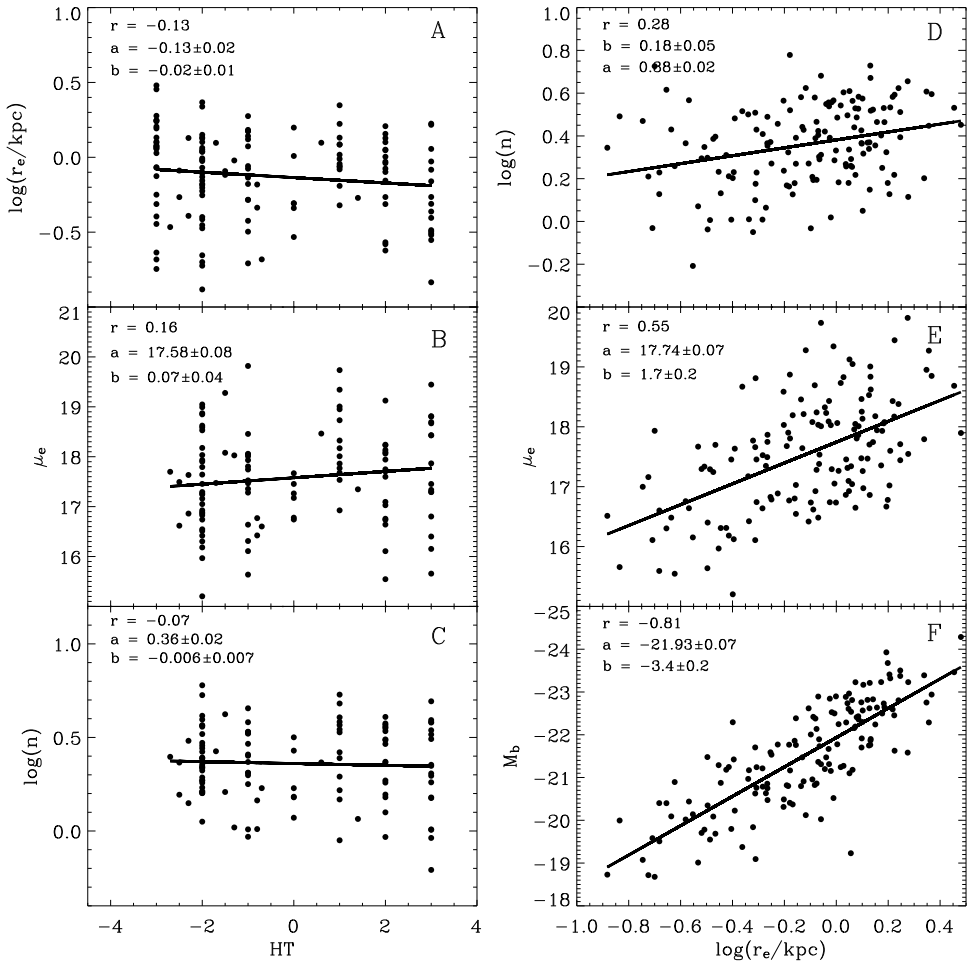

FIGURE 3.3— Correlations between the bulge parameters. Correlation between the Hubble type and effective radius (A), effective surface-brightness (B), and shape parameter (C). Correlations between the effective radius and shape parameter (D), effective surface-brightness (E), and absolute magnitude (F). In each panel the solid line represents the linear regression through all the points. The Pearson correlation coefficient (r), and the results of the linear fit ($y = a + bx$) are also given.

This result holds also when we consider only galaxies with errors on the central velocity dispersion lower than 10 km s^{-1} ($\Delta \log \sigma_0 < 0.018$ dex). In fact, we derived

$$\log \sigma_0 = 0.4(\pm 0.3) - 0.08(\pm 0.01) M_{\rm b} \qquad (r = -0.65), \tag{3.9}$$

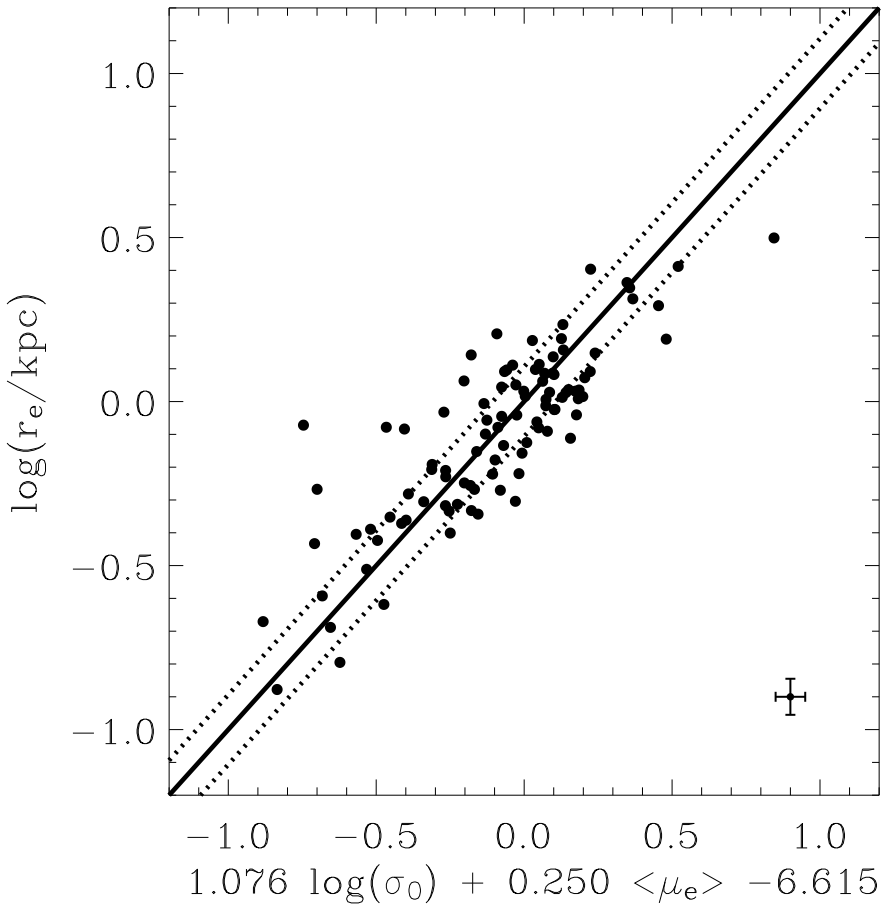

FIGURE 3.4— Edge-on view of the FP for the 98 early-to-intermediate type bulges of our sample with measured velocity dispersion. The solid line represents the linear fit to the data. The dotted lines represent the 1σ deviation from the fit. The error bars in the lower right corner of the panel indicate the mean errors of the data.

which is consistent within errors with Eq. 3.8. From Eq. 3.8 we derived $L \propto \sigma_0^{4.2}$, which is very close to the virial relation and indicates that our bulges share important characteristics with bright elliptical galaxies (Matković & Guzmán 2005). On the other hand, Balcells et al. (2007) found $L \propto \sigma_0^{2.9}$ (close to faint ellipticals) observing a sample of bulges with the Hubble Space Telescope in the $K-$band. This discrepancy is not due to the adopted fitting method and it

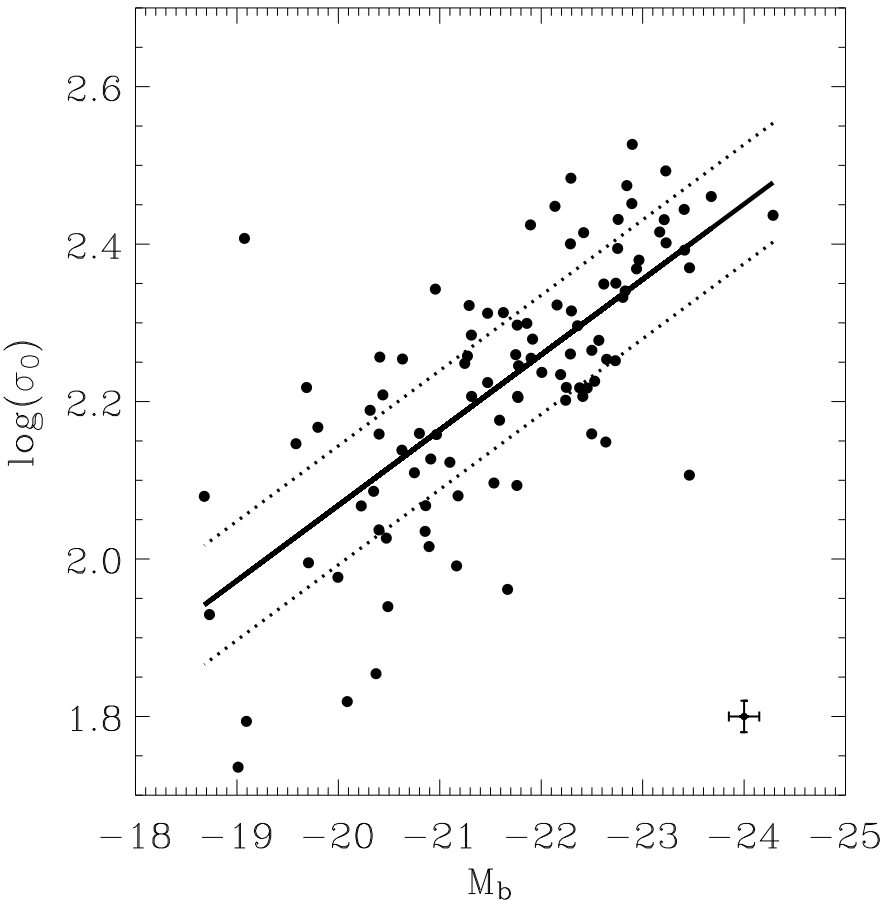

FIGURE 3.5— FJ relation for the 98 early-to-intermediate type bulges of our sample with measured velocity dispersion. The solid line represents the linear fit to the data. The dotted lines represent the 1σ deviation from the fit. The error bars in the lower right corner of the panel indicate the mean errors of the data.

is not observed if only bright bulges ($M_{\rm b} < -20$ mag) are considered. Indeed, we found $L \propto \sigma_0^{(3.9\pm0.4)}$ for our sample and $L \propto \sigma_0^{(3.6\pm0.7)}$ for the sample by Balcells et al. (2007). The different behavior of faint bulges ($M_{\rm b} > -20$ mag) requires further investigation to be explained.

Khosroshahi et al. (2000) noticed that the shape parameter, effective radius and central surface-brightness of elliptical galaxies and bulges are correlated.

This relation was termed photometric plane (PP). Fig. 3.6 shows an edge-on view of the PP of our bulge sample

$$\log n = 0.17(\pm 0.02) \log r_{\rm e} - 0.088(\pm 0.004)\mu_0 + 1.48(\pm 0.05). \qquad (3.10)$$

The coefficients were derived by minimizing the square root of the residuals along the $\log n$ axis. Errors given for every coefficient were calculated by performing a bootstrap analysis with 1000 iterations. No statistically significant difference was observed when only bulges of lenticular or early-to-intermediate spiral galaxies were considered. The dispersion around this relation is $\sigma = 0.04$ and was measured as the rms scatter in the residuals of $\log n$. Our coefficients and those by MH01 are consistent within the errors, although their sample is dominated by bulges of late-type spirals. The presence of the bulges of lenticular and spirals on the same PP hints at a common formation scenario.

3.4.2 Disk parameters

Regarding the disk parameters, we found no correlation between the scale-length and Hubble type ($r = -0.06$, Fig. 3.7A). The same is true for the central surface-brightness. In fact, it shows a large scatter also with Hubble type ($r = -0.05$, Fig. 3.7B). This is consistent with the results of de Jong et al. (1996) and MH01.

On the other hand, the central surface-brightness and the luminosity of the disks are dependent on the scale-length. Larger disks have a lower central surface-brightness (Fig. 3.7D). We found a linear regression

$$\log \mu_0 = 17.36(\pm 0.1) + 1.4(\pm 0.2)\ \log h \qquad (r = 0.49), \qquad (3.11)$$

and brighter disks show larger scale-lengths (Fig. 3.7C)

$$M_{\rm d} = -21.21(\pm 0.09) - 3.5(\pm 0.2)\ \log h \qquad (r = -0.80), \qquad (3.12)$$

where $M_{\rm d}$ is the $J-$band magnitude of the disk.

The coefficients are in agreement within the errors with those given by MH01.

3.4.3 Bulge and disk interplay

We have found that the disk scale-length increases with central velocity dispersion. Since central velocity dispersion correlates with the virial mass of the bulge ($\mathcal{M}_{\rm b} = \alpha r_{\rm e}\sigma_0^2/G$ with $\alpha = 5$, Cappellari et al. 2006), we conclude that larger disks are located in galaxies with more massive bulges (Fig. 3.8A).

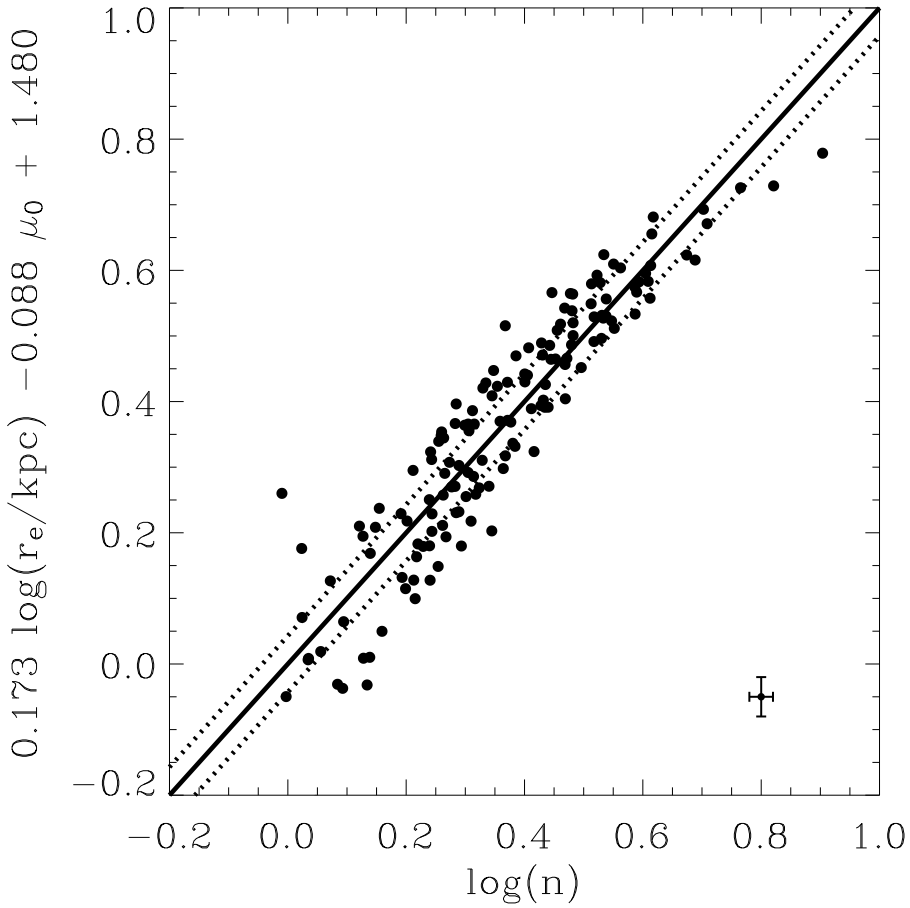

FIGURE 3.6— Edge-on view of the PP for early-to-intermediate bulges of our sample. The solid line represents the linear fit to the data. The dotted lines represent the 1σ deviation from the fit. The error bars in the lower right corner of the panel indicate the mean errors of the data.

For the subsample of 98 early-to-intermediate bulges with a measured velocity dispersion we found

$$\log \sigma_0 = 2.13(\pm 0.03) + 0.27(\pm 0.06)\ \log h \qquad (r = 0.42). \tag{3.13}$$

We also found a strong correlation between the bulge effective radius and the disk scale-length. Larger bulges reside in larger disks (Fig. 3.8B). This

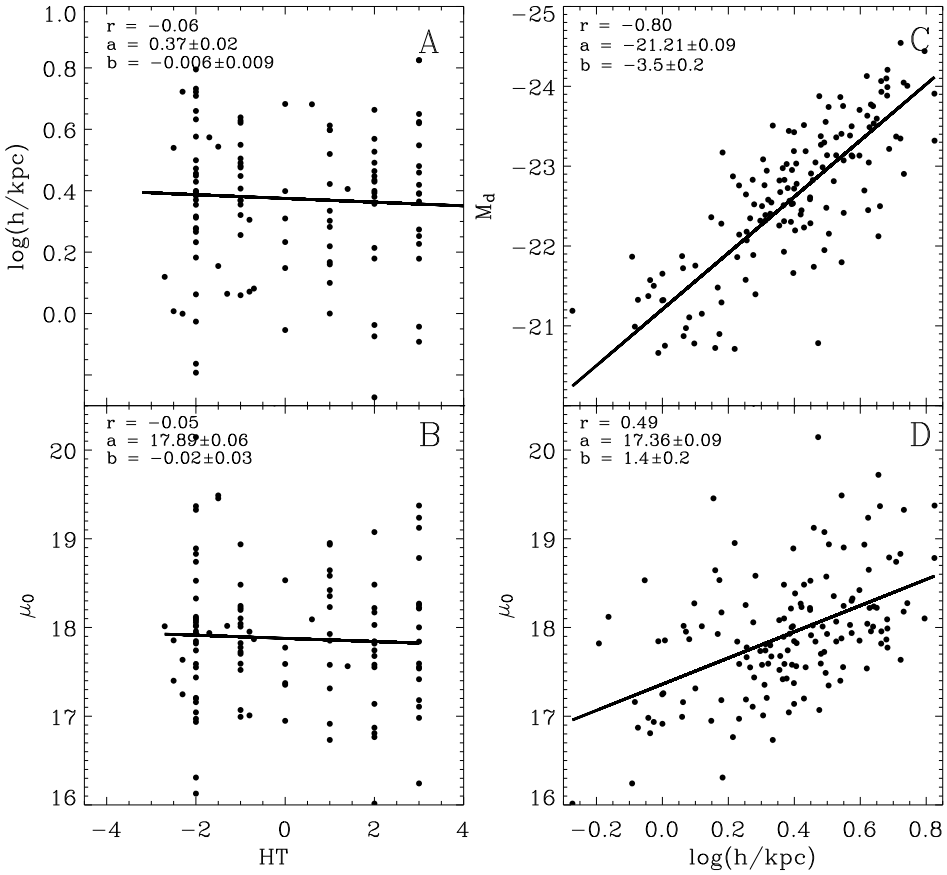

FIGURE 3.7— Correlations between the disk parameters. Correlations between the Hubble type and disk scale-length (A) and central surface-brightness (B). Correlation between the disk scale-length and absolute luminosity (C) and central surface-brightness (D). Solid lines and coefficients as in Fig. 3.3.

relation was already observed by Courteau et al. (1996) and later observed in NIR by MH01, MacArthur et al. (2003). We obtained a linear regression

$$\log r_{\rm e} = -0.45(\pm 0.03) + 0.91(\pm 0.07)\ \log h \qquad (r = 0.74), \tag{3.14}$$

which is in agreement within error bars with the correlation found by MH01. All these correlations between bulge and disk parameters indicate a link between the bulge and disk formation and evolution history. This connection was

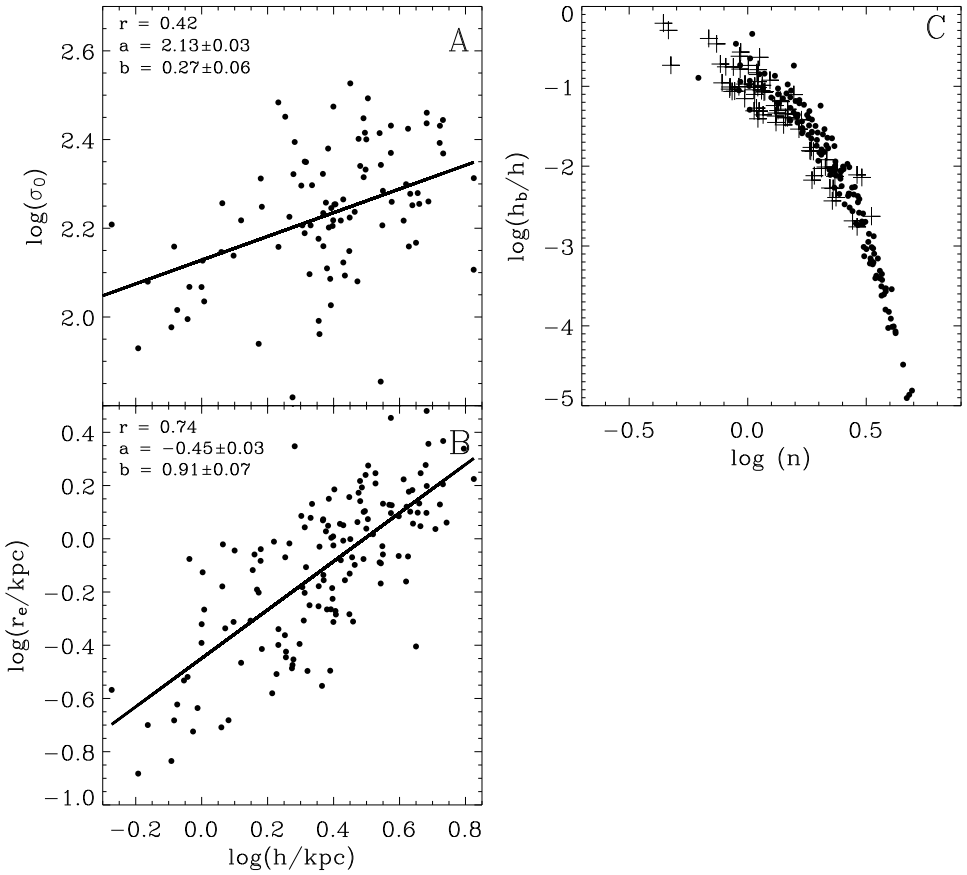

FIGURE 3.8— (A) Correlation between the disk scale-length and central velocity dispersion for the 98 galaxies of our sample with a measured velocity dispersion. (B) Correlation between the disk scale-length and bulge effective radius. (C) The ratio between the bulge and disk exponential scale-lengths as a function of bulge shape parameter. Filled circles and crosses represent the results of our measurements and simulations by Tissera et al. (2006), respectively. Solid lines and coefficients as in Fig. 3.3.

interpreted as an indication of the formation of late-type bulges via secular evolution of the disks (Courteau et al. 1996). However, our measurements of the scale-lengths of bulge and disk and n (Fig. 3.8C) are also fully consistent with the predictions of the numerical simulations by Scannapieco & Tissera (2003) and Tissera et al. (2006). They studied the effects of mergers on the mass

distribution of bulges and disks of galaxies formed in hierarchical clustering scenarios. Our mean value $\langle r_e/h \rangle = 0.36 \pm 0.17$ is also in good agreement with r_e/h found by Naab & Trujillo (2006) for a series of major mergers remnants. These results indicates that these relations are not enough to distinguish between bulges formed by mergers or by secular evolution of the disk, even if a strong crosstalk between both components is present.

3.5 Conclusions

The structural parameters of the bulge and disk of a magnitude-limited sample of 148 unbarred S0–Sb galaxies were investigated to constrain the dominant mechanism at the epoch of bulge assembly. Bulge and disk parameters of the sample galaxies were derived from the $J-$band images which were available in the Two Micron All Sky Survey using the new code GASP2D.

The bulges of the sample galaxies follow the same FP, FJ, and PP relationships found for elliptical galaxies. No statistically significant difference is observed when only bulges of lenticular and early-to-intermediate spiral galaxies were considered. This supports the idea that bulges and ellipticals formed in the same way.

Tight correlations between the parameters of bulges and disks were found. In fact, the disk scale-lengths increase with both the central velocity dispersion and bulge effective radius. Therefore, larger disks reside in galaxies with more massive and larger bulges. This was interpreted as an indication of the formation of bulges via secular evolution of their host disks.

Our measurements of the exponential scale-length of the bulge and disk as well as of bulge shape parameter were also fully consistent with numerical simulations of the effects mergers on the mass distribution of the bulge and disk in galaxies formed in hierarchical clustering scenarios.

These results indicate that the above scaling relations alone are not enough to clearly distinguish between bulges formed by early dissipative collapse, merging or secular evolution, and that a more general picture combining photometry, dynamics and stellar populations is the only way to obtain a more clear view of the assembly history of bulges.

Bibliography

Andredakis, Y. C., Peletier, R. F., & Balcells, M. 1995, MNRAS, 275, 874
Balcells, M., Graham, A. W., & Peletier, R. F. 2007, ApJ, 665, 1104
Bernardi, M., Sheth, R. K., Annis, J., et al. 2003, AJ, 125, 1866
Byun, Y. I., & Freeman, K. C. 1995, ApJ, 448, 563
Cappellari, M., Bacon, R., Bureau, M., et al. 2006, MNRAS, 366, 1126
Courteau, S., de Jong, R. S., & Broeils, A. H. 1996, ApJ, 457, L73

de Jong, R. S. 1996, A&AS, 118, 557
de Jong, R. S., & van der Kruit, P. C. 1994, A&AS, 106, 451
de Vaucouleurs, G., de Vaucouleurs, A., Corwin, H. G., et al. 1991, Third Reference Catalogue of Bright Galaxies (Springer-Verlag, New York) (RC3)
Djorgovski, S., & Davis, M. 1987, ApJ, 313, 59
Dressler, A., Lynden-Bell, D., Burstein, D., et al. 1987, ApJ, 313, 42
Faber, S. M., & Jackson, R. E. 1976, ApJ, 204, 668
Falcón-Barroso, J., Peletier, R. F., & Balcells, M. 2002, MNRAS, 335, 741
Graham, A. W. 2001, AJ, 121, 820
Hunt, L. K., Pierini, D., & Giovanardi, C. 2004, A&A, 414, 905
Jarrett, T. H., Chester, T., Cutri, et al. 2000, AJ, 119, 2498
Jorgensen, I., Franx, M., & Kjaergaard, P. 1995, MNRAS, 276, 1341
Khosroshahi, H. G., Wadadekar, Y., & Kembhavi, A. 2000, ApJ, 533, 162
Kormendy, J. 1977, ApJ, 217, 406
MacArthur, L. A., Courteau, S., & Holtzman, J. A. 2003, ApJ, 582, 689
Matković, A., & Guzmán, R. 2005, MNRAS, 362, 289
Möllenhoff, C. 2004, A&A, 415, 63
Möllenhoff, C., & Heidt, J. 2001, A&A, 368, 16
Naab, T., & Trujillo, I. 2006, MNRAS, 369, 625
Paturel, G., Petit, C., Prugniel, P., et al. 2003, A&A, 412, 45
Scannapieco, C., & Tissera, P. B. 2003, MNRAS, 338, 880
Skrutskie, M. F., Cutri, R. M., Stiening, R., et al. 2006, AJ, 131, 1163
Tissera, P. B., Smith Castelli, A. V., & Scannapieco, C. 2006, A&A, 455, 135
Tonry, J. L., Dressler, A., Blakeslee, J. P., et al. 2001, ApJ, 546, 681

4

Intrinsic shape of bulges: The equatorial ellipticity

Based on J. Méndez-Abreu, J. A. L Aguerri, E. M. Corsini and E. Simonneau, 2008, A&A, 478, 353

The probability distribution function of the equatorial ellipticity of the bulges was derived from the distribution of the observed ellipticities of bulges and misalignments between bulges and disks. About 80% of bulges in unbarred lenticular and early-to-intermediate spiral galaxies are not oblate but triaxial ellipsoids. Their mean axial ratio in the equatorial plane is $\langle B/A \rangle = 0.85$. Their probability distribution function is not significantly dependent on morphology, light concentration or luminosity. The presence of nuclear bars does not influence these results. The scenarios proposed until now in which bulges have assembled monolithically, from mergers and/or have grown over long times through disk secular evolution have to be tested against the derived distribution of bulge intrinsic ellipticities.

4.1 Introduction

Traditionally, the study of the relations between the structural parameters of the galaxies have been used to understand the bulge formation and evolution processes, as we have shown in the previous chapters. However, one piece lost in this study is the three-dimensional shape of the bulges. The shapes of the bulges is the final result of the processes of bulge formation and therefore it can help us to distinguish among the different scenarios proposed until now. A statistical study can provide a crucial piece of information for testing the

results of numerical simulations of bulge formation for different galaxy types along the morphological sequence.

There are several pieces of evidence suggesting that bulges of barred spiral galaxies are triaxial owing to their dynamical interaction with the bars (Kormendy 1982). The idea also growing that spiral galaxies in which no bar structure has been detected in the optical or infrared, could have triaxial bulges (Bertola et al. 1991).

Evidence suggesting that bulges of unbarred galaxies are triaxial structures come from different types of observations. From the photometry, the twisting of the inner isophotes and the misalignment between the disk and bulge major-axis position angles (Zaritsky & Lo 1986; Bertola et al. 1991) are not possible under the hypothesis of axisymmetry for the bulge and disk, so, it is considered as a clear signature of triaxiality. From the kinematics, the rotation curves with higher velocities than expected from the circular motions (Gerhard et al. 1989), the comparison between theoretical rotation curves derived from triaxial potentials with the observed data (Gerhard & Vietri 1986; Bertola et al. 1989; Berman 2001) or the velocity gradients along the minor-axis (Coccato et al. 2004) can be explained invoking triaxiality.

If triaxiality is common in bulges of disk galaxies, asymmetries in the potential of the inner galaxy can play an important role in the motion of interstellar gas, and could provide a method of transporting gas into the galaxy center. Therefore, it must be considered when accounting for fuelling of central starbursts, for the formation of inner rings or because this build up of gas in the galactic center can result in the creation or destruction of bars. Triaxial bulges must be also taken into account when we derive the dark halo density profiles by means of the rotation curve. Contrary to axisymmetric models, where the rotation curve depends only on the galaxy inclination, in a triaxial potential the shape of the rotation curve will depend on the position of the line-of-sight with respect to the major-axis of the non-axisymmetric component. This implies that the observed rotation curve might not trace the real circular velocity of the galaxy. Furthermore, the triaxiality must be also taken into account when the circular velocity is derived from the mass profile (de Zeeuw & Franx 1989), in order to avoid further errors when modeling the dark matter distribution.

The aim of this chapter is therefore to determine the probability distribution function (PDF) of the intrinsic equatorial ellipticity of non-barred bulges in order to quantify how common is triaxiality in bulges of disk galaxies. Following the previous statistical studies on bulges triaxiality (Zaritsky & Lo 1986; Bertola et al. 1991) we used only photometric data and assumed that the disk is axisymmetric and share its rotation axis with the bulge. However, we improve on the previous studies in several ways. First we used a more extensive and

better defined sample of galaxies, excluding misclassified objects through visual inspection of the residual images (see Chapter 3) in order to reject barred galaxies. Moreover, we retrieve the structural galaxy parameters by applying an accurate two-dimensional photometric decomposition algorithm to the galaxy images, GASP2D (see Chapter 2), and finally we determine the PDF using a new method where the equations for the intrinsic axial ratios are inverted analytically.

The Chapter is organized as follows: The geometrical formalism of the projection of a triaxial ellipsoid into a plane is presented in Sect. 4.2. The inverse problem, i.e., the deprojection of an ellipse in a plane into a triaxial ellipsoid is described in Sect. 4.3. The mathematical treatment to derive the PDF of intrinsic equatorial ellipticity for the individual galaxies and for the global sample is derived in Sect. 4.4 and Sect. 4.5, respectively. The PDF of intrinsic equatorial ellipticity for our sample galaxies is presented in Sect. 4.7. The influence of bars in our results is studied in Sect. 4.8. Finally, our conclusions and a summary of the results are given in Sect. 4.9.

4.2 Geometrical formalism

Let (x, y, z) be Cartesian coordinates with the origin in the galaxy center, the $x-$axis and $y-$axis corresponding to the principal axes of the bulge equatorial ellipse, and the $z-$axis corresponding to the polar axis. As the equatorial plane of the bulge coincides with the equatorial plane of the disk, the $z-$axis is also the polar axis of the disk. If A, B, and C are lengths of the ellipsoid semi-axes, the corresponding equation of the bulge in its own reference system is given by

$$\frac{x^2}{A^2} + \frac{y^2}{B^2} + \frac{z^2}{C^2} = 1. \tag{4.1}$$

Let (x', y', z') be now the Cartesian coordinates of the observer system. It has its origin in the galaxy center, the polar $z'-$axis along the line-of-sight (LOS) and pointing toward the galaxy, and the plane of the sky lies on the (x', y') plane.

The projection of the disk onto the sky plane is an ellipse whose major-axis is the line of nodes (LON, i.e., the intersection between the galactic and the sky planes). The angle θ between the $z-$axis and $z'-$axis corresponds to the inclination of the bulge ellipsoid; it can be derived as $\theta = \arccos(d/c)$ from the length c and d of the two semi-axes of the projected ellipse of the disk. We defined ϕ $(0 \leq \phi \leq \pi/2)$ as the angle between the x-axis and the LON on the equatorial plane of the bulge (x, y). Finally, we also defined ψ $(0 \leq \psi \leq \pi/2)$ as the angle between the x'-axis and the LON on the sky plane (x', y'). The

three angles θ, ϕ, and ψ are the usual Euler angles and relate the reference system (x, y, z) of the ellipsoid with that (x', y', z') of the observer by means of three rotations. Indeed, since the location of the LON is known, we can choose the $x'-$axis along it, and consequently $\psi = 0$. By applying these two rotations to Eq. 4.1 it is possible to derive the equation of the ellipsoidal bulge in the reference system of the observer, as well as the equation of the ellipse corresponding to its projection on the sky plane (Simonneau et al. 1998). Now, if we identify this ellipse with the ellipse that forms the observed ellipsoidal bulge, we can determine the corresponding axes of symmetry x_e and y_e. The first one, on which we measured the semi-axis a, forms an angle δ with the LON (the x'-axis in the observed plane); the semi-axis b is taken along the y_e-axis. We always choose $0 \leq \delta \leq \pi/2$, so it is possible that a either be the major or the minor semi-axis, and vice versa for b.

We have

$$a^2 b^2 = A^2 C^2 \sin^2\theta \cos^2\phi + B^2 C^2 \sin^2\theta \sin^2\phi + A^2 B^2 \cos^2\theta. \quad (4.2)$$

$$a^2 + b^2 = A^2(\cos^2\phi + \cos^2\theta \sin^2\phi) + B^2(\sin^2\phi + \cos^2\theta \cos^2\phi) + C^2 \sin^2\theta. \quad (4.3)$$

$$\tan 2\delta = \frac{(B^2 - A^2)\cos\theta \sin 2\phi}{A^2(\cos^2\theta \sin^2\phi - \cos^2\phi) + B^2(\cos^2\theta \cos^2\phi - \sin^2) + C^2 \sin^2\theta}. \quad (4.4)$$

If the ellipsoidal bulge is triaxial ($A \neq B \neq C$) then it is possible to observe a twist ($\delta \neq 0$; see Eq. 4.4) between the axes of the projected ellipses of the bulge and the disk.

4.3 Inverse problem or deprojection

We will now focus our attention on the inverse problem(i.e., deprojection). Following Simonneau et al. (1998), from Eqs. 4.2, 4.3, and 4.4, we are able to express the length of the bulge semi-axes (i.e., A, B, and C) as a function of the length of the semi-axes (i.e., a and b) of the projected ellipse and the position angle (δ)

$$A^2 = \frac{a^2 + b^2}{2}\left[1 + e\left(cos2\delta + sin2\delta \frac{sin\phi}{cos\phi}\frac{1}{cos\theta}\right)\right]. \quad (4.5)$$

$$B^2 = \frac{a^2 + b^2}{2}\left[1 + e\left(cos2\delta - sin2\delta \frac{cos\phi}{sin\phi}\frac{1}{cos\theta}\right)\right]. \quad (4.6)$$

$$C^2 = \frac{a^2 + b^2}{2}\left[1 + e\left(2sin2\delta \frac{cos\theta}{sin^2\theta}\frac{cos2\phi}{sin2\phi} - cos2\delta \frac{1 + cos^2\theta}{sin^2\theta}\right)\right], \quad (4.7)$$

where $e = (a^2 - b^2)/(a^2 + b^2)$ is, in some way, a measure of the ellipticity, lies in the range $-1 \leq e \leq 1$.

Notice that a, b, δ, and θ are all observed variables. Unfortunately, the relation between the intrinsic and projected variables also depends on the spatial position of the bulge (i.e., on the ϕ angle), which is not directly accessible to observations. For this reason, only a statistical determination can be performed to assess the intrinsic shape of bulges.

As A and B are the semi-axes of the equatorial ellipse of the bulge, we have to distinguish between two cases, according to Eqs. 4.5 and 4.6. If $a > b$ (or equivalently $e > 0$) then $A > B$. Otherwise, if $a < b$ (or equivalently $e < 0$) then $A < B$. Thus, if $\delta \neq 0$ the equatorial plane of the bulge ellipsoid is not circular and the bulge ellipsoid is triaxial.

From Eqs. 4.5, 4.6 and 4.7 we can write the axial ratios A/C and B/C as explicit functions of ϕ. Moreover, we assume that the angle ϕ is random and independent of the length of the ellipsoid semi-axes. Thus, the normalized probability distribution $P(\phi)$ of getting a given value of ϕ in $(\phi, \phi+d\phi)$ is

$$P(\phi) = 2/\pi \quad ; \qquad \int_0^{\pi/2} P(\phi) d\phi = 1. \tag{4.8}$$

According to a fundamental theorem of statistics, the probability of obtaining a given value of any function $f(\phi)$ (e.g., one of the axial ratios) will be equal to the probability of getting the corresponding value of ϕ, provided that the ratio $df/d\phi$ between the corresponding differential elements is taken into account.

In this work, we will focus our attention on the intrinsic equatorial ellipticity of bulges, defined as $E = (A^2\text{-}B^2)/(A^2+B^2)$ with $-1<E< 1$.

From Eqs. 4.5 and 4.6, it is straightforward to derive a relation among the intrinsic variables (i.e., equatorial ellipticity E and position angle ϕ), and the measured ones (i.e., θ, e, and δ), which is

$$\frac{E\,\sin 2\phi}{1 + E\,\cos 2\phi} = \frac{1}{\cos\theta}\frac{e \sin 2\delta}{1 + e \cos 2\delta} \equiv Q. \tag{4.9}$$

The second member of the equality in Eq. 4.9 allows us to define the observable Q in terms of the measured variables θ, e, and δ. It must be stressed that for each specific bulge the relation between the equatorial ellipticity E and the unknown parameter ϕ embraces the whole of the measured variables through the single variable Q.

On the one hand, Eq. 4.9 will yield the conditional probability $P_Q(E)$ that a given bulge, with a measured value of Q, takes on any particular value of E (individual statistic); on the other hand, this equation will give the probability $P_E(Q)$ associated to each value of Q for a bulge with intrinsic equatorial ellipticity E. This latter probability will be the kernel of an integral equation that

relates the observed statistical distribution $P(Q)$, corresponding to a sample of galaxies, with the statistical distribution of the equatorial ellipticity $P(E)$ for the same sample.

4.4 Individual statistics

For a given galaxy, we can measure the values of θ, e, and δ, and then derive the value of Q through Eq. 4.9. We want to determine the probability $P_Q(E)$ that such a galaxy (i.e., with such a value of Q) will take on a value of E in the range $(E, E+dE)$. The subindex Q specifies this galaxy. All the galaxies with the same value of Q will have the same probability distribution $P_Q(E)$.

Once the value of Q is prescribed, for some values of E there are not values of ϕ ($0 \leq \phi \leq \pi/2$) that satisfy Eq. 4.9. Hence, it shall hold that $P_Q(E) = 0$. Only for those values of E such that

$$E^2 \geq \frac{Q^2}{1+Q^2} \equiv T^2 \qquad (0 \leq T \leq 1), \tag{4.10}$$

will there exist two values of ϕ that satisfy Eq. 4.9.

Then for any value of $E > T$, the probability $P_Q(E)$ will be given by

$$P_Q(E) = \sum_{j=1,2} \left(P(\phi) \left| \frac{\delta\phi}{\delta E} \right|_Q \right)_{\phi_j} . \tag{4.11}$$

where the sumatory of the probabilities is evaluated over those values of ϕ for which Eq. 4.9 is satisfied.

To derive $\delta\phi/\delta E$ we already know from Eq. 4.9 that

$$\frac{1}{E} = \frac{\sin(2\phi) - Q\cos(2\phi)}{Q}, \tag{4.12}$$

and therefore

$$\frac{\delta E}{\delta \phi} = -E^2 \frac{\delta}{\delta\phi}\left(\frac{1}{E}\right) = -2\,E^2\,\frac{\cos(2\phi) + Q\sin(2\phi)}{Q}. \tag{4.13}$$

Evaluating 4.13 over the possible ϕ angles we obtain

$$\left| \frac{\delta\phi}{\delta E} \right|_{\phi_j} = \frac{T}{2E}\frac{1}{\sqrt{E^2+T^2}}, \tag{4.14}$$

since $P(\phi_1) = P(\phi_2) = 2/\pi$ the PDF is given by

$$P_Q(E) = \frac{2T}{\pi E}\frac{1}{\sqrt{E^2-T^2}} \qquad E \geq T. \tag{4.15}$$

To normalize the PDF, it is important to take into account that for a given value of Q, even if $T \leq E \leq 1$, ϕ cannot take on all the values in the interval $0 \leq \phi \leq \pi/2$, therefore the normalization must be written as

$$\begin{aligned} \int_T^1 P_Q(E)dE &= \frac{2}{\pi}\int_T^1 \frac{T}{E}\frac{1}{\sqrt{E^2-T^2}}dE \\ &= \frac{2}{\pi}\arccos(T). \end{aligned} \tag{4.16}$$

Finally the normalized PDF will be given by

$$P_T(E) = \frac{\frac{T}{E}\frac{1}{\sqrt{E^2-T^2}}}{\arccos T}\ , \tag{4.17}$$

where the subindex T plays the same role as the subindex Q; the two are related through Eq. 4.10.

This means that the possible values of E are very concentrated and slightly larger than T. To get an idea of how $P_T(E)$ is peaked near the value of T, we calculated the value $E_{1/2}$ for which the total probability that $E > E_{1/2}$ is equal to the probability that $E < E_{1/2}$. For every bulge $E_{1/2}$ is a sort of mean value of E, and is given by

$$E_{1/2} = \sqrt{\frac{2}{1+T}}T. \tag{4.18}$$

In Fig. 4.1 we show, as an example, the probability $P_T(E)$ for one galaxy of our sample.

4.5 Global statistics

Likewise, we can define the probability $P_E(Q)$ associated with each value of Q for a given bulge of intrinsic equatorial ellipticity E.

For a prescribed value of E, it will only be possible to get the values of ϕ that satisfy Eq. 4.9 when $T \leq E$. The probability $P(\phi_j)$ for the two values of ϕ_j is given by Eq. 4.8. The probability $P_E(T)$ is equal to the sum of the two probabilities $P(\phi_j)$, weighted with the ratio $(\delta\phi/\delta T)_E$ of the differential elements

$$P_E(Q) = \sum_{j=1,2}\left(P(\phi)\left|\frac{\delta\phi}{\delta Q}\right|_E\right)_{\phi_j}. \tag{4.19}$$

Once the partial derivative from Eq. 4.9 is computed, we obtain

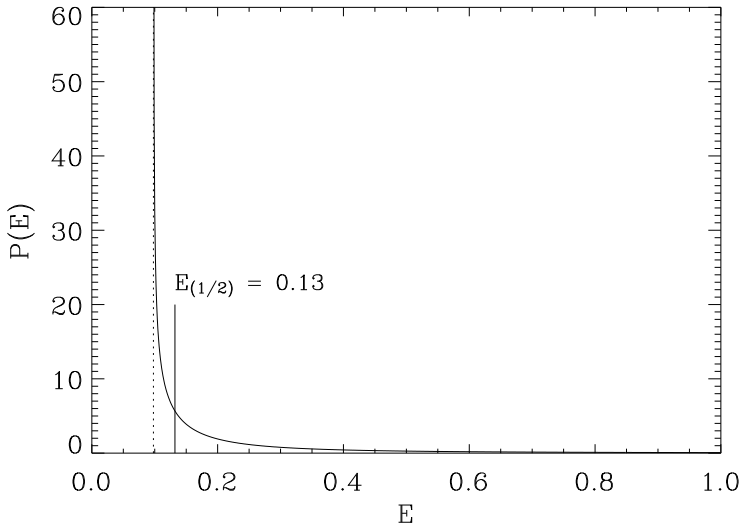

FIGURE 4.1— PDF of E for the galaxy IC 4310. The dotted line represents the value of T=0.098 derived for this galaxy. The value of $E_{1/2}$ is also showed in the plot.

$$P_E(T) = \frac{2}{\pi}\frac{1}{\sqrt{E^2 - T^2}} \qquad (E \geq T). \tag{4.20}$$

Our purpose here is to determine the probability distribution $P(E)$, that is the number of galaxies with a value of E in the interval $(E, E + dE)$, starting from a sample that is sufficiently representative. We have measured for such a sample the distribution $P(T)$, namely the number of bulges whose values of T are within T and $T + dT$. We then write $P(T)$ as the integral over all the values of E of the product of the conditional probability $P_E(T)$ by the so far unknown distribution $P(E)$

$$P(T) = \int_{-1}^{1} P(E)\, P_E(T)\, dE. \tag{4.21}$$

Then, by making use of Eq. 4.20, we obtain an Abel-like integral equation

$$P(T) = \frac{2}{\pi}\int_{T}^{1} \frac{P(E)}{\sqrt{E^2 - T^2}} dE, \tag{4.22}$$

which will allow us to derive $P(E)$ from the observed distribution $P(T)$.

However, as usual, the data $P(T)$ of our statistical problem takes the form of histograms, hence, the relevant equations must be formulated accordingly.

Let T_k with $k = 0, 1, 2, ..., N$ ($T_0 = 0$, $T_N = 1$) be a set of discrete ordinates which defines the histogram of the observed function $P(T)$ (Fig. 4.2). The k^{th}-element of this histogram is defined by

$$P_k(T) = \frac{1}{T_k - T_{k-1}} \int_{T_{k-1}}^{T_k} P(T)\, dT. \tag{4.23}$$

We must now seek the integral equation that relates the variables $P_k(T)$ with the probability distribution $P(E)$.

We notice that the integral of $P(T)$ in Eq. 4.23 is equivalent to the difference between the two quadratures of $P(T)$ over the intervals (T_{k-1},1) and (T_k,1). In both of them, we will replace $P(T)$ by its integral form, given by Eq. 4.22.

Then, by inverting the order of integration, we can easily rewrite the two resulting integrals to obtain

$$\begin{aligned} P_k(T) = & \frac{1}{T_k - T_{k-1}} \int_{T_{k-1}}^{T_k} P(E)\, dE \\ & - \frac{2/\pi}{T_k - T_{k-1}} \left[M(T_{k-1}) - M(T_k) \right], \end{aligned} \tag{4.24}$$

where we defined

$$M(T_k) = \int_{T_k}^{1} P(E) \arcsin(T_k/E)\, dE, \tag{4.25}$$

and $M(T_{k-1})$ in a similar way.

Equation 4.24 is the integral equation that will allow us to obtain the values of $P(E)$. Since it is consistent with the numerical structure of the data, we are confident that we have eliminated most of the numerical problems that arise from the direct inversion of Eq. 4.22, which constitutes a typical ill-posed problem.

At this point, we require for $P(E)$ the same histogram representation that we have already introduced for the data $P(T)$. We introduce a similar set of discrete ordinates for the variable E (i.e., $E_k \sim T_k$), and an analogous definition to obtain the elements $P_k(E)$ of the histogram

$$P_j(E) = \frac{1}{E_j - E_{j-1}} \int_{E_{j-1}}^{E_j} P(E)\, dE. \tag{4.26}$$

Thus, Eq. 4.24 can be rewritten into the form

$$P_k(T) = P_k(E) - \frac{2/\pi}{T_k - T_{k-1}} \left[M(T_{k-1}) - M(T_k) \right]. \tag{4.27}$$

In order to express the integrals $M(T_{k-1})$ and $M(T_k)$ as linear functions of the so far unknown values of $P_j(E)$ (where $j > k-1$), we consider that $P(E)$ is constant and equal to the unknown values of $P_j(E)$ over each interval (E_{j-1}, E_j), according to its histogram representation. Therefore, it is straightforward to compute the coefficients $CM(k,j)$, defined by the linear relation

$$M(T_k) = \sum_{j=k+1}^{N} CM(k,j)\, P_j(E). \tag{4.28}$$

Thus, Eq. 4.27 becomes a simple linear algebraical equation that relates the terms of the two histograms $P_k(T)$ and $P_j(E)$ through a triangular matrix. Once we have the integral Eq. 4.22 into a suitable matrix form, according to the histogram representation of the data and results, a simple matrix inversion could be, in principle, enough to obtain the resulting $P_j(E)$. However, such a procedure may add to the intrinsic difficulties, due to the lack of precision typical of the observational data, which naturally arise in the matrix inversion process; a catastrophic mixture when dealing with an inverse problem.

4.6 Inversion methods for the integral equation

We have considered two different approaches to tackle the numerical problem. The first one is suggested by the method that leads us to the integral Eq. 4.27 for the set of discrete elements $P_k(T)$. We notice that there are two different terms in its right-hand side. The first one is the identity operator. The second one is the difference between two integrals of $P(T)$, multiplied by a kernel that is quickly decreasing. We can consider the former as the leading term, and treat the latter as a corrective term in a iterative perturbation method. Consequently, we can write Eq. 4.27 as

$$P_k(E) = P_k(T) + \frac{2/\pi}{T_k - T_{k-1}} \left[M(T_{k-1}) - M(T_k]) \right], \tag{4.29}$$

where we can determine $\mathrm{P}_k^i(E)$ at the i^{th}-iteration making use of the form of $\mathrm{P}_k^{i-1}(E)$ from the $(i-1)^{th}$-iteration to compute the correction term $[M(T_{k-1}) - M(T_k)]$. As an initial guess, we consider $P_k(E)$ equal to $P_k(T)$ at a zero-order approximation. This iterative process is repeated until convergence is achieved.

From the data $P(T)$ of the histogram shown in Fig. 4.2, we have obtained a satisfactory solution $P(E)$ with a small number (5-10) of iterations. We will

discuss later the physical quality of this solution, but we must recognize here the stability of the method. Actually, we always achieved the same solution with a few number of iterations, starting from any trial initial distribution (namely, any zero-order approximation for $P_k(E)$). Moreover, the greater advantage of solving the integral equation by means of an iterative perturbation method is the possibility to recover, according to Eq. 4.27, the approximate diagram $P_k^i(T)$ that corresponds to any iterative solution $P_k^i(E)$, and this yields a double check on the evolution and quality of results.

However, when dealing with this kind of inverse problem, it may often happen in the practice that the results are correct mathematically, but not from the physical standpoint (i.e., negative values of the probability). In view of this difficulty, and in spite of the excellent quality of the foregoing iterative method, we wished to develop an alternative method of inversion for the integral Eq. 4.22, in order to double check the results.

The other way to treat numerically the integral Eq. 4.22 comes from the analytical inversion. Applying the integral operator $\int_{T'}^{1} T/\sqrt{T^2 - T'^2}\, dT$ to both sides of Eq. 4.22 we found

$$\frac{\pi}{2}\int_{T'}^{1}\frac{T}{\sqrt{T^2-T'^2}}P(T)dT = \int_{T'}^{1}P(E)dE\int_{T'}^{E}\frac{T}{\sqrt{T^2-T'^2}}\frac{1}{\sqrt{E^2-T^2}}dT, \quad (4.30)$$

Integrating, using a change of variable, the last integral of 4.30 we obtain

$$\int_{T'}^{E}\frac{T}{\sqrt{T^2-T'^2}}\frac{1}{\sqrt{E^2-T^2}}dT = \frac{\pi}{2} \quad (4.31)$$

and therefore

$$\int_{T'}^{1}P(E)dE = \int_{T'}^{1}\frac{T}{\sqrt{T^2-T'^2}}\,P(T)\,dT \quad (4.32)$$

Once we have this analytical form for the required solution, we rewrite it for the histogram representation of $P(E)$, by defining $P_k(E)$ as $P_k(T)$ in Eq. 4.26. Again the difference between the two integrals of $P(T)$ shows up. Now, we impose the histogram model of this $P(T)$ to derive analytically the matrix elements that relate any $P_k(E)$ to all the elements $P_k(T)$. The corresponding solutions obtained with the two methods are the same, allowing for the small differences due to round-off errors of the two different numerical algorithms employed.

Now that we are confident of the reliability of both methods of inversion of the integral equation, we can came back to the aforesaid difficulties.

When applying either method to the observed distribution $P(T)$, in the form of a histogram with bins $P_k(T)$ as shown in Fig. 4.2, we may obtain non-physical results, these are negative values for some bins $P_k(E)$. This occurs due to the fact that in the frame of the adopted histogram representation for $P_k(T)$ and $P_k(E)$ and the associated numerical algorithm chosen to represent the matrix operator for the integral Eq. 4.22, the measured values $P_k(T)$ cannot be the integral transform of any physical distribution $P(E)$. However, another set of values $P_k(T)$ that are slightly different from the original, and consequently compatible with the observations, might satisfy the above requirement (i.e., it can be the integral transform of some physical $P(E)$ and its inverse transform will solve our problem).

These considerations claim a statistical regularization process, which can be achieved by considering the histogram $P(T)$ to be the statistical mean of 1000 histograms, all of them compatible with the observations according to Poisson statistics. For each one of the 1000 possible realizations for $P_k(T)$, we have obtained the corresponding $P_k(E)$ by means of the inversion of the integral equation. The non-physical histograms $P_k(E)$ (i.e., those with some negative bins) were rejected. From the physical solutions, we have obtained the mean histogram and the corresponding error bars, as shown in Fig. 4.3. The statistical regularization process also allows us to estimate errors due to the possible lack of statistics in the sample.

4.7 The probability distribution function of intrinsic ellipticities

In Fig. 4.3 we present the PDF of the bulge intrinsic ellipticities $P(E)$. It was obtained by applying the procedure described in Sect. 4.6 using the PDF $P(T)$ shown in Fig. 4.2. The T values for each galaxy were calculated by means of Eqs. 4.9 and 4.10 from the measured values of e, δ, and θ.

The PDF is characterized by a significant decrease of probability for $E<0.07$ (or equivalently $B/A<0.93$), suggesting that the shape of bulge ellipsoids in their equatorial plane is most probably elliptical rather than circular. Such a decrease is caused neither by the lack of statistics (because in the regularization method we took into account the Poisson noise) nor by the width of the bins (because we tried different bin widths).

We have calculated the average E value weighted with the PDF through

$$\langle E\rangle = \frac{\sum_i \mathrm{PDF}(E_i)\, E_i}{\sum_i \mathrm{PDF}(E_i)}, \tag{4.33}$$

obtaining a value of $\langle E\rangle = 0.16$ ($\langle B/A\rangle = 0.85$). This is fully consistent with

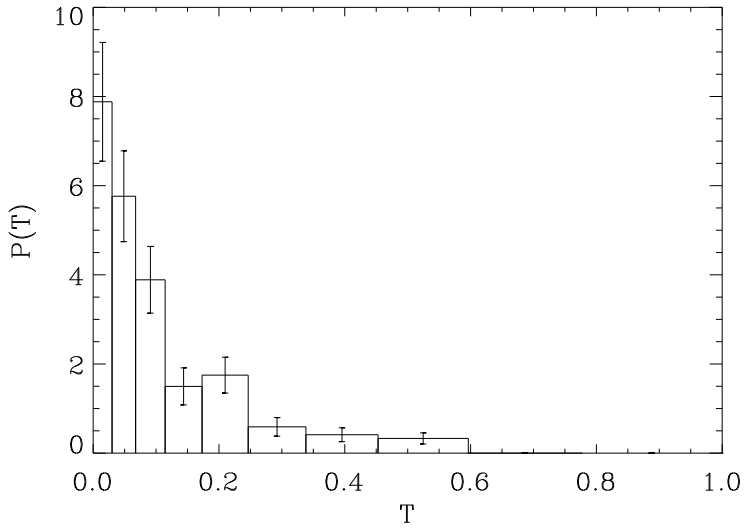

FIGURE 4.2— PDF of T. The probability is normalized over 10 bins, which are geometrically distributed to cover the interval $(0, 1)$. The width of the first bin is 0.03 and the width ratio of two consecutive bins is 1.25. Error bars correspond to Poisson statistics.

previous findings by Bertola et al. (1991) and Fathi & Peletier (2003), based on the analysis of smaller samples of bulges. For the sake of comparison, the value of $\langle B/A \rangle$ was derived from their data using Eq. 45. It is $\langle B/A \rangle = 0.85$ for the bulges studied by Bertola et al. (1991). They adopted a different approach to derive the PDF for intrinsic axial ratio of bulges from the misalignment of the major axes of bulges and disks and the apparent ellipticity of bulges. It is $\langle B/A \rangle = 0.79$ for the early-type bulges of the sample studied by Fathi & Peletier (2003). They measured the bulge equatorial ellipticity by analyzing the deprojected ellipticity of the ellipses fitting the galaxy isophotes within the bulge radius.

A further important result derived from $P(E)$ is that there are not bulges with $E > 0.6$ ($B/A < 0.5$). This is also in good agreement with Bertola et al. (1991) and Fathi & Peletier (2003). They found a minimum axial ratio $B/A = 0.55$ and $B/A = 0.45$, respectively.

We also studied the possible differences in the shape of bulges depending on their observational characteristics (i.e., morphology, light concentration, and luminosity, see Fig. 4.4). First of all, we subdivided our bulges according to the morphological classification $-3 \leq \mathrm{HT} < 0$ and $0 \leq \mathrm{HT} \leq 3$ of their host

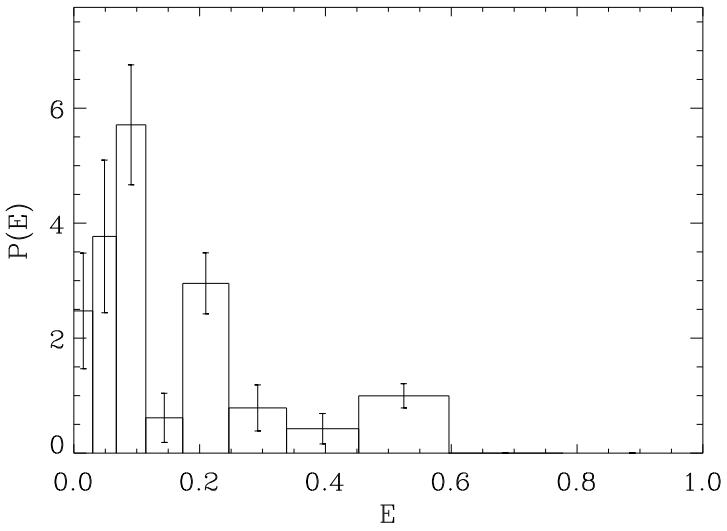

FIGURE 4.3— PDF of E. The probability is normalized over 10 bins, which are geometrically distributed to cover the interval $(0, 1)$. The width of the first bin is 0.03 and the width ratio of two consecutive bins is 1.25. The error bar of each $P_k(E)$ bin corresponds to the Poisson statistics of 1000 realizations of $P_k(T)$ after excluding non-physical cases.

galaxies to look for differences between lenticular and early-type spiral galaxies. A second test was done by subdividing the sample bulge between those with a Sérsic index $n < 2$ and those with $n \geq 2$ to investigate possible correlations of bulge shape with light concentration. Finally, we subdivided our bulge into faint ($M_{\rm b} \geq -22$) and bright ($M_{\rm b} < -22$) in order to search for differences of bulge shape with the $J-$band total luminosity. We did not find any significant difference between the studied subsamples. They are characterized by the same distribution of E, as confirmed at a high confidence level ($> 99\%$) by a Kolmogorov-Smirnov test.

Several authors discussed the problem of the intrinsic shape of elliptical galaxies by means of observations and/or numerical simulations. Ryden (1992), Lambas et al. (1992), and Bak & Statler (2000) agree that the observed distribution of ellipticities cannot be reproduced by any distribution of either prolate or oblate spheroidal systems. Any acceptable distribution of triaxial systems is dominated by nearly-oblate spheroidal rather than nearly-prolate spheroidal systems. The formation of triaxial elliptical galaxies via simulation of merging events in the framework of a hierarchical clustering assembly was studied

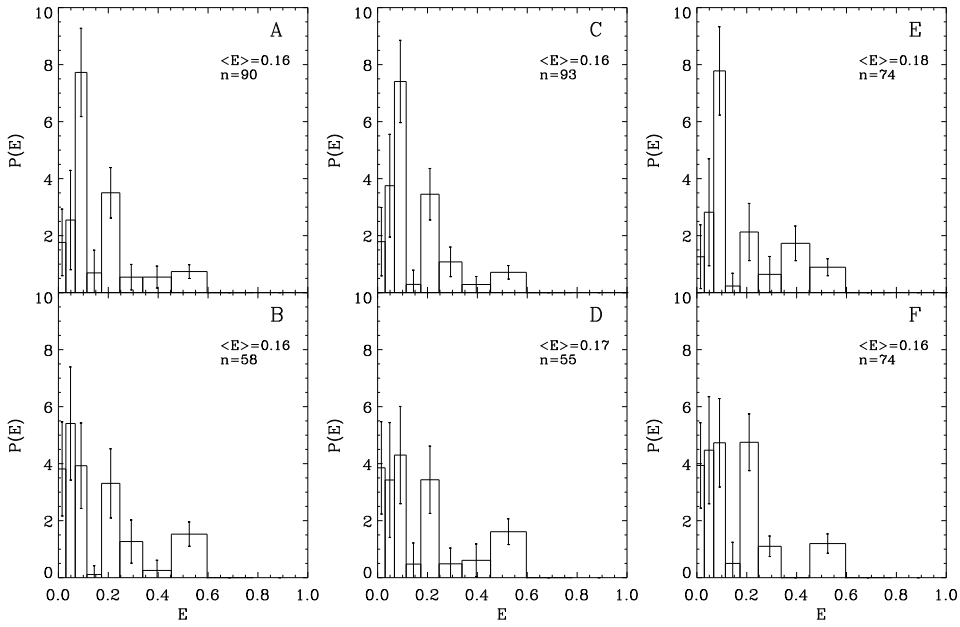

FIGURE 4.4— PDF of E for the different subsamples. (A) Lenticular galaxies ($-3 \leq \mathrm{HT} < 0$). (B) Spiral galaxies ($0 \leq \mathrm{HT} \leq 3$). (C) Galaxies with $n \geq 2$. Panel D: Galaxies with $n < 2$. (E) Faint bulges ($M_\mathrm{b} \geq -22$). (F) Bright bulges ($M_\mathrm{b} < -22$). Bin widths and error bars as in Fig. 4.3. The mean intrinsic ellipticity and the number of galaxies of the subsample are given in each panel.

by Barnes & Hernquist (1996), Naab & Burkert (2003), and Gónzalez-García & Balcells (2005). On the other hand, in the monolithic scenario where the galaxy formation occurs at high redshift after a rapid collapse, we may expect that the final galaxy shape would be nearly spherical or axisymmetric, as recently found in numerical experiments by Merlin & Chiosi (2006). But there is no extensive testing of the predictions of numerical simulations against the derived distribution of bulge intrinsic ellipticities.

4.8 The influence of nuclear bars on $P(E)$

The presence of nuclear bars in galaxy bulges has been known since the former work of de Vaucouleurs (1974). However, it is only in the last decade with the advent of high-resolution imaging that a large number of them have been detected allowing the study of their demography and properties (Erwin 2004).

The sample galaxies were selected as not hosting large-scale bars, according to visual inspection and photometric decomposition of their $J-$band images (Sect. 3.2). These selection criteria did not account for the possible presence of nuclear bars. In fact, our sample has 23 galaxies in common with the samples studied by Mulchaey & Regan (1997), Jungwiert et al. (1997), Martini & Pogge (1999), Márquez et al. (1999), and Laine et al. (2002). They were interested in the demography of nuclear bars. A nuclear bar was found in 6 to 8 out of these 23 galaxies (26%–35%), according to the different authors' classifications.

Since nuclear bars are more elongated than their host bulges and have random orientations, they could affect the measurement of the structural parameters of bulges and consequently their $P(E)$. To address this issue we carried out a series of simulations on a large set of artificial galaxies. They were obtained by adding a nuclear bar to the artificial image of a typical galaxy of the sample and analyzing the structural properties of the resulting image with GASP2D, as done in Sect. 3.3.

We adopted a Ferrers profile (Laurikainen et al. 2005) to describe the surface-brightness of the nuclear bar component

$$I_{\rm nb}(\xi,\eta) = \begin{cases} I_{0,\rm nb}\left(1-\left(\frac{r_{\rm nb}}{a_{\rm nb}}\right)^2\right)^{n_{\rm nb}+0.5} & \text{if } r_{\rm nb} \leq a_{\rm nb} \\ 0 & \text{if } r_{\rm nb} > a_{\rm nb} \end{cases} \tag{4.34}$$

where the coordinates (x, y) are defined as in Sect. 2.2 and $a_{\rm nb}$, $I_{0,\rm nb}$, and $n_{\rm nb}$ are the bar length, its central surface-brightness, and a shape parameter describing the curvature of the surface-brightness profile, respectively. Following Laurikainen et al. (2005), we chose $n_{\rm nb} = 2$. Nuclear bar isophotes are ellipses centered on (x_0, y_0) with constant position angle $\rm PA_{nb}$ and constant ellipticity $\epsilon_{\rm nb} = 1 - q_{\rm nb}$. The radius $r_{\rm nb}$ is given by

$$\begin{aligned} r_{\rm nb} \;=\; & \Big[(-(x-x_0)\sin \rm PA_{nb} + (y-y_0)\cos \rm PA_{nb})^2 + \\ & - ((x-x_0)\cos \rm PA_{nb} + (y-y_0)\sin \rm PA_{nb})^2/q_{nb}^2\Big]^{1/2}. \end{aligned} \tag{4.35}$$

We generated 1000 images of galaxies with a Sérsic bulge, an exponential disk, and a Ferrers nuclear bar. The structural parameters of the bulge and disk were selected to match those of a typical galaxy of the studied sample. It has $J_T = 9.6$ mag, $r_{\rm e} = 0.87$ kpc, $n = 2.32$, $h = 2.47$ kpc, and $B/T = 0.37$ according to the mean values of the structural parameters given in Table 3.2. The apparent ellipticity and position angle of the bulge and disk were randomly

TABLE 4.1— Errors on the ellipticity and position angles of bulge and disk calculated for galaxies with nuclear bar by means of Monte Carlo simulations.

Parameter	Mean	St.Dev.
$\Delta q_{\rm b}$	0.02	0.03
$\Delta q_{\rm d}$	0.005	0.02
$\Delta {\rm PA_b}$ (°)	0.3	7
$\Delta {\rm PA_d}$ (°)	0.1	3

chosen in the ranges defined in Sect. 3.3. The structural parameters of the nuclear bar were randomly chosen in the ranges $0 < a_{\rm nb} < r_{\rm e}$ for the length, $0.2 < q_{\rm nb} < 0.7$ for the ellipticity, $0° < {\rm PA_{nb}} < 180°$ for the position angle, and $0 < L_{\rm nb}/T < 0.02$ for the nuclear bar-to-total luminosity ratio.

The $a_{\rm nb}$ range was estimated from the 5 sample galaxies with a nuclear bar in common with Laine et al. (2002), which are characterized by $\langle a_{\rm nb}/r_{\rm e}\rangle = 0.8$. Detailed studies about luminosities of nuclear bars are still missing. Nevertheless, the $L_{\rm nb}/T$ range was derived by considering that some nuclear bars are secondary bars, which reside in large-scale bars. According to Erwin & Sparke (2002), a typical secondary bar is about 12% of the size of its primary bar. From Wozniak et al. (1995) we derived that the luminosity of the secondary bar is about 18% of that of the primary one. Since a primary bar contributes about 15% to the total luminosity of its galaxy (Prieto et al. 2001; Laurikainen et al. 2005), the typical $L_{\rm nb}/T$ ratio for a nuclear bar is about 2%.

All simulated galaxies were assumed at a distance of 30 Mpc. Pixel scale, CCD gain and RON, seeing, background level and photon noise of the artificial images were assumed as is Sect. 3.3. The two-dimensional parametric decomposition was applied by analyzing with GASP2D the images of the artificial galaxies as if they were real. We defined errors on the parameters as the difference between the input and output values. The mean errors on the fitted ellipticity and position angle of the bulge and disk and their standard deviation are given in Table 4.1. They correspond to systematic and typical errors.

For each sample galaxy the values of e, δ, and θ were derived in Sect. 4.2 from the ellipticity and position angle measured for the bulge and disk. We randomly generated a series of $q_{\rm b}$, $q_{\rm d}$, ${\rm PA_b}$, and ${\rm PA_d}$ by assuming they were normally distributed with the mean and standard deviation given in Table 4.1. We tested whether bulges are axisymmetric structures, which appear elongated and twisted with respect to the disk component due to the presence of a nuclear bar. To this aim, for each galaxy we selected 1000 realizations of $q_{\rm b}$, $q_{\rm d}$, ${\rm PA_b}$,

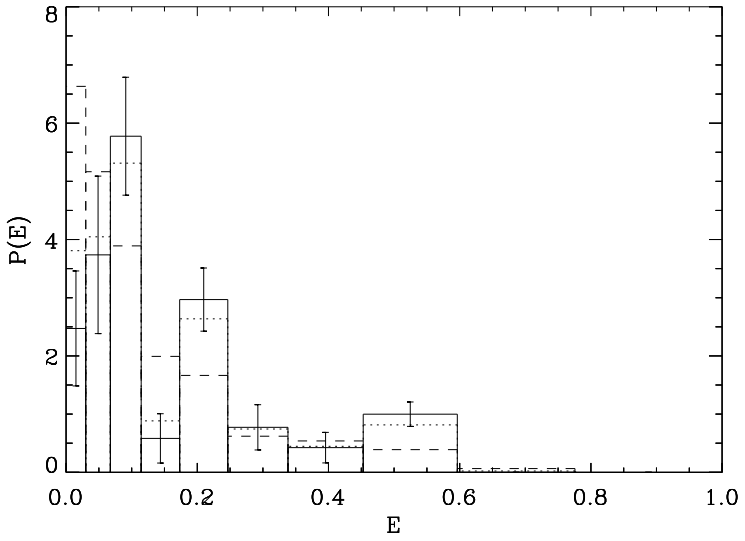

FIGURE 4.5— PDF of E for the original sample (solid lines), for a sample with 30% of bulges with a nuclear bar (dotted line) and for a 100% fraction of galaxies hosting a nuclear bar (dashed line). Bin widths and error bars as in Fig. 4.3.

and $\mathrm{PA_d}$ which gave smaller e (i.e., a rounder bulge) and smaller δ (i.e., a smaller misalignment between bulge and disk) with respect to the observed ones. This correction can be considered as an upper limit to the bulge axisymmetry. We obtained 1000 $P(T)$ distributions and calculated $P(E)$ from their mean.

Following this procedure, if we consider that all galaxies in our sample host a nuclear bar, we obtain a $P(E)$ where the decrease of the probability for $E < 0.07$ disappears (Fig. 4.5). This means that most of the bulges are circular in the equatorial plane. The average value of the ellipticity of $\langle E \rangle = 0.12$ ($\langle B/A \rangle = 0.89$). However, if we consider a more realistic fraction of galaxies that host a nuclear bar (i.e., 30% as found by Laine et al. 2002 and Erwin & Sparke 2002), the resulting $P(E)$ is consistent within errors with the $P(E)$ derived in Sect. 4.7 (Fig. 4.5). The average value is $\langle E \rangle = 0.15$ ($\langle B/A \rangle = 0.86$).

4.9 Conclusions

The non-axisymmetry of bulges has important implications from the dynamical point of view: it offers a possible method for fueling the galactic center, problems in deriving the real galaxy rotation curve and therefore modeling the dark matter distribution; and also for the formation of these structures, since

the scenarios in which bulges assembled monolithically or from mergers and/or grew over long times through disk secular evolution have to be tested against the derived PDF of bulge intrinsic ellipticities.

In this chapter, the PDF of the intrinsic equatorial ellipticity of the bulges was derived from the distribution of the observed ellipticities of bulges and their misalignments with disks. About 80% of bulges in unbarred lenticular and early-to-intermediate spiral galaxies are not oblate but triaxial ellipsoids. Their mean axial ratio in the equatorial plane is $\langle B/A \rangle = 0.85$. This is consistent with previous findings by Bertola et al. (1991) and Fathi & Peletier (2003). There is no significant dependence of the PDF on the morphology, light concentration, and luminosity of bulges. The derived PDF is independent of the possible presence of nuclear bars.

Bibliography

Bak, J., & Statler, T. S. 2000, AJ, 120, 110
Barnes, J. E., & Hernquist, L. 1996, ApJ, 471, 115
Berman, S. 2001, A&A, 371, 476
Bertola, F., Zeilinger, W. W., & Rubin, V. C. 1989, ApJ, 345, L29
Bertola, F., Vietri, M., & Zeilinger, W. W. 1991, ApJ, 374, L13
Coccato, L., Corsini, E. M., Pizzella, A., et al. 2004, A&A, 416, 507
de Vaucouleurs, G. 1974, The Formation and Dynamics of Galaxies, ed. J. R. Shakeshaft (Reidel, Boston), 58, 335
de Zeeuw, T., & Franx, M. 1989, ApJ, 343, 617
Erwin, P. 2004, A&A, 415, 941
Erwin, P., & Sparke, L. S. 2002, AJ, 124, 65
Fathi, K., & Peletier, R. F. 2003, A&A, 407, 61
Gerhard, O. E., & Vietri, M. 1986, MNRAS, 223, 377
Gerhard, O. E., Vietri, M., & Kent, S. M. 1989, ApJ, 345, L33
González-García, A. C., & Balcells, M. 2005, MNRAS, 357, 753
Jungwiert, B., Combes, F., & Axon, D. J. 1997, A&AS, 125, 479
Kormendy, J. 1982, ApJ, 257, 75
Laine, S., Shlosman, I., Knapen, J. H., & Peletier, R. F. 2002, ApJ, 567, 97
Lambas, D. G., Maddox, S. J., & Loveday, J. 1992, MNRAS, 258, 404
Laurikainen, E., Salo, H., & Buta, R. 2005, MNRAS, 362, 1319
Márquez, I., Durret, F., González Delgado, R. M., et al. 1999, A&AS, 140, 1
Martini, P., & Pogge, R. W. 1999, AJ, 118, 2646
Merlin, E., & Chiosi, C. 2006, A&A, 457, 437
Mulchaey, J. S., & Regan, M. W. 1997, ApJ, 482, L135
Naab, T., & Burkert, A. 2003, ApJ, 597, 893
Prieto, M., Aguerri, J. A. L., Varela, A. M., & Muñoz-Tuñón, C. 2001, A&A, 367, 405
Ryden, B. 1992, ApJ, 396, 445
Simonneau, E., Varela, A. M., & Muñoz-Tuñón, C. 1998, Nuovo Cimento B Serie 113, 927
Wozniak, H., Friedli, D., Martinet, L., Martin, P., & Bratschi, P. 1995, A&AS, 111, 115
Zaritsky, D., & Lo, K. Y. 1986, ApJ, 303, 66

5

Structure and stellar populations of bulges in spiral galaxies

Based on L. Morelli, E. Pompei, A. Pizzella, J. Méndez-Abreu, E. M. Corsini, L. Coccato, R. P. Saglia, M. Sarzi and F. Bertola, 2008, MNRAS, in press (arXiv:0806.2988)

Photometry and long-slit spectroscopy are presented for 14 S0 and spiral galaxies of the Fornax, Eridanus, and Pegasus clusters, and NGC 7582 group. The structural parameters of the galaxies are derived from the $R-$band images by performing a two-dimensional photometric decomposition of the surface-brightness distribution. The rotation curves, velocity dispersion profiles and $\mathbf{H}_\beta$, Mg, and Fe line-strength are measured from the spectra obtained along the major-axis of galaxies. Correlations between the central values of Mg_2, $\langle\mathrm{Fe}\rangle$, $\mathbf{H}_\beta$, and σ are found. Three classes of bulges are identified. The youngest bulges (~ 2 Gyr) with ongoing star formation, intermediate-age bulges (4-8 Gyr) have solar metallicity, and old bulges (~ 10 Gyr) have high metallicity. Most of the sample bulges display a solar α/Fe ratio, no gradient in age, and a negative gradient of metallicity. This metallicity radial profile favors a scenario with bulge formation via dissipative collapse. This implies strong inside-out formation that should give rise to a negative gradient in the $[\alpha/\mathrm{Fe}]$ratio too. But, no gradient is measured in the $[\alpha/\mathrm{Fe}]$ radial profiles for all the galaxies, except for NGC 1366. In this galaxy there is a kinematically-decoupled component, which is younger than the rest of host bulge. It is possibly formed by enriched material, probably acquired via interaction or minor merging. The bulge of NGC 1292 is the most reliable pseudobulge of our sample. The properties of its stellar population are consistent with a slow buildup within a scenario of secular evolution.

5.1 Introduction

In the current paradigm, early-type bulges were formed by rapid collapse and merging events while late-type bulges have been slowly assembled by internal and environmental secular processes (Kormendy & Kennicutt 2004). But many questions are still open. For instance, monolithic collapse can not explain the presence in bulges of kinematically-decoupled components (Pizzella et al. 2002; Krajnović & Jaffe 2004; Emsellem et al. 2004; McDermid et al. 2006). Moreover, the environment plays a role in defining the properties of galaxies (Dressler 1980; Coziol et al. 2001; Clemens et al. 2006; Brough et al. 2007). Recent studies of early-type galaxies in different environments (Beuing et al. 2002; Thomas et al. 2005; Thomas & Davies 2006) have shown that age, metallicity, and α/Fe enhancement are more correlated with the total mass of the galaxy than with local environment.

To investigate the formation and evolution of bulges, there are two possible approaches: to go backward in redshift and look at evolution of galaxies through cosmic times or analyze in detail nearby galaxies to understand the properties of their stellar population in terms of a dominant mechanism at the epochs of star formation and mass assembly. In this work, we present a photometric and spectroscopic study of the bulge dominated region of a sample of spiral galaxies in the Fornax, Eridanus, and Pegasus clusters. Our aim is to estimate the age and metallicity of the stellar population and the efficiency and timescale of the last episode of star formation to distinguish between early rapid assembly and later, slower, growth.

The Chapter is organized as follows: the galaxy sample is presented in Sect. 5.2. The photometric observations are described in Sect. 5.3.1. The structural parameters of the bulge and disk of the sample galaxies derived using GASP2D are presented in Sect. 5.3.2. The spectroscopic observations are described in Sect. 5.4.1. The stellar kinematics and line-strength indices are measured from long-slit spectra in Sect. 5.4.2. The central values of the line-strength indices are derived in Sect. 5.5. They are used to estimate the age, metallicity, and α/Fe enhancement of the stellar population of the bulge in Sect. 5.6 . Their gradients in the bulge dominated region are discussed in Sect. 5.7. The identification of pseudobulges hosted by sample galaxies is performed in Sect. 5.8. Finally, conclusions are given in Sect. 5.9.

5.2 Sample selection

The main goal of this chapter is to study the stellar populations in bulges. In order to simplify the interpretation of the results we selected a sample of disk galaxies, which do not show any morphological signature of having undergone a

TABLE 5.1— Properties of the sample galaxies.

Galaxy	Type (RC3)	PA (°)	$D_{25} \times d_{25}$ (arcmin)	B_T (mag)	$V_{\rm CMB}$ (km s^{-1})	D (Mpc)	$M^0_{B_T}$ (mag)	Cluster
(1)	(2)	(3)	(4)	(5)	(6)	(7)	(8)	(9)
ESO 358-50	SA0^0?	173	1.7×0.7	13.87	1154	17.0	−17.34	F
ESO 548-44	SA(r)0$^+$:	60	1.2×0.5	14.53	1561	22.6	−17.66	E
IC 1993	(R′)SAB(rs)b	57	2.5×2.1	12.43	877	17.0	−18.81	F
IC 5267	SA(s)0/a	140	5.2×3.9	11.43	1480	21.5	−20.38	N 7582
IC 5309	Sb	23	1.3×0.6	14.52	3840	50.2	−19.64	P
NGC 1292	SAb(s)	7	3.0×1.3	11.29	1227	17.0	−18.90	F
NGC 1351	SA$^-$pec:	140	2.8×1.7	12.46	1407	17.0	−18.67	F
NGC 1366	S0^0	2	2.1×0.9	11.97	1182	17.0	−18.30	F
NGC 1425	SA(s)b	129	5.8×2.6	11.29	1402	17.0	−20.25	F
NGC 7515	S?	15	1.7×1.6	13.16	4117	50.2	−20.44	P
NGC 7531	SAB(r)bc	15	4.5×1.8	12.04	1361	21.5	−19.25	N 7582
NGC 7557	S?	163	0.6×0.6	15.15	3366	50.2	−18.74	P
NGC 7631	SA(r)b:	79	1.8×0.7	13.93	3396	50.2	−20.38	P
NGC 7643	S?	45	1.4×0.7	14.12	3520	50.2	−19.88	P

NOTE. The columns show the following: (2) the morphological classification from RC3; (3) major-axis position angle adopted for spectroscopic observations; (4) apparent isophotal diameter measured at a surface-brightness level of $\mu_B = 25$ mag arcsec^{-2} from RC3; (5) total observed blue magnitude from RC3, except for ESO 358-50 from Lyon Extragalactic Database (LEDA); (6) radial velocity with respect to the CMB radiation from RC3; (7) distance obtained as luminosity-weighted mean radial velocity (Garcia 1993) divided by $H_0 = 75$ km s^{-1} Mpc^{-1}; (8) absolute total blue magnitude from B_T corrected for inclination and extinction as in LEDA and adopting D; (9) membership to Fornax (F), Eridanus (E), or Pegasus (P) cluster or NGC 7582 group according to Ferguson (1989), Fouque et al. (1992), Garcia (1993), Nishiura et al. (2000).

recent interaction event. All the observed galaxies are classified as unbarred or weakly barred galaxies by (de Vaucouleurs et al. 1991, hereafter RC3). They are bright ($B_T \leq 13.5$, RC3) and nearby ($V_{\rm CMB} < 4500$ km s^{-1} , RC3) lenticulars and spirals with a low-to-intermediate inclination ($i \leq 65°$, RC3). 12 of them were identified as member of either the Fornax, Eridanus, and Pegasus clusters and 2 are member of the NGC 7582 group (Ferguson 1989; Fouque et al. 1992; Garcia 1993; Nishiura et al. 2000). The final sample is formed by 12 cluster galaxies and 2 group galaxies. An overview of their basic properties is given in Table 5.1.

5.3 Surface photometry

5.3.1 Observations and data reduction

The photometric observations of the sample galaxies were carried out in two runs at the European Southern Observatory (ESO) in La Silla (Chile) from 9-12 December 2002, and from 26-28 September 2003 (run 2).

We imaged the galaxies at the ESO 3.6-m Telescope with the ESO Faint Object Spectrograph and Camera 2 (EFOSC2). The detector was the No. 40 Loral/Lesser CCD with 2048×2048 pixels of 15×15 μm^2. A 2×2 pixel binning was adopted giving an effective scale of 0.314 arcsec pixel^{-1} with a field of view of 5.3×8.6 arcmin^2. The gain and readout noise were 1.3 e$^-$ ADU^{-1} and 9 e$^-$, respectively.

We used the No. 642 Bessel R-band filter centered at 6431 Å with a FWHM of 1654 Å. For each galaxy we took $2 \times 60-$s images with an offset of few pixels to be able to clean cosmic rays and bad pixels. Every night we observed several fields of standard stars at different air-masses to be used for the flux calibration. For each field we took different exposures ranging from 5 to 15 s to provide good signal-to-noise ratio (S/N) and well sampled PSF for all the standard stars. The typical value of the seeing FWHM during the galaxy exposures was $1\farcs0$ arcsec as measured by fitting a two-dimensional Gaussian to the field stars.

All images were reduced using standard IRAF[1] tasks. We first subtracted a bias frame consisting of ten exposures for each night. The images were flat-fielded using sky flats taken at the beginning and/or end of each observing night. The sky background level was removed by fitting a second-order polynomial to the regions free of sources in the images. Special care was taken during sky subtraction to reach the outermost parts of the objects. Cosmic rays and bad pixels were removed by combining the different exposures using field stars as a reference and adopting a sigma clipping rejection algorithm. Residual cosmic rays and bad pixels were corrected by manually editing the combined image.

The photometric calibration constant includes only the correction for atmospheric extinction, which is taken from the differential aerosol extinction for ESO (**?**). No color term has been considered and no attempt was made to correct for internal and Galactic extinction. Figure 5.1 shows the calibrated R-band images of the sample galaxies.

Isophote-fitting with ellipses, after masking foreground stars and residual bad columns, was carried out using the IRAF task ELLIPSE. In all cases, we first fit ellipses allowing their centers to vary. Within the errors, no variation

[1] `IRAF` is distributed by NOAO, which is operated by AURA Inc., under contract with the National Science Foundation.

in the ellipse centers was found for all the galaxies studied in this paper. The final ellipse fits were performed using fixed ellipse centers. The ellipse-averaged profiles of surface-brightness, position angle, and ellipticity are shown in Fig. 5.1 for all the sample galaxies.

5.3.2 Photometric decomposition

The structural parameters of the bulges and disks of our sample were derived using our new code for two-dimensional photometric decomposition GASP2D (see Chapter 2). We assumed the galaxy surface-brightness distribution to be the sum of the contributions of a bulge and a disk component. Bulge isophotes are ellipses with constant position angle $\mathrm{PA_b}$ and constant axial ratio q_b. Disk isophotes are also ellipses with constant position angle $\mathrm{PA_d}$ and constant axial ratio q_d, implying that the galaxy inclination is $i = \arccos q_\mathrm{d}$. We adopted the Sérsic profile (Sérsic 1968) and an exponential profile (Freeman 1970) to describe the surface-brightness of the bulge and disk components, respectively.

Each image pixel was weighted according to the variance of its total observed photon counts due to the contribution of both the galaxy and sky, and determined assuming photon noise limitation and taking into account for the detector read-out noise.

The seeing effects were taken into account by convolving the model image with a circular Gaussian point spread function (PSF) with the FWHM measured from the stars in the galaxy image. The convolution was performed as a product in Fourier domain before the least-squares minimization.

The parameters derived for the structural components of the sample galaxies are collected in Table 5.2. The result of the photometric decomposition of the surface-brightness distribution of the sample galaxies is shown in Fig. 5.1.

The errors given in Table 5.2 were obtained through a series of Monte Carlo simulations. Because the formal errors obtained from the χ^2 minimization method are usually not representative of the real errors in the structural parameters. We have carried out extensive simulations on artificial galaxies in order to give a reliable estimate of these errors.

We generated a set of 2000 images of galaxies with a Sérsic bulge and an exponential disk. The structural parameters of the artificial galaxies were randomly chosen among the following ranges

$$0.5 \leq r_e \leq 3 \text{ kpc} \qquad 0.5 \leq \mathrm{q_b} \leq 0.9 \qquad 0.5 \leq \mathrm{n} \leq 6 \tag{5.1}$$

for the bulges, and

$$1 \leq h \leq 6 \text{ kpc} \qquad 0.5 \leq \mathrm{q_b} \leq 0.9 \tag{5.2}$$

for the disks. The artificial galaxies also satisfy the following conditions

$$q_d \leq q_b \qquad 10 \leq m_R \leq 14 \text{ mag}, \tag{5.3}$$

where m_R is the total R-band magnitude of the galaxy. The simulated galaxies were assumed to be at a distance of 29 Mpc, which corresponds to a scale of ~ 141 pc arcsec^{-1}. The pixel scale used was 0.314 arcsec pixel^{-1} and the CCD gain and RON were 0.7 e$^-$ ADU^{-1} and 8 e$^-$ to mimic the instrumental setup of the observed galaxies. Finally, a background level and a photon noise were added to the resulting images to yield a S/N ratio similar to that of the observed images.

To estimate the errors associated with the decomposition, the code GASP2D was applied to the artificial images as if they were real. Then, the relative errors (1- v_i/v_o) were estimated by comparing the input (v_i) and output (v_o) values. To assign to every single galaxy the corresponding error for every structural parameter, we divided our catalogue of artificial galaxies in bins of 0.5 magnitudes, assuming that the errors were normally distributed, with mean and standard deviation corresponding to the systematic and typical error respectively. Then we placed our observed galaxy in its magnitude bin and assigned to every parameter the corresponding error.

5.4 Long-slit spectroscopy

5.4.1 Observations and data reduction

The spectroscopic observations of the sample galaxies were carried out in three runs at ESO in La Silla (Chile) from 9-12 December 2002 (run 1), from 26-28 September 2003 (run 2), and on 25st January 2005 (run 3).

In run 1 and 2 the 3.6-m ESO Telescope mounted the EFOSC2 spectrograph. The grism No. 9 with 600 grooves mm^{-1} was used in combination with the $1\farcs0$ arcsec $\times$ 5.0 arcmin slit and the No. 40 Loral/Lesser CCD with 2048 $\times$ 2048 pixels of 15 $\times$ 15 μm^2. A 2 $\times$ 2 pixel binning was adopted. The wavelength range between 4700 and 6770 Å was covered with a reciprocal dispersion of 1.98 Å pixel^{-1} after pixel binning. This guarantees an adequate oversampling of the instrumental broadening function. Indeed, the instrumental resolution, obtained by measuring the width of emission lines of a comparison spectrum after the wavelength calibration, was 5.10 Å (FWHM). This corresponds to $\sigma_{\rm inst} \sim 110$ km s^{-1} at 5735 Å. The spatial scale was 0.314 arcsec pixel^{-1} after pixel binning.

In run 3 the New Technology Telescope mounted the ESO Multi-Mode Instrument (EMMI) in red medium-dispersion spectroscopic (REMD) mode. It

used the grating No. 6 with 1200 grooves mm^{-1} with a 1.″0 arcsec × 5'.5 arcmin slit. The detector was a mosaic of the No. 62 and No. 63 MIT/LL CCDs. Each CCD has 2048 × 4096 pixels of 15 × 15 $\mu\mathrm{m}^2$. We adopted a 2×2 pixel binning. This yielded a wavelength coverage between about 4850 Å and 5490 Å with a reciprocal dispersion of 0.40 Å pixel^{-1} after pixel binning. The instrumental resolution is 1.00 Å (FWHM) corresponding to $\sigma_{\mathrm{inst}} \sim 25$ km s^{-1} at 5170 Å. The spatial scale was 0.332 arcsec pixel^{-1} after pixel binning.

We obtained 2 × 45-minutes spectra for all the sample galaxies in run 1 and 2. In run 3 we obtained new 30-minutes spectra of ESO 358-50, ESO 548-44, NGC 1292, and IC 1993 which turned out to have a central velocity dispersion lower than 100 km s^{-1} . At the beginning of each exposure, the slit was positioned on the galaxy nucleus using the guiding camera. Then it was aligned along the galaxy major-axis, according to the position angle given in Table 5.1. During the three observing runs, we took spectra of several giant stars which were selected from Worthey et al. (1994) to be used as templates in measuring the stellar kinematics and line strength indices. In run 1 and 2 we observed HR 296 (K0III-IV), HR 489 (K3III), HR 2429 (K1III), HR 2503 (K4III), HR 2701 (K0III), HR 2970 (K0III), HR 3145 (K2III), HR 3418 (K2III), HR 7149 (K2III), HR 7317 (K3III), and HR 7430 (G9III). In run 3 we observed HR 294 (K0III), HR 510 (G8III), HR 1318 (K3III), and HR 2035 (G8III). Additionally, we observed three spectrophotometric standard stars in order to flux-calibrate the galaxy and line strength standard stars before the line indices were measured. A spectrum of the comparison helium-argon arc lamp was taken before and/or after each target exposure to allow an accurate wavelength calibration. The value of the seeing FWHM during the galaxy exposures ranged between 0.″5 and 1.″3 as measured by fitting a two-dimensional Gaussian to the guide star.

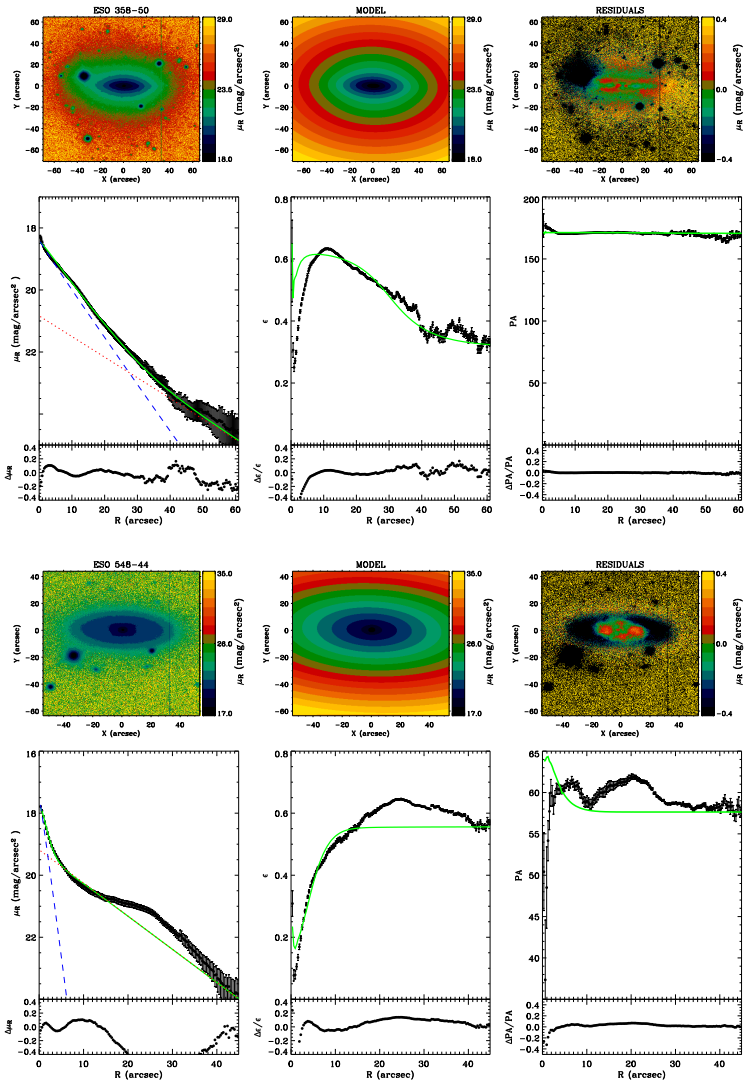

FIGURE 5.1— Two-dimensional photometric decomposition of the sample galaxies obtained from GASP2D. Upper panels (from left to right): Map of the observed, modeled, and residual (observed-modeled) surface-brightness distribution of the galaxy. The surface-brightness range of each image is indicated at the right of the panel. All images were rotated to leave the galaxy major-axis parallel to rows. In each panel the spatial coordinates with respect to the galaxy center are given in arcsec. Lower panels (from left to right): Ellipse-averaged radial profile of surface-brightness, position angle, and ellipticity measured in the observed (dots with error-bars) and modeled image (solid line). The dashed and dotted lines represent the intrinsic surface-brightness contribution of the bulge and disk, respectively. The difference between the ellipse-averaged radial profiles extracted from the observed and modeled images is also shown.

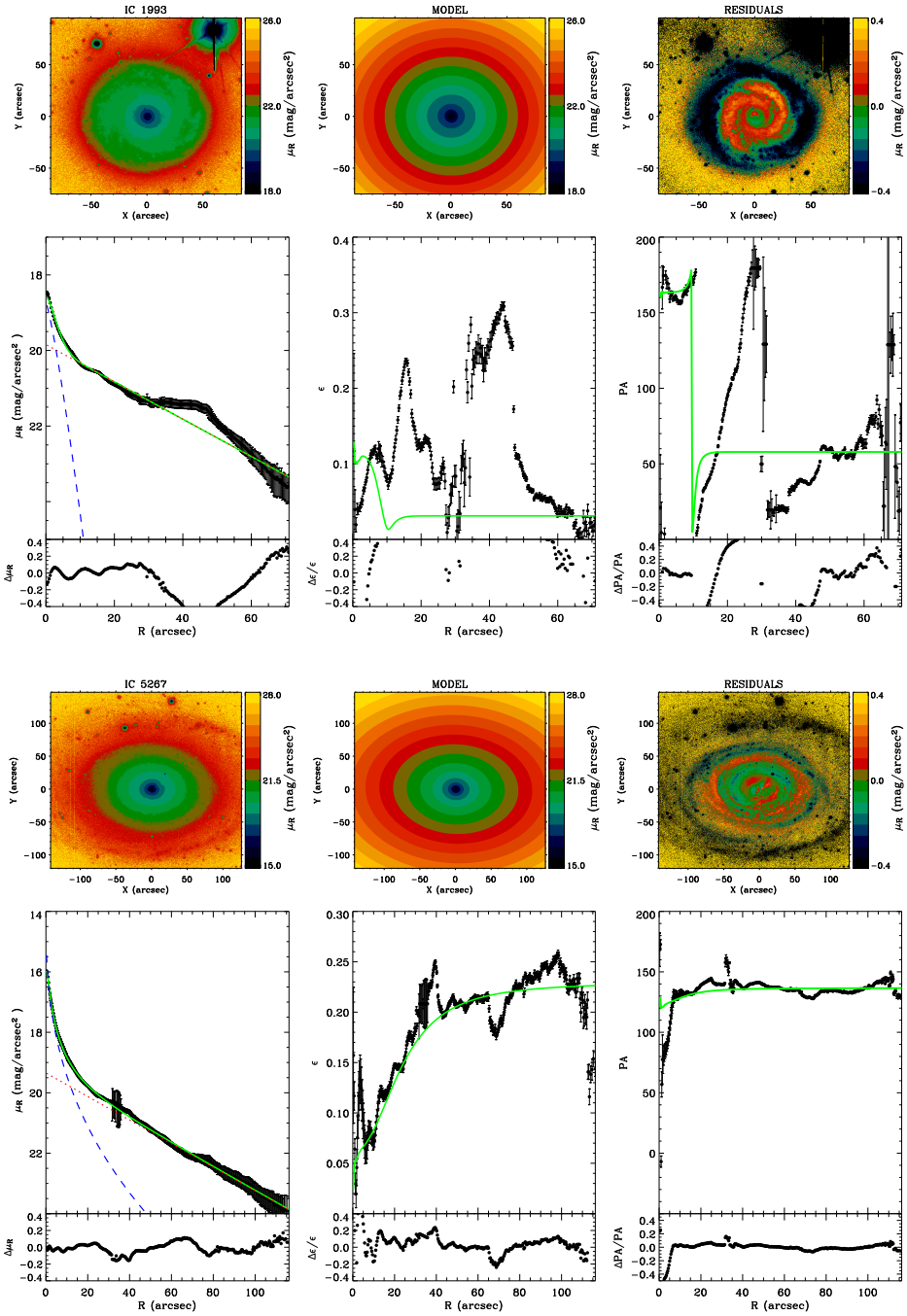

FIGURE 5.1— Continued.

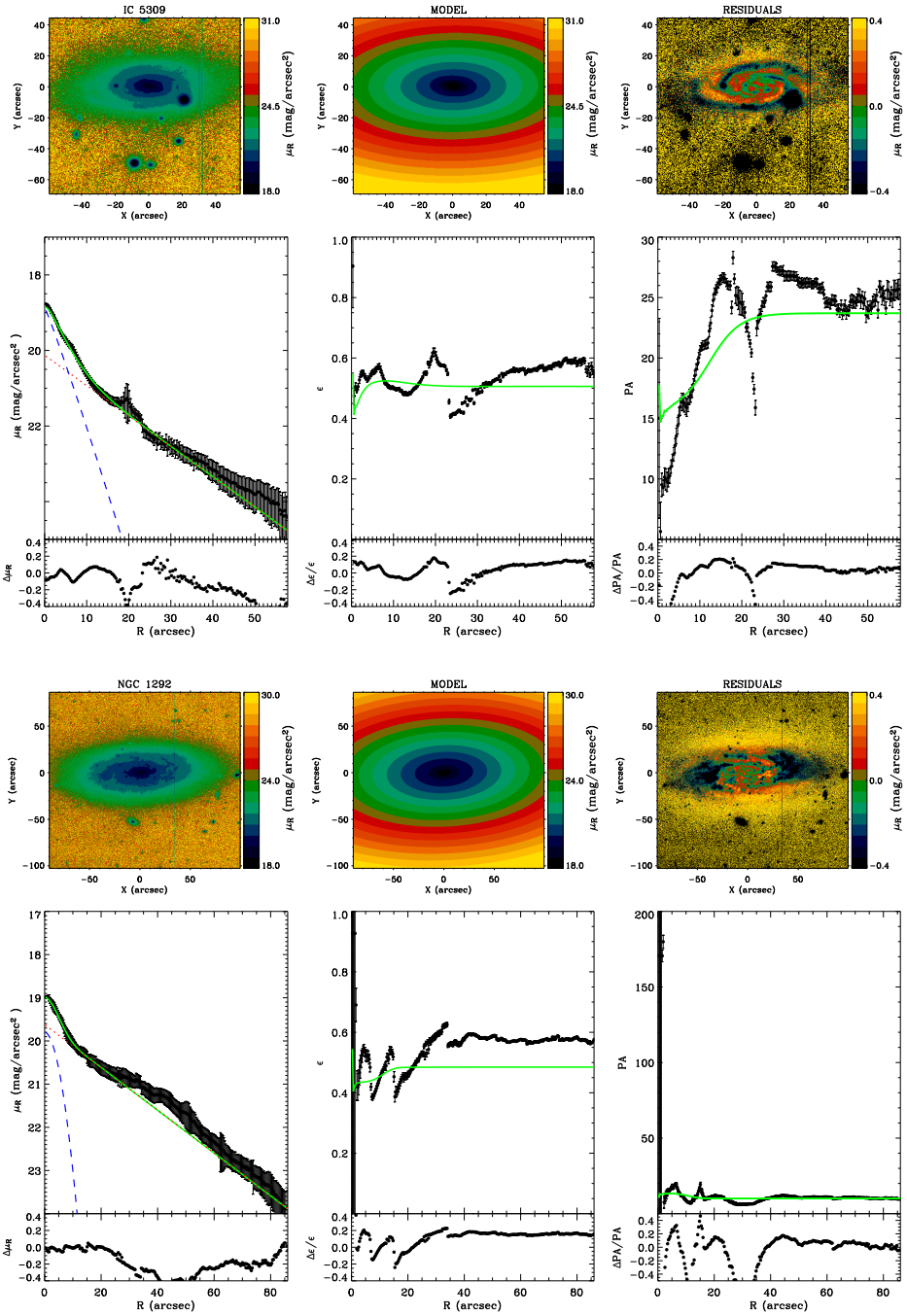

FIGURE 5.1— Continued.

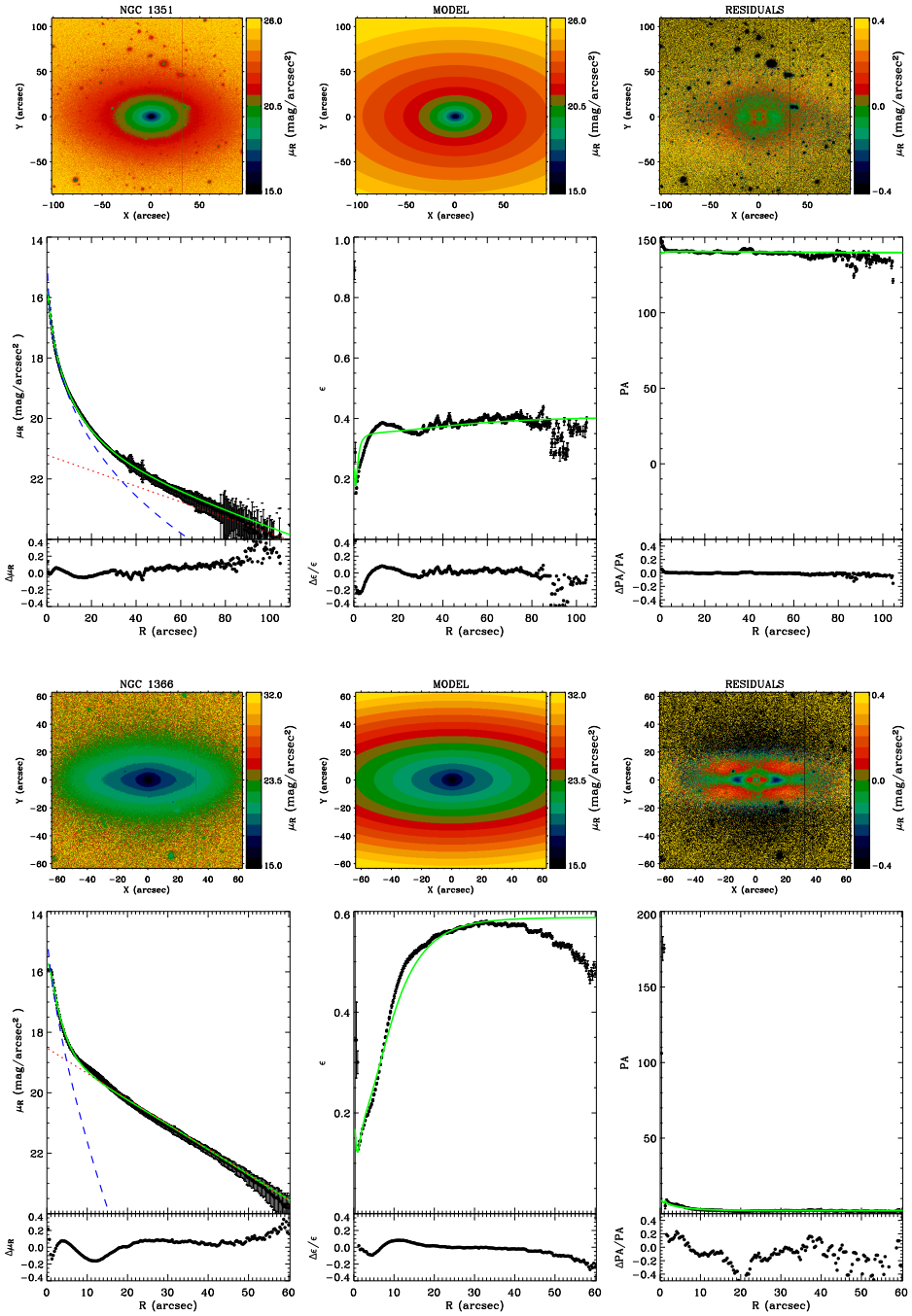

FIGURE 5.1— Continued.

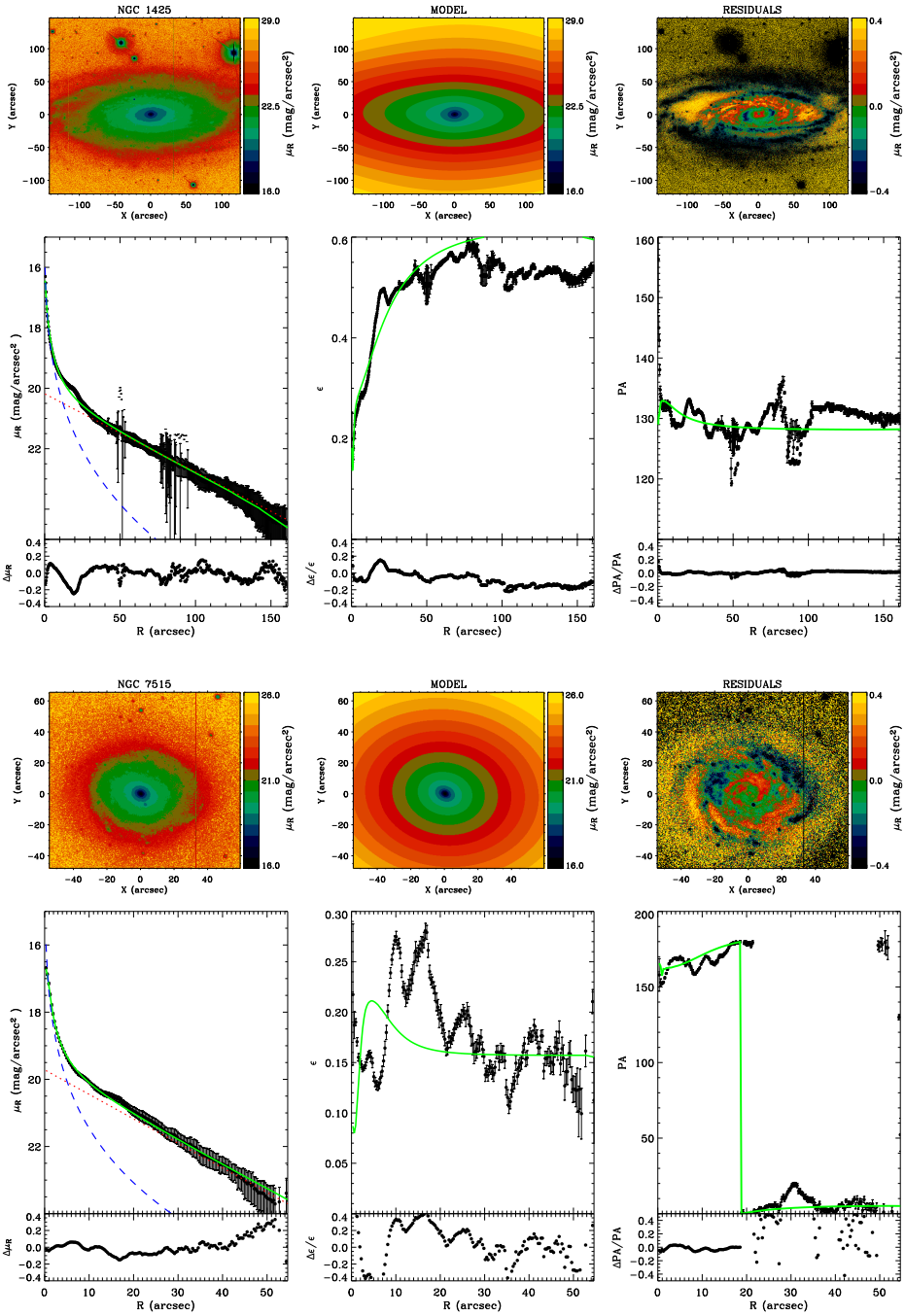

FIGURE 5.1— Continued.

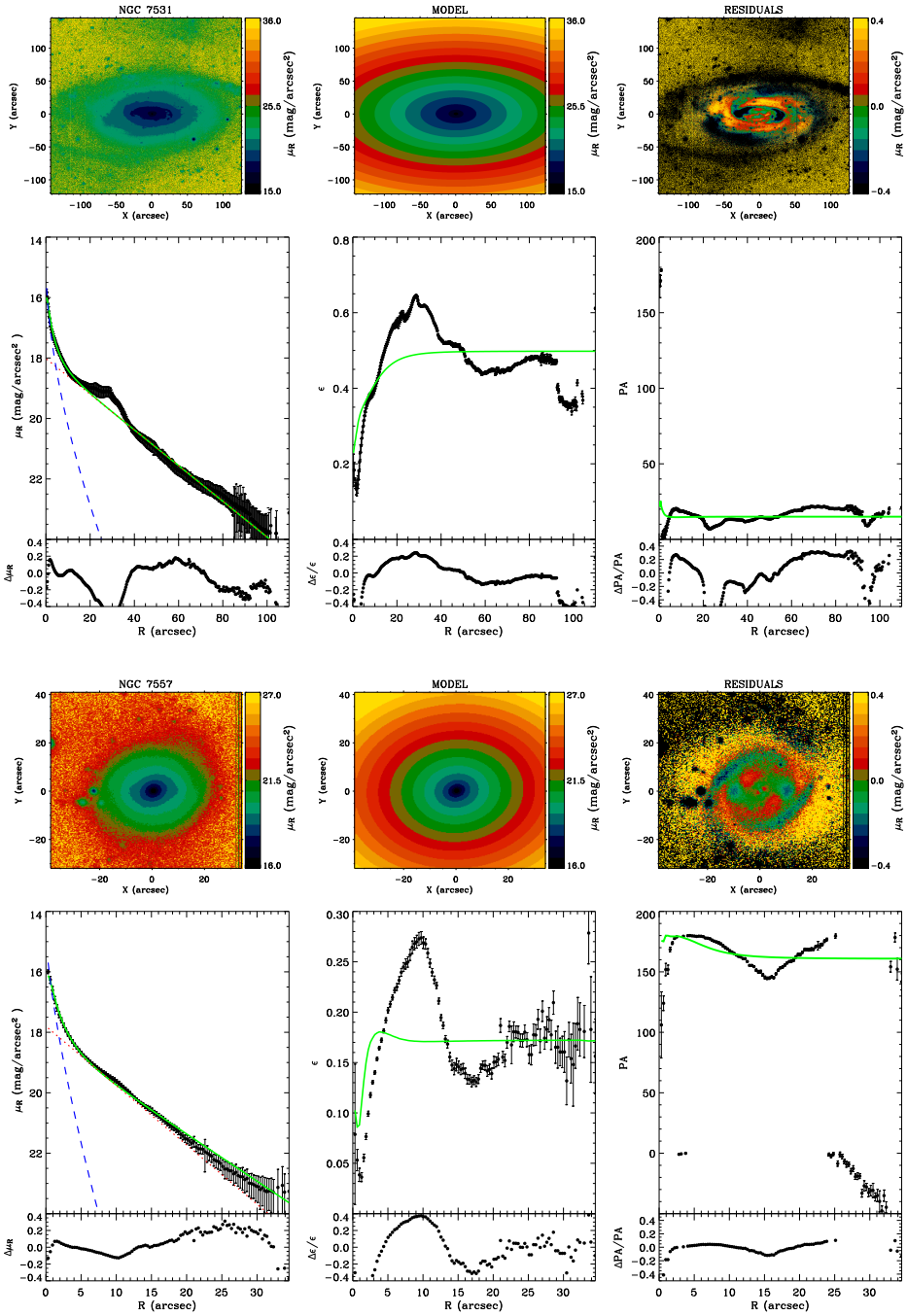

FIGURE 5.1— Continued.

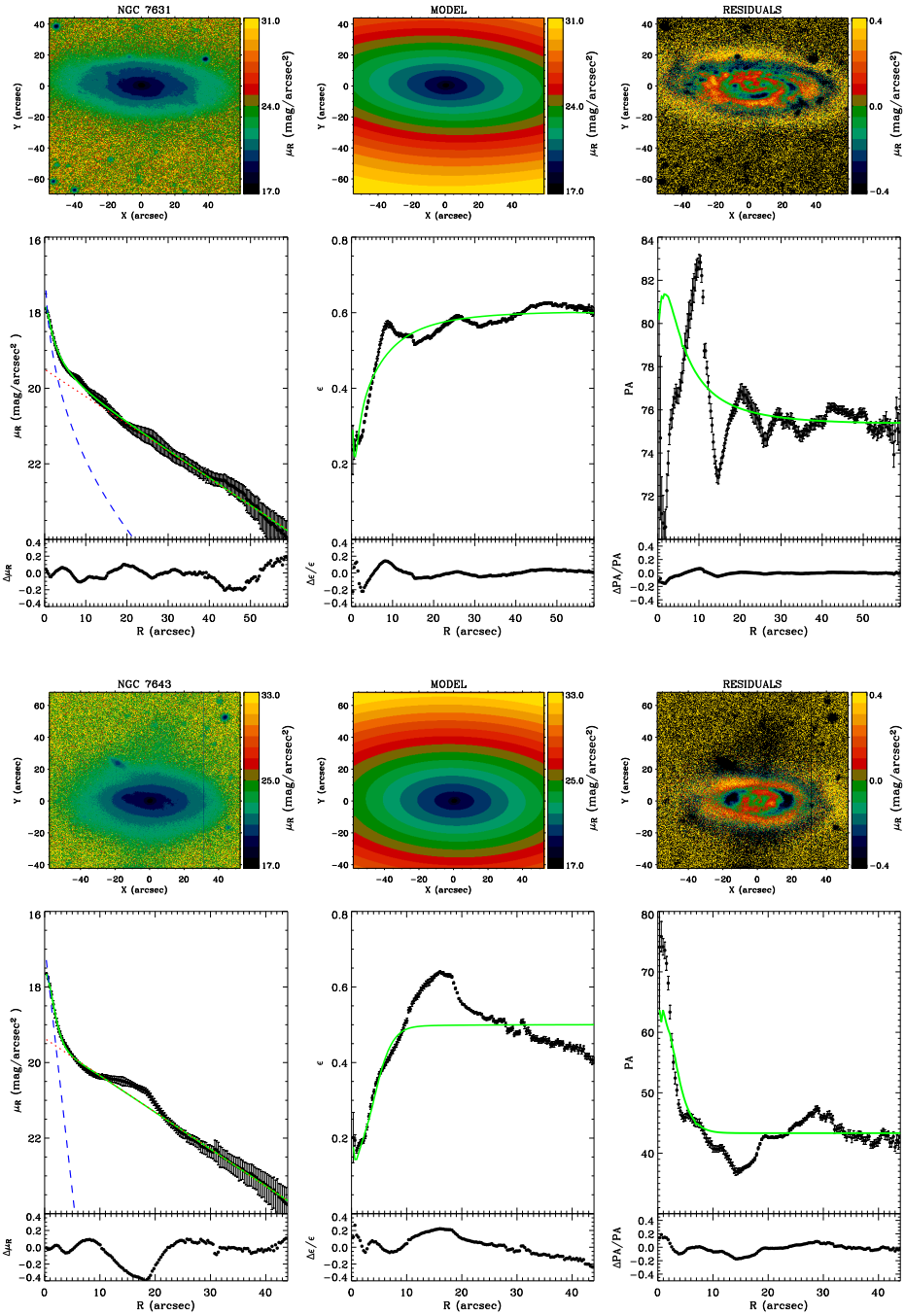

FIGURE 5.1— Continued.

TABLE 5.2— The photometric parameters of bulge and disk in the sample galaxies.

Galaxy	μ_e (mag/arcsec^2)	r_e (arcsec)	n	q_b	PA$_b$ (°)	μ_0 (mag/arcsec^2)	h (arcsec)	q_d	PA$_d$ (°)	B/T	r_{db} (arcsec)	m_R (mag)
(1)	(2)	(3)	(4)	(5)	(6)	(7)	(8)	(9)	(10)	(11)	(12)	(13)
ESO 358-50	20.00 ± 0.05	11.63 ± 0.48	1.03 ± 0.03	0.36 ± 0.01	171.25 ± 2.85	20.57 ± 0.05	16.12 ± 0.67	0.68 ± 0.02	170.62 ± 2.84	0.63 ± 0.10	27.0 ± 1.1	-17.83 ± 0.22
ESO 548-44	19.59 ± 0.05	1.72 ± 0.07	0.94 ± 0.02	0.79 ± 0.02	65.72 ± 3.19	19.62 ± 0.05	10.02 ± 0.42	0.44 ± 0.01	57.64 ± 2.84	0.05 ± 0.01	2.2 ± 0.5	-16.23 ± 0.22
IC 1993	19.21 ± 0.04	3.22 ± 0.09	0.82 ± 0.01	0.87 ± 0.02	163.01 ± 0.41	18.91 ± 0.03	21.70 ± 0.55	0.97 ± 0.02	57.87 ± 2.34	0.03 ± 0.01	4.8 ± 0.6	-15.93 ± 0.21
IC 5267	18.76 ± 0.02	9.01 ± 0.17	2.56 ± 0.06	0.94 ± 0.02	123.51 ± 2.05	18.86 ± 0.02	27.46 ± 0.51	0.77 ± 0.01	136.63 ± 2.36	0.25 ± 0.04	14.0 ± 0.7	-20.30 ± 0.20
IC 5309	20.80 ± 0.06	5.41 ± 0.24	0.93 ± 0.02	0.44 ± 0.01	15.28 ± 2.62	20.40 ± 0.06	13.34 ± 0.68	0.49 ± 0.01	23.71 ± 3.01	0.17 ± 0.02	7.0 ± 0.9	-18.44 ± 0.23
NGC 1292	20.77 ± 0.04	4.71 ± 0.14	0.52 ± 0.01	0.57 ± 0.01	14.60 ± 2.67	19.82 ± 0.03	21.62 ± 0.59	0.51 ± 0.01	10.06 ± 2.80	0.03 ± 0.01	...	-15.77 ± 0.21
NGC 1351	19.87 ± 0.03	13.14 ± 0.33	3.39 ± 0.07	0.64 ± 0.01	140.53 ± 2.60	21.20 ± 0.02	41.51 ± 0.87	0.59 ± 0.01	139.61 ± 2.44	0.53 ± 0.12	32.5 ± 1.2	-19.71 ± 0.20
NGC 1366	18.00 ± 0.04	2.59 ± 0.07	1.50 ± 0.03	0.80 ± 0.01	5.38 ± 2.40	19.07 ± 0.03	12.81 ± 0.32	0.41 ± 0.01	2.08 ± 2.32	0.20 ± 0.06	5.0 ± 0.4	-18.45 ± 0.21
NGC 1425	21.66 ± 0.03	15.52 ± 0.40	3.70 ± 0.07	0.71 ± 0.01	133.42 ± 2.71	20.83 ± 0.02	41.37 ± 0.87	0.34 ± 0.01	127.85 ± 2.42	0.18 ± 0.06	15.0 ± 1.3	-19.09 ± 0.20
NGC 7515	20.88 ± 0.04	8.14 ± 0.24	5.09 ± 0.10	0.76 ± 0.01	162.23 ± 1.56	19.55 ± 0.03	14.68 ± 0.40	0.84 ± 0.02	8.20 ± 2.50	0.27 ± 0.07	6.0 ± 0.6	-20.25 ± 0.20
NGC 7531	18.24 ± 0.02	4.58 ± 0.08	1.70 ± 0.04	0.66 ± 0.01	14.02 ± 2.49	17.92 ± 0.02	18.15 ± 0.34	0.50 ± 0.01	15.00 ± 2.45	0.10 ± 0.02	5.0 ± 0.4	-18.53 ± 0.20
NGC 7557	17.06 ± 0.05	1.31 ± 0.05	1.38 ± 0.03	0.82 ± 0.01	180.46 ± 3.09	17.45 ± 0.04	5.46 ± 0.18	0.87 ± 0.02	172.667 ± 3.16	0.16 ± 0.04	2.1 ± 0.9	-19.34 ± 0.21
NGC 7631	21.34 ± 0.05	7.01 ± 0.26	2.68 ± 0.06	0.63 ± 0.01	83.40 ± 2.55	19.67 ± 0.04	14.90 ± 0.50	0.38 ± 0.01	75.06 ± 2.55	0.12 ± 0.04	3.0 ± 0.8	-19.27 ± 0.21
NGC 7643	19.08 ± 0.05	1.37 ± 0.05	1.01 ± 0.03	0.75 ± 0.02	63.30 ± 3.50	19.73 ± 0.05	10.97 ± 0.46	0.50 ± 0.01	43.32 ± 2.86	0.05 ± 0.01	2.5 ± 0.5	-17.89 ± 0.22

NOTE: The columns show the following: (2) the effective surface-brightness of the bulge; (3) effective radius of the bulge; (4) shape parameter of the bulge; (5) axial ratio of the bulge isophotes; (6) position angle of the bulge major-axis; (7) central surface-brightness of the disk; (8) scale-length of the disk; (9) axial ratio of the disk isophotes; (10) position angle of the disk major-axis; (11) bulge-to-total luminosity ratio; (12) radius where the bulge and the disk surface-brightness are the same; (13) total absolute magnitude of the bulge.

All the spectra were bias subtracted, flat-field corrected, cleaned of cosmic rays, and wavelength calibrated using standard IRAF routines. The bias level was determined from the bias frames obtained during the observing nights to check the CCD status. The flat-field correction was performed by means of both quartz lamp and twilight sky spectra (which were normalized and divided into all the spectra) to correct for pixel-to-pixel sensitivity variations and large-scale illumination patterns due to slit vignetting. Cosmic rays were identified by comparing the counts in each pixel with the local mean and standard deviation (as obtained from Poisson statistics by taking into account the gain and read-out noise of the detector) and then corrected by interpolating over the masked regions. The residual cosmic rays were corrected by manually editing the spectra. Each spectrum was rebinned using the wavelength solution obtained from the corresponding arc-lamp spectrum. We checked that the wavelength rebinning had been done properly by measuring the difference between the measured and predicted wavelengths for the brightest night-sky emission lines in the observed spectral range (Osterbrock et al. 1996). The resulting accuracy in the wavelength calibration is better than 5 $\mathrm{km\,s^{-1}}$. All the spectra were corrected for CCD misalignment following Bender et al. (1994, BSG94). The spectra obtained for the same galaxy in the same run were co-added using the center of the stellar continuum as reference. This allowed us to improve the S/N of the resulting two-dimensional spectrum. In such a spectrum, the contribution of the sky was determined by interpolating a one-degree polynomial along the outermost $20''$ at the two edges of the slit, where the galaxy light was negligible, and then subtracting it. A sky subtraction better than 1% was achieved. A one-dimensional spectrum was obtained for each kinematic template star as well as for each flux standard star. The spectra of the kinematic templates were deredshifted to laboratory wavelengths.

5.4.2 Measuring stellar kinematics and line-strength indices

We measured the stellar kinematics from the galaxy absorption features present in the wavelength range and centered on the Mg line triplet ($\lambda\lambda$ 5164, 5173, 5184 Å) by applying the Fourier Correlation Quotient method (Bender 1990) as done by BSG94. The spectra were rebinned along the dispersion direction to a natural logarithmic scale, and along the spatial direction to obtain a $S/N \geq 40$ per resolution element. For run 3 it was necessary to average the whole spectrum obtaining a one-dimensional spectrum in order to achieve the desired S/N. In a few of the spectra of run 1 and 2 the S/N decreases to 10 at the outermost radii. To measure the stellar kinematics of the sample galaxies we adopted HR 296, HR 2429, and HR 2701 as kinematic templates for runs 1

TABLE 5.3— The central values (averaged over 0.3 r_e) of the velocity dispersion and line-strengths of the measured Lick indices.

Galaxy	σ	$\langle$Fe$\rangle$	[MgFe]$'$	Mg$_2$	Mg$_b$	H$_\beta$
	(km s^{-1})	(Å)	(Å)	(mag)	(Å)	(Å)
(1)	(2)	(3)	(4)	(5)	(6)	(7)
ESO 358-50	39.0 ± 3.4	2.45 ± 0.24	2.60 ± 0.05	0.004 ± 2.719	2.72 ± 0.18	2.35 ± 0.15
ESO 548-44	63.8 ± 7.0	2.71 ± 0.52	2.91 ± 0.30	0.190 ± 0.012	3.04 ± 0.40	2.01 ± 0.35
IC 1993	182.8 ± 15.0	2.71 ± 0.30	2.94 ± 0.10	0.176 ± 0.008	3.07 ± 0.23	2.05 ± 0.21
IC 5267	203.1 ± 15.1	3.05 ± 0.28	3.80 ± 0.14	0.281 ± 0.007	4.65 ± 0.26	1.58 ± 0.17
IC 5309	108.0 ± 15.9	2.01 ± 0.26	2.15 ± 0.05	0.131 ± 0.005	2.27 ± 0.20	2.62 ± 0.17
NGC 1292	31.7 ± 3.4	1.63 ± 0.61	1.67 ± 0.23	0.103 ± 0.011	1.61 ± 0.46	2.72 ± 0.41
NGC 1351	193.9 ± 11.0	2.85 ± 0.23	3.67 ± 0.07	0.279 ± 0.005	4.66 ± 0.17	1.60 ± 0.14
NGC 1366	175.8 ± 9.2	3.13 ± 0.17	3.67 ± 0.04	0.263 ± 0.004	4.23 ± 0.13	1.78 ± 0.11
NGC 1425	126.9 ± 12.4	2.59 ± 0.21	3.06 ± 0.05	0.214 ± 0.004	3.52 ± 0.16	1.72 ± 0.14
NGC 7515	157.7 ± 15.6	2.73 ± 0.27	3.15 ± 0.10	0.209 ± 0.006	3.56 ± 0.22	2.04 ± 0.17
NGC 7531	132.8 ± 10.0	2.75 ± 0.17	2.94 ± 0.04	0.199 ± 0.004	3.15 ± 0.14	2.00 ± 0.11
NGC 7557	104.6 ± 15.0	2.58 ± 0.21	2.78 ± 0.04	0.176 ± 0.004	2.91 ± 0.16	2.80 ± 0.13
NGC 7631	155.5 ± 15.8	2.45 ± 0.37	2.83 ± 0.14	0.170 ± 0.008	3.20 ± 0.28	1.93 ± 0.24
NGC 7643	116.9 ± 13.0	2.18 ± 0.25	2.46 ± 0.06	0.141 ± 0.005	2.71 ± 0.19	2.88 ± 0.17

and 2 and HR 296 and HR 510 for run 3. We considered the wavelength range 4817-6503 Å in runs 1 and 2 and 5167-5378 Å in run 3 around the redshifted Mg lines of the galaxies. We derived for each galaxy spectrum, the line-of-sight velocity distribution (LOSVD) along the slit and measured the radial velocity v and velocity dispersion σ. At each radius, they have been derived by fitting the LOSVD with a Gaussian. The errors on the LOSVD moments were derived from photon statistics and CCD read-out noise, calibrating them by Monte Carlo simulations as done by BSG94. In general, errors are in the range 5–20 km s^{-1}, becoming larger in the outer regions of some galaxies where $10 \leq S/N \leq 20$. These errors do not take into account the possible systematic effects arising from template mismatch. The measured stellar kinematics are plotted in Fig. 5.2.

Detailed measurement of kinematics is important not only to study the dynamical properties of galaxies but also to derive the line strengths of the Lick indices. Following (Mehlert et al. 2000), we measured the Mg, Fe, and H$_\beta$ line-strength indices (as defined by Faber et al. 1985 and Worthey et al. 1994) from the flux-calibrated spectra of run 1 and 2. Spectra were rebinned in the dispersion direction as well as in the radial direction as before. We indicate the average Iron index by $\langle \mathrm{Fe} \rangle = (\mathrm{Fe5270} + \mathrm{Fe5335})/2$ (Gorgas et al. 1990), and the newly defined Magnesium-Iron index by [MgFe]$'$ =

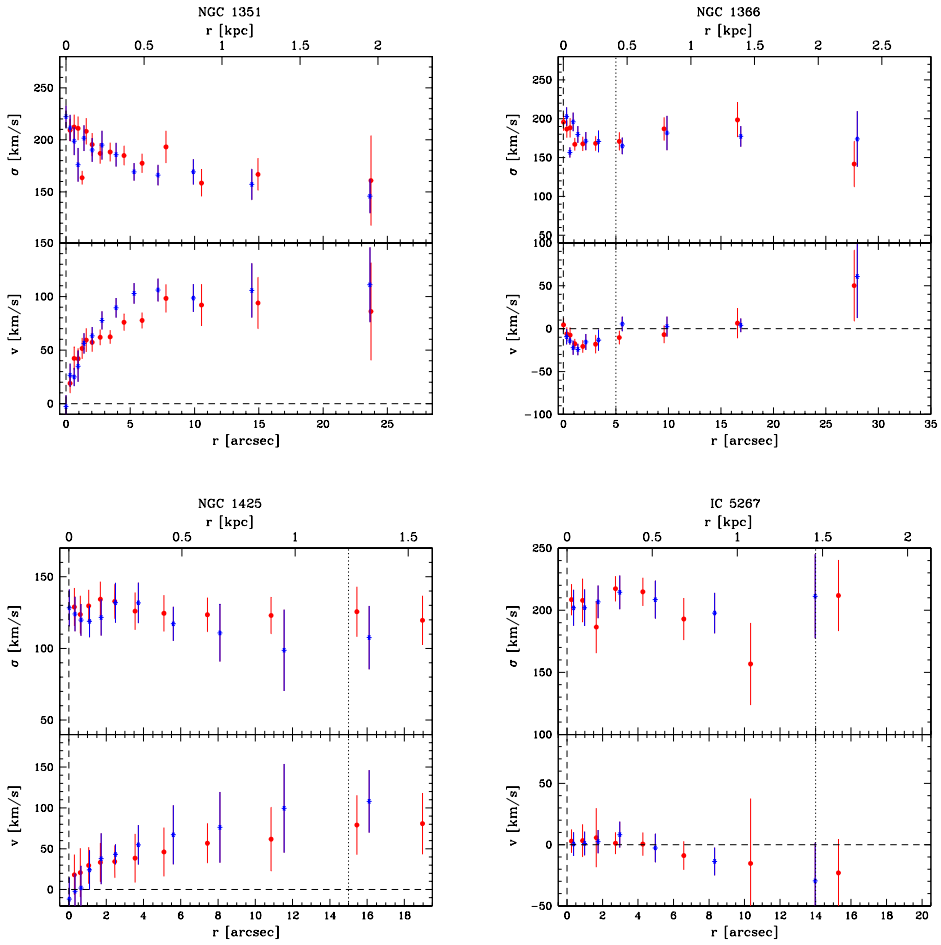

FIGURE 5.2— Kinematic parameters measured along the major axis of the galaxies. For each galaxy the curve is folded around the nucleus. Asterisks and dots refer to the two sides (est/west) of the galaxy. The radial profiles of the line-of-sight velocity (v) after the subtraction of the systemic velocity and velocity dispersion (σ) are shown from top to bottom. For NGC 1292, IC 1993, ESO 358-50, and ESO 548-44, only the central value of σ was measured and it is tabulated in Tab. 5.3. The vertical dashed line indicates the radius ($r_{\rm db}$) where the surface-brightness contributions of bulge and disk are the same.

$\sqrt{\mathrm{Mg}\,b\,(0.72 \times \mathrm{Fe5270} + 0.28 \times \mathrm{Fe5335})}$ (Thomas et al. 2003). We corrected all the measured indices for the velocity dispersion broadening. No focus correction was applied because the atmospheric seeing was the dominant effect during

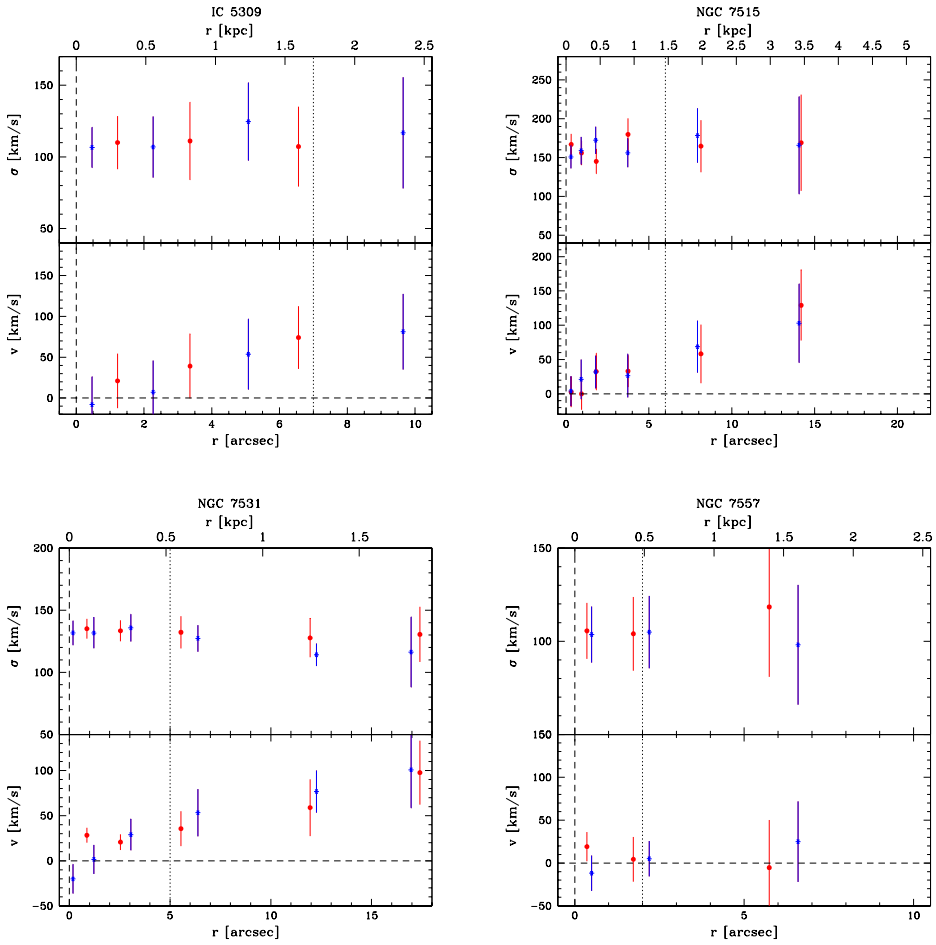

FIGURE 5.2— Continued.

observations (Mehlert et al. 1998). The errors on the indices were derived from photon statistics and CCD read-out noise, and calibrated by means of Monte Carlo simulations. We calibrated our measurements on the Lick system using the stars from Worthey et al. (1994) which we observed in run 1 and 2. A well-known problem when deriving age and metallicity of galaxy stellar populations is the contamination of the H_β index by H_β emission. To address this issue we adopted the code GANDALF (Gas AND Absorption Line fitting) to fit the galaxy spectra with synthetic population models as done by Sarzi et

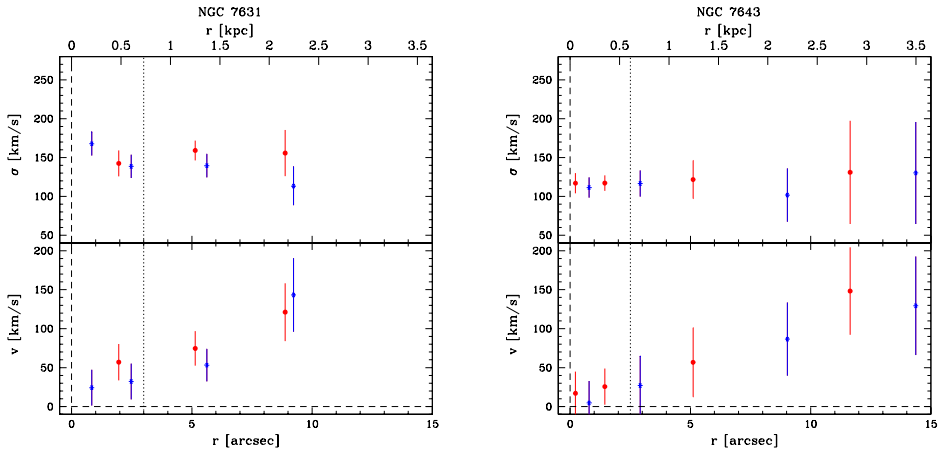

FIGURE 5.2— Continued.

al. (2006). The models were built with different templates from the stellar libraries by Bruzual & Charlot (2003) and Tremonti et al. (2004). We adopted the Salpeter initial mass function (Salpeter 1955), ages ranging between 1 Myr and 10 Gyr, and metallicities between 1 and 2.5 $(Z/\mathrm{H})_{\odot}$. The spectral resolution of the stellar templates (FWHM$\sim$ 3 Å) was degraded to match that of our galaxy spectra. We simultaneously fitted the observed spectra using emission lines in addition to the stellar templates. The H_{β} emission line was detected ($S/N > 3$) in NGC 1292, NGC 7531, NGC 7631, NGC 7643, IC 5267, and IC 5309. The equivalent with of H_{β} emission line ranged from 0 to 4 Å depending on the galaxy and radius. The emission line was subtracted from the observed spectrum and we measured the H_{β} line-strength index from the resulting H_{β} absorption line.

The measured values for the line-strength indices for the stars in common with Worthey et al. (1994) are shown in Fig. 5.3. The agreement is good within the errors for all the indices and we did not apply any zero-point correction.

Kuntschner et al. (2000) measured the central velocity dispersion and line-strength indices for NGC 1351 and ESO 358-G50. The comparison is shown in Fig. 5.4. All the values are consistent with ours within 3σ.

The measured values of H_{β}, [MgFe]$'$, $\langle\mathrm{Fe}\rangle$, $\mathrm{Mg}\,_{b}$, and $\mathrm{Mg}\,_{2}$ for all the sample galaxies are plotted in Fig. 5.5.

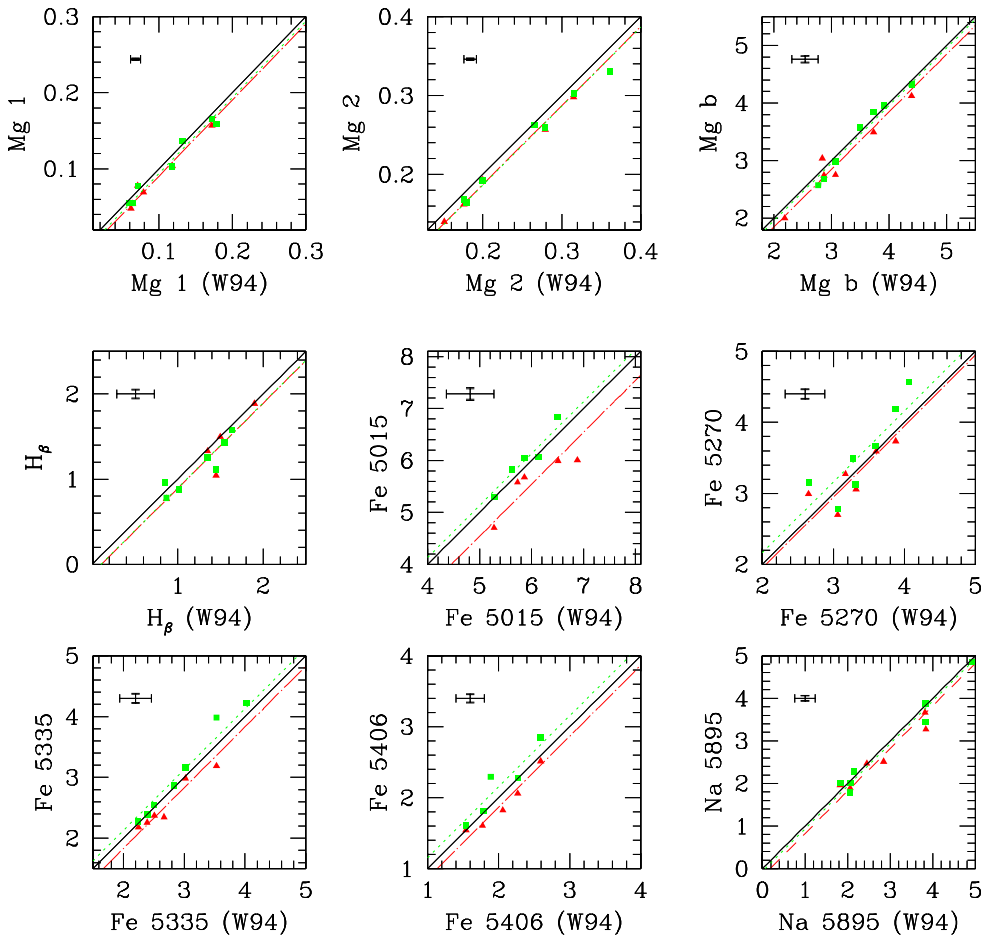

FIGURE 5.3— Comparison of the values of the line-strength indices of the stars in common with Worthey et al. (1994, W94). The error bars in the upper left corner of each panel indicate the median errors of the measurements and the solid line defines the identity. Negligible offsets for all indices were obtained by assuming the the straight line fitting the data in run 1 (squares) and 2 (triangles) has slope 1. The dotted and dot-dashed lines correspond to the data fit obtained in run 1 and 2, respectively.

5.5 Line-strength indices: central values

Central values of velocity dispersion σ, Mg_b, Mg_2, H_β, $\langle\mathrm{Fe}\rangle$, and $[\mathrm{MgFe}]'$ line-strength indices were derived from the major-axis profiles. The data points inside 0.3 r_e were averaged adopting a relative weight proportional to their S/N. The resulting values are listed in Tab. 5.3.

The correlations between the velocity dispersion and Mg_2, H_β, and $\langle\mathrm{Fe}\rangle$

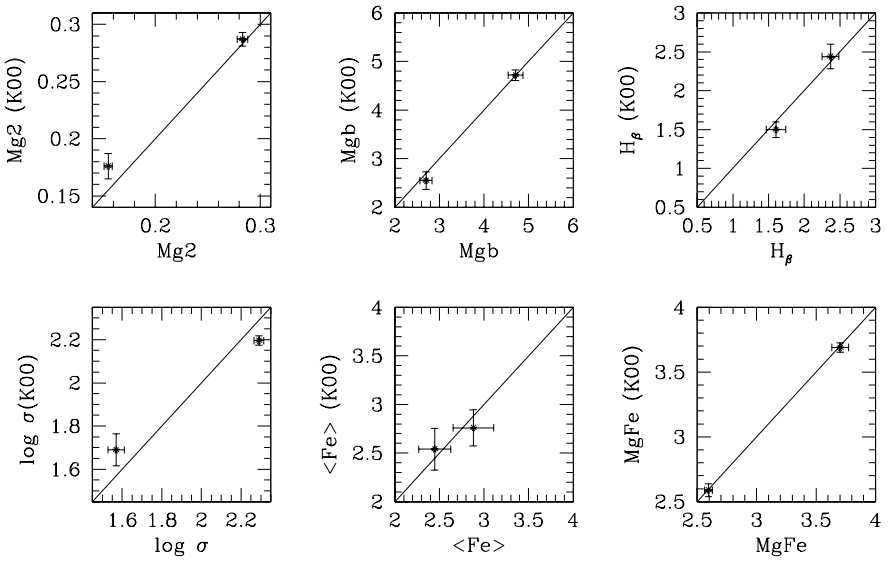

FIGURE 5.4— Comparison of the values of the central velocity dispersion and line-strength indices between us and Kuntschner (2000, K00) measured for NGC 1351 and ESO 358-G50. Velocity dispersions are given in $\mathrm{km\,s^{-1}}$, $\mathrm{Mg_2}$ in mag, and all the other line-strength indices in Å.

line-strength indices for the sample galaxies are plotted in Fig. 5.8. They were extensively studied for early-type galaxies (Fisher et al. 1996; Bernardi et al. 1998; Jørgensen 1999a; Kuntschner 2000; Moore et al. 2002; Mehlert et al. 2003; Rampazzo et al. 2005; Sánchez-Blázquez et al. 2006b; Collobert et al. 2006; Annibali et al. 2007).

The $\mathrm{Mg_2}$ line-strength index is generally adopted as the tracer of the α elements giving an estimate of the enrichment, while σ is related to the gravitational potential. In elliptical and S0 galaxies the $\mathrm{Mg_2}$–σ correlation shows that more massive galaxies host a more metallic stellar population (Idiart et al. 1996; Bernardi et al. 1998; Jørgensen 1999a; Mehlert et al. 2003). For bulges we measured the same trend and scatter (rms=0.049) found by Jablonka et al. (1996), Idiart et al. (1996), and Prugniel et al. (2001). But the fitted slope is steeper than the typical values found for the early-type galaxies (Bernardi et al. 1998; Jørgensen 1999a; Kuntschner 2000; Mehlert et al. 2003).

Although the correlation between $\langle\mathrm{Fe}\rangle$ and σ was predicted by models of dissipative collapse (Kodama et al. 1998), it was not found to be very tight in early-type galaxies (Fisher et al. 1996; Jørgensen 1999a; Trager et al. 1998; Mehlert et al. 2003) except for those studied by Kuntschner et al. (2000). On

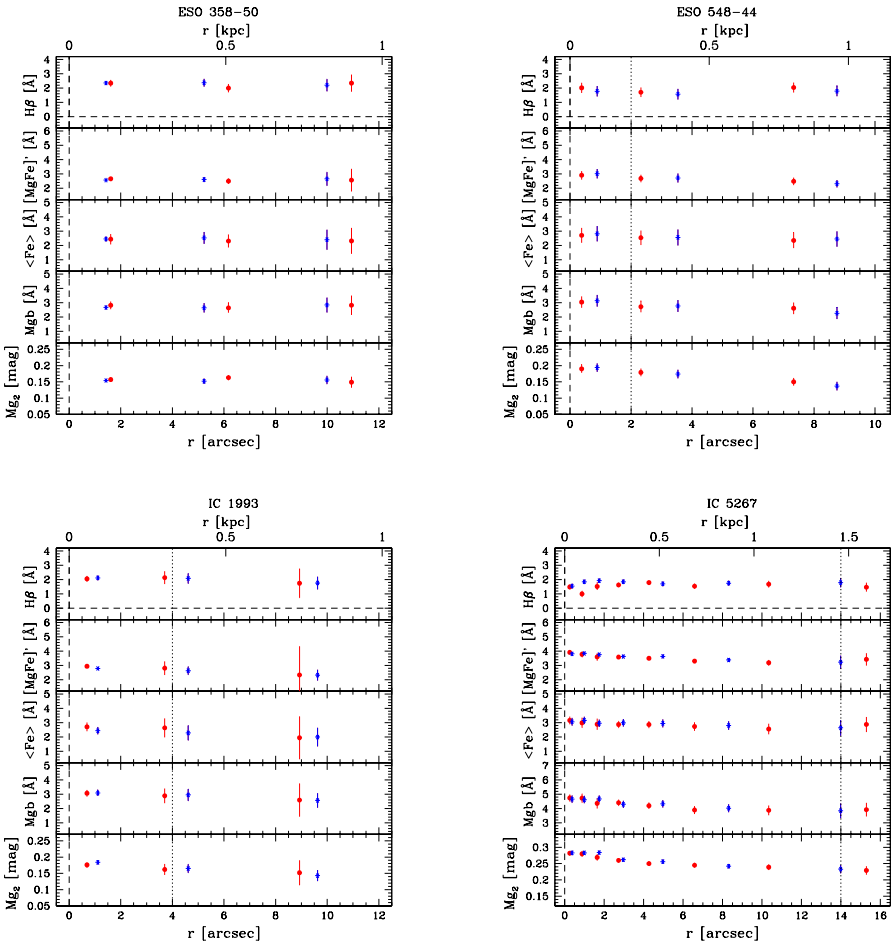

FIGURE 5.5— The line-strength indices measured along the major axes of the sample galaxies. From top to bottom: folded radial profiles of H_β, [MgFe]′, ⟨Fe⟩, Mg_b, and Mg_2. Asterisks and dots refer to the two sides (est/west) of the galaxy. The vertical dashed line indicates the radius(r_{db}) where the surface-brightness contributions of the bulge and disk are equal.

the other hand, the ⟨Fe⟩$-\sigma$ relation is well defined for spiral bulges (Idiart et al. 1996; Prugniel et al. 2001; Proctor & Sansom 2002). The slope we found for our sample bulges is consistent with previous findings.

We also found a tight anti-correlation between H_β and σ. Its slope is steeper than that measured for early-type galaxies in Coma and Fornax clusters by Jørgensen (1999a) and Kuntschner (2000), respectively. Comparison with previous results depends on the correction of the H_β line-strength index for the

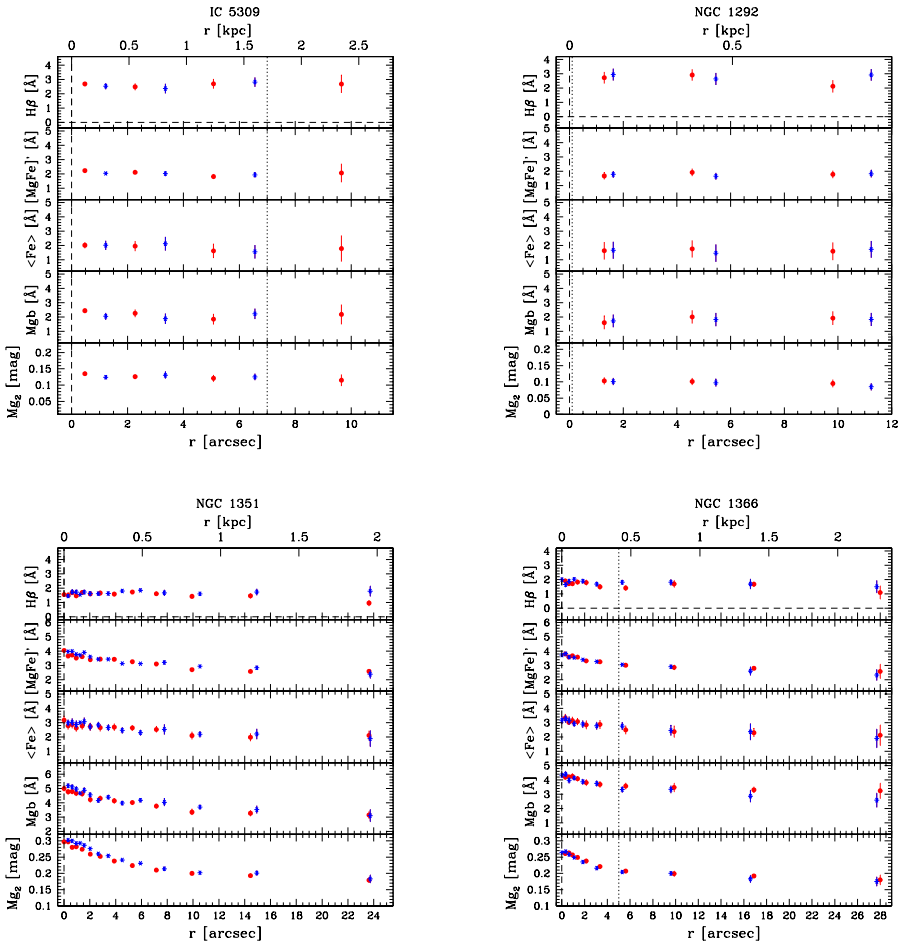

FIGURE 5.5— Continued.

contamination of the H_β emission line.

5.6 Ages, metallicities, and α/Fe enhancement: central values

From the central line-strength indices we derived the mean ages, total metallicities, and total α/Fe ratios of the stellar populations in the centers of the sample bulges by using the stellar population models by Thomas et al. (2003). These models predict the values of the line-strength indices for a single stellar population as function of the age, metallicity and [α/Fe] ratios.

The distribution of the central H_β and [MgFe]′ with the stellar population

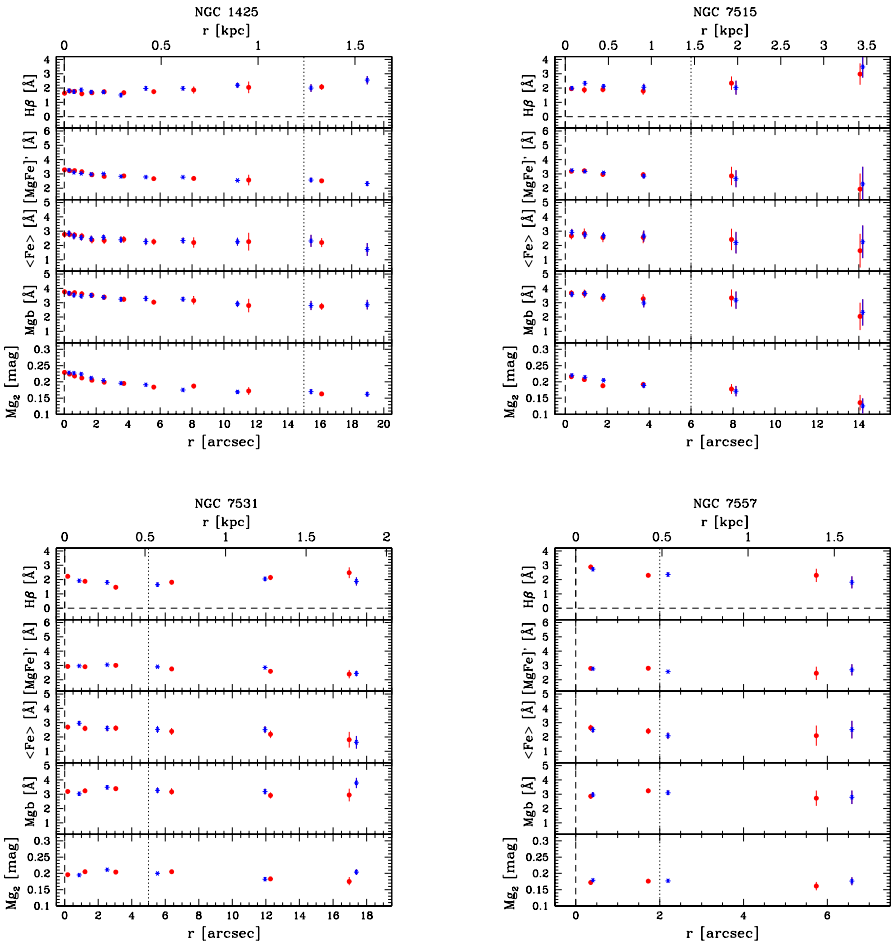

FIGURE 5.5— Continued.

models by Thomas et al. (2003) is shown in Fig. 5.10 (left panel). The models are plotted for two fixed [α/Fe] ratios (0 and 0.5 dex) corresponding to stellar populations with solar and supersolar α/Fe enhancements, respectively. In this parameters space the mean age and total metallicity appear to be almost insensitive to the variations of the α/Fe enhancement. The distribution of the central Mg_b and $\langle\mathrm{Fe}\rangle$ within the prediction of the stellar population models by Thomas et al. (2003) is shown in Fig. 5.10 (right panel). The models are plotted for two fixed ages (3 and 12 Gyr) corresponding to intermediate-age and old stellar populations, respectively. In this parameter space the α/Fe

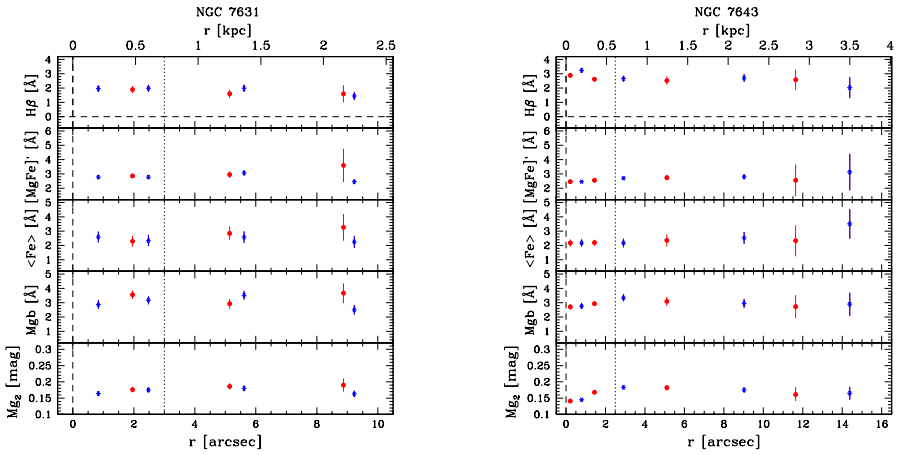

FIGURE 5.5— Continued.

ratio and total metallicity appear to be almost insensitive to the variations of age. Central age, metallicity, and total α/Fe ratio of each bulge were derived by a linear interpolation between the model points using the iterative procedure described in Mehlert et al. (2003). The derived values and their corresponding errors are listed in Tab. 5.4. The histograms of their number distribution are plotted in Fig. 5.11. According to age and metallicity, three classes of objects were identified. The young bulges are scattered about an average age of 2 Gyr with hints of star formation as shown by the presence of the H_β emission line in their spectra. The intermediate-age bulges span the age range between 4 and 8 Gyr. They are characterized by solar metallicity ($[Z/H] = 0.0$ dex). Finally, the old bulges have a narrow distribution in age around 10 Gyr and high metallicity ($[Z/H] = 0.30$ dex). This is in agreement with recent findings by Moorthy & Holtzman (2006). Kuntschner (2000) and Mehlert et al. (2003) found that elliptical galaxies in Fornax and Coma clusters are on average older and more metal rich than S0 galaxies. We did not observe any correlation between the age and metallicity of bulge stellar population and the galaxy morphology. The same is true for the lenticular and spiral galaxies studied by Thomas et al. (2006) and Ganda et al. (2007). This was interpreted as an indication of independent evolution of the stellar populations of bulges and disks (Thomas & Davies 2006).

Most of the sample bulges display solar α/Fe ratios with the median of the distribution at $[\alpha/Fe] = 0.07$. A few have a central super-solar ratio ($[\alpha/Fe] = 0.3$). These values are similar to those found for the elliptical galax-

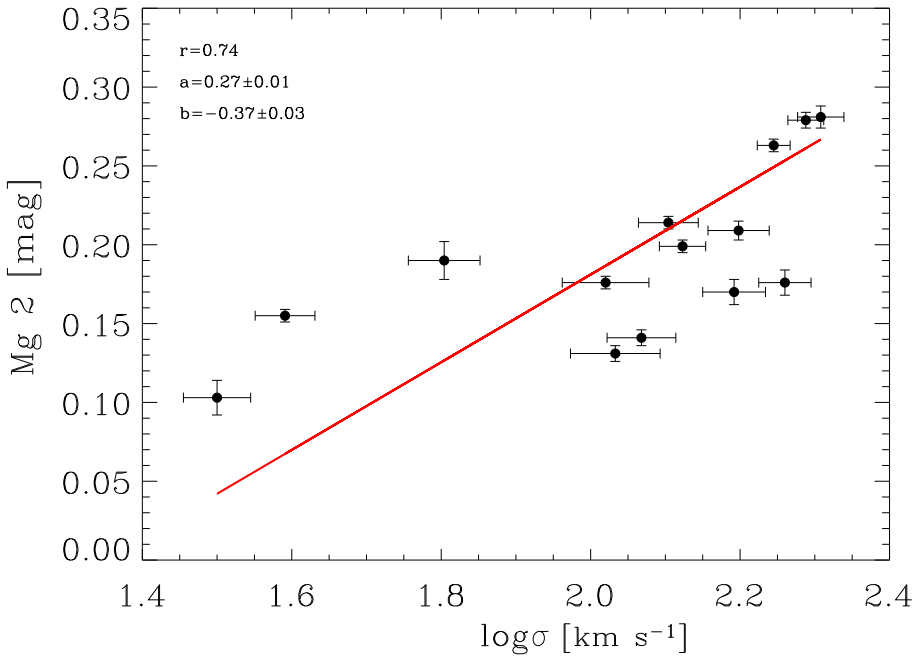

FIGURE 5.6— Central value of line strength index Mg_2 versus the velocity dispersion. The solid line represents the linear regression ($y = ax+b$) through all the data points. The Pearson correlation coefficient (r) and the results of the linear fit are given.

ies in clusters (Peletier 1989; Jørgensen 1999b; Trager et al. 2000; Kuntschner 2000; Kuntschner et al. 2001) and imply a star-formation timescale ranging from 1 to 5 Gyr.

Age, metallicity, and α/Fe ratio correlate with velocity dispersion (Fig. 5.12). In early-type galaxies the metallicity and α/Fe ratio are well correlated with the central velocity dispersion, while the correlation is less evident with age (Mehlert et al. 2003; Sánchez-Blázquez et al. 2006b; Denicoló et al. 2005). In our bulges both the metallicity and α/Fe ratio correlate with the velocity dispersion and this is probably driving the correlation observed between the metallicity and α/Fe ratio (Fig. 5.13). Age is mildly correlated with velocity dispersion (Fig. 5.12), and α/Fe enhancement (Fig.5.13). Recently, Thomas & Davies (2006) proved that these correlations are tighter when the age estimate is based on bluer Balmer line-strength indices instead of H_β. We conclude that the more massive bulges of our sample galaxies are older, more metal rich and

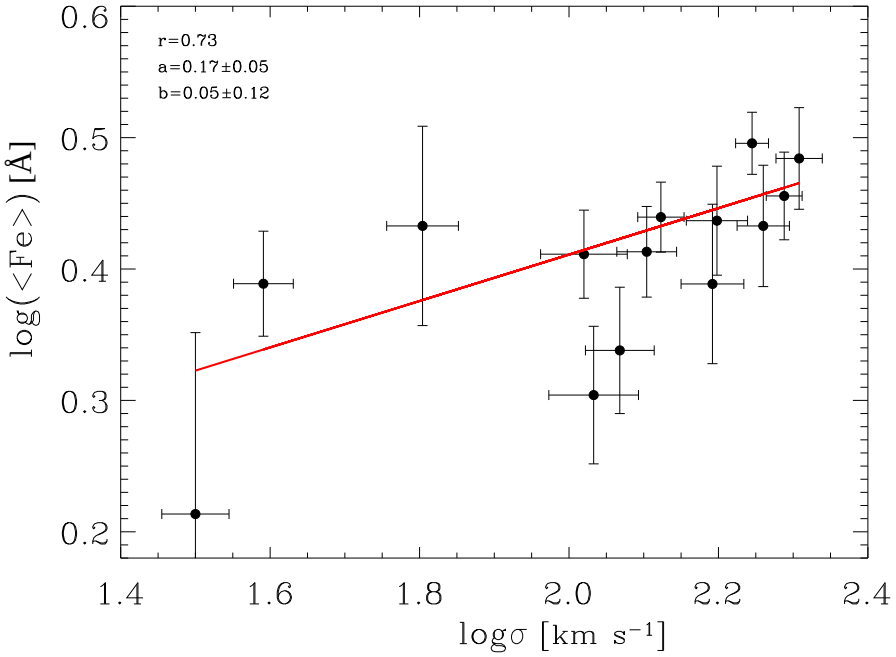

FIGURE 5.7— Central value of line strength index ⟨Fe⟩ versus the velocity dispersion. The solid line represents the linear regression ($y = ax+b$) through all the data points. The Pearson correlation coefficient (r) and the results of the linear fit are given.

characterized by a fast star formation. Since we did not found any correlation with galaxy morphology we exclude a strong interplay between the bulge and the disk components.

5.7 Ages, metallicities, and α/Fe enhancement: gradients

Different formation scenarios predict different radial trends of age, metallicity, and α/Fe ratio. Therefore, the radial gradients of the properties of the stellar populations of bulges are key information for understanding the processes of their formation and evolution.

The total metallicity of a stellar population depends on the efficiency of the star formation and on the amount of gas transformed into stars (**?**) and on the gas metallicity. In the monolithic collapse scenario gas dissipation toward the galaxy center with subsequent occurrence of star formation and blowing of galactic winds produces a steep metallicity gradient (Eggen et al. 1962; Larson

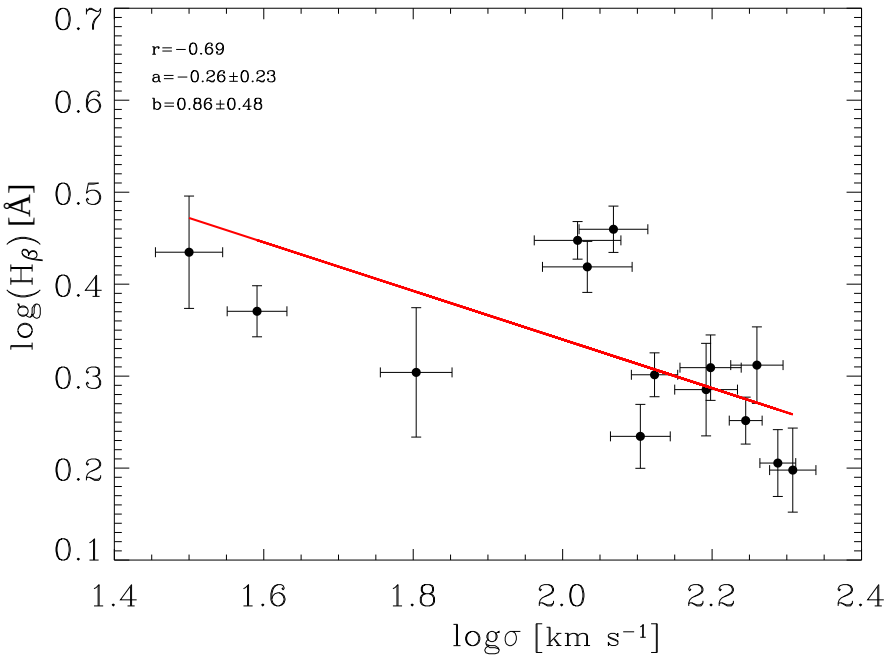

FIGURE 5.8— Central value of line strength index H_β versus the velocity dispersion. The solid line represents the linear regression ($y = ax+b$) through all the data points. The Pearson correlation coefficient (r) and the results of the linear fit are given.

1974; Arimoto & Yoshii 1987). A strong gradient in α/Fe ratio is expected too (Ferreras & Silk 2002). The predictions for bulges forming through a long time-scale processes such as dissipation-less secular evolution are more contradictory. In this scenario the bulge is formed by redistribution of disk stars. The gradients eventually present in the progenitor disk, could be either amplified since the resulting bulge has a smaller scale-length than the progenitor or erased as a consequence of disk heating (Moorthy & Holtzman 2006).

An issue in measuring the gradients of age, metallicity and α/Fe ratio in bulge, could be the contamination of the stellar population by the light coming from the underlying disk stellar component. This effect is negligible in the galaxy center but it could increase in the outer regions of the bulge, where the light starts to be dominated by the disk component. In order to reduce the impact of disk contamination but to extend as far as possible the region in which deriving gradients, we map them inside $r_{\rm bd}$, the radius where the bulge

TABLE 5.4— The central ages, metallicities and α/Fe enhancements of the sample bulges derived from the line-strength indices listed in Tab. 5.3 using the stellar population models by Thomas et al. (2003).

Galaxy	$[Z/H]$	Age [Gyr]	$[\alpha/Fe]$
(1)	(2)	(3)	(4)
ESO 358-50	-0.04 ± 0.08	2.8 ± 1.1	-0.00 ± 0.11
ESO 548-44	-0.00 ± 0.20	4.7 ± 4.6	-0.05 ± 0.17
IC 1993	0.04 ± 0.14	4.2 ± 2.8	-0.04 ± 0.13
IC 5267	0.34 ± 0.15	9.5 ± 4.2	0.18 ± 0.10
IC 5309	-0.24 ± 0.08	2.7 ± 1.3	0.05 ± 0.13
NGC 1292	-0.68 ± 0.28	4.2 ± 2.6	-0.12 ± 0.22
NGC 1351	0.25 ± 0.09	9.9 ± 3.3	0.23 ± 0.08
NGC 1366	0.39 ± 0.08	5.1 ± 1.7	0.11 ± 0.05
NGC 1425	-0.07 ± 0.07	10.3 ± 2.9	0.08 ± 0.10
NGC 7515	0.17 ± 0.13	4.0 ± 2.0	0.09 ± 0.11
NGC 7531	0.01 ± 0.06	4.8 ± 1.5	-0.03 ± 0.07
NGC 7557	0.27 ± 0.08	1.5 ± 0.2	0.06 ± 0.09
NGC 7631	-0.10 ± 0.14	6.9 ± 3.3	0.07 ± 0.17
NGC 7643	0.05 ± 0.06	1.8 ± 0.2	0.14 ± 0.13

and disk give the same contribution to the total surface-brightness. This is a region slightly larger than r_e of the galaxy (Fig. 5.14). Deriving gradients in the bulge dominated region with this approach, will not remove completely the contamination by the disk stellar population but it will assure always a similar degree of contamination in comparing the gradients of different galaxies.

For each galaxy, we derived the Mg_2, H_β, and $\langle Fe \rangle$ line-strength indices at the radius r_{bd} (see Tab. 5.2). The ages, metallicities, and α/Fe ratios were derived by using the stellar population models by Thomas et al. (2003) as for the central values.

The gradients were set as the difference between the values at center and r_{bd} and their corresponding errors were calculated through Monte Carlo simulations taking into account the errors in the gradients and the logarithmic fit to the adopted indices. For NGC 1292 no gradients were obtained since it was not possible to estimate r_{bd}. The galaxy bulge is fainter than the disk at all radii (Fig. 5.1). Indeed, the surface-brightness radial profile of the galaxy could be fitted by adopting only an exponential disk (Tab. 5.2).

The final gradients of age, metallicity and α/Fe ratio and their errors are listed in Tab. 5.5. In Tab. 5.5 we also report the age, metallicity and α/Fe ratio

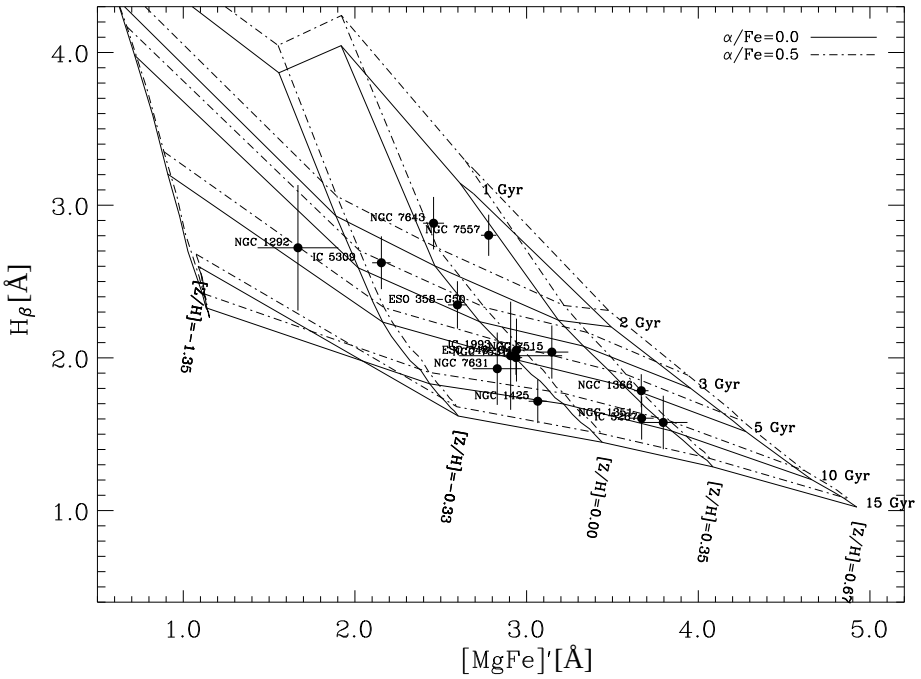

FIGURE 5.9— The distribution of the central values of H_β and [MgFe]′ indices averaged over 0.3 r_e for the 15 sample galaxies . The lines indicate the models by Thomas et al. (2003). The age-metallicity grids are plotted with two different α/Fe ratios: [α/Fe] = 0.0 dex (continuous lines) and [α/Fe] = 0.5 dex (dashed lines).

gradients rescaled to a fixed radius value of 1 kpc. For two galaxies (ESO 358-G50 and NGC 7531) the small values of r_{bd} combined with the big values of gradients give meaningless values of age extrapolated at 1 kpc and we omit them in the table. The histograms of their number distribution are plotted in Fig. 5.15.

Most of the sample galaxies show no gradient in age (median=0.4), in agreement with the earlier findings by Mehlert et al. (2003) and Sánchez-Blázquez et al. (2006) for the early-type galaxies, and by Jablonka et al. (2007) for bulges. Only NGC 1366 and NGC 7531 display steep age gradients.

Negative gradients of metallicity were observed in the sample bulges. The number distribution show a clear peak at $\Delta([Z/H]) = -0.15$. This was already known for the stellar populations in early-type galaxies (Proctor & Sansom 2002; Mehlert et al. 2003; Sánchez-Blázquez et al. 2006a), and it has been recently found for spiral bulges too by Jablonka et al. (2007). The presence of

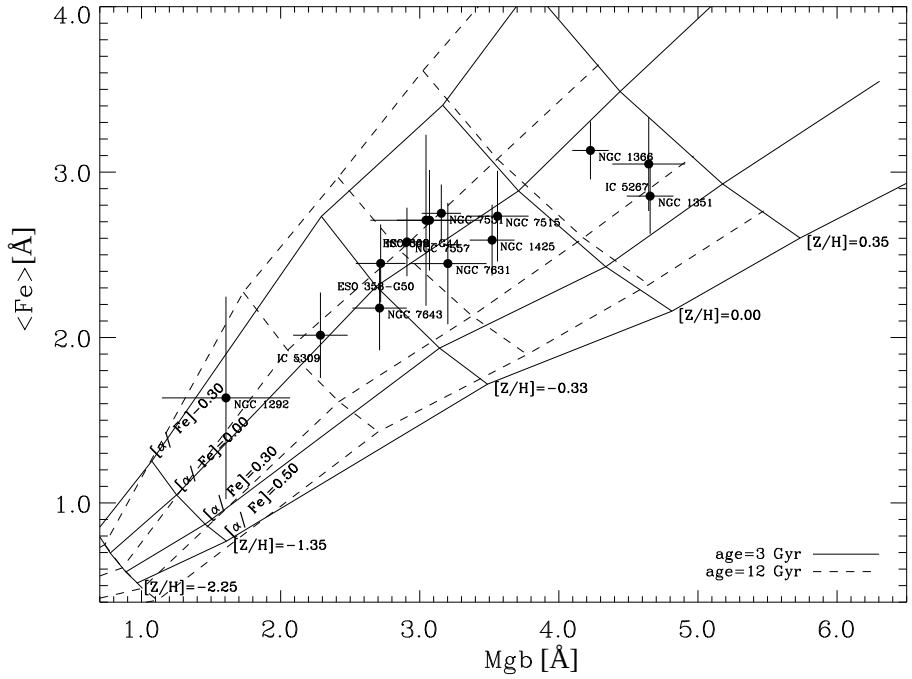

FIGURE 5.10— The distribution of the central values of ⟨Fe⟩and Mg $_b$ indices averaged over 0.3 r_e for the 15 sample galaxies . The lines indicate the models by Thomas et al. (2003). The [α/Fe]-metallicity grids are plotted with two different ages: 3 Gyr (continuous lines) and 12 Gyr (dashed lines).

negative gradient in the metallicity radial profile favors a scenario with bulge formation via dissipative collapse (Larson 1974).

Dissipative collapse implies strong inside-out formation that should give rise to a negative gradient in the α/Fe ratio too (Ferreras & Silk 2002). But no gradient was measured in the [α/Fe] radial profiles for almost all the galaxies. Only 1 object of 14 lie outside a 3 σ of distribution (Fig. 5.15). All the deviations from the median values of the other objects can be explained by their errors only (Tab. 5.5).

The absence of gradients in α/Fe ratio is not necessarily in contrast with the presence of a metallicity gradient and could be due to the different enrichment of the material fueling the star formation.

No correlation was found between the central value and gradient of α/Fe enhancement as in Reda et al. (2007), while the central value and gradient of metallicity are related in spite of the large error-bars (Fig. 5.16). All these hints

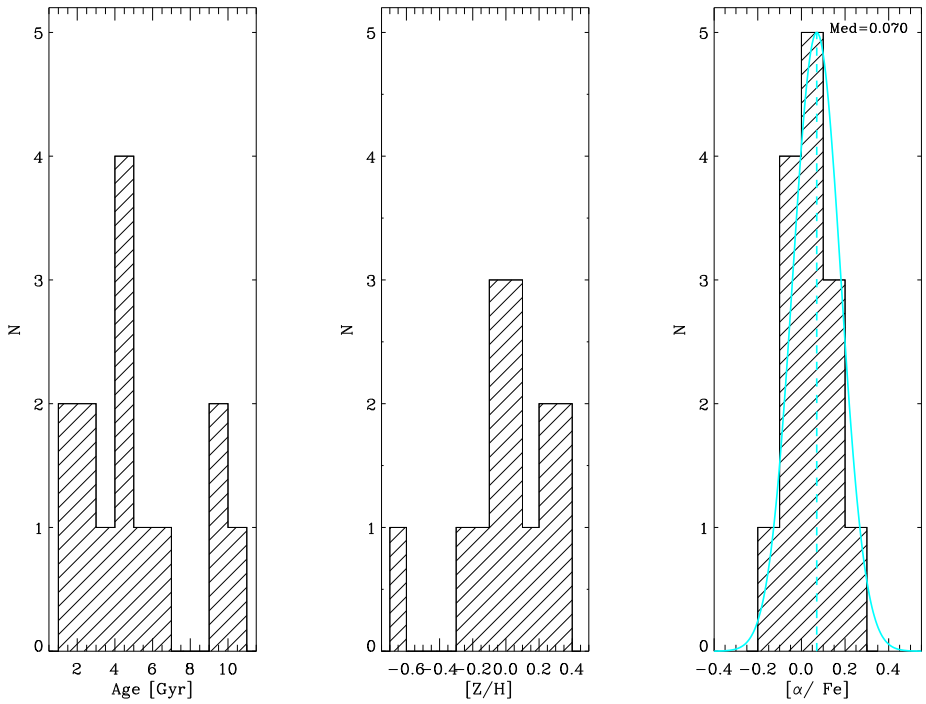

FIGURE 5.11— Distribution of age (left panel), metallicity (central panel), and [α/Fe] ratio (right panel) for the central regions of the sample galaxies. The solid line in the right panel represents a Gaussian centered in the median value [α/Fe] = 0.07 of the distribution. Its σ = 0.11 is approximated by the value containing the 68% of the objects of the distribution.

suggest that a pure dissipative collapse is not able to explain the formation of bulges and that other phenomena such mergers or acquisition events need to be invoked (Bekki & Shioya 1999; Kobayashi & Arimoto 1999).

The peculiar gradients observed for the stellar population of the bulges of NGC 1366 and NGC 7531 suggest they have different characteristics with respect to the rest of the sample. NGC 1366 shows a steep positive age gradient (from about 5 to 11 Gyr) a strong negative metallicity gradient (from about 0.5 to 0 dex) within 5″ from the center. In this region rapid rotation is measured while immediately further out the galaxy is almost not rotating. Moreover, the rotation in the innermost regions is opposite to that observed at large radii (Fig. 5.2). Even if a disk-bulge decoupling (Bertola et al. 1999; Sarzi et al. 2000; Matthews & de Grijs 2004) could give a similar kinematic signature, the stellar population analysis is more suggestive of the presence of a counter-rotating nuclear stellar disk similar to those already observed in both elliptical

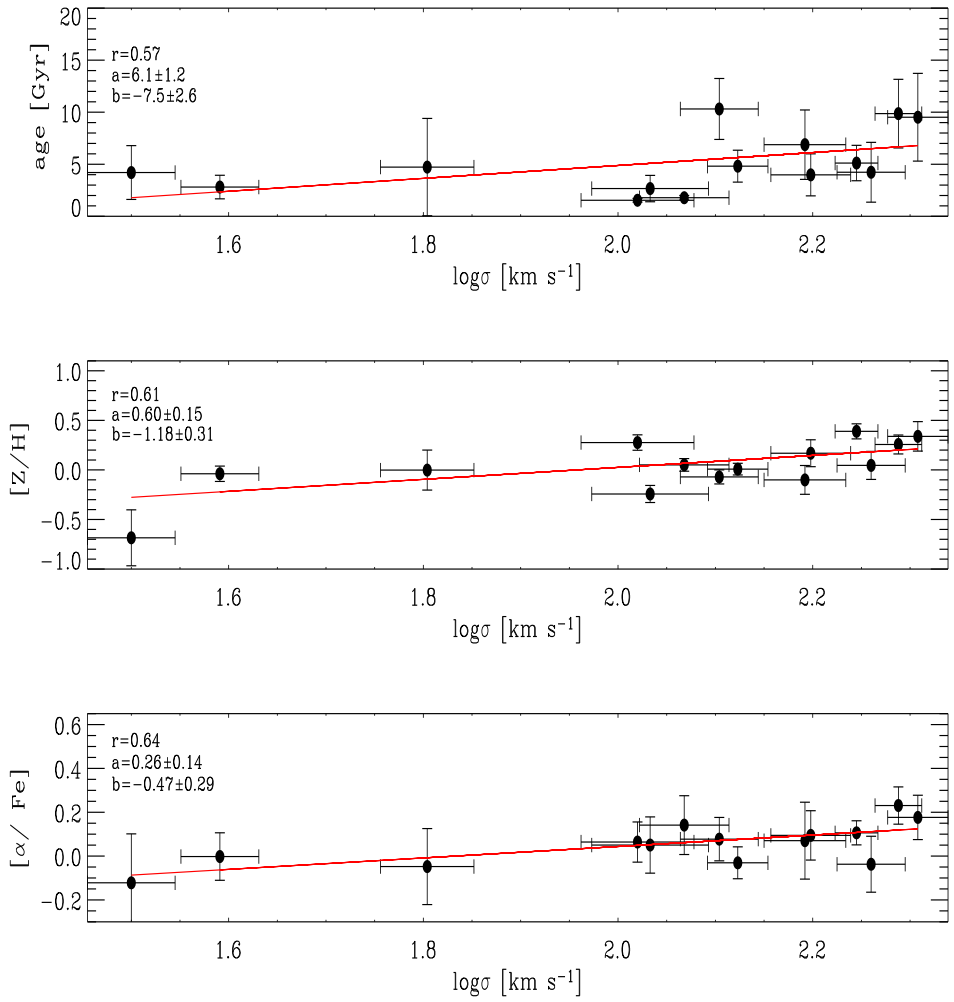

FIGURE 5.12— Correlation between central values of age, metallicity, and α-enhancement with central velocity dispersion. In each panel the solid line represents the linear regression ($y = ax + b$) through all the data points. The Pearson correlation coefficient (r) and the results of the linear fit are given.

(Morelli et al. 2004) and spiral galaxies (Corsini et al. 1999; Pizzella et al. 2002; Krajnović & Jaffe 2004; Emsellem et al. 2004; McDermid et al. 2006). The nuclear disk is younger than the rest of host bulge and formed by enriched material probably acquired via interaction or minor merging. The age of the stellar population of NGC 7531 rises from a central value of about 2 Gyr to 12

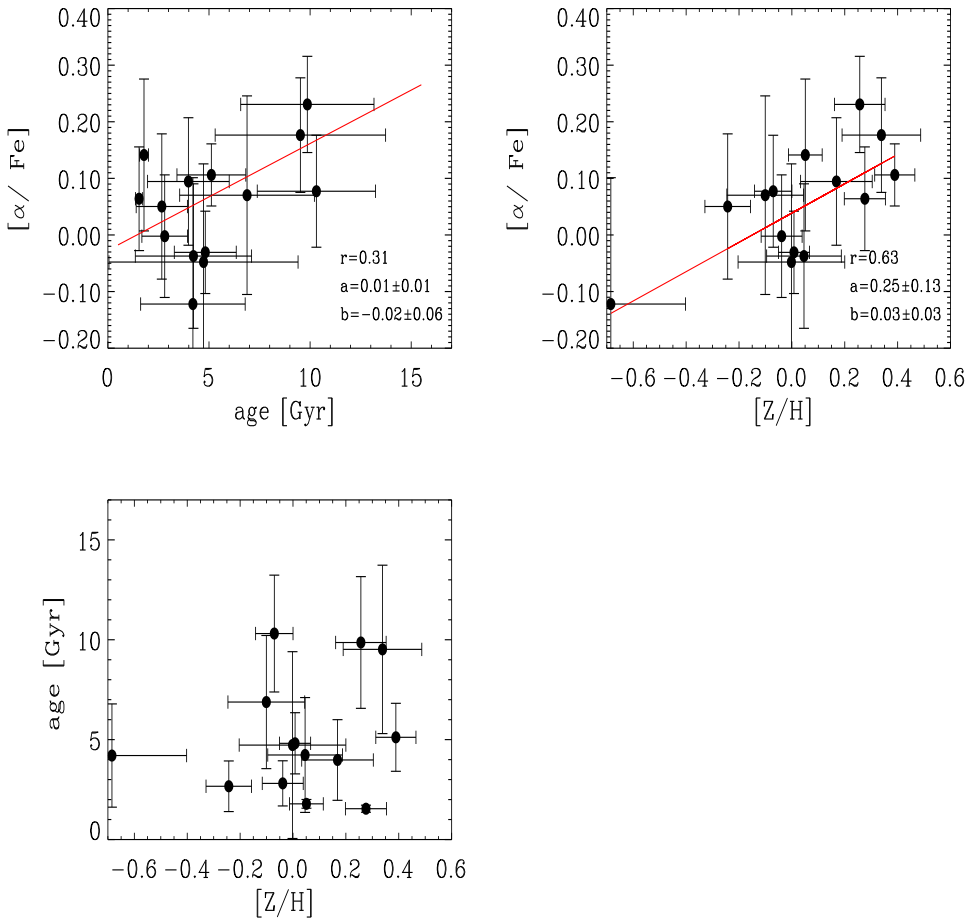

FIGURE 5.13— The central ages, metallicities, and α/Fe ratios of the sample bulges listed in Tab.5.4. In each panel the solid line represents the linear regression ($y = ax + b$) through all the data points. The Pearson correlation coefficient (r) and the results of the linear fit are given.

Gyr at 4". Further out it decreases to 2 Gyr at 6" from the center. Despite this change, no gradient in either metallicity or α/Fe ratio was found. We suggest that this is due to the presence of a component which is structurally but not kinematically decoupled from the rest of the galaxy (McDermid et al. 2006).

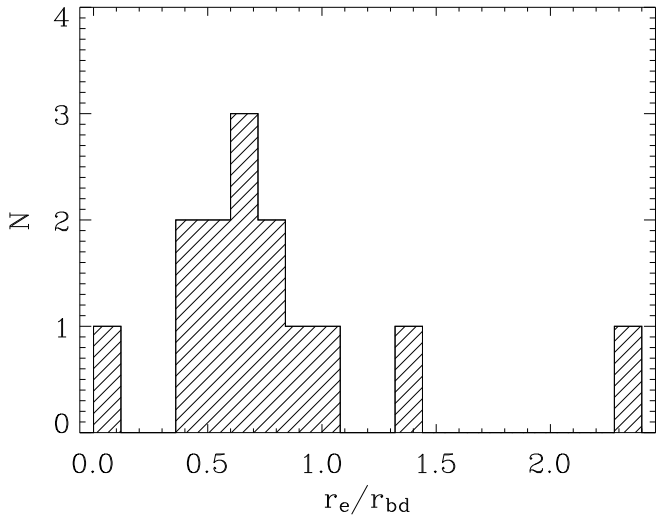

FIGURE 5.14— Distribution of the ratio between r_e and r_{bd}; For most of the galaxies it is r_e/r_{bd}=0.7, the gradient evaluated up to r_{bd} is mapping a region slightly larger than r_e.

5.8 Pseudobulges

The current picture of bulge demography reveals that disk galaxies can host bulges with a variety of photometric and kinematic properties (Kormendy & Kennicutt 2004). Classical bulges are similar to low-luminosity ellipticals and are thought to be formed by mergers and/or rapid collapse. Pseudobulges are disk-like or bar-like components which were slowly assembled by acquired material, efficiently transferred to the galaxy center where it formed stars. Pseudobulges can be identified according to their morphological, photometric, and kinematic properties, following the list of characteristics compiled by Kormendy & Kennicutt (2004). The more apply, the safer the classification becomes.

The apparent flattening of the bulge is similar to that of the disk in NGC 1292, NGC 1351 (Tab. 5.2). Moreover, most of the sample bulges have a Sérsic index $n \leq 2$. Only IC 5267, NGC 1351, NGC 1425, NGC 7515, and NGC 7631 have $n > 2$ (Tab. 5.2).

Pseudobulges are expected to be more rotation-dominated than classical bulges which are more rotation-dominated than giant elliptical galaxies (Kormendy & Kennicutt 2004). We measured the maximum rotation velocity V_{max} within r_{bd} from the stellar velocity curve and central velocity dispersion σ_0 from the velocity dispersion profile. The ellipticity ϵ of the bulge was measured by the photometric decomposition (Tab. 5.2). For each galaxy we derived the ratio V_{max}/σ_0. In Fig. 5.17 we compared it to the value predicted for an oblate

TABLE 5.5— Age, metallicity and [α/Fe]gradients for the galaxies in the sample.

Galaxy	$\Delta([Z/H])$	Δ(Age) [Gyr]	$\Delta([\alpha/Fe])$	$\Delta([Z/H])_{kpc}$	$\Delta(\mathrm{Age})_{kpc}$ [Gyr]	$\Delta([\alpha/Fe])_{kpc}$
(1)	(2)	(3)	(4)	(5)	(6)	(7)
ESO 358-50	-0.15 ± 0.23	2.95 ± 3.47	-0.008 ± 0.25	-0.06 ± 0.10	1.34 ± 1.63	-0.003 ± 0.11
ESO 548-44	-0.01 ± 0.35	1.04 ± 10.80	-0.078 ± 0.26	-0.05 ± 1.44	...	-0.325 ± 1.02
IC 1993	-0.14 ± 0.26	0.20 ± 4.30	0.098 ± 0.23	-0.35 ± 0.62	0.51 ± 11.09	0.251 ± 0.63
IC 5267	-0.22 ± 0.21	-0.76 ± 7.77	-0.024 ± 0.20	-0.15 ± 0.13	-0.52 ± 5.29	-0.016 ± 0.14
IC 5309	-0.31 ± 0.22	1.48 ± 4.67	-0.087 ± 0.22	-0.18 ± 0.10	0.87 ± 2.85	-0.051 ± 0.12
NGC 1351	-0.17 ± 0.26	-0.73 ± 6.43	-0.043 ± 0.15	-0.06 ± 0.09	-0.27 ± 2.38	-0.016 ± 0.05
NGC 1366	-0.29 ± 0.24	4.58 ± 4.95	-0.038 ± 0.13	-0.71 ± 0.52	11.16 ± 12.97	-0.092 ± 0.31
NGC 1425	-0.07 ± 0.17	-1.73 ± 6.24	0.053 ± 0.18	-0.05 ± 0.13	-1.39 ± 4.91	0.042 ± 0.15
NGC 7515	-0.15 ± 0.18	0.40 ± 4.89	-0.040 ± 0.21	-0.10 ± 0.11	0.27 ± 3.38	-0.027 ± 0.14
NGC 7531	-0.21 ± 0.14	9.54 ± 3.93	0.029 ± 0.12	-0.40 ± 0.23	...	0.055 ± 0.24
NGC 7557	-0.31 ± 0.08	1.43 ± 3.90	0.164 ± 0.22	-0.60 ± 0.10	2.81 ± 8.85	0.321 ± 0.57
NGC 7631	0.02 ± 0.19	0.89 ± 5.82	0.324 ± 0.23	0.02 ± 0.26	1.22 ± 8.29	0.443 ± 0.43
NGC 7643	0.04 ± 0.11	0.19 ± 0.44	0.080 ± 0.17	0.06 ± 0.19	0.31 ± 0.79	0.133 ± 0.31

NOTE: The columns show the following: (2),(3),(4) the gradients of the ages, metallicities, and α/Fe enhancements of the sample bulges derived from the central values and values at r_{bd} listed Tab. 5.2. (5),(6),(7) the gradients of the ages, metallicities, and α/Fe enhancements of the sample bulges rescaled at 1 kpc. Stellar population models by Thomas et al. (2003) were used.

spheroid with isotropic velocity dispersion and the same observed ellipticity (Binney 1978; Binney 1980; Binney & Tremaine 1987). The large error-bars on the $V_{\mathrm{max}}/\sigma_0$ are driven by uncertainties on the central velocity dispersion. Most of the sample bulges rotate as fast as both bulges of unbarred (Kormendy 1982; Kormendy 1993; Kormendy & Illingworth 1982) and barred galaxies (Kormendy 1982; Aguerri et al. 2005). However, the values of $V_{\mathrm{max}}/\sigma_0$ measured for NGC 1292, NGC 1425, ESO 548-44, and NGC 5267 are significantly larger than that predicted for the oblate spheroids.

Another characteristic listed by (Kormendy & Kennicutt 2004) is the position of pseudobulges with respect to the Faber-Jackson relation. The Faber-Jackson (FJ) relation (Faber & Jackson 1976) relates the luminosity of the elliptical galaxies and early-type bulges to their central velocity dispersion. Pseudobulges show a central velocity dispersion lower than foreseen from their luminosity (Kormendy & Kennicutt 2004). Sample bulges, except for ESO 358-G50 and NGC 1292, are consistent with the $R-$band FJ relation we built from Forbes & Ponman (1999, $L \propto \sigma^{3.92}$) as done by Matković & Guzmán (2005). They are characterized by a lower velocity dispersion or equivalently a higher

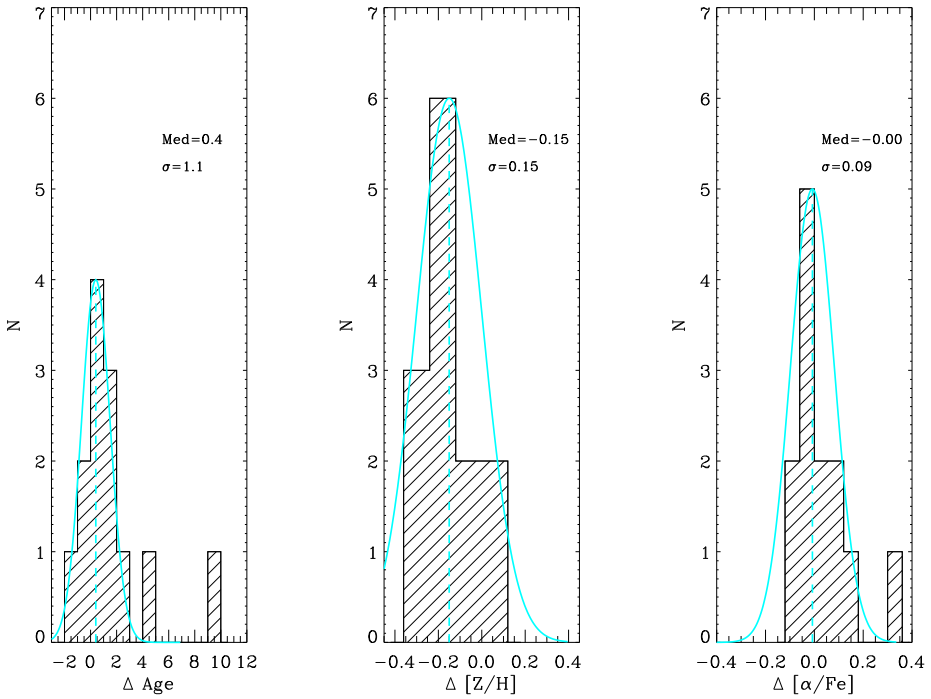

FIGURE 5.15— Distribution of the gradients of age (left panel), the metallicity (central panel), and [α/Fe] ratio (right panel) for the sample galaxies. Dashed line represents the median of the distribution and its values is reported. The solid line represents a Gaussian centered on the median value of distribution. Their σ, which is approximated by the value containing the 68% of the objects of the distribution, are reported.

luminosity with respect to their early-type counterparts (Fig. 5.18). ESO 358-G50 and NGC 1292 are also low-σ (or high-L) outliers with respect to the relationship found for faint early-type galaxies by Matković & Guzmán (2005, $L \propto \sigma^{2.01}$).

According to the prescriptions by Kormendy & Kennicutt (2004), the bulge of NGC 1292 is the most reliable pseudobulges in our sample. Information about its stellar population gives more constraints on its nature and formation process. In fact, the bulge population has an intermediate age (3 Gyr) and low metal content ([Z/H]= -0.7 dex). The α/Fe ratio is the lowest in our sample ([α/Fe]= -0.12 dex) suggesting a prolonged star formation history. The presence of emission lines in the spectrum shows that star formation is still ongoing. These properties are consistent with a slow buildup of the bulge of NGC 1292 within a scenario of secular evolution.

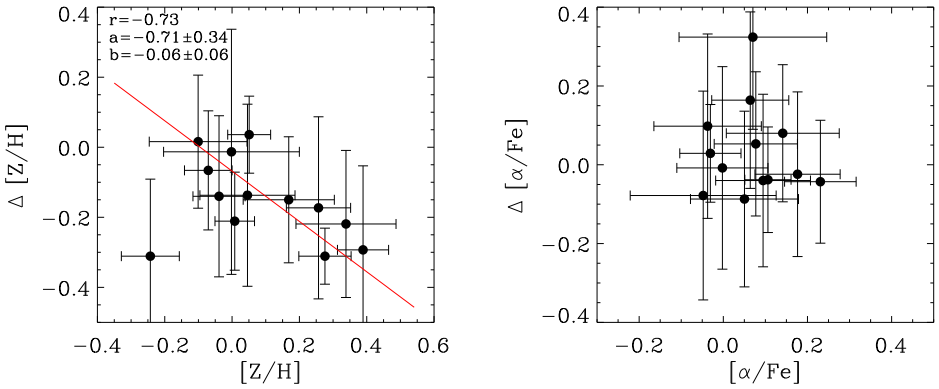

FIGURE 5.16— The gradient and central values of metallicity (left panel) and α/Fe ratio (right panel). In the left panel the solid line represents the linear regression ($y = ax + b$) through all the data points. The Pearson correlation coefficient (r) and the results of the linear fit are given.

5.9 Conclusions

The structural parameters and properties of the stellar population of the bulges of sample of 14 S0 and spiral galaxies of the Fornax, Eridanus, and Pegasus clusters, and NGC 7582 group were investigated to constrain the dominant mechanism at the epoch of their assembly.

- The bulge and disk parameters of the sample galaxies were derived performing a two-dimensional photometric decomposition of their $R-$band images. The surface-brightness distribution of the galaxy was assumed to be the sum of the contribution of a Sérsic bulge and an exponential disk. The two components were characterized by elliptical and concentric isophotes with constant (but possibly different) ellipticity and position angles. Most of the bulges have a Sérsic index $n \leq 2$ and for few of them the apparent flattening of the bulge is similar to that of the disk. According to Kormendy & Kennicutt (2004) the disk-like flattening and radial profile are the photometric signature of a pseudobulge.

- The central values of velocity dispersion σ and Mg_b, Mg_2, H_β, $\langle\mathrm{Fe}\rangle$, and $[\mathrm{MgFe}]'$ line-strength indices were derived from the major-axis spectra. Correlations between Mg_2, $\langle\mathrm{Fe}\rangle$, H_β, and σ were found. The $\mathrm{Mg}_2-\sigma$ and $\mathrm{H}_\beta-\sigma$, correlations are steeper than those found for early-type galaxies (Bernardi et al. 1998; Jørgensen 1999a; Kuntschner 2000; Mehlert et al.

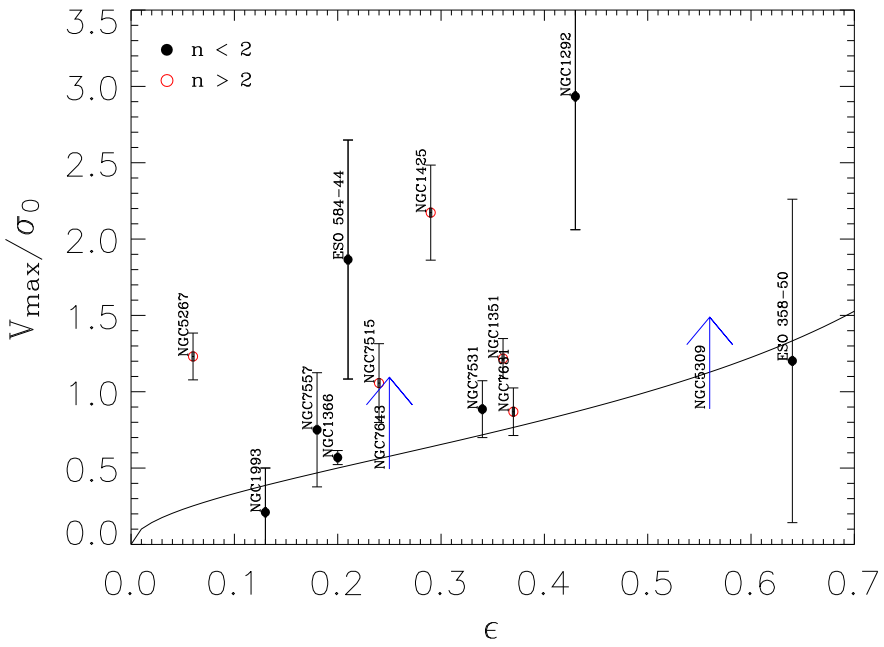

FIGURE 5.17— The location of the sample bulges in the $(V_{max}/\sigma_0, \epsilon)$ plane. Filled and open circles correspond to bulges with Sérsic index $n \leq 2$ and $n > 2$, respectively. The continuous line corresponds to oblate-spheroidal systems that have isotropic velocity dispersions and that are flattened only by rotation.

2003). The $\langle$Fe$\rangle-\sigma$ correlation is consistent with previous findings for spiral bulges (Idiart et al. 1996; Prugniel et al. 2001; Proctor & Sansom 2002).

- The mean ages, total metallicities, and total α/Fe ratio in the centers of the sample bulges were derived by using the stellar population models by Thomas et al. (2003). The youngest bulges have an average age of 2 Gyr. They are characterized by ongoing star formation. The stellar population of intermediate-age bulges is 4 to 8 Gyr old. It has solar metallicity ($[Z/H] = 0.0$ dex). The older bulges have a narrow distribution in age around 10 Gyr and high metallicity ($[Z/H] = 0.30$ dex). Most of the sample bulges display solar α/Fe ratios. A few have a central super-solar ratio ($[\alpha/Fe] = 0.3$).

- There is no correlation between age, metallicity, and α/Fe ratio of the

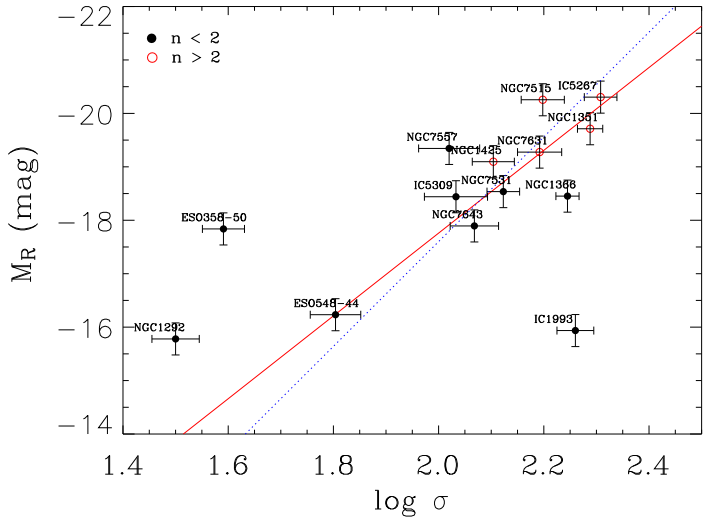

FIGURE 5.18— The location of the sample bulges with respect to the FJ relation by Forbes & Ponman (1999, blue dashed line). Filled and open circles correspond to bulges with Sérsic index $n \leq 2$ and $n > 2$, respectively and the linear fit is shown (red continuous line).

sample bulges with the membership of the host galaxy in a given cluster. There is a correlation with the velocity dispersion. The more massive bulges of our sample galaxies are older, more metal rich, and characterized by rapid star formation. Since we did not find any correlation with galaxy morphology we exclude a strong interplay between the bulge and disk components.

- Most of the sample galaxies show no gradient in age and a negative gradient in metallicity. This is in agreement with the earlier findings by Mehlert et al. (2003) and Sánchez-Blázquez et al. (2006) for early-type galaxies, and by Jablonka et al. (2007) for bulges. The presence of negative gradient in the metallicity radial profile favors a scenario with bulge formation via dissipative collapse. This implies strong inside-out formation that should give rise to a negative gradient in the α/Fe ratio too (Ferreras & Silk 2002). But, no gradient was measured in the [α/Fe] radial profiles for all the galaxies, except for NGC 1366 and NGC 7531. Moreover, the correlation between the central value and gradient of metallicity can not be derived from pure dissipative collapse (Bekki & Shioya 1999; Kobayashi & Arimoto 1999) and suggests that mergers or acquisition events need to

be invoked during bulge assembly.

- The peculiar gradients observed for the stellar population of the bulges of NGC 1366 and NGC 7531 suggest that they host a substructure. Very interestingly, in NGC 1366 we found the presence of a kinematically-decoupled component. It is younger than the host bulge and formed by enriched material probably acquired via interaction or minor merging.

- According to the prescriptions by Kormendy & Kennicutt (2004) the bulge of NGC 1292 is a pseudobulge. The properties of its stellar population are consistent with a slow buildup within a scenario of secular evolution. Indeed, the bulge of NGC 1292 has an intermediate age (3 Gyr) and low metal content ($[Z/\mathrm{H}] = -0.7$ dex). The α/Fe ratio is the lowest in our sample ($[\alpha/\mathrm{Fe}] = -0.12$ dex) suggesting a prolonged star formation history. The presence of emission lines in the spectrum is a signature of ongoing star formation.

Bibliography

Aguerri, J. A. L., Iglesias-Páramo, J., Vílchez, J. M., Muñoz-Tuñón, C., & Sánchez-Janssen, R. 2005, AJ, 130, 475

Annibali, F., Bressan, A., Rampazzo, R., Zeilinger, W. W., & Danese, L. 2007, A&A, 463, 455

Arimoto, N., & Yoshii, Y. 1987, A&A, 173, 23

Bekki, K., & Shioya, Y. 1999, ApJ, 513, 108

Bender, R. 1990, A&A, 229, 441

Bender, R., Saglia, R. P., & Gerhard, O. E. 1994, MNRAS, 269, 785

Bernardi, M., Renzini, A., da Costa, L. N., et al. 1998, ApJ, 508, L143

Bertola, F., Corsini, E. M., Vega Beltrán, J. C., et al. 1999, ApJ, 519, L127

Beuing, J., Bender, R., Mendes de Oliveira, C., Thomas, D., & Maraston, C. 2002, A&A, 395, 431

Binney, J. 1978, MNRAS, 183, 501

Binney, J. 1980, Royal Society of London Philosophical Transactions Series A, 296, 329

Binney, J., & Tremaine, S. 1987, Galactic dynamics (Princeton University Press, Princeton), 747 p.

Brough, S., Proctor, R., Forbes, D. A., et al. 2007, MNRAS, 378, 1507

Bruzual, G., & Charlot, S. 2003, MNRAS, 344, 1000

Clemens, M. S., Bressan, A., Nikolic, B., et al. 2006, MNRAS, 370, 702

Collobert, M., Sarzi, M., Davies, R. L., Kuntschner, H., & Colless, M. 2006, MNRAS, 370, 1213

Corsini, E. M., Pizzella, A., Sarzi, M., et al. 1999, A&A, 342, 671

Coziol, R., Doyon, R., & Demers, S. 2001, MNRAS, 325, 1081

de Vaucouleurs, G., de Vaucouleurs, A., Corwin, H. G., et al. 1991, Third Reference Catalogue of Bright Galaxies (Springer-Verlag, New York) (RC3)

Denicoló, G., Terlevich, R., Terlevich, E., Forbes, D. A., & Terlevich, A. 2005, MNRAS, 358, 813
Dressler, A. 1980, ApJ, 236, 351
Eggen, O. J., Lynden-Bell, D., & Sandage, A. R. 1962, ApJ, 136, 748
Emsellem, E., Cappellari, M., Peletier, R. F., et al. 2004, MNRAS, 352, 721
Faber, S. M., & Jackson, R. E. 1976, ApJ, 204, 668
Faber, S. M., Friel, E. D., Burstein, D., & Gaskell, C. M. 1985, ApJS, 57, 711
Ferguson, H. C. 1989, AJ, 98, 367
Ferreras, I., & Silk J. 2002, MNRAS, 336, 1181
Fisher, D., Franx, M., & Illingworth, G. 1996, ApJ, 459, 110
Forbes, D. A., & Ponman, T. J. 1999, MNRAS, 309, 623
Fouque, P., Gourgoulhon, E., Chamaraux, P., & Paturel, G. 1992, A&AS, 93, 211
Freeman, K. C. 1970, ApJ, 160, 811
Ganda, K., Peletier, R. F., McDermid, R. M., et al. 2007, MNRAS, 380, 506
Garcia, A. M. 1993, A&AS, 100, 47
Gorgas, J., Efstathiou, G., & Aragon Salamanca, A. 1990, MNRAS, 245, 217
Idiart, T. P., de Freitas Pacheco, J. A., & Costa R. D. D. 1996, AJ, 112, 2541
Jablonka, P., Martin, P., & Arimoto, N. 1996, AJ, 112, 1415
Jablonka, P., Gorgas, J., & Goudfrooij, P. 2007, A&A, 474, 763
Jørgensen I. 1999a, MNRAS, 306, 607
Jørgensen I. 1999b, MNRAS, 306, 607
Kobayashi, C., & Arimoto, N. 1999, ApJ, 527, 573
Kodama, T., Arimoto, N., Barger, A. J., & Aragón-Salamanca, A. 1998, A&A, 334, 99
Kormendy, J. 1982, ApJ, 257, 75
Kormendy, J. 1993, Galactic Bulges, ed. H. Dejonghe & H. J. Habing (Kluwer Academic Publishers, Dordrecht), 153, 209
Kormendy, J., & Illingworth, G. 1982, ApJ, 256, 460
Kormendy, J., & Kennicutt, R. C. 2004, ARA&A, 42, 603
Krajnović, D., & Jaffe, W. 2004, A&A, 428, 877
Kuntschner, H. 2000, MNRAS, 315, 184
Kuntschner, H., Lucey, J. R., Smith, R. J., Hudson, M. J., & Davies, R. L. 2001, MNRAS, 323, 615
Larson, R. B. 1974, MNRAS, 166, 585
Matković, A., & Guzmán, R. 2005, MNRAS, 362, 289
Matthews, L. D., & de Grijs, R. 2004, AJ, 128, 137
McDermid, R. M., Emsellem, E., Shapiro, K. L., et al. 2006, MNRAS, 373, 906
Mehlert, D., Saglia, R. P., Bender, R., & Wegner, G. 1998, A&A, 332, 33
Mehlert, D., Saglia, R. P., Bender, R., & Wegner, G. 2000, A&AS, 141, 449
Mehlert, D., Thomas, D., Saglia, R. P., Bender, R., & Wegner, G. 2003, A&A, 407, 423
Moore, S. A. W., Lucey, J. R., Kuntschner, H., & Colless, M. 2002, MNRAS, 336, 382
Moorthy, B. K., & Holtzman, J. A. 2006, MNRAS, 371, 583
Morelli, L., Halliday, C., Corsini, E. M., et al. 2004, MNRAS, 354, 753
Nishiura, S., Shimada, M., Ohyama, Y., Murayama, T., & Taniguchi, Y. 2000, AJ, 120, 1691
Osterbrock, D. E., Fulbright, J. P., Martel, A. R., et al. 1996, PASP, 108, 277
Peletier, R. F. 1989, PhD thesis, University of Groningen

Pizzella, A., Corsini, E. M., Morelli, L., et al. 2002, ApJ, 573, 131
Proctor, R. N., & Sansom, A. E. 2002, MNRAS, 333, 517
Prugniel, P., & Maubon, G., & Simien, F. 2001, A&A, 366, 68
Rampazzo, R., Annibali, F., Bressan, A., Longhetti, M., Padoan, F., & Zeilinger, W. W. 2005, A&A, 433, 497
Reda, F. M., Proctor, R. N., Forbes, D. A., Hau, G. K. T., & Larsen, S. S. 2007, MNRAS, 377, 1772
Salpeter, E. E. 1955, ApJ, 121, 161
Sánchez-Blázquez, P., Gorgas, J., & Cardiel, N. 2006a, A&A, 457, 823
Sánchez-Blázquez, P., Gorgas, J., Cardiel, N., & González, J. J. 2006b, A&A, 457, 809
Sarzi, M., Corsini, E. M., Pizzella, A., et al. 2000, A&A, 360, 439
Sarzi, M., Falcón-Barroso, J., Davies, R. L., et al. 2006, MNRAS, 366, 1151
Sérsic J. L. 1968, Atlas de galaxias australes (Observatorio Astronómico, Cordoba)
Thomas, D., & Davies, R. L. 2006, MNRAS, 366, 510
Thomas, D., Maraston, C., & Bender, R. 2003, MNRAS, 339, 897
Thomas, D., Maraston, C., Bender, R., & Mendes de Oliveira, C. 2005, ApJ, 621, 673
Trager, S. C., Worthey, G., Faber, S. M., Burstein, D., & Gonzalez, J. J. 1998, ApJS, 116, 1
Trager, S. C., Faber, S. M., Worthey, G., González, J. J. 2000, AJ, 119, 1645
Tremonti, C. A., Heckman, T. M., Kauffmann, G., et al. 2004, ApJ, 613, 898
Worthey, G., Faber, S. M., Gonzalez, J. J., & Burstein, D. 1994, ApJS, 94, 687

6

Structure and dynamics of galaxies with low surface-brightness disks

Based on A. Pizzella, E. M. Corsini, M. Sarzi, J. Magorrian, J. Méndez-Abreu, L. Coccato, L. Morelli and F. Bertola, 2008, MNRAS, 387, 1099

Photometry and long-slit spectroscopy are presented for a sample of 6 galaxies with low surface-brightness stellar disks and for 4 galaxies with a high surface-brightness disk. The characterizing parameters of the bulge and disk components were derived by means of a two-dimensional photometric decomposition of the images of the sample galaxies. The stellar and ionized-gas kinematics were measured along the major and minor-axis in half of the sample galaxies, whereas the other half was observed only along two diagonal axes. Spectra along two diagonal axes were obtained also for one of the objects with major and minor-axes spectra. The kinematic measurements extend in the disk region out to a surface-brightness level $\mu_R \approx 24$ mag arcsec^{-2}, reaching in all cases the flat part of the rotation curve. The stellar kinematics is, as expected, more regular and symmetric than the ionized-gas kinematics, which often shows the presence of non-circular, off-plane, and disordered motions. This raises the question about the reliability of the use of the ionized gas as the tracer of the circular velocity in the modeling of the mass distribution, in particular in the central regions of low surface-brightness galaxies.

6.1 Introduction

Low surface-brightness (LSB) galaxies are operatively defined as galaxies with a central face-on surface-brightness fainter than 22.6 $B-$mag arcsec^{-2}. Therefore they are more difficult to find and study than their high surface-

brightness (HSB) counterparts. Most but not all of them are dwarf galaxies (Schombert & Bothun 1988; Schombert et al. 1992; Impey et al. 1996). Giant LSB galaxies are fairly well described as exponential disks with no significant bulge components (Romanishin et al. 1983; McGaugh & Bothun 1994; Sprayberry et al. 1995). They fall within the range of luminosities defined by HSB disks. At fixed luminosity, the LSB disks have lower central surface-brightnesses and larger scale-lengths than the disks of HSB galaxies, although few of them has structural parameters as extreme as the prototype Malin 1 (Bothun et al 1987). It is apparent that LSB galaxies exist in a wide range of morphological types. Most LSB galaxies discovered so far are bulgeless, but there are some galaxies with LSB disks that have a significant bulge component (Beijersbergen et al. 1999).

The amount and distribution of the dark matter (DM) in galaxies are usually determined using the gas rotation curve and through the study of an excess of galactic rotation compared to what can be induced by the luminous matter, the contribution of which is generally estimated by adjusting the mass-to-light ratio until the central velocity gradient can be matched. The structure of the DM halo is more directly revealed in galaxies where the luminous component gives a low contribution to the mass budget, because this makes mass modeling easier and the derived DM distribution less uncertain. This is the case for the giant LSB galaxies. They are DM dominated at all radii when a stellar mass-to-light ratio consistent with population synthesis modeling is adopted to fit the observed rotation curves (Swaters et al. 2000). These results are in agreement with the findings of Zwaan et al. (1995), who realized that LSB galaxies follow the same Tully-Fisher relation as HSB galaxies. They argued that this implies that the mass-to-light ratio of LSB galaxies is typically a factor of 2 larger than that of normal galaxies of the same total luminosity and morphological type. For these reasons, LSB galaxies were considered ideal targets for studying the properties of DM halos and for testing whether they have a central cuspy power-law mass density distribution as predicted by the most common models based on cold dark matter (CDM) cosmology (Navarro et al. 1996; Navarro et al. 1997; Moore et al. 1998; Moore et al. 1999).

Different methods are used to measure the inner slope of the DM density profile in LSB galaxies: fitting a mass model which takes into account the contribution of stars, gas and DM to the rotation curve (van den Bosch et al. 2000; van den Bosch & Swaters 2001; Swaters et al. 2003a), fitting a power law to the rotation curve (Simon et al. 2003), and fitting a power law to the density distribution derived by inverting the rotation curve (de Blok et al. 2001; de Blok & Bosma 2002; Swaters et al. 2003a). For most galaxies the inner density slope is unconstrained. Although DM halos with constant density cores generally

provide better fits, also those with cuspy radial profiles are consistent with the data. Systematic errors of long-slit (e.g., not-perfect positioning of the slit on the galaxy nucleus and errors in the position angle of the disk) and radio (e.g., beam smearing) observations may lead to an underestimate of the inner slope and contribute to the total uncertainties on the interpretation of the observed kinematics (Swaters et al. 2003a; Swaters et al. 2004).

High-resolution two-dimensional velocity fields obtained with integral-field spectroscopy (Bolatto et al. 2002; Swaters et al. 2003b; Kuzio de Naray et al. 2006; Pizzella et al. 2008) remove most systematic errors. But, they are not conclusive. The analysis of these data in the inner regions of most of the observed galaxies reveals that the gas is not moving on circular orbits in a disk coplanar to the stellar disk (Swaters et al. 2003b; Rhee et al 2004; Hayashi & Navarro 2006). This is a common phenomenon in the centers of HSB galaxies too. In fact, non-circular (Gerhard et al. 1989; Berman 2001) pressure-supported (Fillmore et al. 1986; Kormendy & Westpfahl 1989; Bertola et al. 1995; Cinzano et al 1999) and off-plane (Corsini et al. 1999, 2003; Pignatelli et al. 2001) gas motions are often observed in unbarred HSB galaxies for which dynamical modeling allows a direct comparison between the gas and circular velocity. Recently, Christlein & Zaritsky (2008) found kinematic anomalies in the outer disk region of nearby disk galaxies.

This poses a question about the reliability of central mass distribution derived in both LSB and HSB galaxies from the analysis of the gas rotation curves. To address this issue in LSB galaxies a crucial piece of information is needed, which has been missed so far: the stellar kinematics. This Chapter is organized as follows: the galaxy sample is presented in Sect. 6.2. The photometric and spectroscopic observations are described in Sect. 6.3. The structural parameters of the bulge and disk of the sample galaxies derived using GASP2D are presented in Sect. 6.4. The stellar and ionized-gas kinematics are measured from the long-slit spectra out to 0.5–1.5 optical radii with high signal-to-noise ratio in Sect. 6.5. The results and conclusions are given in Sect. 6.7. Dynamical modeling of the data is deferred to a companion work (Magorrian et al. 2008).

6.2 Galaxy sample

We set out to find LSB disks in spiral galaxies without necessarily excluding the presence of a bulge. An initial sample of 10 target galaxies was initially selected on the basis of the central disk surface-brightness estimate derived from The Surface Photometry Catalog of the ESO-Uppsala Galaxies (Lauberts & Valentijn 1989, ESO-LV). An exponential law was fitted to the surface-brightness

TABLE 6.1— Parameters of the sample galaxies.

Galaxy	Type	$V_\odot$	D	PA	i	R_{25}	M_R	σ_c	V_c	R_g/R_{25}	$R_\star/R_{25}$
		(km s^{-1})	(Mpc)	(°)	(°)	(arcsec)	(mag)	(km s^{-1})	(km s^{-1})		
(1)	(2)	(3)	(4)	(5)	(6)	(7)	(8)	(9)	(10)	(11)	(12)
ESO-LV 1860550	Sab(r)?	4640	60.1	105	63	40	13.39	91.7 ± 2.0	235 ± 11	1.0	0.6
ESO-LV 2060140	SABc(s)	4648	60.5	174	39	35	13.74	54.3 ± 2.0	141.0 ± 4.5	1.4	1.4
ESO-LV 2340130	Sbc	4703	60.9	172	69	42	13.43	64.1 ± 2.0	194 ± 19	1.2	0.5
ESO-LV 4000370	SBcd(s) pec	3016	37.5	68	50	46	13.64	42.0 ± 2.5	128.7 ± 1.8	1.0	1.5
ESO-LV 4880490	SBdm(s)	1790	25.0	136	67	46	14.38	48.2 ± 2.5	102.7 ± 8.2	1.2	0.9
ESO-LV 5340200	Sa:	17320	226.7	167	46	19	14.97	153.9 ± 7.1	297 ± 11	1.4	0.5

NOTE. The columns show the following: (2) morphological classification from RC3, except for ESO-LV 5340200 (NASA/IPAC Extragalactic Database); (3) heliocentric systemic velocity of the galaxy derived at the center of symmetry of the rotation curve of the gas (this Chapter). The typical error on the systemic velocity is $\Delta V_\odot = 10$ km s^{-1}; (4) distance obtained as V_0/H_0 with $H_0 = 75$ km s^{-1} Mpc^{-1} and V_0 the systemic velocity derived from $V_\odot$ corrected to the CMB reference frame assuming the dipole direction by Fixsen et al. (1996); (5) major-axis position angle from ESO-LV; (6) inclination derived as $\cos^2 i = (q^2 - q_0^2)/(1 - q_0^2)$. The observed axial ratio q was taken from ESO-LV, except for ESO-LV 4460170 (Palunas & Williams 2000) and ESO-LV 2060140 (McGaugh et al. 2001). The intrinsic flattening $q_0 = 0.11$ was assumed following Guthrie (1992) ; (7) radius of the 25 $B-$mag arcsec^{-2} isophote derived as $D_{25}/2$ with D_{25} from ESO-LV; (8) total observed red magnitude from ESO-LV catalog; (9) central velocity dispersion of the stellar component (this chapter); (10) galaxy circular velocity (this chapter); (11) radial extension of the ionized-gas rotation curve in units of R_{25} (this chapter); (12) radial extension of the stellar rotation curve in units of R_{25} (this chapter).

radial profile at large radii, where the light distribution of the galaxy is expected to be dominated by the disk contribution. The fit was done using a non-linear least-squares minimization method. It was based on the robust Levenberg-Marquardt method (Press et al 1992) implemented by Moré et al. (1980). The computation was done using the MPFIT algorithm implemented by C. B. Markwardt in the IDL environment[1]. All the sample galaxies are classified as spiral galaxies with a morphological type ranging from Sa to Sm (de Vaucouleurs et al 1991, RC3). The Galactic latitudes were chosen so as to minimize the foreground extinction ($|b| > 15°$, RC3). The inclinations were selected to be larger than 30° (ESO-LV) to allow a reliable measurement of the stellar and ionized-gas kinematics. Finally, the galaxies were chosen to be morphologically undisturbed and have a clean stellar foreground so as not to complicate the photometric and spectroscopic analysis.

This sample was subsequently culled to 6 galaxies following a scrupulous two-dimensional photometric decomposition of our own images (see Sect. 6.4),

[1]The updated version of this code is available on http://cow.physics.wisc.edu/ craigm/idl/idl.html

TABLE 6.2— Log of spectroscopic observations of the sample galaxies.

Galaxy	Run	Position	PA	Single Exp. Time	Tot. Exp. Time
			(°)	(s)	(h)
(1)	(2)	(3)	(4)	(5)	(6)
ESO-LV 1860550	2	MJ−30°	75	3×2750	2.3
	2	MN−30°	165	2×2750	1.5
ESO-LV 2060140	3	MJ	175	$3 \times 2620 + 1 \times 2600$	2.9
	3	MN	85	1×2600	0.7
ESO-LV 2340130	2	MJ+16°	8	3×2750	2.3
	2	MN+16°	98	2×2750	1.5
ESO-LV 4000370	2	MJ+44°	112	3×2750	2.3
	2	MN+44°	22	2×2750	1.5
ESO-LV 4880490	3	MJ	46	3×2750	2.3
	3	MN	136	3×2750	2.3
ESO-LV 5340200	2	MJ	167	3×3050	2.5
	2	MN	77	1×2750	0.8
	2	MJ+26°	13	1×2400	0.7
	2	MN+26°	103	1×2750	0.8

NOTE. The columns show the following: (2) observing run; (3) slit position: MJ = major-axis, MN = minor-axis; (4) slit position angle; (5) number and exposure time of the single exposures; (6) total exposure time.

which led us to find that 4 targets were in fact hosting HSB disks. The basic properties, photometry, and kinematics of these HSB spiral galaxies are given in Sect. 6.6. In the rest of the paper we discuss only the 6 galaxies which host a LSB disk. Our selection criteria are similar to those of Beijersbergen et al. (1999). The result of this selection is that the galaxies in our sample host HSB bulges with a central face-on surface-brightness brighter than 22.6 $B-$mag arcsec^{-2}. The sample galaxies and their basic properties are listed in Table 6.1.

6.3 Observations and data reduction

6.3.1 Broad-band imaging and long-slit spectroscopy

The photometric and spectroscopic data of the sample galaxies were obtained at the Very Large Telescope (VLT) of the European Southern Observatory (ESO) at Paranal Observatory during three different runs between 2001 and 2003. The observations were carried out in service mode on May 05 – July 03, 2001 (run 1), April 13 – June 03, 2002 (run 2), and October 30, 2002 – February 04, 2003 (run 3).

The Focal Reducer Low Dispersion Spectrograph 2 (FORS2) mounted the volume-phased holographic grism GRIS_1400V18 with 1400 grooves mm^{-1} and the $1''.0 \times 6'.8$ slit. In run 1 the detector was a Site SI-424A CCD with 2048×2048 pixels of 24×24 μm^2. The wavelength range from 4750 to 5800 Å was covered with a reciprocal dispersion of 0.51Å $pixel^{-1}$ and a spatial scale of 0.20 arcsec $pixel^{-1}$. In run 2 and 3 the detector was a mosaic of two MIT/LL CCDID-20 2k × 4k CCDs. Each CCD had 2048×4096 pixels of 15×15 μm^2. The wavelength range from 4630 to 5930 Å was covered with a reciprocal dispersion of 0.65Å $pixel^{-1}$ and a spatial scale of 0.250 arcsec $pixel^{-1}$ after a 2×2 pixel binning.

Major and minor-axis spectra were obtained for half of the sample galaxies, whereas the other half was observed along only two diagonal axes (see Tab. 6.2). Spectra along two diagonal axes were obtained also for ESO-LV 5340200, which has major and minor-axis spectra as well. The integration time of the galaxy spectra ranged between 2400 and 3050 s. The log of the spectroscopic observations as well as total integration times and slit position angle are given in Table 2. At the beginning of each exposure, the galaxy was centered on the slit. The acquisition images were obtained with no filter in run 1. The Site CCD efficiency curve roughly corresponded to a broad V band. In run 2 and 3 the acquisition images were obtained with the Gunn $z-$band filter ($\lambda_{\rm eff} = 9100$ Å, FWHM = 1305 Å). The total integration times are listed in Table 6.3. In run 2 and 3 an offset of $10''$ along the direction of the slit was applied between repeated exposures in order to deal with the gap between the two CCDs in the mosaic spectrum.

In run 1 and 3 a number of spectra of giant stars with spectral type ranging from G to K were obtained to be used as templates in measuring stellar kinematics. Integration times and spectral type the template stars as well as the log of the observations are given in Table 6.4. Additionally, at least one flux standard star per night was observed to calibrate the flux of the spectra. The standard calibration frames (i.e., biases, darks, and flat-field spectra) as well as the spectra of the comparison arc lamp were taken in the afternoon before each observing night.

The mean value of the seeing FWHM during the spectroscopic exposures as measured by fitting a two-dimensional Gaussian to the guide star ranged from $0''.8$ to $2''.7$.

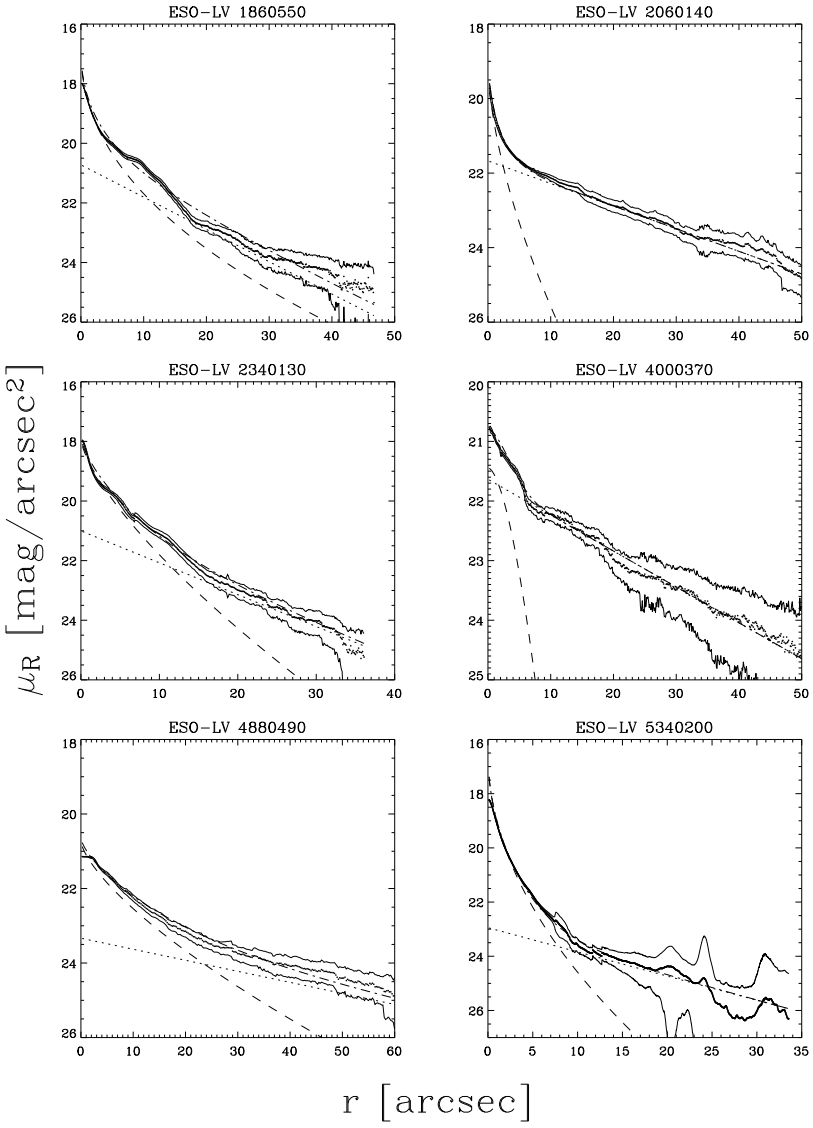

FIGURE 6.1— Surface-brightness radial profile and photometric decomposition of the sample galaxies. The radial profiles were obtained by fitting ellipses to the isophotes of the image of the galaxy (thick continuous line), model bulge (dashed line), model disk (dotted line), and bulge-disk model (dot-dashed line). All the profiles are given as a function of the semi-major axes of the fitting ellipses. The bulge and disk contributions are shown before the convolution with PSF. The surface-brightness of the bulge-disk model takes into account the PSF. The two thin continuous lines show the $\pm 1\sigma$ confidence region from the ellipse fit of the galaxy image.

TABLE 6.3— Log of photometric observations of the sample galaxies.

Galaxy	Run	Filter	Single Exp. Time (s)	FWHM (arcsec)
(1)	(2)	(3)	(4)	(5)
ESO-LV 1860550	2	Gunn z	3×50	0.9
ESO-LV 2060140	3	Gunn z	6×100	0.7
ESO-LV 2340130	2	Gunn z	5×50	1.0
ESO-LV 4000370	2	Gunn z	3×50	1.4
ESO-LV 4880490	3	Gunn z	9×100	0.8
ESO-LV 5340200	2	Gunn z	7×50	1.1

NOTE. The columns show the following: (2) observing run; (3) filter; (4) number and exposure time of the single exposures; (5) seeing FWHM of the combined image.

6.3.2 Reduction of the photometric data

All the images were reduced using standard MIDAS[2] routines. First, the images were bias subtracted and then they were corrected for pixel-to-pixel intensity variations by using a mean flat field for each night. The sky-background level was removed by fitting a second-order polynomial to the regions free of sources in the images. The different frames of each galaxy were rotated, shifted, and aligned to an accuracy of a few hundredth of a pixel using common field stars as reference. After checking that their point spread functions (PSFs) were comparable, the frames were combined to obtain a single image. The cosmic rays were identified and removed using a sigma-clipping rejection algorithm. Two-dimensional Gaussian fits to the field stars in the resulting images yielded the final FWHM measurement of seeing PSF listed in Table 6.3. Finally, the mean residual sky level was measured in each combined and sky-subtracted image, and the error on the sky subtraction was estimated. The median value of the residual sky level was determined in a large number of 5×5 pixel areas. These areas were selected in empty regions of the frames, which were free of objects and far from the galaxy to avoid the contamination of the light of field stars and galaxies as well as of the target galaxy itself. The mean of these median values was zero, as expected. For the error in the sky determination we adopted half of the difference between the maximum and minimum of the median values obtained for the sampled areas.

[2]MIDAS is developed and maintained by the European Southern Observatory.

TABLE 6.4— Log of spectroscopic observations of the kinematical template stars.

Star	Sp. Type	m_B (mag)	Run	Exp. Time (s)	σ (km s^{-1})
(1)	(2)	(3)	(4)	(5)	(6)
SAO 99192	G0	9.84	3	7	43
SAO 119387	K0	10.64	1	8	65
SAO 119458	G0	10.49	3	12	50
SAO 123779	K0	8.08	1	1	51
SAO 137138	G5	10.47	3	12	47
SAO 137330	G8	10.78	1	5	49

NOTE. The columns show the following: (2) observing run; (3) filter; (4) number and exposure time of the single exposures; (5) seeing FWHM of the combined image.

For each galaxy, we derived a 'luminosity growth curve' by measuring the integrated magnitudes within circular apertures of increasing radius by means of the IRAF[3] task ELLIPSE within the STSDAS package. Photometric calibration was performed by fitting this growth curve to that given in $R-$band for the same circular apertures by ESO-LV. The surface-brightness radial profiles of the sample galaxies are shown in Fig. 6.1. According to the color gradients measured by Beijersbergen et al. (1999) in a sample of bulge-dominated LSB galaxies, we estimated that the accuracy of the absolute calibration was better than 0.3 mag arcsec^{-2}. The $R-$band radial of ESO-LV 2060140 by Beijersbergen et al. (1999) was used to test the accuracy of our calibration (Fig. 6.2).

6.3.3 Reduction of the spectroscopic data

All the spectra were bias subtracted, flat-field corrected, cleaned of cosmic rays, corrected for bad columns, and wavelength calibrated using standard MIDAS routines.

The flat-field correction was performed by means of a quartz lamp, which were normalized and divided into all the spectra, to correct for pixel-to-pixel sensitivity variations and large-scale illumination patterns due to slit vignetting.

[3]IRAF is distributed by the National Optical Astronomy Observatories which are operated by the Association of Universities for Research in Astronomy under cooperative agreement with the National Science Foundation.

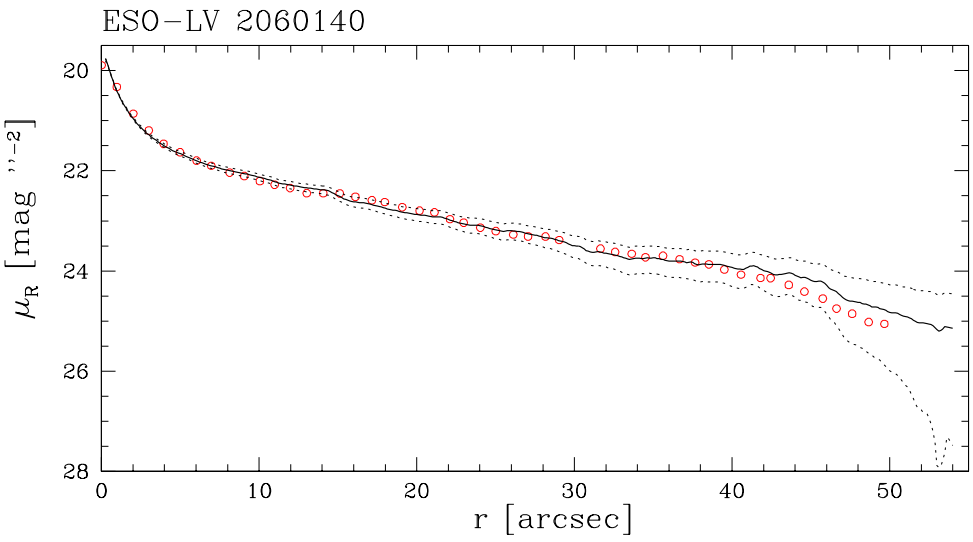

FIGURE 6.2— Comparison between the elliptically-averaged radial profiles of surface-brightness of ESO-LV 2060140 measured in this work (continuous line, with the $\pm 1\sigma$ confidence region indicated by the dotted lines) and by Beijersbergen (1999, circles).

TABLE 6.5— Photometric parameters of the bulge and disk in the sample galaxies.

Galaxy	μ_e (mag/arcsec^2)	r_e (arcsec)	n	q_b	PA$_b$ (°)	μ_0 (mag/arcsec^2)	h (arcsec)	q_d	PA$_d$ (°)	B/T
(1)	(2)	(3)	(4)	(5)	(6)	(7)	(8)	(9)	(10)	(11)
ESO-LV 1860550	21.16 ± 0.04	9.7 ± 0.3	2.16 ± 0.05	0.51 ± 0.01	126 ± 3	20.72 ± 0.03	12.5 ± 0.3	0.25 ± 0.01	111 ± 3	0.68
ESO-LV 2060140	22.27 ± 0.04	3.1 ± 0.1	1.64 ± 0.04	0.76 ± 0.02	18 ± 1	21.67 ± 0.03	17.9 ± 0.5	0.80 ± 0.02	4 ± 1	0.04
ESO-LV 2340130	20.62 ± 0.05	7.5 ± 0.3	1.40 ± 0.04	0.54 ± 0.01	72 ± 2	21.00 ± 0.04	12.7 ± 0.4	0.30 ± 0.01	77 ± 2	0.66
ESO-LV 4000370	22.36 ± 0.05	4.2 ± 0.2	0.59 ± 0.01	0.58 ± 0.01	107 ± 3	21.63 ± 0.04	22.5 ± 0.7	0.54 ± 0.01	140 ± 4	0.03
ESO-LV 4880490	23.48 ± 0.04	18.2 ± 0.6	1.43 ± 0.03	0.32 ± 0.01	83 ± 2	23.33 ± 0.03	36.6 ± 0.8	0.56 ± 0.01	88 ± 2	0.21
ESO-LV 5340200	20.44 ± 0.06	3.0 ± 0.6	1.96 ± 0.07	0.62 ± 0.01	10 ± 1	22.94 ± 0.05	15.2 ± 0.7	0.50 ± 0.02	178 ± 6	0.56

NOTE. The columns show the following: (2) effective surface-brightness of the bulge; (3) effective radius of the bulge; (4) shape parameter of the bulge; (5) axial ratio of the bulge isophotes; (6) position angle of the bulge major-axis; (7) central surface-brightness of the disk; (8) scale-length of the disk; (9) axial ratio of the disk isophotes; (10) position angle of the disk major-axis; (11) bulge-to-total luminosity ratio.

The cosmic rays were identified by comparing the photon counts in each pixel with the local mean and standard deviation and eliminated by interpolating over a suitable value. The residual cosmic rays were eliminated by manually editing the spectra.

The wavelength calibration was performed by means of the MIDAS package XLONG. Each spectrum was re-binned using the wavelength solution obtained from the corresponding arc-lamp spectrum. We checked that the wave-

length re-binning had been done properly by measuring the difference between the measured and predicted wavelengths of about 20 unblended arc-lamp lines which were distributed over the whole spectral range of a wavelength-calibrated spectrum. The resulting rms about the dispersion solution was 0.10 Å corresponding to an accuracy in the wavelength calibration of 6 km s^{-1} at 5280 Å. The instrumental resolution was derived as the mean of the Gaussian FWHMs measured for the same unblended arc-lamp lines we measured for assessing the accuracy of the wavelength calibration. The mean FWHM of the arc-lamp lines was 2.04 ± 0.08 Å, 2.11 ± 0.07 Å, and 2.10 ± 0.07 Å for run 1, 2, and 3, respectively. In run 1 the $1\farcs0$ wide slit was projected onto 6 pixels. In run 2 and 3 it was projected onto 4 pixels. Therefore, the sampling of the arc-lamp lines was lower than in run 1. Nevertheless, the FWHM values of the different runs are in agreement within the errors. They correspond to an instrumental velocity dispersion $\sigma_{\rm inst} = 50$ km s^{-1} at 5280 Å.

All the spectra were corrected for the misalignment between the CCD mosaic and slit following Bender et al. (1994). The spectra obtained for the same galaxy along the same axis were coadded using the center of the stellar continuum as a reference. This allowed us to improve the signal-to-noise ratio (S/N) of the resulting two-dimensional spectrum. The accuracy in the wavelength calibration and instrumental velocity dispersion as a function of position along the slit were derived from the brightest night-sky emission line in the observed spectral range of the coadded two-dimensional spectra of the galaxies. This was the [O I] λ5577.3 emission line. Its velocity curve and velocity dispersion profile were measured along the full slit extension as in Corsini et al. (1999). The central wavelength and FWHM of the night-sky line were evaluated fitting a Gaussian at each radius to the emission line and a straight line to its adjacent continuum. Then the values were converted to velocity and velocity dispersion, respectively. The velocity curve was fitted by a quadratic polynomial assuming the rms of the fit to be the 1σ velocity error. No velocity gradient was found and the fit rms was 5 km s^{-1}. The instrumental velocity dispersion derived from the FWHM of the [O I] λ5577.3 line increased from 46 km s^{-1} at the slit center to 53 km s^{-1} at the slit edges. Both the error on the wavelength calibration and instrumental velocity dispersion measured from the [O I] λ5577.3 line in the coadded spectra of the galaxies are consistent with those derived from the lamp lines in the arc spectra.

A one-dimensional spectrum was obtained for each kinematic template star as well as for each flux standard star. The spectra of the kinematic templates were de-redshifted to laboratory wavelengths. In the galaxy and stellar spectra the contribution of the sky was determined by interpolating along the outermost $60\farcs$ at the two edges of the slit, where the target light was negligible, and then

TABLE 6.6— Central surface-brightness of the LSB disks.

Galaxy	R_e (arcsec)	$B-R$ (mag)	$\mu^0_{0,B}$ (mag/arcsec^2)
(1)	(2)	(3)	(4)
ESO-LV 1860550	15	1.23	22.81
ESO-LV 2060140	26	1.14	23.08
ESO-LV 2340130	18	1.10	23.22
ESO-LV 4000370	28	0.97	23.08
ESO-LV 4880490	29	0.53	24.88
ESO-LV 5340200	11	0.88	24.22

NOTE. The columns show the following: (2) effective radius of the galaxy from ESO-LV; (3) mean color outside R_e from ESO-LV; (4) central blue surface-brightness of the disk corrected for inclination.

subtracted. The galaxy spectra always extended to less than 90″ from the center. A sky subtraction better than 1% of the sky level was achieved.

6.4 Two-dimensional photometric decomposition

The structural parameters of the sample galaxies were derived by applying a two-dimensional bulge-disk photometric decomposition to their images. To this aim the GASP2D algorithm (see chapter 2) was used.

The galaxy surface-brightness distribution was assumed to be the sum of the contributions of a bulge and a disk component. The Sérsic law (Sérsic 1968) was adopted to describe the surface-brightness of the bulge component. The bulge isophotes are ellipses centered on the galaxy center, with constant position angle PA_b and constant axial ratio q_b. The surface-brightness distribution of the disk component was assumed to follow an exponential law (Freeman 1970). The disk isophotes are ellipses with constant position angle PA_d and constant axial ratio q_d.

Since the fitting algorithm of GASP2D is based on a χ^2 minimization, it was important to adopt initial trials for free parameters as close as possible to their true values. To this aim the ellipse-averaged radial profiles of surface-brightness, ellipticity, and position angle were analyzed by following the prescriptions given in Chapter 2. For all the sample galaxies the ellipse-averaged profiles of surface-brightness are shown in Fig. 6.1.

Each image pixel has been weighted according to the variance of its total observed photon counts due to the contribution of both galaxy and sky, and

determined assuming photon noise limitation and taking the detector read-out noise into account. The seeing effects were taken into account by convolving the model image with a circular Gaussian PSF with the FWHM measured using the stars in the galaxy image (Table 6.3). The convolution was performed as a product in Fourier domain before the least-squares minimization.

The parameters derived for the structural components of the sample galaxies are collected in Table 6.5. No correction for galaxy inclination was applied. The result of the photometric decomposition of the surface-brightness distribution of the sample galaxies is shown in Fig. 6.1.

The formal errors obtained from the χ^2 minimization method are not representative of the real errors in the structural parameters (see Chapter 2). Therefore, the errors given in Table 6.5 were obtained through a series of Monte Carlo simulations. A set of 3000 images of galaxies with a Sérsic bulge and an exponential disk was generated. The structural parameters of the artificial galaxies were randomly chosen among the following ranges

$$0.5 \leq r_{\rm e} \leq 3 \text{ kpc} \qquad 0.5 \leq q_{\rm b} \leq 0.9 \qquad 0.5 \leq n \leq 6 \tag{6.1}$$

for the bulges, and

$$1 \leq h \leq 6 \text{ kpc} \qquad 0.5 \leq q_{\rm d} \leq 0.9 \tag{6.2}$$

for the disks. The artificial galaxies also satisfied the following conditions

$$q_d \leq q_b \qquad 11 \leq M_R \leq 16 \text{ mag.} \tag{6.3}$$

The simulated galaxies were assumed to be at a distance of 45 Mpc, which corresponds to a scale of 222 pc arcsec^{-1}. The adopted pixel scale, CCD gain, and read-out-noise were respectively 0.25 arcsec pixel^{-1}, 2.52 e$^-$ ADU^{-1}, and 3.87 e$^-$ to mimic the instrumental setup of the photometric observations. Finally, a background level and photon noise were added to the artificial images to yield a signal-to-noise ratio similar to that of the observed ones. The images of artificial galaxies were analyzed with GASP2D as if they were real. The errors on the fitted parameters were estimated by comparing the input $p_{\rm in}$ and measured $p_{\rm out}$ values. The artificial and observed galaxies were divided in bins of 0.5 magnitudes. The relative errors $1 - p_{\rm in}/p_{\rm out}$ on the parameters of the artificial galaxies were assumed to be normally distributed. In each magnitude bin the mean and standard deviation of relative errors of artificial galaxies were adopted as the systematic and typical errors for the observed galaxies.

The structural parameters of ESO-LV 2060140 were obtained from multiband photometry by Beijersbergen et al. (1999). They assumed the bulge

and disk to have both an exponential surface-brightness radial profile and a one-dimensional photometric decomposition was applied. The $R-$band bulge ($\mu_{0,\rm b} = 20.19$ mag arcsec^{-2}, $h_{\rm b} = 1.62$ arcsec) and disk parameters ($\mu_{0,\rm d} = 21.57$ mag arcsec^{-2}, $h_{\rm b} = 17.75$ arcsec) are in good agreement with those we derived (Table 6.5), although we adopted for the bulge a Sérsic profile with $n = 1.64$ ($\mu_{0,\rm b} = 20.35$ mag arcsec^{-2}, $h_{\rm b} = 0.52$ arcsec).

The six sample galaxies hosting a LSB disk were identified among the 10 originally selected galaxies, according to the structural parameters derived from the two-dimensional photometric decomposition (Tab. 6.5). The central surface-brightness of each disk was corrected for galaxy inclination (Tab. 6.1). The face-on $B-$band central surface-brightness of the disk was derived by adopting the mean $(B - R)$ color given by ESO-LV for radii larger than the galaxy effective radius in order to minimize the contamination due to the bulge light. All the bulges have a Sérsic index $n \lesssim 2$, and two of them (ESO-LV 2060140, ESO-LV 4000370) have an apparent flattening similar to that of the disk (Tab. 6.5). According to Kormendy & Kennicutt (2004), these disk-like features are the photometric signatures of pseudobulges.

6.5 Measuring stellar and ionized-gas kinematics

6.5.1 Stellar kinematics and central velocity dispersion

The stellar kinematics was measured from the galaxy absorption features present in the wavelength range between 5050 and 5550 Å, and centered on the Mg line triplet ($\lambda\lambda\, 5164, 5173, 5184$ Å) by applying the Fourier Correlation Quotient method (Bender 1990, FCQ) as done in Bender et al. (1994). The spectra were re-binned along the dispersion direction to a natural logarithmic scale, and along the spatial direction to obtain $S/N \geq 20$ per resolution element. In a few spectra the S/N decreases to 10 at the outermost radii. The galaxy continuum was removed row-by-row by fitting a fourth to sixth order polynomial as in Bender et al. (1994). The star SAO 137330 was adopted as kinematic template to measure the stellar kinematics of the sample galaxies for runs 1 and 2, and SAO 99192 for run 3. These stars were selected as having narrower auto-correlation functions (Table 6.4) and to minimize the mismatch with the galaxy spectra (Fig. 6.3).

For each galaxy spectrum the line-of-sight velocity distribution (LOSVD) was derived along the slit and its moments, namely the radial velocity $v_\star$, velocity dispersion $\sigma_\star$, and values of the coefficients h_3 and h_4 were measured. At each radius, they were derived by fitting the LOSVD with a Gaussian plus third- and fourth-order Gauss-Hermite polynomials H_3 and H_4, which describe the asymmetric and symmetric deviations of the LOSVD from a pure Gaussian

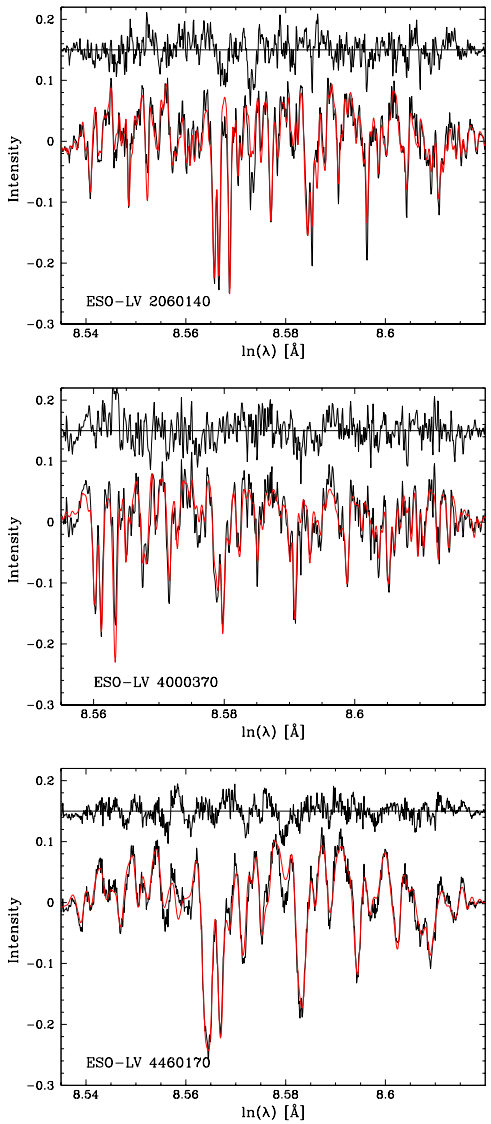

FIGURE 6.3— Examples of the central spectra (continous line) for three sample galaxies. They are compared with the template spectra (dotted line) convolved with their corresponding LOSVDs. The galaxy and template spectra have been continuum-subtracted and tapered at the ends with a cosine bell function. Residuals are plotted in the upper part of each panel and have false zero points for viewing convenience. ESO-LV 2060140 (upper panel) was observed in run 3 and fitted with SAO 99192. ESO-LV 4000370 (central panel) and ESO-LV 4460170 (see Sect. 6.6, lower panel) were observed in runs 2 and 1, respectively. They were fitted with SAO 137330.

profile (van der Marel & Franx 1993; Gerhard 1993). The errors on the LOSVD moments were derived from photon statistics and CCD read-out noise, calibrating them by Monte Carlo simulations as done by Gerhard et al. (1998). A large number of artificial spectra was generated for each measured set of LOSVD moments by first convolving the spectrum of the stellar template with the measured LOSVD and then adding different realizations of photon and read-out noises. The artificial spectra were analyzed with FCQ as if they were real. The errors on the fitted parameters were estimated by comparing the input $p_{\rm in}$ and measured $p_{\rm out}$ values. The relative errors $(1-p_{\rm in}/p_{\rm out})$ were assumed to be normally distributed, with mean and standard deviation corresponding to the systematic and typical error on the relevant parameter, respectively. These errors do not take into account possible systematic effects due to template mismatch or the presence of dust and/or faint emission.

The stellar velocity dispersion measured at large radii for many sample galaxies is comparable to the instrumental velocity dispersion ($\sigma_\star \simeq \sigma_{\rm inst} \approx 50$ km s^{-1}). The reliability of such measurements was assessed by means of a second series of Monte Carlo simulations. Artificial spectra were generated by convolving the spectrum of the stellar template with a LOSVD with $\sigma_\star = 20, 30, ..., 80, 100, 120$ km s^{-1}, $h_3 = 0$ and $h_4 = 0, -0.1$, or $h_3 = 0, -0.1$ and $h_4 = 0$ and adopting different values of $S/N = 10, 20, ..., 100$. The artificial spectra were measured with FCQ. Finally, the values of $\Delta h_3 = h_{3,\rm in} - h_{3,\rm out}$, $\Delta h_4 = h_{4,\rm in} - h_{4,\rm out}$ were computed. The correlation of $|\Delta h_3|$ and $|\Delta h_4|$ with $\sigma_\star$ and S/N is shown in Fig. 6.4. The measured values of h_3 and h_4 were considered unreliable when $|\Delta h_3| > 0.1$ and/or $|\Delta h_4| > 0.1$. For this range of $\sigma_\star$ and S/N, only $v_\star$ and $\sigma_\star$ were measured and it was assumed $h_3 = h_4 = 0$. Moreover, the stellar velocity dispersion was systematically underestimated for $\sigma_\star \leq 30$ km s^{-1}. This was found by measuring $\Delta\sigma_\star = \sigma_{\star,\rm in} - \sigma_{\star,\rm out}$ in artificial spectra with $|\Delta h_3| \leq 0.1$ and $|\Delta h_4| \leq 0.1$ (Fig. 6.5). Such a small value of $\sigma_\star$ is far below the velocity dispersions measured for the sample galaxies indicating that these measurements are genuine and are not strong affected by instrumental broadening. This is not the case of the small velocity dispersions ($\simeq 25$ km s^{-1}) measured for the faint foreground stars ($S/N \simeq 20$) which happened to fall into the slit when some of the galaxy spectra were obtained. These results are consistent with previous findings by Joseph et al. (2001) and Pinkney et al. (2003).

The measured stellar kinematics of all the sample galaxies is plotted in Fig. 6.6. The central velocity dispersion of the stellar component $\sigma_{\rm c}$ was derived by extrapolating the velocity dispersion radial profile to $r = 0''$. This was done by fitting the eight innermost data points with an empirical function. The best-fitting function was selected to be either exponential, or Gaussian, or constant.

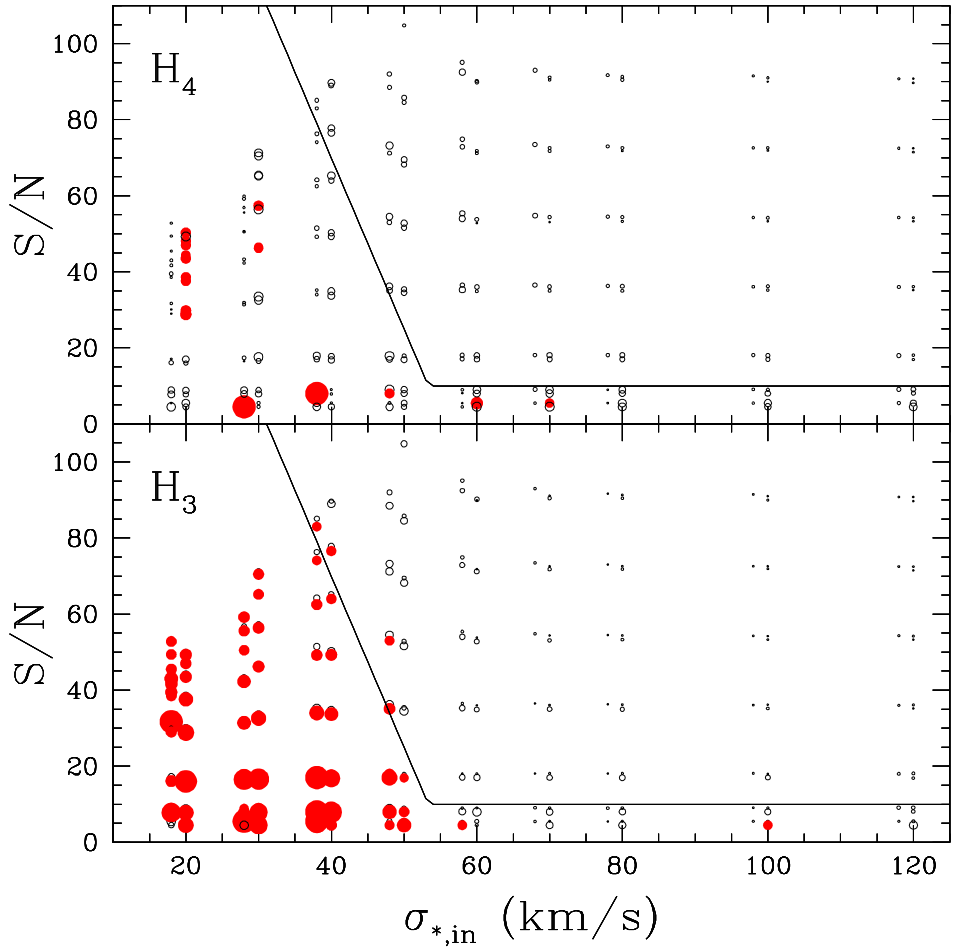

FIGURE 6.4— Reliability of the h_3 and h_4 measurements from Monte Carlo simulations. Upper panel: The value of $|\Delta h_4|$ obtained for $h_3 = 0$ as a function of $\sigma_{\star,\rm in}$ and S/N. The values obtained for $h_4 = 0$ are shifted from those obtained with $h_4 = -0.1$ for viewing convenience. Symbol size is proportional to the measured value. Open and filled symbols correspond to $|\Delta h_4|$ smaller and larger than 0.1, respectively. The minimum S/N ratios to obtain reliable measurements of h_4 for the different $\sigma_{\star,\rm in}$ are connected by a continuous line. Lower panel: As in the upper panel but for $|\Delta h_3|$.

No aperture correction was applied to $\sigma_{\rm c}$, as discussed by Baes et al. (2003) and Pizzella et al. (2004). The derived values for $\sigma_{\rm c}$ of our sample galaxies are given Table 6.1.

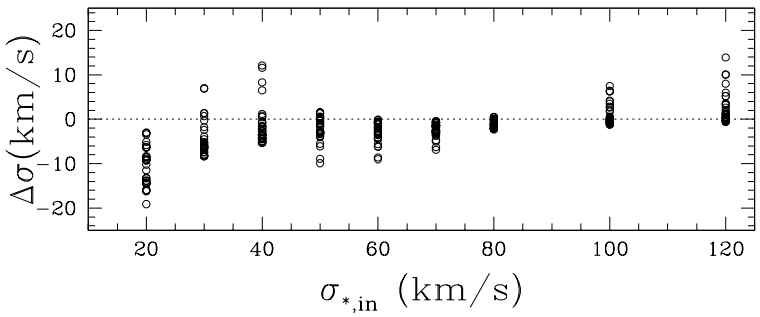

FIGURE 6.5— Reliability of $\sigma_\star$ measurements from Monte Carlo simulations. The values of $\Delta\sigma_\star$ is plotted as a function of $\sigma_\star$ only for the artificial spectra with reliable measurements of h_3 and h_4.

6.5.2 Ionized-gas kinematics, circular velocity, and minor-axis rotation

The ionized-gas kinematics was measured by the simultaneous Gaussian fit of the H_β and [O III]$\lambda\lambda 4959, 5007$ emission lines present in the galaxy spectra. The galaxy continuum was removed from the spectra as done for measuring the stellar kinematics. A Gaussian was fitted to each emission line, assuming they have the same line-of-sight velocity v_g, and velocity dispersion σ_g. An additional absorption Gaussian was considered in the fitting function to take into account the presence of the H_β absorption line. Far from the galaxy center, adjacent spectral rows were average to increase the signal-to-noise ratio ($S/N > 10$) of both the emission lines. The fitting routine developed by Pizella et al. (2004) is based on the MPFIT algorithm to perform the non-linear least-squares minimization in the IDL environment.

We checked for some galaxies that the error in the kinematic parameter determination derived by Monte Carlo simulations did not differ significantly from the formal errors given as output by the least-squares fitting routine. We therefore decided to assume the latter as the errors on the gas kinematics. For each galaxy we derived the heliocentric systemic velocity, $V_\odot$, as the velocity of the center of symmetry of the ionized-gas rotation curve (Table 6.1). The measured ionized-gas kinematics of all the sample galaxies are plotted in Fig. 6.6. The ionized-gas kinematics along the major-axis of some of the sample galaxies have been measured by other authors. A comparison with these data sets was performed to assess the accuracy and reliability of our measurements (Fig. 6.7).

The H_α rotation curves obtained for ESO-LV 2060140 (McGaugh et al.

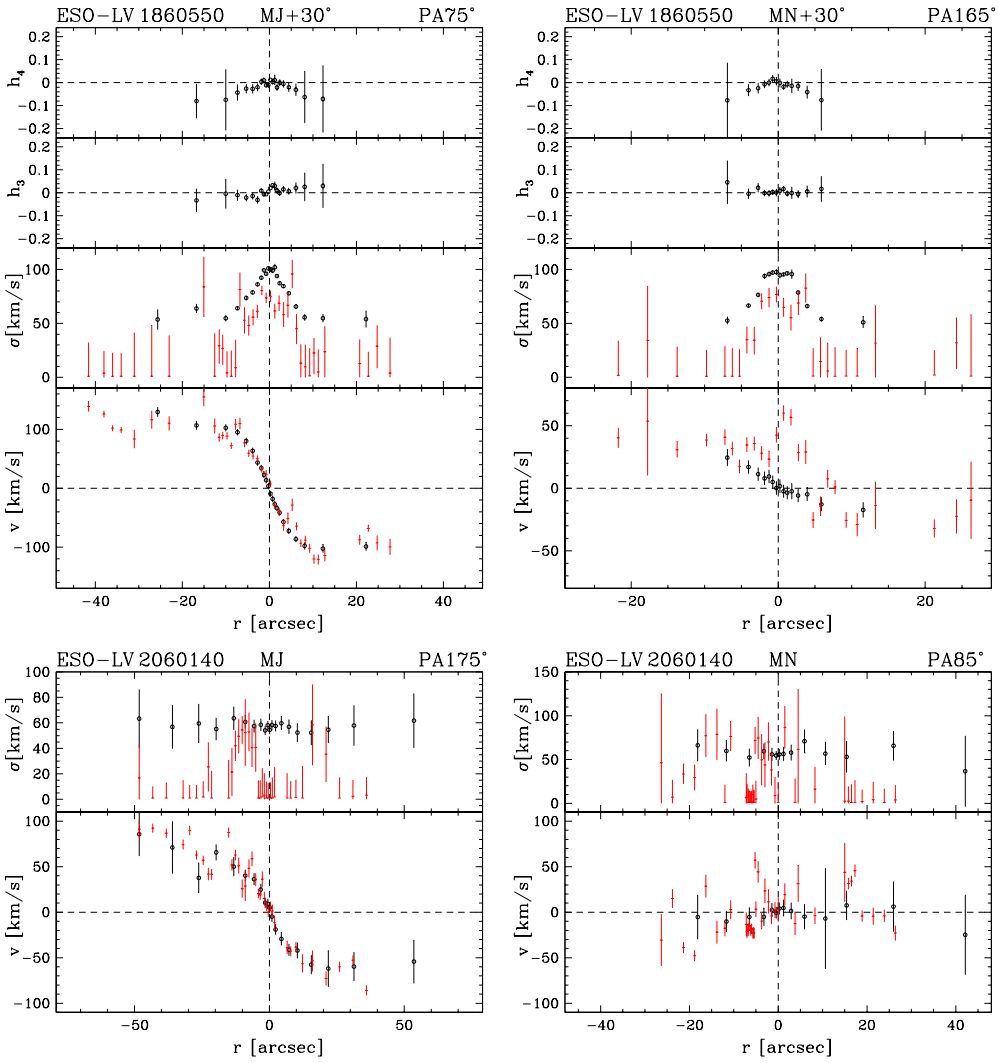

FIGURE 6.6— Kinematic parameters for stars (circles) and ionized-gas (crosses) measured along the observed axes of the sample galaxies. The radial profiles of the line-of-sight velocity (after the subtraction of systemic velocity and with no correction for inclination), velocity dispersion (corrected for instrumental velocity dispersion), third and fourth order coefficient of the Gauss-Hermite decomposition (when measured) of the stellar LOSVD are shown (from bottom to top). For each panel the galaxy name, location and position angle of the slit are given.

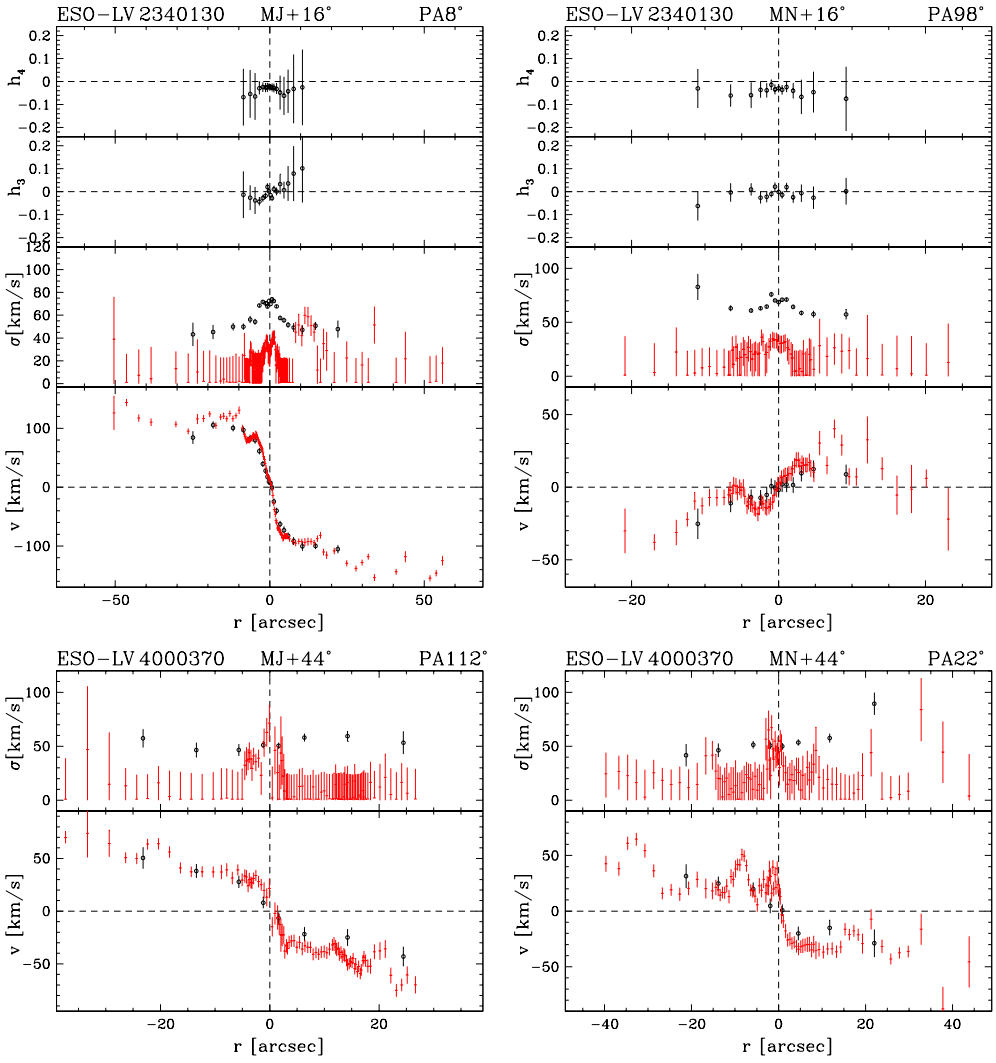

FIGURE 6.6— Continued

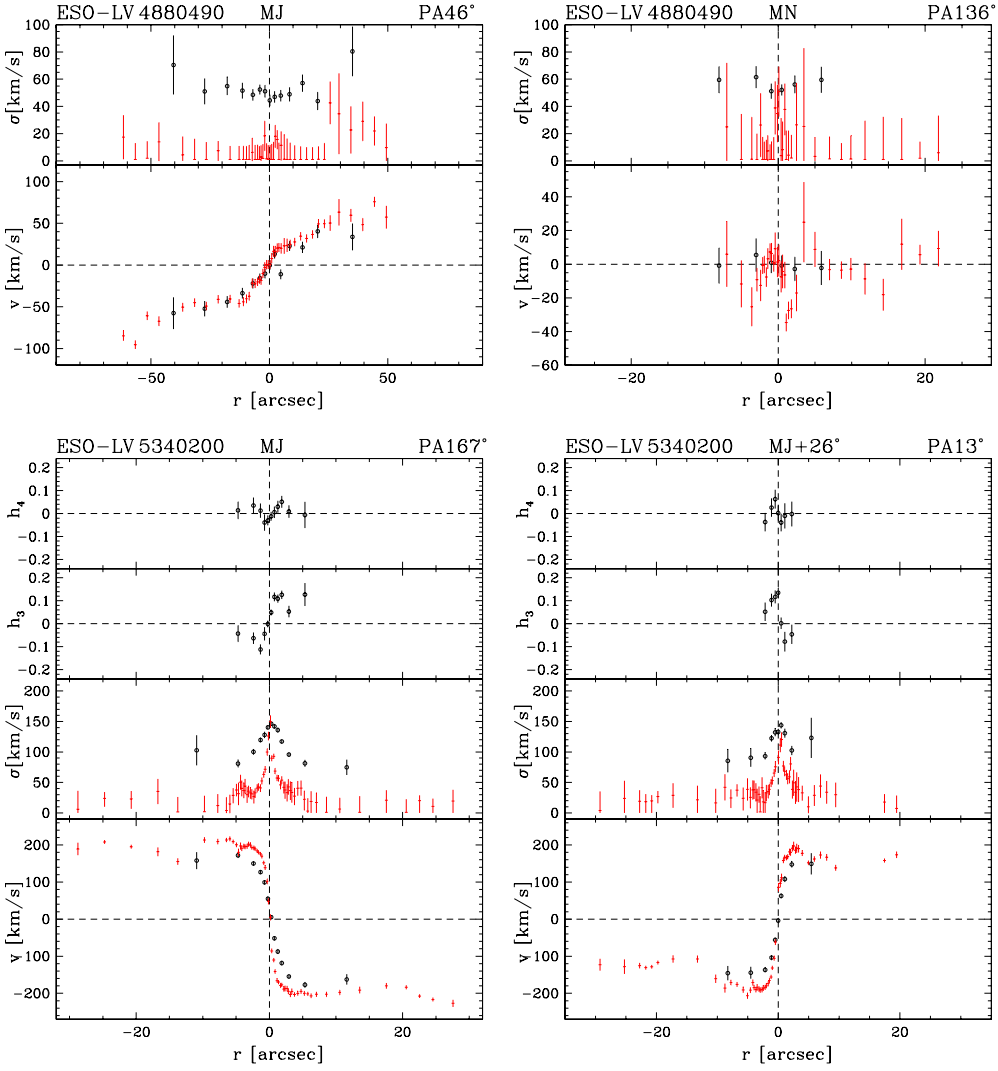

FIGURE 6.6— Continued

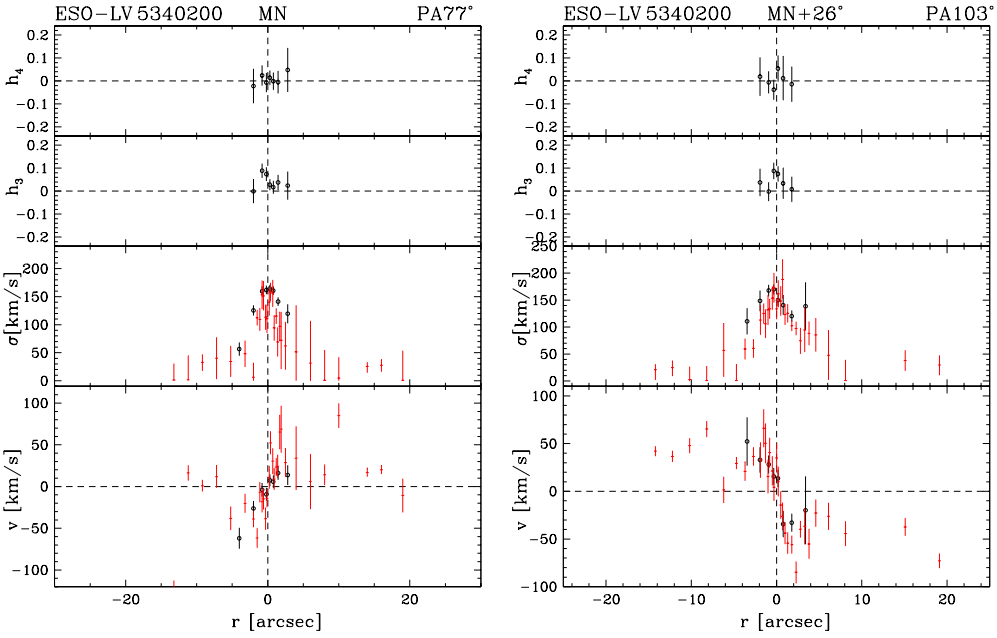

FIGURE 6.6— Continued

2001, Fig. 6.7a), ESO-LV 2340130 (Mathewson et al. 1992, Fig. 6.7b), ESO-LV 4880490 (McGaugh et al. 2001, Fig. 6.7c), and ESO-LV 5140100 (Mathewson et al. 1992, see Sect. 6.6, Fig. 6.7d), are in agreement within the errors with those measured by us after applying a small offset in their systemic velocities ($\Delta V \leq 30$ km s^{-1}). As a general comment, we can notice that our data are characterized by a finer spatial sampling. This allows to reveal kinematic details that were not evident in previous observations. The extension of the kinematic data are comparable. It has to be noted that our measurements are based on the H$_\beta$ and [O III] emission lines, while the data available in the literature are based on the H$_\alpha$ emission line.

For all the sample galaxies, the ionized-gas rotation curve measured along the major-axis (or along diagonal axis which was closer to the major-axis) was obtained by folding the observed line-of-sight velocities around the galaxy center and systemic velocity after averaging the contiguous data points. The curve was deprojected by taking into account the inclination of the disk (Table 6.1) and the misalignment between the observed axis and the position angle of the galaxy major-axis (Table 2). The galaxy circular velocity V_c was derived by averaging the outermost values of the flat portion of deprojected rotation curve.

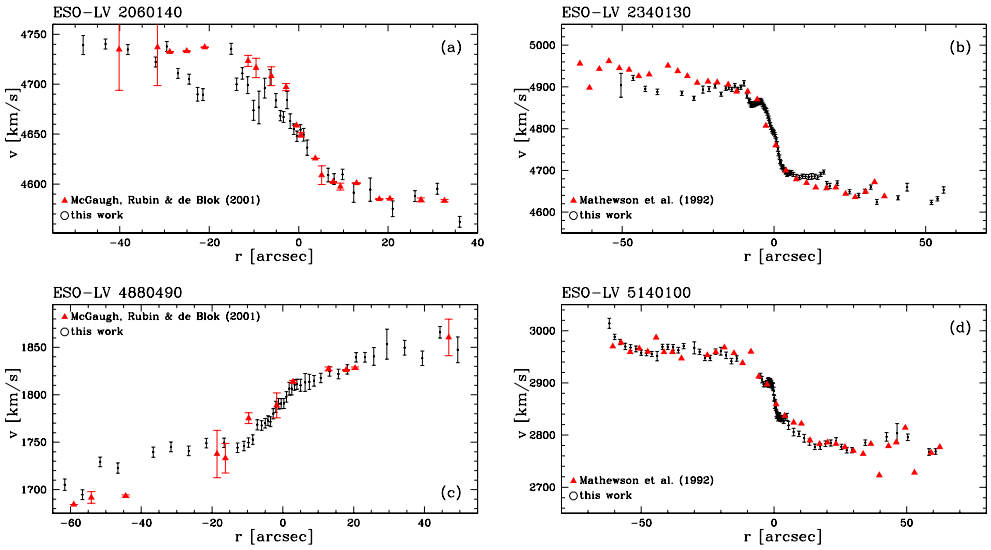

FIGURE 6.7— The line-of-sight velocities of the ionized gas derived in this study (circles) for ESO-LV 2060140, ESO-LV 2340130, ESO-LV 4880490, and ESO-LV 5140100 compared with those (triangles) obtained by Mathewson et al. (1992) and McGaugh et al. (2001).

The flatness of each rotation curve was checked by fitting it with a linear law, $V(R) = AR+B$ for $R \geq 0.35R_{25}$. The radial range was chosen in order to avoid the bulge-dominated region of the rotation curve as in Pizzella et al. (2004). The rotation curves with $|A| \geq 2$ km s^{-1} kpc^{-1} within 3σ were considered not to be flat. In this way the galaxies resulted as having a flat rotation curve. Their V_c are listed in Table 6.1.

For five out of six sample galaxies the ionized-gas kinematics were measured either along the minor-axis (ESO-LV 2060140, ESO-LV 4880490, and ESO-LV 5340200) or along a diagonal axis close to the minor one (by 30° and 16° for ESO-LV 1860550 and ESO-LV 2340130, respectively). The corresponding rotation curves are either irregular and asymmetric (ESO-LV 1860550, ESO-LV 2060140, ESO-LV 4880490) or characterized by a well-defined velocity gradient (ESO-LV 2340130, ESO-LV 5340200). Significant velocity values are not expected along the galaxy minor-axis if the gas is moving in circular orbits in a disk coplanar to the stellar one. The asymmetry of the rotation curve of ESO-LV 1860550 (PA = 165°) and the reversal of the velocities measured for ESO-LV 2340130 (PA = 98°) can not be attributed to the small misalignment (ΔPA = 30° and 16°) between the slit and the galaxy minor-axis. They are

TABLE 6.7— As in Tab. 6.3 but for the HSB galaxies.

Galaxy	Run	Filter	Single Exp. Time (s)	FWHM (arcsec)
(1)	(2)	(3)	(4)	(5)
ESO-LV 1890070	1	none	4×20	0.8
ESO-LV 4460170	1	none	4×20	1.4
ESO-LV 4500200	1	none	2×20	1.1
ESO-LV 5140100	1	none	4×20	1.1

suggestive of a more complex gas distribution. As a consequence, the ionized-gas velocity measured along the major-axis is not tracing the circular velocity in the inner regions of the galaxy. To address this issue properly it is crucial to map the entire velocity field of gas. This is the case of ESO-LV 1860550, ESO-LV 4000370, and ESO-LV 5340200. The two-dimensional velocity field of their gaseous component has been recently measured by Pizzella et al. (2008). They found the presence of non-ordered gas motions in ESO-LV 1860550, of a kinematically-decoupled component in ESO-LV 4000370, and of a misalignment between the photometric and kinematic major-axis of ESO-LV 5340200.

6.6 Notes on the HSB disks

ESO-LV 1890070, ESO-LV 4460170, ESO-LV 4500200, and ESO-LV 5140100 (Tab. 6.10) were originally selected according to the criteria given in Sect. 6.2. Their photometric (Tab. 6.7) and spectroscopic (Tab. 6.9) observations were carried out and data analyzed together with the sample galaxies, as discussed in the paper.

In spite of the selection criteria, ESO-LV 1890070, ESO-LV 4460170, ESO-LV 4500200, and ESO-LV 5140100 do not host a LSB disk, according to the structural parameters derived from the two-dimensional photometric decomposition (Tab. 6.8).

The central surface-brightness of the disks derived from ESO-LV photometry was overestimated with respect to that from the available CCD images (Tab. 6.11). This is due to the limited radial extension of ESO-LV data and to the shallow surface-brightness radial profile observed at the largest measured radii. The flattening of the light profile is actually due to the presence of a

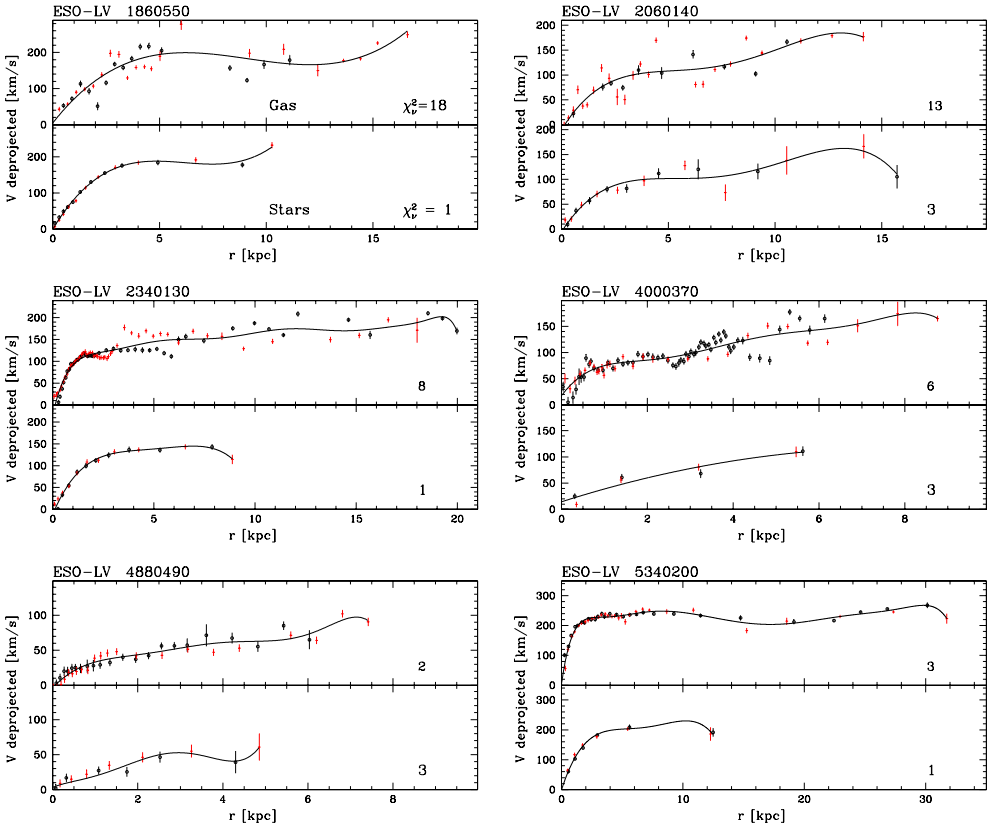

FIGURE 6.8— Ionized-gas and stellar rotation curves of the sample galaxies. The velocities of the ionized gas (upper panel) and stellar component (lower panel) are shown after being folded around the symmetry center and deprojected by taking into account the disk inclination and the misalignment between the observed axis and the galaxy major-axis. The reduced χ^2 of the data points with respect to the fitted polynomial is given in the lower right corner of each panel.

bar in ESO-LV 1890070, ESO-LV 4460170, and ESO-LV 4500200 (as found by subtracting the photometric model from the observed image of the galaxy), and by the downbending of the disk radial profile in ESO-LV 5140100 (Fig. 6.9).

The stellar and ionized-gas kinematics of the HSB galaxies is plotted in Fig. 6.10. These data allowed to derive the bulge velocity dispersion σ and disk circular velocity V_c (Tab. 6.10), which were used by Pizzella et al. (2005) to study the $V_c - \sigma_c$ relationship in HSB and LSB galaxies. The rotation curves of the ionized gas and stars are plotted in Fig. 6.11.

TABLE 6.8— As in Tab. 6.5 but for the HSB galaxies.

Galaxy	μ_e	r_e	n	q_b	PA_b	μ_0	h	q_d	PA_d	B/T
	(mag/arcsec^2)	(arcsec)			(°)	(mag/arcsec^2)	(arcsec)		(°)	
(1)	(2)	(3)	(4)	(5)	(6)	(7)	(8)	(9)	(10)	(11)
ESO-LV 1890070	19.24 ± 0.03	3.4 ± 0.1	0.99 ± 0.02	0.71 ± 0.01	178 ± 4	20.32 ± 0.03	31.1 ± 0.8	0.46 ± 0.01	3 ± 1	0.09
ESO-LV 4460170	18.97 ± 0.03	3.0 ± 0.1	1.23 ± 0.03	0.85 ± 0.02	177 ± 4	20.11 ± 0.03	19.4 ± 0.5	0.51 ± 0.01	1 ± 1	0.19
ESO-LV 4500200	18.01 ± 0.03	3.3 ± 0.1	1.79 ± 0.04	0.70 ± 0.01	179 ± 4	19.03 ± 0.03	17.3 ± 0.4	0.67 ± 0.01	4 ± 1	0.19
ESO-LV 5140100	20.19 ± 0.03	2.2 ± 0.1	0.93 ± 0.02	0.91 ± 0.02	171 ± 4	20.45 ± 0.03	27.1 ± 0.7	0.78 ± 0.02	175 ± 5	0.02

TABLE 6.9— As in Tab. 6.2 but for the HSB galaxies.

Galaxy	Run	Position	PA	Single Exp. Time	Tot. Exp. Time
			(°)	(s)	(h)
(1)	(2)	(3)	(4)	(5)	(6)
ESO-LV 1890070	1	MJ	18	3×2400	2.0
	1	MN	108	2×2900	1.6
ESO-LV 4460170	1	MJ	155	3×2400	2.0
	1	MN	65	2×3000	1.7
ESO-LV 4500200	1	MJ	154	3×2400	2.0
	1	MN	64	3×2400	2.0
ESO-LV 5140100	1	MJ	50	$3 \times 2520 + 2 \times 2400$	4.8
	1	MN	140	1×2400	0.7

TABLE 6.10— As in Tab. 6.1 but for the HSB galaxies. The inclination of ESO-LV 4460170 is from Palunas & Williams (2000).

Galaxy	Type	$V_\odot$	D	PA	i	R_{25}	M_R	σ_c	V_c	R_g/R_{25}	$R_\star/R_{25}$
		(km s^{-1})	(Mpc)	(°)	(°)	(arcsec)	(mag)	(km s^{-1})	(km s^{-1})		
(1)	(2)	(3)	(4)	(5)	(6)	(7)	(8)	(9)	(10)	(11)	(12)
ESO-LV 1890070	SABbc(rs)	2973	37.5	18	49	90	11.63	91.3 ± 2.0	185.9 ± 6.9	1.0	1.0
ESO-LV 4460170	(R)SBb(s)	4193	58.9	155	54	54	12.22	133.6 ± 2.0	196 ± 33	1.2	1.3
ESO-LV 4500200	SBbc(s):	2247	31.6	154	30	58	11.27	112.4 ± 2.4	245 ± 35	1.0	1.0
ESO-LV 5140100	SABc(s):	2857	40.4	50	36	50	11.62	60.2 ± 4.0	181 ± 15	0.8	1.2

All the galaxies show non-zero velocities for the ionized gas and stars along the minor axes. The minor-axis velocity gradients measured for ESO-LV 1890070, ESO-LV 4460170, and ESO-LV 4500200 can be explained as due to the non-circular motions induced by the bar. Moreover ESO-LV 1890070 and ESO-LV 5140100 host a dynamically cold component in their nucleus.

The $\sigma_\star$ radial profiles of ESO-LV 1890070 along both the major and minor-

TABLE 6.11— As in Tab. 6.6 but for the HSB galaxies.

Galaxy	$R_{\rm e}$ (arcsec)	$B-R$ (mag)	$\mu^0_{0,B}$ (mag/arcsec^2)
(1)	(2)	(3)	(4)
ESO-LV 1890070	48	0.89	21.67
ESO-LV 4460170	24	1.24	21.92
ESO-LV 4500200	23	1.68	20.87
ESO-LV 5140100	42	1.16	21.84

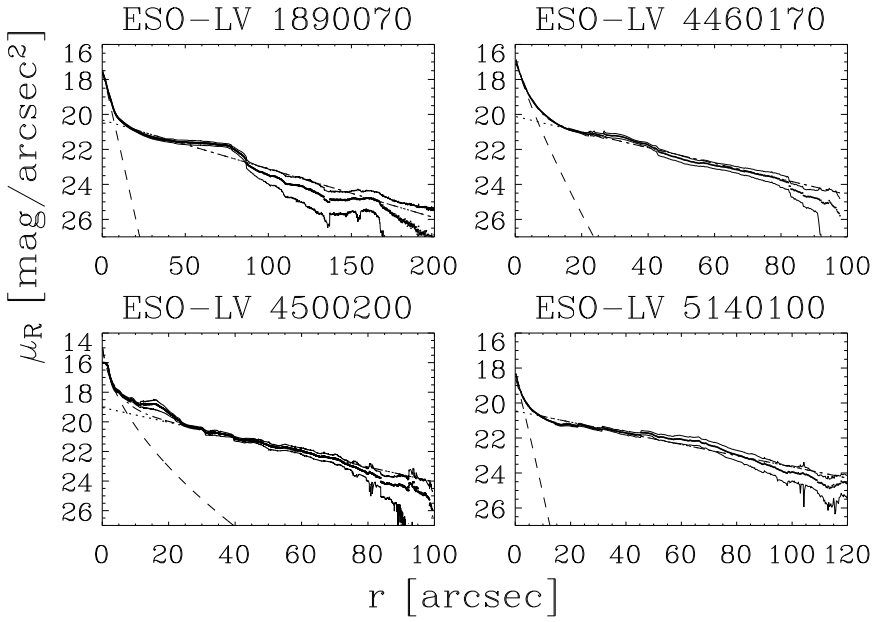

FIGURE 6.9— As in Fig. 6.1 but for the HSB galaxies.

axis are characterized by a central minimum. A similar phenomenon was observed by Emsellem et al. (2001) in a number of barred galaxies and interpreted as the signature of a nuclear stellar disk or bar. The presence of such a fast-rotating nuclear component in ESO-LV 1890070 is also supported by the steep stellar velocity gradient ($\sim 300\,{\rm km\ s^{-1}\ kpc^{-1}}$) measured along the galaxy major-axis. A central drop was observed in the $\sigma_\star$ radial profile of ESO-

LV 5140100 too. But this is an unbarred galaxy according to the results of the photometric decomposition. Therefore, the lower central value of $\sigma_\star$ has to be attributed to the small, low-luminosity, and exponential bulge of the galaxy.

6.7 Summary and Conclusions

We have presented and investigated the structural parameters and kinematic properties of 6 galaxies with LSB disks, for which we obtained deep photometric and spectroscopic VLT observations. Initially chosen following selection criteria similar to those of Beijersbergen et al. (1999) and using published photometric profiles, we subsequently confirmed the presence of a LSB disk in the majority of our sample galaxies by carrying out a careful two-dimensional photometric bulge-disk decomposition.

Our photometric analysis further revealed that our LSB galaxies have bulges that can are well described by a Sérsic profile with an index $n \lesssim 2$, with few of them displaying an apparent flattening rather similar to that of their surrounding disk. According to Kormendy & Kennicutt (2004), these disk-like features are the photometric signature of a pseudobulge.

We obtained spectroscopic observations along the major and minor-axis in half of our sample galaxies (ESO-LV 2060140, ESO-LV 4880490 and ESO-LV 5340200), while we observed the other half along two diagonal axes. Spectra along two diagonal directions were obtained also for ESO-LV 5340200. In all targets, the depth of our data allowed us to measure the stellar and ionized-gas kinematics out to a surface-brightness level $\mu_R \approx 24$ mag arcsec^{-2}, comfortably reaching the outer disk regions where the rotation curve flattens.

We derived central values for the stellar velocity dispersion of $\sigma_{\rm c}$ and measured the circular velocity in the outskirts of our sample galaxy $V_{\rm c}$ by following the flat portion of the gas rotation curve. Ferrarese (2002) found a correlation between $\sigma_{\rm c}$ and $V_{\rm c}$ and interpreted it as evidence for a connection between the mass of the central supermassive black hole and that of the DM halo (Baes et al. 2003; Buyle et al. 2006). Using the σ_c and $V_{\rm c}$ measurements presented in this paper, Pizzella et al. (2005) found that galaxies hosting LSB disks follow a different $V_{\rm c} - \sigma_{\rm c}$ relation from their HSB counterparts. In fact, they show either higher $V_{\rm c}$ or lower $\sigma_{\rm c}$. This behavior has been recently explained by Courteau et al. (2007) and Ho (2007) in terms of morphology or, equivalently, total light concentration. They claim that the actual relation does not depend only on two parameters $V_{\rm c}$ and $\sigma_{\rm c}$ but also on a third variable which is the light concentration.

We have shown that the vast majority of our sample galaxies show non-zero gas velocities along or close to their minor axes. Significant velocities

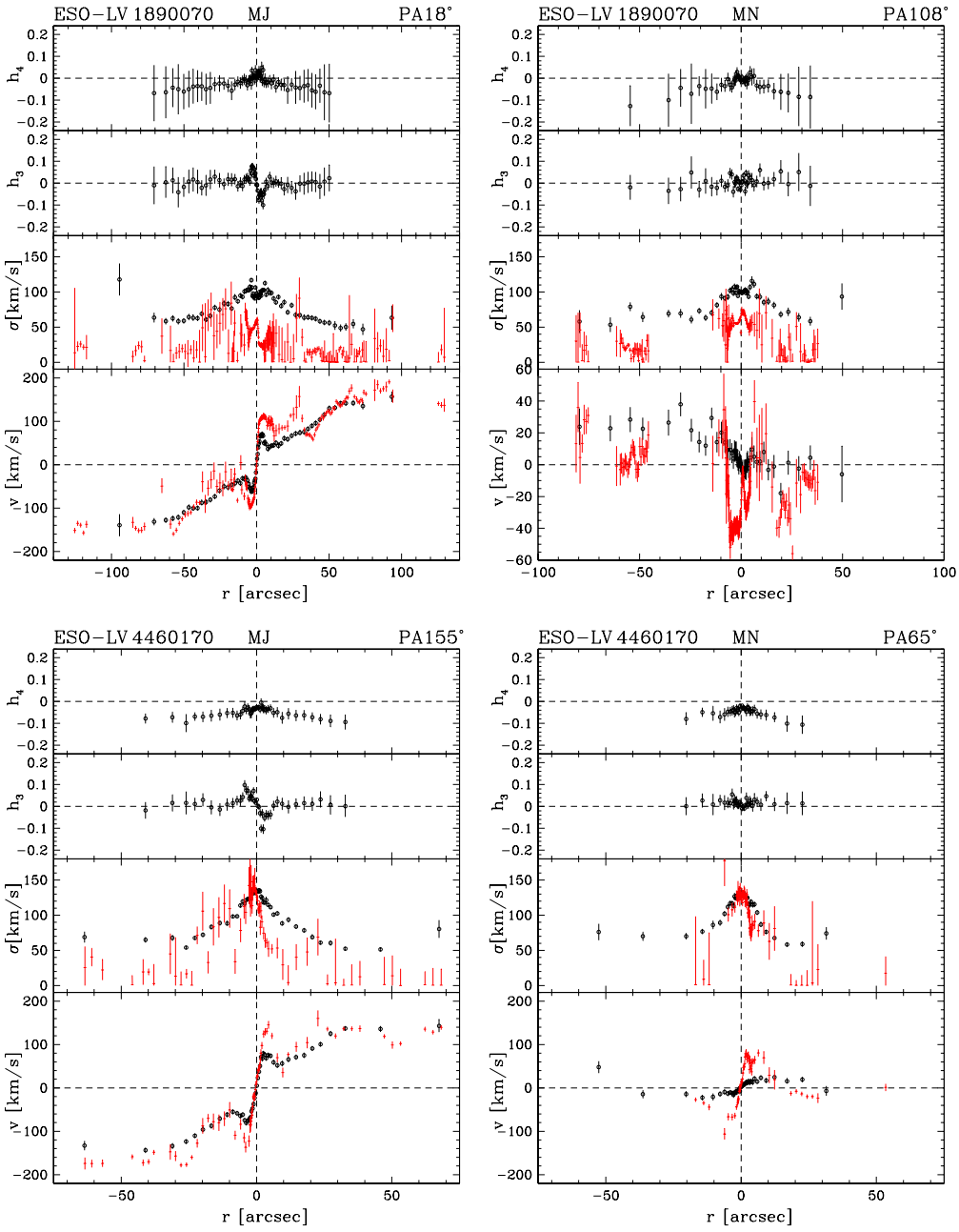

FIGURE 6.10— As in Fig. 6.6 but for the HSB galaxies.

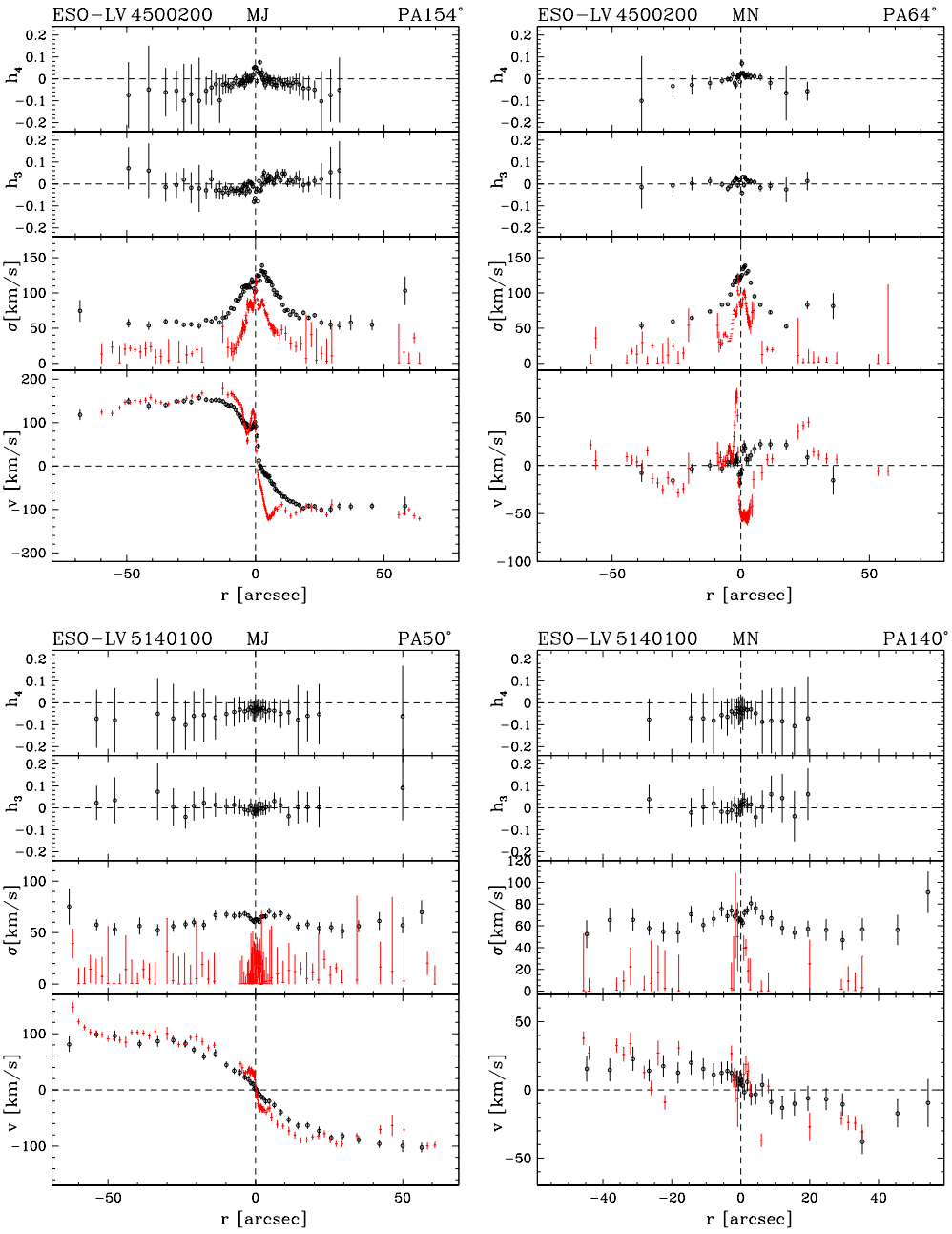

FIGURE 6.10— Continued

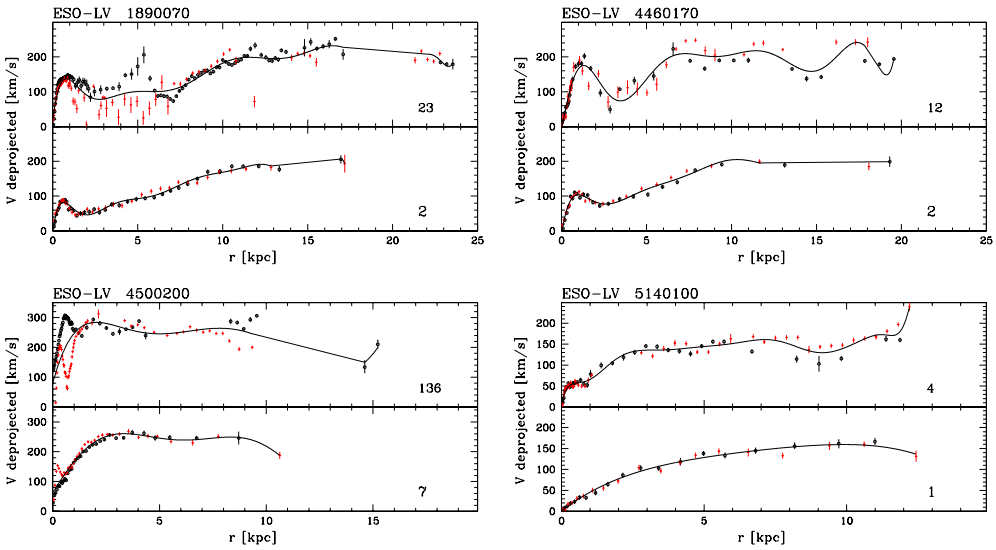

FIGURE 6.11— As in Fig. 6.8 but for the HSB galaxies.

are not expected along the galaxy minor-axis if the gas is moving in circular orbits in a disk coplanar to the stellar one. They can be explained as due to non-ordered motions or by invoking a warp and/or non-circular motions of the gaseous component. As a consequence, the ionized-gas velocity measured along the major-axis is not tracing the circular velocity in the inner regions of the galaxy.

Deviations from perfect circular gas motions are by no means limited to the minor-axis direction in our sample galaxies. Along the major-axis of our targets (or the closest diagonal direction) the ionized-gas velocity curve is characterized by a higher degree of asymmetry and irregularity with respect to the stellar rotation curve. As a consequence, to derive the gas rotation curve it is often necessary to smooth the data over large radial bins before folding the gas velocities around the center of symmetry. This is not the case for the stars, since their measured velocities fold quite well and do not show sharp wiggles and bumps. The rotation curves of the ionized gas and stars are plotted in Fig.6.8 for all the sample galaxies. Data were folded around the center of symmetry and deprojected taking into account the inclination of the disk (Table 6.1) and the misalignment between the observed axis and the position angle of the galaxy major-axis (Table 2). To asses the degree of symmetry and regularity of the stellar and gaseous rotation curves we fitted them with low-order

polynomial functions, using the reduced χ^2 of each fit as a gauge of the level of fluctuations and asymmetries of the stellar and ionized-gas kinematics. The reduced-χ^2 values corresponding to each rotation curve are given in Fig. 6.8. Invariably, the reduced-χ^2 values of the fit to the ionized-gas rotation curves exceed the reduced-χ^2 values derived in the case of the stellar curves, except for ESO-LV 4880490 where the gas reduced-χ^2 is slightly smaller than its stellar counterpart. The average reduced χ^2 of the rotation curves of gas and stars are 8.3 ± 1.0 km s^{-1} and 2.0 ± 0.2 km s^{-1}, respectively. Globally the gas rotation curves of the sample galaxies are more asymmetric, irregular, and affected by scatter than the corresponding stellar ones. The presence of more disturbed gas motions and a regular stellar kinematics is particularly clear in ESO-LV 1860550 and ESO-LV 2340130. Nevertheless, locally both gas and stellar rotation can both appear pretty smooth, in particular toward the center (e.g., ESO-LV 2340130 and ESO-LV 5340200). On the other hand, the most obvious scatter of the gas data points at larger radii is intrinsic and neither due to low S/N nor to the underlying H_β absorption line, since this is observed only at small radii (where the kinematics is constrained also by [O III] emission doublet).

While it is easy to spot non-circular, off-plane and non-ordered velocities along the minor-axis, their presence along major-axis may remain undetected. This can affect the correct estimate of the central velocity gradient, posing severe limitations to the use of the ionized gas as the tracer of the circular velocity to derive the mass content and distribution in the central region of galaxies. To address this issue, it is crucial to measure the kinematics along different axes and ideally to have integral-field data. The two-dimensional velocity field of the ionized gas in LSB galaxies has been mapped only recently by means of integral-field spectroscopy (Kuzio de Naray et al. 2006; Coccato et al. 2008; Pizzella et al. 2008). Pizzella et al. (2008) reported the detection in ESO-LV 1890070 and ESO-LV 4000370 of strong non-ordered motions of the ionized gas, which prevent to disentangle between core and cuspy radial profiles of the DM mass density.

The main conclusion of this work is that the stellar kinematics of galaxies with LSB disks is less affected than the ionized-gas kinematics one by large-scale asymmetries and small-scale irregularities. The gas velocities have been found to deviate from the from the circular velocity in particular and more often in the inner regions of our sample galaxies. Unless the regularity of the ionized-gas motions can be established with integral-field data, our findings strongly suggest that stars are more suitable to trace the mass distribution of galaxies with a LSB disk, in particular when the inner slope of the DM halo is

the central question that one wishes to answer.

Building a complete dynamical model to address the question of the mass distribution of our sample galaxies is beyond the scope of this thesis, and will be presented in a companion work Magorrian et al. (2008).

Bibliography

Baes, M., Buyle, P., Hau, G. K. T., & Dejonghe, H. 2003, MNRAS, 341, L44
Beijersbergen, M., de Blok, W. J. G., & van der Hulst, J. M. 1999, A&A, 351, 903
Bender, R. 1990, A&A, 229, 441
Bender, R., Saglia, R. P., & Gerhard, O. E. 1994, MNRAS, 269, 785
Berman, S. 2001, A&A, 371, 476
Bertola, F., Cinzano, P., Corsini, E. M., Rix, H., & Zeilinger, W. W. 1995, ApJ, 448, L13
Bolatto, A. D., Simon, J. D., Leroy, A., & Blitz, L. 2002, ApJ, 565, 238
Bothun, G. D., Impey, C. D., Malin, D. F., & Mould, J. R. 1987, AJ, 94, 23
Buyle, P., Ferrarese, L., Gentile, G., et al. 2006, MNRAS, 373, 700
Christlein, D., & Zaritsky, D. 2008, Formation and Evolution of Disk Galaxies, ed. J. G. Funes & E. M. Corsini (ASP, San Francisco), in press
Cinzano, P., Rix, H.-W., Sarzi, M., et al. 1999, MNRAS, 307, 433
Coccato, L., Swaters, R., Rubin, V. C., D'Odorico, S., & McGaugh, S. 2008, Formation and Evolution of Galaxies, ed. J. G. Funes & E. M. Corsini (ASP, San Francisco), in press, (arXiv:0711.4466)
Corsini, E. M., Pizzella, A., Sarzi, M., et al. 1999, A&A, 342, 671
Corsini, E. M., Pizzella, A., Coccato, L., & Bertola, F. 2003, A&A, 408, 873
Courteau, S., McDonald, M., Widrow, L. M., & Holtzman, J. 2007, ApJ, 655, L21
de Blok, W. J. G., & Bosma, A. 2002, A&A, 385, 816
de Blok, W. J. G., McGaugh, S. S., Bosma, A., & Rubin, V. C. 2001, ApJ, 552, L23
de Vaucouleurs, G., de Vaucouleurs, A., Corwin, H. G., et al. 1991, Third Reference Catalogue of Bright Galaxies (Springer-Verlag, New York) (RC3)
Emsellem, E., Greusard, D., Combes, F., et al. 2001, A&A, 368, 52
Ferrarese, L. 2002, ApJ, 578, 90
Fillmore, J. A., Boroson, T. A., & Dressler, A. 1986, ApJ, 302, 208
Fixsen, D. J., Cheng, E. S., Cottingham, D. A., et al. 1996, ApJ, 470, 63
Freeman, K. C. 1970, ApJ, 160, 811
Gerhard, O. E. 1993, MNRAS, 265, 213
Gerhard, O. E., Vietri, M., & Kent, S. M. 1989, ApJ, 345, L33
Gerhard, O., Jeske, G., Saglia, R. P., & Bender, R. 1998, MNRAS, 295, 197
Guthrie, B. N. G. 1992, A&AS, 93, 255
Hayashi, E., & Navarro, J. F. 2006, MNRAS, 373, 1117
Ho, L. C. 2007, ApJ, 668, 94
Impey, C. D., Sprayberry, D., Irwin, M. J., & Bothun, G. D. 1996, ApJS, 105, 209
Joseph, C. L., Merritt, D., Olling, R., et al. 2001, ApJ, 550, 668
Kormendy, J., & Kennicutt, R. C. 2004, ARA&A, 42, 603
Kormendy, J., & Westpfahl, D. J. 1989, ApJ, 338, 752
Kuzio de Naray, R., McGaugh, S. S., de Blok, W. J. G., & Bosma, A. 2006, ApJS, 165, 461

Lauberts, A., & Valentijn, E. A. 1989, The Surface Photometry Catalogue of the ESO-Uppsala Galaxies (European Southern Observatory, Garching)
Magorrian, J., Sarzi, M., Corsini, E. M., et al. 2008, MNRAS, in preparation
Mathewson, D. S., Ford, V. L., & Buchhorn, M. 1992, ApJS, 81, 413
McGaugh, S. S., & Bothun, G. D. 1994, AJ, 107, 530
McGaugh, S. S., Rubin, V. C., & de Blok, W. J. G. 2001, AJ, 122, 2381
Moore, B., Governato, F., Quinn, T., Stadel, J., & Lake, G. 1998, ApJ, 499, L5
Moore, B., Quinn, T., Governato, F., Stadel, J., & Lake, G. 1999, MNRAS, 310, 1147
Moré, J. J., Garbow, B. S., & Hillstrom, K. E. 1980, User guide for MINPACK-1.Argonne National Laboratory Report ANL-80-74
Navarro, J. F., Frenk, C. S., & White, S. D. M. 1996, ApJ, 462, 563
Navarro, J. F., Frenk, C. S., & White, S. D. M. 1997, ApJ, 490, 493
Palunas, P., & Williams, T. B. 2000, AJ, 120, 2884
Pignatelli, E., Corsini, E. M., Vega Beltrán, et al. 2001, MNRAS, 323, 188
Pinkney, J., Gebhardt, K., Bender, R., et al. 2003, ApJ, 596, 903
Pizzella, A., Corsini, E. M., Vega Beltrán, J. C., & Bertola, F. 2004, A&A, 424, 447
Pizzella, A., Corsini, E. M., Dalla Bontà, et al. 2005, ApJ, 631, 785
Pizzella, A., Tamburro, D., Corsini, E. M., & Bertola, F. 2008, A&A, 482, 53
Press, W. H., Teukolsky, S. A., Vetterling, W. T., & Flannery, B. P. 1992, Numerical Recipes in FORTRAN. The Art of Scientific Computing, 2nd edn (Cambridge Univ. Press, Cambridge)
Rhee, G., Valenzuela, O., Klypin, A., Holtzman, J., & Moorthy, B. 2004, ApJ, 617, 1059
Romanishin, W., Strom, K. M., & Strom, S. E. 1983, ApJS, 53, 105
Schombert, J. M., & Bothun, G. D. 1988, AJ, 95, 1389
Schombert, J. M., Bothun, G. D., Schneider, S. E., & McGaugh, S. S. 1992, AJ, 103, 1107
Sérsic, J. L. 1968, Atlas de galaxias australes (Observatorio Astronómico, Cordoba)
Simon, J. D., Bolatto, A. D., Leroy, A., & Blitz, L. 2003, ApJ, 596, 957
Sprayberry, D., Bernstein, G. M., Impey, C. D., & Bothun, G. D. 1995, ApJ, 438, 72
Swaters, R. A., Madore, B. F., & Trewhella, M. 2000, ApJ, 531, L107
Swaters, R. A., Madore, B. F., van den Bosch, F. C., & Balcells, M. 2003, ApJ, 583, 732
Swaters, R. A., Verheijen, M. A. W., Bershady, M. A., & Andersen, D. R. 2003, ApJ, 587, L19
Swaters, R. A., Verheijen, M. A. W., Bershady, M. A., & Andersen, D. R. 2004,Dark Matter in Galaxies, ed. Ryder, S., Pisano, D., Walker, M., Freeman, K. (ASP, San Francisco), p. 77
van den Bosch, F. C., & Swaters, R. A. 2001, MNRAS, 325, 1017
van den Bosch, F. C., Robertson, B. E., Dalcanton, J. J., & de Blok, W. J. G. 2000, AJ, 119, 1579
van der Marel, R. P., & Franx, M. 1993, ApJ, 407, 525
Zwaan, M. A., van der Hulst, J. M., de Blok, W. J. G., & McGaugh, S. S. 1995, MNRAS, 273, L35

7

Properties of bars in the local universe

Based on J. A. L. Aguerri, J. Méndez-Abreu and E. M. Corsini, 2008, A&A, submitted

Bars are common structures in the disks of spiral galaxies. Their presence may strongly determine the evolution of the galactic disk exchanging angular momentum between the disk and the dark matter halo. Large galaxy surveys such as the Sloan Digital Sky Survey (SDSS) provide the opportunity of study the bar properties in large galaxy samples. The fraction of barred disk galaxies and their properties was studied in a sample of ~ 3000 galaxies from SDSS fifth data release (SDSS-DR5). This represents a volume limited sample with all galaxies located in the redshift range $0.01 < z < 0.04$, brighter than $M_{\rm r} = -20$, and with i <60°. Galaxies with signs of interactions were excluded from the sample. The bar fraction was determined by two methods: ellipse fitting and Fourier analysis. Both methods were tested and calibrated with extensive simulations of barred and non-barred galaxies similar to the observed ones. The fraction of barred galaxies in our sample turned out to be 45%. We split the sample into different morphological types, finding that 32% of S0s, 55% of early-type spirals, and 52% of late-type spirals, are barred galaxies. Bars in S0 galaxies were weaker than those in the galaxies of later morphological types. We also found a correlation between the bar length and galaxy size, larger bars being located in larger galaxies. Neither the bar strength nor the bar length correlates with the local galaxy density, indicating that local environment does not play an important role in bar formation and evolution. In contrast, internal galaxy properties (such as the central light concentration) determine bar properties.

Thus, galaxies with high central light concentrations (i.e., the S0 galaxies) have fewer and weaker bars than late-type ones.

7.1 Introduction

Strong bars are observed in optical images of roughly half of all the nearby disk galaxies (Marinova & Jogee 2007; Barazza et al. 2008). This fraction rises to about 70% when near-infrared images are analyzed (Knapen et al. 2000; Eskridge et al. 2000; Menéndez-Delmestre et al. 2007). The presence of a bar is found by visual inspection (e.g., de Vaucouleurs et al. 1991, RC3), by analyzing the shape and orientation of the galaxy isophotes (e.g., Wozniak et al. 1995; Knapen et al. 2000; Laine et al. 2002; Sheth et al. 2003; Elmegreen et al. 2004; Marinova & Jogee 2007; Barazza et al. 2008), by studying the Fourier modes of the light distribution (e.g., Elmegreen & Elmegreen 1985; Ohta et al. 1990; Aguerri et al. 2000; Buta et al. 2006; Laurikainen et al. 2007), and by performing the photometric decomposition of the galaxy surface-brightness distribution (e.g., Prieto et al. 2001, Aguerri et al. 2005; Laurikainen et al. 2005) Bars are clearly a common feature in the central regions of the galaxies of the local universe. But, this is also true at high redshift. In fact, the bar fraction apparently remains constant out to $z \approx 1$ (Jogee et al. 2004; Elmegreen et al. 2004; Barazza et al. 2008), although there are some claims that this is not the case (Sheth et al. 2008).

The presence of bars in the centers of disk galaxies make them ideal probes of the dynamics of the central regions and dark matter content. In fact, bars are efficient agents of angular momentum, energy, and mass redistribution. They act on both luminous and dark matter components (Weinberg 1985; Debattista & Sellwood 1998; Debattista & Sellwood 2000; Athanassoula 2003) driving the evolution of galaxy structure and morphology. In particular, the amount of angular momentum exchanged is related to specific properties of the galaxies, such as the bar mass, halo density and halo velocity dispersion (Sellwood 2006; Sellwood & Debattista 2006) Moreover, they funnel material towards the galaxy center building bulge-like structures (e.g., Kormendy & Kennicutt 2004), nuclear star-forming rings (e.g., Buta et al. 2003), and nuclear bars (e.g., Erwin 2004), and feeding the central black hole (e.g., Shlosman et al. 2000).

The most important parameters of bars are the length, strength, and pattern speed. Their evolution depends on the effectiveness of the angular momentum exchange between luminous and dark matter. Different methods have been proposed to measure bar properties.

The bar length is obtained by eye estimates on galaxy images (Kormendy 1979; Martin 1995), locating the maximum ellipticity of the galaxy isophotes

(Wozniak et al. 1995; Laine et al. 2002; Marinova & Jogee 2007), looking for variations of the isophotal position angle (Sheth et al. 2003; Erwin 2005) or of the phase angle of the Fourier modes of the galaxy light distribution (Quillen et al. 1994; Aguerri et al. 2003), analyzing the bar-interbar contrast (Aguerri et al. 2000; Aguerri et al. 2003), or by photometric decomposition of the surface-brightness distribution (Prieto et al. 1997; Aguerri et al. 2005; Laurikainen et al. 2005). The bar length is correlated with the disk scale, suggesting that the two components are affecting each other (Marinova & Jogee 2007; Laurikainen et al. 2007).

The bar strength is derived by measuring the bar torques (Buta & Block 2001), isophotal ellipticity (Martinet & Friedli 1997; Aguerri 1999; Whyte et al. 2002; Marinova & Jogee 2007), the maximum amplitude of the $m = 2$ Fourier mode (Athanassoula & Misiriotis 2002; Laurikainen et al. 2005), or integrating the $m = 2$ Fourier mode in the bar region (Ohta et al. 1990; Aguerri et al. 2000). The bar strength is almost constant with Hubble type (Marinova & Jogee 2007), but lenticular galaxies host weaker bars than spirals (Laurikainen et al. 2007).

The pattern speed of bars is indirectly estimated by identifying rings with the location of the Lindblad resonances (e.g., Vega Beltrán et al. 1997; Jeong et al. 2007), matching the observed velocity and density fields with numerical models of the gas flows (e.g., Lindblad 1996; Aguerri et al. 2001; Weiner et al. 2001), analyzing the offset and shape of the dust lanes, which trace the location of shocks in the gas flows (Athanassoula 1992), looking for color changes (Aguerri et al. 2000) and minima in the star formation (Cepa & Beckman 1990) outside the bar region, or by adopting the Tremaine-Weinberg method (see Corsini 2007, for a review). This is a model-independent way to measure pattern speed (Tremaine & Weinberg 1984), which has been successfully applied to double (Corsini et al. 2003) and dwarf barred galaxies (Corsini 2007), too. Observed pattern speeds imply that barred galaxies host maximal disks (Debattista & Sellwood 1998; Debattista & Sellwood 2000), since bars in dense dark matter halos are rapidly decelerated by dynamical friction (Weinberg 1985; Sellwood 2006; Sellwood & Debattista 2006).

Nowadays, the large galaxy surveys, such as the Sloan Digital Sky Survey (York et al. 2000, SDSS) or the 2 Micron All Sky Survey (Skrutskie et al. 2006, 2MASS) allow us to study bar parameters in samples of thousands of barred galaxies. It is now possible to correlate bar and galaxy properties in a statistically significant way. To this aim in this paper we analyze the $r-$band SDSS images of a sample of about 3000 galaxies.

The chapter is organized as follows: The galaxy sample is presented in Sect. 7.2; the methods we adopted to detect the bars in the sample galaxies are

explained in Sect. 7.3; they are tested using artificial galaxy images in Sect. 7.4; the fraction, length, and strength of bars of the sample galaxies are measured in Sect. 7.5 and compared to galaxy properties in Sect. 7.6; discussion and conclusions are given in Sect. 7.7.

7.2 Sample selection and data reduction

The sample galaxies were selected in the spectroscopic catalogue of the SDSS Fifth Data Release (Adelman-McCarthy et al. 2007, SDSS-DR5). From the ∼675,000 galaxies available in the catalogue, we took all the galaxies in the redshift range $0.01 < z < 0.04$ and down to an absolute magnitude $M_{\rm r} < -20$ ($\approx M_*$, Blanton et al. 2005). This is a volume-limited sample, because the apparent magnitude of a galaxy with $M_{\rm r} = -20$ at $z = 0.04$ ($m_{\rm r} \sim 15.5$) is within the completeness limit ($m_{\rm r} = 17.77$) of the SDSS-DR5 spectroscopic catalogue.

In order to deal with projection effects, we restricted our sample to galaxies with $b/a > 0.5$, a and b being the semi-major and semi-minor axis lengths of the galaxies. For disk galaxies, this is equivalent to say that we have selected objects with inclination $i < 60°$. Moreover, our selection criteria do not bias the elliptical sample because they show $b/a > 0.6 - 0.7$.

Then, we rejected all the disturbed/interacting galaxies. To this aim, we excluded all the galaxies with a companion which was closer than $2 \times r_{90}$, where r_{90} is defined as the radius which contains 90% of the total galaxy light. Moreover, we add the constraint that the companion must be within 3 magnitudes of the target galaxy. In this way, galaxies with faint companions or contaminated by foreground/background objects are not discarded in our study.

The resulting sample consisted of 3060 galaxies. We are interested in detecting and characterizing bars in the disks of the sample galaxies.

According to Marinova & Jogee (2007) the bar length of barred galaxies in the local universe ranges between about 0.5 and 5 kpc. At $z = 0.04$ the shortest bars project onto 2.17 pixel in the SDSS images, which have a scale of $0\farcs3946$ arcsec pixel^{-1}. The PSF of the SDSS images can be modeled assuming a Moffat function. We fit a bidimensional Moffat function of the form

$$PSF(r) = \frac{\beta - 1}{\pi \alpha^2} \left(1 + \frac{r^{\,2}}{\alpha}\right)^{-\beta}, \tag{7.1}$$

to several stars in each galaxy field obtaining a typical FWHM and β parameter of $1\farcs09$ (2.77 pixel) and 3.05, respectively. Therefore, we are sure to resolve the shortest bars throughout our range of distances.

The morphological classification was available only for a subsample of 612 galaxies, which are listed in RC3. Automatic galaxy morphological classifications divide galaxies according to some photometric observables. In particular, the light concentration is strongly correlated with the Hubble type (Abraham et al. 1996; Conselice et al. 2000; Conselice 2003). In fact, it is larger in early-type galaxies than in late-type ones. The light concentration can be defined as $C = r_{90}/r_{50}$, where r_{50} and r_{90} are the radii enclosing 50% and 90% of the total galaxy light, respectively. These radii are available in the SDSS database for all objects of our sample. We calculated the median value of C for elliptical ($T \leq -4$), lenticular ($-3 \leq T \leq -1$), early-type spiral ($0 \leq T \leq 3$), and late-type spiral ($T \geq 4$) galaxies of the RC3 subsample. They are given in Table 7.1 and shown in Fig. 7.1. Although the dispersion of the data is large, the median light concentration decreases with increasing Hubble type.

If the light traces mass, then we expect a relation between the mass concentration and morphological type too. The central mass concentration of a galaxy can be traced by the central velocity dispersion σ_0. This was available in the SDSS for 298 of the sample galaxies listed RC3. We calculated the median values of σ_0 for the different Hubble types. They are given in Table 7.1 and shown in Fig. 7.1. The median velocity dispersion decreases with increasing Hubble type, too.

Fig. 7.2 shows the relation between C and σ_0 for the galaxies in our sample with both the morphological and kinematic information. Each galaxy can be assigned to a morphological bin according to its values of C and σ_0. The assigned bin is that of the closest median values listed in Table 7.1. The resulting classification is consistent with that given by RC3. This allowed us to classify the remaining sample galaxies, for which only the light concentration was known. They were assigned to the morphological bin corresponding to the closest median value of C (Table 7.1).

We found that 30.4%, 26.1%, 18.4%, and 25.1% of the selected galaxies are ellipticals, lenticulars, early-type and late-type spirals, respectively. We focussed on the 1951 disk galaxies. This is our final sample.

The $r-$band image of each sample galaxy was retrieved from the SDSS archive. All the images were bias subtracted, flat-field corrected, and sky subtracted according to the associated calibration information stored in the Data Archive Server (DAS).

7.3 Methods for detecting and analyzing bars

In the present work, we discuss the advantages and drawbacks of the ellipse fitting (Sect. 7.3.1) and Fourier analysis (Sect. 7.3.2). Both methods are first

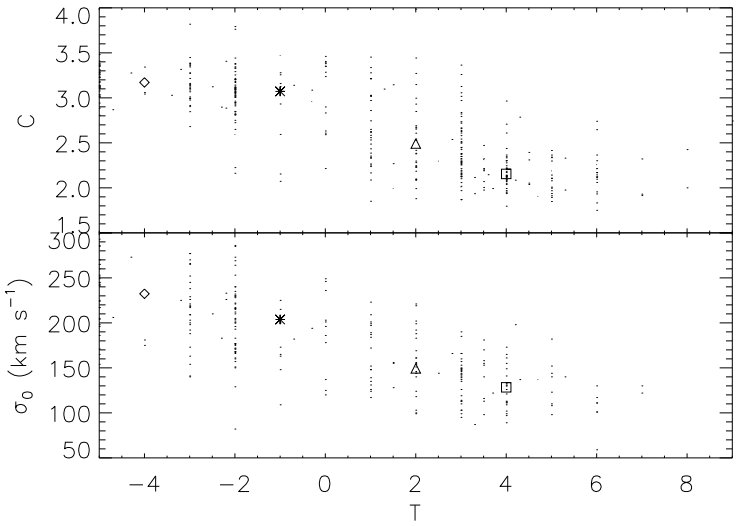

FIGURE 7.1— Values of C (top panel) and central velocity dispersion σ_0 (bottom panel) as function of the morphological parameter T. The galaxies plotted are only those from our sample and also in the RC3 catalogue. Mean values of C and σ_0 for E (diamond), S0 (asterisk), early-type spirals (triangle), and late-type spirals (square) are also overplotted.

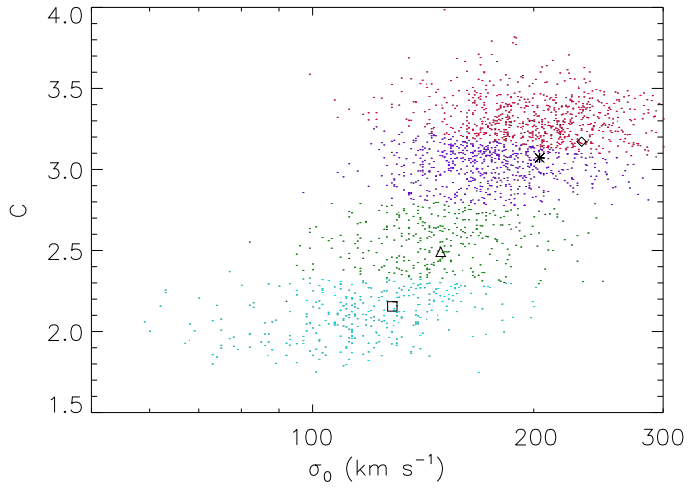

FIGURE 7.2— Values of C and σ_0 for our sample galaxies. Mean values of those parameters for E (diamond), S0 (asterisk), early-type spirals (triangle), and late-type spirals (square) are overplotted. The different colors represent the galaxies classified as E (red), S0 (blue), early-spirals (green), and late spirals (violet).

TABLE 7.1— Median values of light concentration and central velocity dispersion for the different galaxy types.

Galaxy Type	C	σ_0 [km s^{-1}]
(1)	(2)	(3)
E	3.17±0.16	232.33±40.19
S0	3.07±0.30	203.74±43.13
S0/a-Sb	2.49±0.40	149.41±30.59
Sbc-Sm	2.15±0.25	128.38±27.37

NOTE: The columns show the following: (1) Morphological type, (2) light concentration calculated as $C = r_{90}/r_{50}$, (3) central velocity dispersion.

tested by means of extensive simulations on a large set of artificial disk galaxies (Sect. 7.4) and then applied to the sample galaxies.

7.3.1 Ellipse fitting method

This method is based on the fit of the galaxy isophotes by ellipses.

As a first step, each image was cleaned of field stars and galaxies. This was done by rotating the original image by 180° and subtracting the rotated frame from the original one. Then, the residual image was clipped at 1σ, where σ was the rms contributed at each pixel by the background. Finally, the clipped image was subtracted from the original image to get a cleaned and symmetrized frame.

The ellipses were fitted to the isophotes of the symmetrized images of the sample galaxies using the IRAF[1] task ELLIPSE (Jedrzejewski 1987). In order to get a good fit at all radii out to an intensity level corresponding to the background rms, we implemented the fitting method described by Jogee et al. (2004) and Marinova & Jogee (2007). This is an iterative "wrapped" procedure, which runs ellipse fitting several times changing the trial values at each fit iteration. Nevertheless, the ellipse fit failed for a small fraction (about 3%) of the sample galaxies. Thus, the final number of galaxies studied was 2962. For each of them, we obtained the radial profiles of the ellipticity ϵ and position

[1]IRAF is distributed by NOAO, which is operated by AURA Inc., under contract with the National Science Foundation.

angle PA of the major-axis of the fitted ellipses.

The radial profile of ϵ in a non-barred galaxy usually increases from low values in the center to a constant value at large radii. At large radii the radial profile of the PA is constant too. The constant values of ϵ and PA are related to the inclination and orientation of the line-of-node of the galactic disk. On the contrary, barred galaxies are characterized by the presence of a local maximum in the radial profile of ϵ and constant PA in the bar region (Wozniak et al. 1995). This is due to the shape and orientation of the stellar orbits of the bar (Contopoulos & Grosbol 1989; Athanassoula 1992).

This allowed us to identify bars by analyzing the radial profiles of ϵ and PA. We considered that a galaxy hosts a bar when: (1) the ellipticity radial profile shows a significant increase followed by a significant decrease ($\Delta\epsilon \geq 0.08$) and (2) the PA of the fitted ellipses is roughly constant within the bar region ($\Delta\mathrm{PA} \leq 20^\circ$).

The values adopted for $\Delta\epsilon$ and ΔPA were determined by applying the method to artificial galaxies (see Sect. 7.4.2). The bar length was derived as the radius $r^{\epsilon}_{\mathrm{bar}}$ at which the maximum ellipticity was reached (Wozniak et al. 1995; Laine et al. 2002; Marinova & Jogee 2007) or as the radius $r^{\mathrm{PA}}_{\mathrm{bar}}$ at which the PA changes by 5° with respect to the value corresponding to the maximum ellipticity (Wozniak et al. 1995; Sheth et al. 2003; Erwin & Sparke 2003; Erwin 2005; Michel-Dansac & Wozniak 2006).

This method was already successfully applied by different authors both in the optical and near-infrared wavebands to detect bars in galaxies at low (Knapen et al. 2000; Laine et al. 2002; Marinova & Jogee 2007) and high redshift (Jogee et al. 2004; Elmegreen et al. 2004).

7.3.2 Fourier analysis method

An alternative way to detect and characterize bars is with a Fourier analysis of the azimuthal luminosity profile (Ohta et al. 1990; Elmegreen & Elmegreen 1985; Aguerri et al. 2000).

We began by deprojecting the image of each sample galaxy by a flux-conserving stretch along the minor-axis by the factor $1/\cos i$, where i is the galaxy inclination. Therefore, we needed a good estimation of the inclination and major-axis PA of the galaxy. They were derived from the ellipticity and PA of the ellipses fitting the outermost isophotes of the galaxy, where the total luminosity is dominated by the disk contribution.

The deprojected luminosity profile, $I(R, \phi)$, where (R, ϕ) are plane polar

coordinates in the galaxy frame, was decomposed into a Fourier series

$$I(R,\phi) = \frac{A_0(R)}{2} + \sum_{m=1}^{\infty} (A_m(R)\cos(m\phi) + B_m(R)\sin(m\phi)), \qquad (7.2)$$

where the coefficients are defined by

$$A_m(R) = \frac{1}{\pi}\int_0^{2\pi} I(R,\phi)\cos(m\phi)d\phi, \qquad (7.3)$$

and

$$B_m(R) = \frac{1}{\pi}\int_0^{2\pi} I(R,\phi)\sin(m\phi)d\phi. \qquad (7.4)$$

The Fourier amplitude of the m-th component is defined as

$$I_m(R) = \begin{cases} A_0(R)/2 & m = 0 \\ \sqrt{A_m^2(R) + B_m^2(R)} & m \neq 0 \end{cases} \qquad (7.5)$$

The even ($m = 2, 4, 6, ...$) relative Fourier amplitudes $I_{\rm m}/I_0$ of galaxies with bars are large, while the odd ($m = 2, 4, 6, ...$) ones are small. In particular, the bar is evidenced by a strong $m = 2$ component. Similarly to the ellipse fitting method, we considered that a galaxy hosts a bar when (1) the $m = 2$ relative Fourier component shows a local maximum ($\Delta(I_2/I_0) \geq 0.2$), and (2) the phase angle of the $m = 2$ mode ϕ_2 is roughly constant within the bar region ($\Delta\phi_2 \leq 20^\circ$).

The values adopted for $\Delta(I_2/I_0)$ and $\Delta\phi_2$ were determined by applying the method to artificial galaxies (see Sect. 7.4.3).

The bar length $r_{\rm bar}^{\rm Fourier}$ was calculated using the bar/interbar intensity ratio as in Aguerri et al. (2000). The bar intensity, I_b, is defined as the sum of the even Fourier components, $I_0 + I_2 + I_4 + I_6$, while the inter-bar intensity, I_{ib}, is given by $I_0 - I_2 + I_4 - I_6$ (Ohta et al. 1990; Elmegreen & Elmegreen 1985; Aguerri et al. 2000). Ohta et al. (1990) arbitrarily defined the bar length as the outer radius for which $I_b/I_{ib} = 2$. But, Aguerri et al. (2000) pointed out, a fixed value of I_b/I_{ib} cannot account for the wide variety of bar luminosities present in galaxies. Instead, they defined the bar length as the FWHM of the curve of I_b/I_{ib}. This method was applied by Athanassoula & Misiriotis (2002) to analytic models demonstrating its accuracy in measuring the bar length.

7.4 Test on artificial galaxies

7.4.1 Structural parameters of the artificial galaxies

Extensive simulations on a large set of artificial disk galaxies were carried out to test the reliability and accuracy of the ellipse fitting (Sect. 7.3.1) and Fourier

analysis (Sect. 7.3.2) in detecting bars. Moreover, they were used to fine tune the free parameters of the two analysis methods, i.e., $\Delta\epsilon$ and ΔPA in the ellipse fitting, and $\Delta(I_2/I_0)$ and $\Delta\phi_2$ in the Fourier analysis. The surface-brightness distribution of the artificial galaxies was assumed to be the sum of the contributions of three structural components: a bulge, a disk, and a bar (Prieto et al. 2001; Aguerri et al. 2003; Aguerri et al. 2005; Laurikainen et al. 2007). The surface-brightness distribution of each individual component was assumed to follow a parametric law, which has to be strictly considered as an empirical fitting function.

The Sérsic law (Sérsic 1968) was assumed for the radial surface-brightness profile of the bulge

$$I_{\rm bulge}(r) \; = \; I_{0,\rm bulge}\, 10^{-b_n (r/r_{\rm e})^{1/n}}, \tag{7.6}$$

where $r_{\rm e}$, I_0 and n are the effective (or half-light) radius, the central surface-brightness, and a shape parameter describing the curvature of the profile, respectively. The value of b_n is coupled to n so that half of the total flux is always within $r_{\rm e}$ and can be approximated as $b_n = 0.868n - 0.142$ (Caon et al. 1993).

The exponential law (Freeman 1970) was assumed to describe the the radial surface-brightness profile of the disk

$$I_{\rm disk}(r) = I_{0,\rm disk} e^{-r/h}, \tag{7.7}$$

where h and $I_{0,\rm disk}$ are the scale-length and central surface-brightness of the disk, respectively.

Several parametric laws were adopted in the literature to describe the surface-brightness distribution of bars. Ferrers (Laurikainen et al. 2005), flat (Prieto et al. 1997), and elliptical (Freeman 1966) bars were considered for the artificial galaxies.

The surface-brightness distribution was assumed to be axially symmetric with respect to a generalized ellipse (Athanassoula et al. 1990). When the principal axes of the ellipse are aligned with the coordinate axes, the radial coordinate is defined as

$$r = \left(|x|^c + \left| \frac{y}{(1-\epsilon_{\rm bar})} \right|^c \right)^{1/c}, \tag{7.8}$$

where $\epsilon_{\rm bar}$ is the ellipticity and c controls the shape of the isophotes. It serves the same purpose as the $\cos 4\theta$ Fourier coefficient which is usually adopted to describe the boxiness/diskyness of the isophotes (Jedrzejewski 1987). But, it applies to all the isophotes of the component. A bar with pure elliptical

isophotes has $c = 2$. It is $c > 2$ if the isophotes are boxy, and $c < 2$ if they are disky. The parameters $\epsilon_{\rm bar}$ and c are constant as a function of radius.

The radial surface-brightness profile of a Ferrers ellipsoid (Ferrers 1877) is given by

$$I_{\rm bar}^{\rm Ferrers}(r) = \begin{cases} I_{0,\rm bar}\left(1-\left(\frac{r}{r_{\rm bar}}\right)^2\right)^{n_{\rm bar}+0.5} & r \le r_{\rm bar} \\ 0 & r > r_{\rm bar}, \end{cases} \tag{7.9}$$

where $I_{0,\rm bar}$, $r_{\rm bar}$ and $n_{\rm bar}$ are the central surface-brightness, the length and a shape parameter of the bar, respectively. The simulated bars were generated by adopting $n_{\rm bar} = 2$ (e.g., Laurikainen et al. 2005).

The radial surface-brightness profile of a flat bar is

$$I_{\rm bar}^{\rm flat} = I_{0,\rm bar}\left(\frac{1}{1+e^{\frac{r-r_{\rm bar}}{r_{\rm s}}}}\right), \tag{7.10}$$

where $I_{0,\rm bar}$ and $r_{\rm bar}$ are the central surface-brightness and length of the bar. For radii larger than $r_{\rm bar}$ the surface-brightness profile falls off with a scale-length $r_{\rm s}$ (Prieto et al. 1997).

Finally, the radial surface-brightness profile of a Freeman bar (Freeman 1966) is

$$I_{\rm bar}^{\rm Freeman} = I_{0,\rm bar}\sqrt{1-\left(\frac{r}{r_{\rm bar}}\right)^2}, \tag{7.11}$$

where $I_{0,\rm bar}$ and $r_{\rm bar}$ are the central surface-brightness and length of the bar, respectively.

We generated a set of 8000 images of artificial galaxies with a Sérsic bulge and an exponential disk. Among these galaxies, 2000 have a Ferrers bar, 2000 a flat bar, 2000 a Freeman bar, and 2000 without bar.

The apparent magnitudes of the artificial galaxies were randomly chosen in the range

$$10 < m_{\rm r} < 16, \tag{7.12}$$

corresponding to that of the sample galaxies. To redistribute the total galaxy luminosity among the three galaxy components, the bulge-to-total $L_{\rm bulge}/L_{\rm tot}$ and bar-to-disk $L_{\rm bar}/L_{\rm disk}$ luminosity ratio were taken into account. They were considered to be

$$0 < L_{\rm bulge}/L_{\rm tot} < 0.7, \tag{7.13}$$

and

$$0 < L_{\rm bar}/L_{\rm disk} < 0.3, \tag{7.14}$$

following Laurikainen et al. (2005). The adopted ranges for the effective radius of the bulge, scale-length of the disk, and bar length were selected according to the values measured for spiral galaxies by Mölenhoff & Heidt (2001), MacArthur et al. (2003), Möllenhoff (2004), Laurikainen et al. (2007), and Méndez-Abreu et al. (2008). They are

$$0.5 < r_{\rm e} < 3 \text{ kpc}, \tag{7.15}$$

$$1 < h < 6 \text{ kpc}, \tag{7.16}$$

and

$$0.5 < r_{\rm bar} < 5 \text{ kpc}, \tag{7.17}$$

respectively. The ellipticities of the structural components were also selected to mimic those measured in real galaxies (Marinova & Jogee 2007). They are

$$0.8 < 1 - \epsilon_{\rm bulge} < 1, \tag{7.18}$$

$$0.5 < 1 - \epsilon_{\rm disk} < 1, \tag{7.19}$$

and

$$0.2 < 1 - \epsilon_{\rm bar} < 0.7, \tag{7.20}$$

with

$$\epsilon_{\rm bulge} < \epsilon_{\rm disk} < \epsilon_{\rm bar}. \tag{7.21}$$

Finally, the position angles of the three components were selected randomly between 0° and 180° to allow each component to be independently oriented with respect to the others.

In each pixel of the resulting images noise was added to yield a signal-to-noise ratio (S/N) similar to that of the available SDSS images. It was given by the Poisson noise associated to the photon counts due to both the galaxy and sky background and read-out noise (RON) of the CCD. The pixel scale used was $0\farcs3946$ arcsec pixel^{-1}, and the CCD gain and RON were 4.72 e$^-$ ADU^{-1} and 5.52 e$^-$ in order to mimic the instrumental setup of the SDSS data.

In order to account for seeing effects, the images of the artificial galaxies were convolved with a Moffat PSF with FWHM=2.77 pixels and $\beta = 3.05$ (see Sect. 7.2).

The simulated galaxies were sized such that the shortest physical scale (i.e., 0.5 kpc) was resolved at the largest distance ($z = 0.04$) in order to ensure that we cover the whole range of scale at every redshift. Therefore, our simulations are somehow "dimensionless", since the limits to our method can be calculated at every distance just transforming pixel distances to physical distances.

In no sense the artificial galaxies represent the real sample of galaxies since we doid not have into account their redshift distribution. However, they are

useful to test the efficiency of the two methods proposed for detecting bars, in order to tune their free parameters and understand possible biases in the results.

7.4.2 Testing the ellipse fitting method

The ellipse fitting method has two free parameters, $\Delta\epsilon$ and ΔPA. Laine et al. (2002) adopted $\Delta\epsilon = 0.1$ and $\Delta\text{PA} = 20°$, Marinova & Jogee (2007) and Menéndez-Delmestre et al. (2007) adopted $\Delta\epsilon = 0.1$ and $\Delta\text{PA} = 10°$.

We applied the ellipse fitting method to the artificial galaxies by adopting $\Delta\epsilon = 0.1, 0.08, 0.05$ and $\Delta\text{PA} = 10°, 20°, 30°$ to find the best combination of $\Delta\epsilon$ and ΔPA maximizing the bar identification and minimizing the bad and/or spurious detections. The results are given in Table 7.2.

The flat and Freeman bars are the most difficult and easiest bars to be detected, respectively. This means that the ellipse fitting method detects more efficiently the bars with sharp ends than those characterized by a smooth transition to the disk. Moreover, adopting $\Delta\text{PA} = 20°$ instead of $\Delta\text{PA} = 10°$ increases the fraction of bar detections by 10% for all the bar types, while the increment between $\Delta\text{PA} = 20°$ and $\Delta\text{PA} = 30°$ is only 4%.

Spurious detections correspond to non-barred galaxies which are erroneously found to be barred. In order to estimate their fraction, we applied the method to the sample of non-barred artificial galaxies we built to this aim. The results for the different values of $\Delta\epsilon$ and ΔPA are given in Table 7.2.

Bad detections are also made if real barred galaxies yield a bad measurement of the bar length. In order to estimate this fraction, we compared the bar lengths known for the artificial galaxies with the $r_{\text{bar}}^{\text{ellipse}}$ derived by applying the ellipse fitting method. We derived the median and standard deviation of the relative error between the known and measured bar length using a 3σ clipping iterative procedure. We considered as bad detections the measurements with a relative error larger than 3σ with respect to the median.

The fraction of galaxies classified as barred versus the bad/spurious detections are shown in Fig. 7.3 as a function of $\Delta\epsilon$ and ΔPA. The optimal configuration is given by $\Delta\epsilon = 0.08$ and $\Delta\text{PA} = 20°$ since the fraction of detections increases by more than 10% with respect to $\Delta\epsilon = 0.1$ and $\Delta\text{PA} = 10°$, while the fraction of bad/spurious detections is always lower than 6%.

The bar lengths we measured as $r_{\text{bar}}^{\epsilon}$ and $r_{\text{bar}}^{\text{PA}}$ in the artificial galaxies are shown in Fig. 7.4. The bar length is underestimated when $r_{\text{bar}}^{\epsilon}$ is used, as found by Michel-Dansac & Wozniak (2006) too. This is particularly true for the Ferrers bars where the measured bar lengths are 50% shorter than the real ones. In contrast, Freeman and flat bars were better determined, their measurements

TABLE 7.2— Percentage of galaxies classified as barred by applying the ellipse fit method to the mock galaxy catalogue.

Δ PA	$\Delta\epsilon = 0.1$			
	Ferrers	Exp.	Flat	Non-barred
10°	39	46	22	2
20°	53	58	34	3
30°	57	63	37	4
Δ PA	$\Delta\epsilon = 0.08$			
	Ferrers	Exp.	Flat	Non-barred
10°	48	55	30	3
20°	62	67	40	5
30°	66	71	43	6
Δ PA	$\Delta\epsilon = 0.05$			
	Ferrers	Exp.	Flat	Non-barred
10°	65	70	43	9
20°	77	81	54	13
30°	79	83	57	15

being shorter by 30% and 19%, respectively. The bar length is underestimated when $r_{\rm bar}^{\rm PA}$ is used for the Ferrers bars (11%), but is overestimated for the flat (28%) and Freeman bars (8%). These results show the possibility of defining an empirical correction to the bar length, knowing the bar type in advance.

7.4.3 Testing the Fourier analysis method

The deprojection of the galaxy image is a crucial step in applying the Fourier method, which has two free parameters, $\Delta(I_2/I_0)$ and $\Delta\phi_2$. The inclination and major-axis position angle of the galaxy disk can be obtained by either fitting ellipse to the outermost galaxy isophotes (e.g., Aguerri et al. 2003) or minimizing the $m = 2$ Fourier mode in the outermost regions of the galaxy (e.g., Grosbol 1985). We applied these two methods to the artificial galaxies and found that ellipse fitting gave lower errors (about 3°) on both i and PA.

We applied the Fourier method to the artificial galaxies by adopting $\Delta(I_2/I_0)$ =0.2, 0.1, 0.08, 0.05 and $\Delta\phi_2 = 10°, 20°, 30°$ to find the best combination of $\Delta(I_2/I_0)$ and $\Delta\phi_2$, maximizing the bar identification and minimizing the bad and/or spurious detections. The results are given in Table 7.3 and in Fig. 7.5.

In general, the Fourier method is less efficient in detecting bars than the ellipse fitting method. We found that $\Delta(I_2/I_0) = 0.2$ has to be adopted to have a fraction of bad/spurious detections lower than 10%. We also adopted

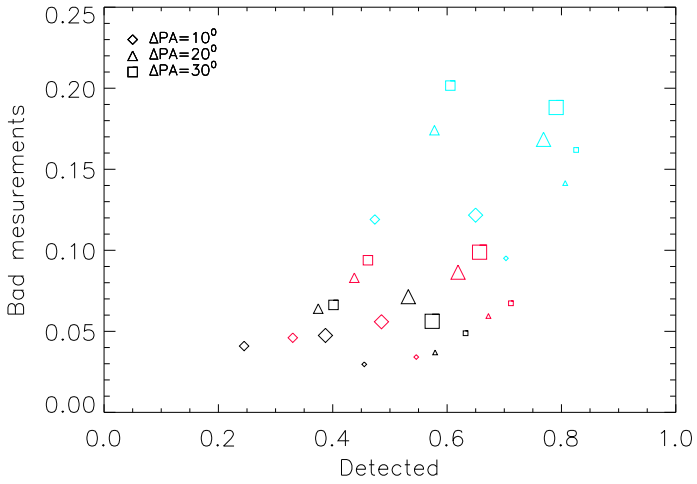

FIGURE 7.3— Fraction of galaxies classified as barred versus fraction of bad/spurious bar measurements using the ellipse fit method with ΔPA=10° (diamonds), 20° (triangles) and 30° (squares). The black, red and blue colors represent $\Delta\epsilon$ =0.1, 0.08, and 0.05, respectively. The size of the symbols shows the different simulated bar types: Ferrers ellipsoids (large), exponential (medium), and flat (small) bars.

$\Delta\phi_2 = 20°$ because it increases detections by more than 10% and gives less bad/spurious detections with respect to $\Delta\phi_2 = 30°$.

7.5 Bar properties

7.5.1 Bar fraction

Both the ellipse fitting and Fourier method were applied to our sample of 1951 disk galaxies.

We found that the fraction of galaxies classified as barred depends strongly on the technique adopted for the analysis: it is 45% with the ellipse fitting method and 26% with the Fourier method. Although the Fourier method was demonstrated to be less efficient than ellipse fitting in detecting bars, this difference is larger than that expected from the analysis of the artificial galaxies. To investigate this issue, we took into account the morphological classification of the galaxies found to be barred. According to the ellipse fit method 32%, 55%, and 52% of the lenticular, early-type and late-type spiral galaxies, respectively, are barred. They are 29%, 33%, and 17%, respectively, with the Fourier method. Therefore, both methods obtained a similar of fraction of

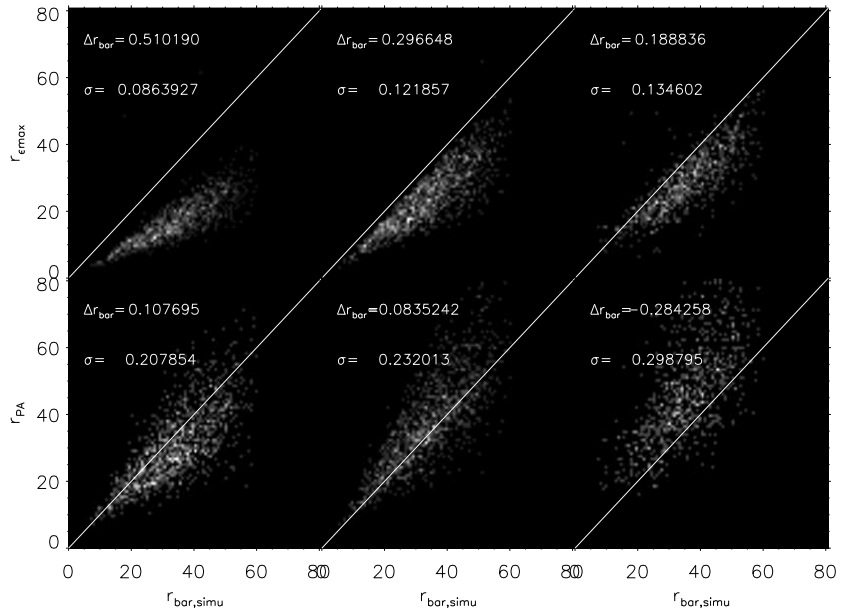

FIGURE 7.4— Bar radius measured with the maximum ellipticity method (top panels) and the PA method (lower panels) for Ferrers (left panels), exponential (central panels), and flat (right panels) simulated bars as function of the bar radius introduced in the simulations. The numbers overplotted in each panel gives the mean relative error and its standard deviation of the bar radius.

barred lenticular galaxies, while the Fourier method is less efficient in detecting bars in spirals, and particularly in late-type spiral galaxies. An example is shown in Fig. 7.6.

The early-type spiral SDSSJ031947.01+003504.4 and the late-type spiral SDSSJ020159.33-081441.9 are analyzed by both methods. The bar of the early-type spiral was detected by both methods and the measured bar lengths are in agreement. In fact, the radial profiles of ϵ and I_2/I_0 show a local maximum at about $5''$, where the PA and ϕ_2 are constant. On the contrary, the bar of the late-type spiral was detected only by the ellipse fit method. The radial profiles of ϵ and I_2/I_0 show a local maximum at different radii. The I_2/I_0 maximum is located in the spiral arm region, where ϕ_2 is not constant. Therefore, the bar of this galaxy was not detected by the Fourier method.

We conclude that the bars with sharp ends are detected by both ellipse fitting and Fourier methods. But, the bars of galaxies with lenses or strong spiral arms are more easily detected with the ellipse fitting method. This kind

TABLE 7.3— Percentage of galaxies classified as barred by applying the Fourier method to the mock galaxy catalogue.

$\Delta\phi_2$	$\Delta(I_2/I_0 = 0.2)$			
	Ferrers	Exp.	Flat	Non-barred
10°	29	26	18	5
20°	44	42	31	8
30°	51	51	37	8
$\Delta\phi_2$	$\Delta(I_2/I_0 = 0.1)$			
	Ferrers	Exp.	Flat	Non-barred
10°	47	44	35	19
20°	63	62	52	26
30°	69	70	60	31
$\Delta\phi_2$	$\Delta(I_2/I_0) = 0.08$			
	Ferrers	Exp.	Flat	Non-barred
10°	53	50	40	22
20°	67	67	58	32
30°	73	74	65	36
$\Delta\phi_2$	$\Delta(I_2/I_0) = 0.05$			
	Ferrers	Exp.	Flat	Non-barred
10°	62	61	53	29
20°	75	76	70	41
30°	81	82	75	48

of bars is usually found in late-type spirals. These large differences in the bar fractions between the two methods could bias our conclusions. For this reason, we will study the photometric parameters of the bars by adopting only the ellipse fitting method.

Our bar fraction (45%) of disk galaxies in the local universe is in good agreement with previous results obtained in optical bands by Marinova & Jogee (2007, 44% in the B band) and Reese et al. (2007, 47% in the I band). However, Marinova & Jogee (2007) did not find any difference in the bar fraction as a function of the Hubble type. The same is true for Knapen et al. (2000) and Eskridge et al. (2000), who analyzed near-infrared images. We argue that their results were biased by their smaller samples.

7.5.2 Bar length

The distributions of the bar lengths and normalized bar lengths we derived for the sample galaxies are shown in Fig. 7.7. Both $r^{\epsilon}_{\rm bar}$ and $r^{\rm PA}_{\rm bar}$ were considered,

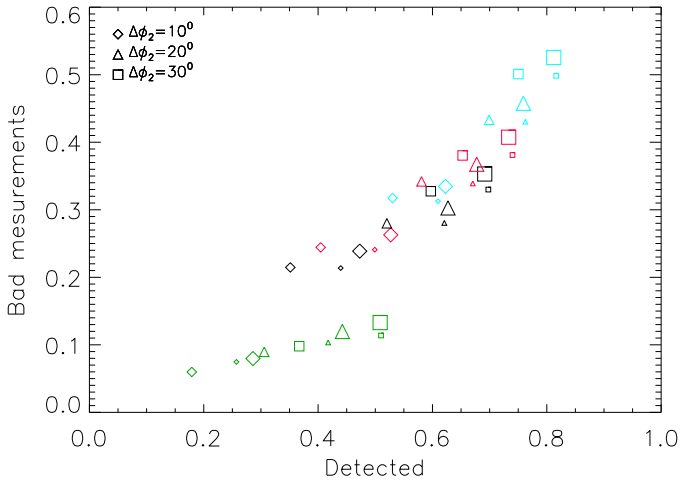

FIGURE 7.5— Fraction of galaxies classified as barred versus fraction of bad/spurious bar measurements using the Fourier method with $\Delta\phi_2$ =10° (diamonds), 20° (triangles) and 30° (squares). The green, black, red and blue colors represent $\Delta\epsilon$ =0.2, 0.1, 0.08, and 0.05, respectively. The size of the symbols shows the different simulated bar types: Ferrers ellipsoids (large), exponential (medium), and flat (small) bars.

TABLE 7.4— Median values of the bar radius for the different galaxy types.

Bar radius	S0	Early-type	Late-type
$r_{\rm bar}^{\epsilon_{\rm max}}$ (kpc)	4.13	5.19	5.22
$r_{\rm bar}^{\rm PA}$ (kpc)	6.88	7.12	6.61
$r_{bar}^{\epsilon_{\rm max}}/r_{90}$	0.50	0.53	0.53
$r_{\rm bar}^{\rm PA}/r_{90}$	0.81	0.73	0.66

and the galaxy size was defined as $r_{\rm gal} = 2.5 \times r_{90}$. The median values derived for the different morphological bins are given in Tab. 7.4.

The values of $r_{\rm bar}^{\rm PA}$ we measured are in agreement with previous findings (Elmegreen & Elmegreen 1985; Martin 1995; Menéndez-Delmestre et al. 2007; Laurikainen et al. 2007).

There is no clear trend between the absolute and relative bar length and the morphological type, because different bar length methods give different trends.

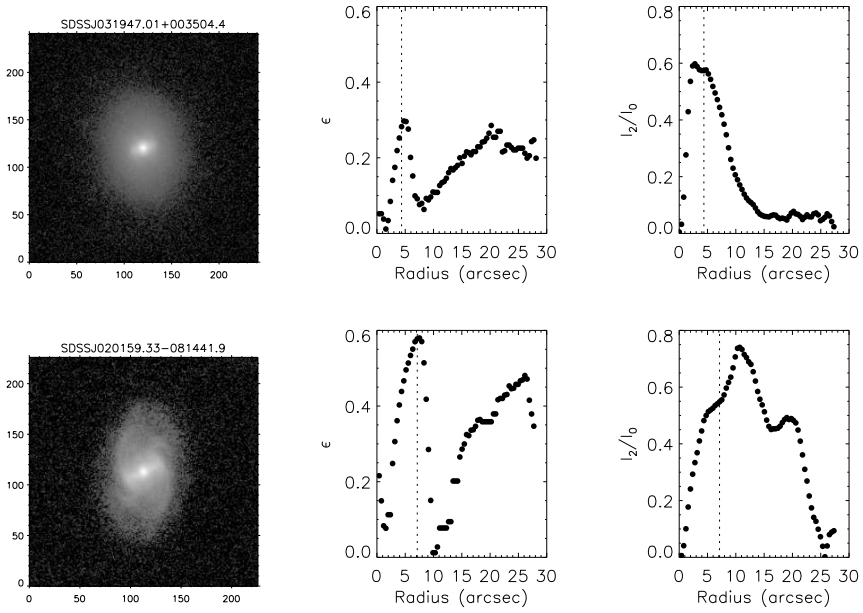

FIGURE 7.6— The r-band images (left panels), ellipticity profiles (middle panels) and $m = 2$ Fourier amplitude (right panels) of an early-type galaxy (upper panel) and a late-type galaxy (lower panel) of the sample. The vertical dotted lines represent the radius of the bar reported by the ellipse fit method.

A correlation between the bar length and galaxy size was found. Thus, larger bars are located in bigger galaxies (see Fig. 7.8). Therefore, the correlation is independent of the adopted method to measure the bar length. It holds for the different morphological bins too, being stronger for late-type spirals ($r = 0.52$) and weaker for S0 galaxies ($r = 0.38$). This relation could indicate a link between the formation and evolution processes between of bars and galaxy disks. A similar correlation was found by Marinova & Jogee (2007).

7.5.3 Bar strength

The bar strength represents the contribution of the bar to the total galaxy potential. Several methods have been developed to measure it (see Laurikainen et al. 2007 and references therein). Nowadays, the most commonly used parameter measuring the bar strength is $Q_{\rm g}$ defined by Buta & Block (2001). It can be accurately estimated by analyzing near-infrared images (Buta et al. 2003; Block et al. 2004; Laurikainen et al. 2007), which are not available for our sample galaxies drawn from the SDSS. However, Whyte et al. (2002) defined

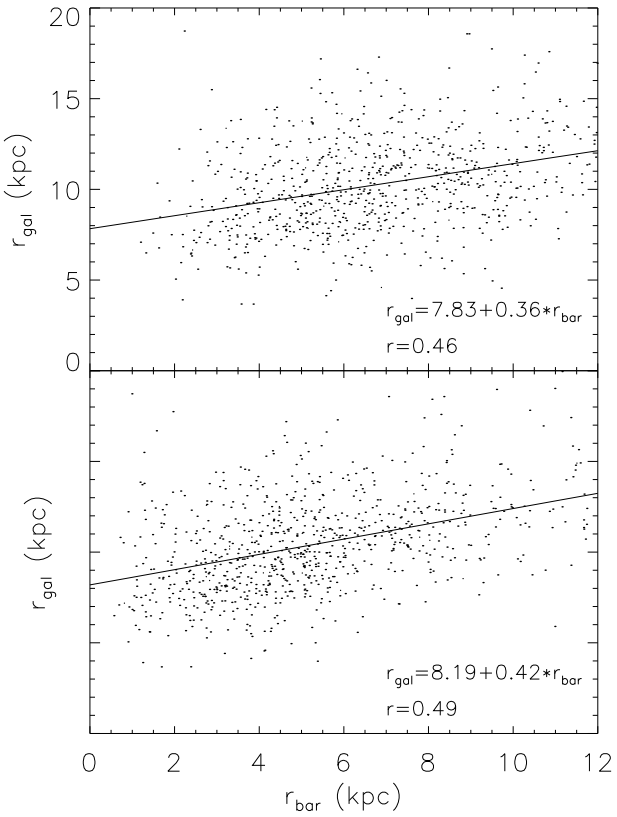

FIGURE 7.7— Galaxy radius versus bar length defined as $r_{\rm bar}^{\rm PA}$ (top panel) and $r_{\rm bar}^{\epsilon_{\rm max}}$ (bottom panel). The fitted correlations and Pearson's coefficients are given.

another bar strength parameter

$$f_{\rm bar} = \frac{2}{\pi}\left((1-\epsilon_{\rm bar})^{-1/2} + (1-\epsilon_{\rm bar})^{+1/2}\right), \tag{7.22}$$

where $\epsilon_{\rm bar}$ is the bar ellipticity measured at $r_{\rm bar}^{\epsilon}$. It correlates with $Q_{\rm g}$ (e.g., Laurikainen et al. 2007) and was adopted for our sample galaxies.

The distributions of the bar strengths we derived for the different morphological types are shown in Fig. 7.9. The mean values for the bar strengths of the lenticular, early-type, and late-type spiral galaxies are 0.16, 0.19, and 0.20, respectively. Indeed, we found a significant difference between the lenticular and spiral galaxies. They are characterized by different distributions, as con-

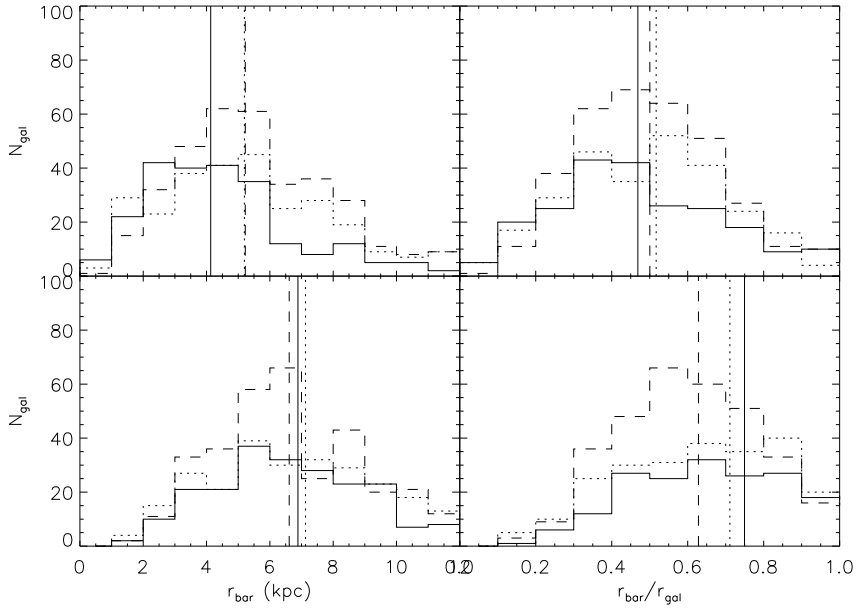

FIGURE 7.8— Bar radius (left panel) and normalized bar radius (right panel) of S0 (full line), early-type (dotted line), and late-type (dashed line) galaxies. The bar radius was measured with the maximum ellipticity method (top panels) and the PA method (low panels). The vertical lines represent the mean values of the bar radius and normalized bar radius of the different types of galaxies.

firmed at a high confidence level ($> 95\%$) by a Kolmogorov-Smirnov (KS) test. Also Laurikainen et al. (2007) found that S0 galaxies host significantly weaker bars than the rest of disk galaxies.

7.6 Bars and galaxy properties

7.6.1 Galaxy local environment

Due to our selection criteria we excluded all the interacting galaxies. Nevertheless, the sample galaxies can be located in groups and cluster, where the role of the environment could be important in their evolution.

In order to investigate the relation between bar properties and local environment, we calculated for each sample galaxy the local density following the prescriptions of Balogh et al. (2004a,b). The number density of local galaxies was computed using the distance d_5 of the galaxy to its fifth nearest neighbor

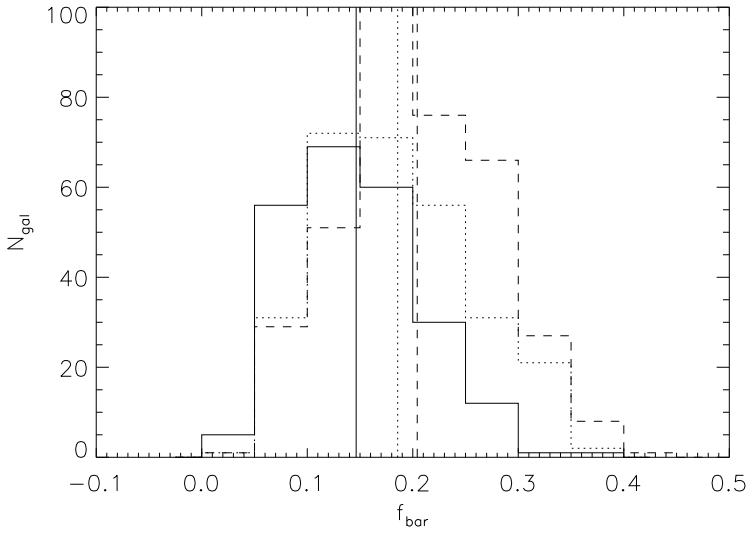

FIGURE 7.9— Bar strength of S0 (full line), early-type (dotted line), and late-type (dashed line) galaxies. The vertical lines represent the mean values of the bar radius and normalized bar radius of the different types of galaxies.

galaxy. Thus, a projected galaxy density could be defined as

$$\Sigma_5 = \frac{5}{\pi d_5^2}. \tag{7.23}$$

This was computed with those galaxies located in a velocity range of ± 1000 km s^{-1} from the target galaxy to avoid background/foreground contamination. For galaxies without measured redshift we impose a luminosity constraint to derive the galaxy density as done by Balogh et al. (2004a,b).

A series of caveats must be taken into account when the distance neighbor method is applied.

The limited area of sky covered by the survey implies that usually the estimated density is lower than real. In fact, due to edges and holes in the survey, the value of d_5 could be overestimated and the derived density underestimated. To address this issue, we checked that only 0.5% of the sample galaxies fall close to the edges of the SDSS. These galaxies were excluded from this analysis. Also the finite redshift range could lead to underestimate the local density. Therefore, we circumvent this problem by defining a new volume-limited sample in the redshift range $0 < z < 0.06$ taking into account for the adopted velocity range. Finally, the local density distribution could be biased by the criteria of the sample selection. For example, we rejected all the interacting galaxies

and therefore we could have favored the selection of galaxies residing in low-density environments. In order to test the selection biases, we compared the local density distribution of our galaxy sample with that obtained by Gómez et al. (2003) from an earlier data release of the SDSS (Fig. 7.10). The overall trend of the two distributions is in good agreement as confirmed at a high confidence level ($> 99\%$) by a KS test. Therefore, we are confident to consider our result as a robust first approximation to the local density distribution.

According to numerical simulations, galaxy mergers and interactions are mechanisms which should drive the formation of bars (Gerin et al. 1990; Miwa & Noguchi 1998; Mastropietro et al. 2005). But, the observational proofs about the influence of the environment on bar formation and evolution are rare. For example, Thompson (1981) suggested a link between bar formation and local galaxy environment by observing that the fraction of barred galaxies increases towards the core of Coma cluster. Fig. 7.11 shows the fraction of barred and non-barred galaxies in our sample as function of the local galaxy density. There is no relation between the presence of a bar and the environment of the host galaxy. The same is true even if galaxies of different morphological type are considered independently. We did not find any correlation between the bar strength or bar length and the local galaxy density. These results suggest that local environment does not play an crucial role in the processes driving the formation and evolution of the bars of the sample galaxies. They were mainly affected by internal processes.

7.6.2 Central light concentration

Fig. 7.12 shows the cumulative distribution functions of the C parameter for the sample galaxies. Barred and unbarred galaxies are characterized by different distributions as confirmed at a high confidence level ($> 99\%$) by a KS test. Bars are hosted by less concentrated galaxies. This is true for both the light and mass distribution, since the light concentration is correlated to the central velocity dispersion as discussed in Sect. 7.2. This explains the lower fraction (see Sect. 7.5.1) and strength (see Sect. 7.5.3) of bars in S0 galaxies with respect to spirals. In fact, bars are weakened by large galactic bulges (Athanassoula & Misiriotis 2002), which are characterized by higher light and mass concentration.

7.6.3 Galaxy colors

Fig. 7.13 shows the cumulative distribution functions of the $g - r$ color for the sample galaxies. Barred and unbarred galaxies are characterized by different distributions, as confirmed at a high confidence level ($> 99\%$) by a KS test. This

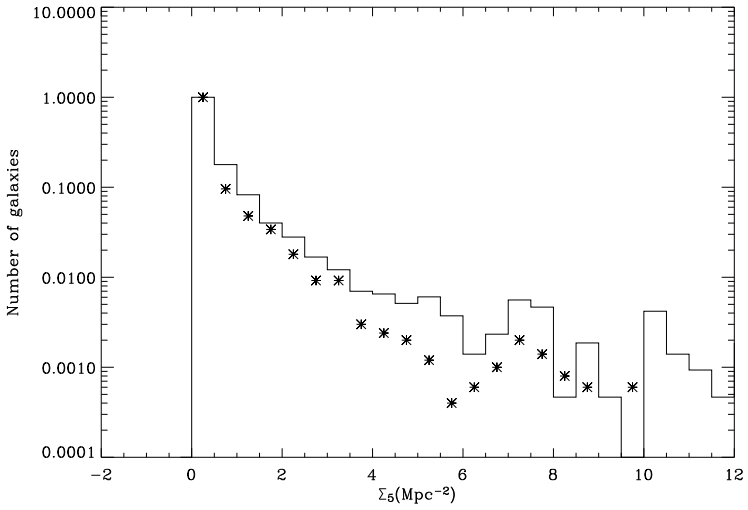

FIGURE 7.10— Distribution of local galaxy densities for galaxies in our sample (solid lines) and for Gómez et al. (2003) sample (asterisks).

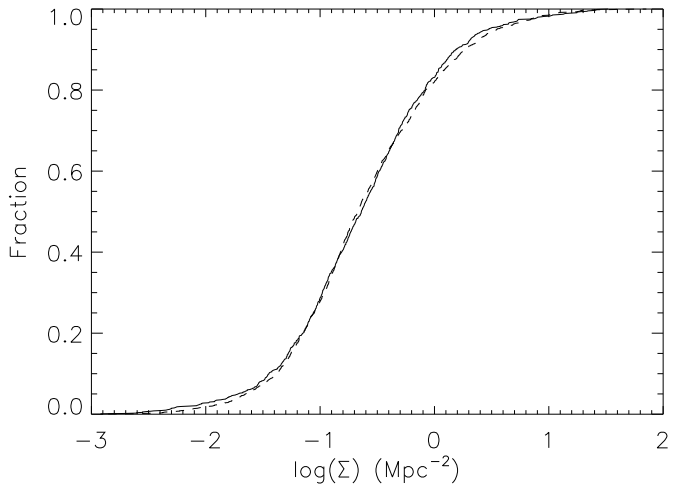

FIGURE 7.11— Fraction of barred (full line) and non-barred (dashed-line) as function of the local galaxy density (see text for details).

difference is due to the late-type spirals, because the $g-r$ colors of barred and unbarred S0 and early-type spiral galaxies are very similar. We can conclude

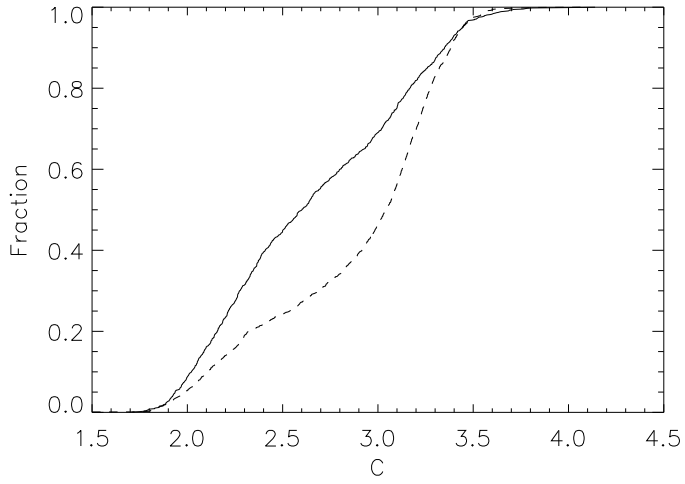

FIGURE 7.12— Fraction of barred (full line) and non-barred (dashed-line) as function of the light galaxy concentration.

that late-type spiral bars are hosted by bluer galaxies. This is in agreement with previous results showing that the star formation is higher in barred than in unbarred galaxies based on smaller samples of local galaxies (Martinet & Friedli 1997; Aguerri 1999).

7.7 Conclusions

We have studied the fraction and properties of bars in a sample of $\sim$ 3000 galaxies extracted from the SDSS-DR5. This is a volume-limited sample of non-interacting galaxies in the redshift range $0.01 < z < 0.04$, with an absolute magnitude $M_{\rm r} < -20$, and an inclination $i < 60^{\circ}$.

The galaxies have been classified according to their light concentration. The correlation between the light concentration and morphological type was derived from a subsample of 612 galaxies, whose morphological classification was already known. We found that 30.4%, 26.1%, 18.4%, and 25.1% of the sample galaxies were ellipticals, lenticulars, early and late-type spirals, respectively.

We derived the fraction of barred galaxies by analyzing the SDSS $r-$band images of the disk galaxies of the sample with the ellipse fitting and Fourier methods. They consist in looking for a local maximum in the radial profile of ellipticity (with constant position angle; e.g., Wozniak et al. 1995) and $m = 2$ relative Fourier component (with constant phase angle; e.g., Aguerri et

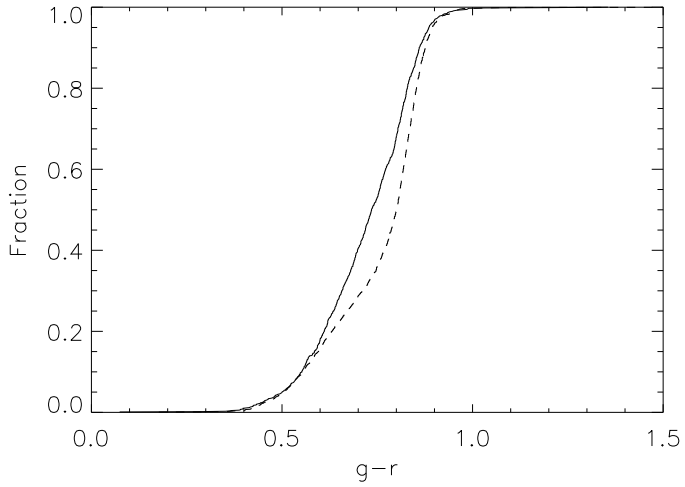

FIGURE 7.13— Fraction of barred (full line) and non-barred (dashed-line) as function of the $g - r$ galaxy color.

al. 2000), respectively.

The bar fraction depends strongly on the technique adopted for the analysis. By extensive testing on a large set of artificial galaxies, we concluded that the both methods are efficient in detecting the bars with sharp ends, such as the Ferrers and Freeman bars. On the contrary, the flat bars, which are characterized by a smooth transition to the disk, are more easily detected by the ellipse fitting method. This is particularly true for the barred galaxies hosting lenses and spiral arms, where the $m = 2$ relative Fourier component shows multiple maxima. This is the case for late-type spiral galaxies. For this reason, we decided to rely only onto the results obtained with the ellipse fitting method. We found that 45% of the disk galaxies in the sample host a bar in agreement with previous findings in optical wavebands (Marinova & Jogee 2007; Reese et al. 2007). The fraction of bars in the three different morphological bins is 32%, 55%, and 52% for lenticulars, early and late-type spirals, respectively.

The bar length was obtained by measuring the radius $r^{\epsilon}_{\rm bar}$ at which the maximum ellipticity was reached (e.g., Wozniak et al. 1995) or as the radius $r^{\rm PA}_{\rm bar}$ at which the PA changes by 5° with respect to the value corresponding to the maximum ellipticity (e.g., Erwin & Sparke 2003).

According to the analysis of the artificial galaxies, the bar length is underestimated when $r^{\epsilon}_{\rm bar}$ is used, as found by Michel-Dansac & Wozniak (2006) too. This is particularly true for the Ferrers bars. The bar length is underestimated

when $r_{\rm bar}^{\rm PA}$ is used for the Ferrers bars, but it is overestimated for the flat and Freeman bars. Nevertheless, we found a a correlation between the bar length and galaxy size. This correlation is independent of the method used for measuring the bar length and of morphological type. The larger bars are located in larger galaxies, indicating an interplay between the bar and disk in galaxy evolution.

The bar strength $f_{\rm bar}$ was estimated following the parameterization by Whyte et al. (2002) which requires the measurement of the bar ellipticity. The median values for the bar strengths of the lenticular, early-type, and late-type spiral galaxies are 0.16, 0.19, and 0.20, respectively. The bars of lenticular galaxies were found to be weaker than those in spirals, as found by Laurikainen et al. (2007) too.

No difference between the local galaxy density was found between barred and non-barred galaxies in our sample. Thus, the local environment does not seem to influence bar formation. Moreover, neither the length nor strength of the bars are correlated with the local galaxy environment. These results indicate that formation and evolution of the bars studied depend mostly on internal galaxy processes rather than external ones.

A statistically significant difference between the central light concentration of barred and non-barred galaxies was found. The bars are mostly located in less concentrated galaxies. This difference could explain the lower fraction and strength of bars detected in S0 galaxies with respect to spirals. In fact, according to the numerical simulations by Athanassoula & Misiriotis (2002) bar are weakened by large bulges. Finally, bars are hosted by bluer galaxies. This is in agreement with previous results showing that the star formation is higher in barred galaxies (Martinet & Friedli 1997; Aguerri 1999).

Bibliography

Abraham, R. G., Tanvir, N. R., Santiago, B. X., et al. 1996, MNRAS, 279, L47
Adelman-McCarthy, J. K., Ageros, M. A., Allam, S. S., et al. 2007, ApJS, 172, 634
Aguerri, J. A. L. 1999, A&A, 351, 43
Aguerri, J. A. L., Muñoz-Tuñón, C., Varela, A. M., & Prieto, M. 2000, A&A, 361, 841
Aguerri, J. A. L., Hunter, J. H., Prieto, M., et al. 2001, A&A, 373, 786
Aguerri, J. A. L., Debattista, V. P., & Corsini, E. M. 2003, MNRAS, 338, 465
Aguerri, J. A. L., Elias-Rosa, N., Corsini, E. M., & Muñoz-Tuñón, C. 2005, A&A, 434, 109
Athanassoula, E. 1992, MNRAS, 259, 328
Athanassoula, E. 2003, MNRAS, 341, 1179
Athanassoula, E., & Misiriotis, A. 2002, MNRAS, 330, 35
Athanassoula, E., Morin, S., Wozniak, H., et al. 1990, MNRAS, 245, 130
Balogh, M. L., Baldry, I. K., Nichol, R., et al. 2004a, ApJ, 615, L101

Balogh, M., Eke, V., Miller, C., et al. 2004b, MNRAS, 348, 1355
Barazza, F. D., Jogee, S., & Marinova, I. 2008, ApJ, 675, 1194
Blanton, M. R., Lupton, R. H., Schlegel, D. J., et al. 2005, ApJ, 631, 208
Block, D. L., Buta, R., Knapen, J. H., et al. 2004, AJ, 128, 183
Buta, R., & Block, D. L. 2001, ApJ, 550, 243
Buta, R., Block, D. L., & Knapen, J. H. 2003, AJ, 126, 1148
Buta, R., Laurikainen, E., Salo, H., Block, D. L., & Knapen, J. H. 2006, AJ, 132, 1859
Caon N., Capaccioli M., & D'Onofrio M., 1993, MNRAS, 265, 1013
Cepa, J., & Beckman, J. E. 1990, ApJ, 349, 497
Conselice, C. J. 2003, ApJS, 147, 1
Conselice, C. J., Bershady, M. A., & Jangren, A. 2000, ApJ, 529, 886
Contopoulos, G., & Grosbol, P. 1989, A&A Rev., 1, 261
Corsini, E. M., Debattista, V. P., & Aguerri, J. A. L. 2003, ApJ, 599, L29
Corsini, E. M., Aguerri, J. A. L., Debattista, V. P., et al. 2007, ApJ, 659, L121
Corsini, E. M. 2007, Formation and Evolution of Galaxy Bulges, eds. M. Bureau, E. Athanassoula, and B. Barbuy (Cambridge University Press, Cambridge), in press (arXiv:0709.3815)
Debattista, V. P., & Sellwood, J. A. 1998, ApJ, 493, L5
Debattista, V. P., & Sellwood, J. A. 2000, ApJ, 543, 704
de Vaucouleurs, G., de Vaucouleurs, A., Corwin, H. G., et al. 1991, Third Reference Catalogue of Bright Galaxies (Springer-Verlag, New York) (RC3)
Elmegreen, B. G., & Elmegreen, D. M. 1985, ApJ, 288, 438
Elmegreen, B. G., Elmegreen, D. M., & Hirst, A. C. 2004, ApJ, 612, 191
Erwin, P. 2004, A&A, 415, 941
Erwin, P. 2005, MNRAS, 364, 283
Erwin, P., & Sparke, L. S. 2003, ApJS, 146, 299
Eskridge, P. B., Frogel, J. A., Pogge, R. W., et al. 2000, AJ, 119, 536
Ferrers, N. M., 1877, Quart. J. Pure and Appl. Math., 14, 1
Freeman, K. C. 1966, MNRAS, 133, 47
Freeman, K. C. 1970, ApJ, 160, 811
Gerin, M., Combes, F., & Athanassoula, E. 1990, A&A, 230, 37
Gómez, P. L., Nichol, R. C., Miller, Christopher J., et al. 2003, ApJ, 584, 210
Grosbol, P. J. 1985, A&AS, 60, 261
Jedrzejewski, R. I. 1987, MNRAS, 226, 747
Jeong, H., Bureau, M., Yi, S. K., Krajnović, D., & Davies, R. L. 2007, MNRAS, 376, 1021
Jogee, S., Barazza, F. D., Rix, H-W., et al. 2004, ApJ, 615, L105
Knapen, J. H., Shlosman, I., & Peletier, R. F. 2000, ApJ, 529, 93
Kormendy, J. 1979, ApJ, 227, 714
Kormendy, J., & Kennicutt, R. C. 2004, ARA&A, 42, 603
Laine, S., Shlosman, I., Knapen, J. H., & Peletier, R. F. 2002, ApJ, 567, 97
Laurikainen, E., Salo, H., & Buta, R. 2005, MNRAS, 362, 1319
Laurikainen, E., Salo, H., Buta, R. & Knapen, J., 2007, MNRAS, 381, 401
Lindblad, P. A. B., Lindblad, P. O., & Athanassoula, E. 1996, A&A, 313, 65
MacArthur, L. A., Courteau, S., & Holtzman, J. A. 2003, ApJ, 582, 689
Mastropietro, C., Moore, B., Mayer, L., et al. 2005, MNRAS, 364, 607
Marinova, I., & Jogee, S. 2007, ApJ, 659, 1176
Martin, P. 1995, AJ, 109, 2428

Martinet, L., & Friedli, D. 1997, A&A, 323, 363
Méndez-Abreu, J., Aguerri, J. A. L., Corsini, E. M. & Simonneau, E. 2008, A&A, 478, 353
Menéndez-Delmestre, K., Sheth, K., Schinnerer, E., et al. 2007, ApJ, 657, 790
Michel-Dansac, L., & Wozniak, H. 2006, A&A, 452, 97
Miwa, T., & Noguchi, M. 1998, ApJ, 499, 149
Möllenhoff, C. 2004, A&A, 415, 63
Möllenhoff, C., & Heidt, J. 2001, A&A, 368, 16
Ohta, K., Hamabe, M., & Wakamatsu, K.-I. 1990, ApJ, 357, 71
Prieto, M., Gottesman, S. T., Aguerri, J.-A. L., & Varela, A.-M. 1997, AJ, 114, 1413
Prieto, M., Aguerri, J. A. L., Varela, A. M., & Muñoz-Tuñón, C. 2001, A&A, 367, 405
Quillen, A. C., Frogel, J. A., & Gonzalez, R. A. 1994, ApJ, 437, 162
Reese, A. S., Williams, T. B., Sellwood, J. A., Barnes, E. I., & Powell, B. A. 2007, AJ, 133, 2846
Sellwood, J. A. 2006, ApJ, 637, 567
Sellwood, J. A., & Debattista, V. P. 2006, ApJ, 639, 868
Sérsic J. L. 1968, Atlas de galaxias australes (Observatorio Astronómico, Cordoba)
Sheth, K., Regan, M. W., Scoville, N. Z., & Strubbe, L. E. 2003, ApJ, 592, L13
Sheth, K., Elmegreen, D. M., Elmegreen, B. G., et al. 2008, ApJ, 675, 1141
Shlosman, I., Peletier, R. F., & Knapen, J. H. 2000, ApJ, 535, L83
Skrutskie, M. F., Cutri, R. M., Stiening, R., et al. 2006, AJ, 131, 1163
Thompson, L. A. 1981, ApJ, 244, L43
Tremaine, S., & Weinberg, M. D. 1984, ApJ, 282, L5
Vega Beltrán,J. C., Corsini, E. M., Pizzella, A., & Bertola, F. 1997, A&A, 324, 485
Weinberg, M. D. 1985, MNRAS, 213, 451
Weiner, B. J., Sellwood, J. A., & Williams, T. B. 2001, ApJ, 546, 931
Whyte, L. F., Abraham, R. G., Merrifield, M. R., et al. 2002, MNRAS, 336, 1281
Wozniak, H., Friedli, D., Martinet, L., Martin, P., & Bratschi, P. 1995, A&AS, 111, 115
York, D. G., Adelman, J., Anderson, J. E., et al. 2000, AJ, 120, 1579

8

GASP2D v2.0: Photometric decomposition of bars

We present a new version of the fitting algorithm GASP2D to perform two-dimensional photometric decomposition of galaxy surface-brightness distributions taking into account the presence of bars. We adopted a Sérsic and an exponential profile to describe the surface-brightness distribution of the bulge and disk, respectively. The bar surface-brightness distribution can be described by either flat, elliptical or Ferrers profiles. The bulge and the disk are characterized by elliptical and concentric isophotes with constant (but possibly different) ellipticity and position angles. On the contrary, the bar component is built on a frame of generalized ellipses, where boxy and disky shapes are allowed. These ellipses have constant ellipticity and are concentric to those of the other components. We demostrate the ability of GASP2D v2.0 to recover the correct photometric structural parameters for the bulge, disk and bar components. In addition, we confirm the capacity of the code to work efficiently with the data from the Sloan Digital Sky Survey.

8.1 Introduction

While most ellipticals may be described photometrically by only one major spheroidal component, as we saw in Chapter 2, lenticular and spiral galaxies in general need at least two components: a spheroidal bulge and a flattened disk. However, the presence of bars is common in the disk of spiral galaxies. Their fraction is $\sim 70\%$ in the near-infrared (Knapen et al. 2000; Eskridge et al. 2000; Menéndez-Delmestre et al. 2007).

We would like a reliable procedure to separate the bar light from that of the disk and bulge in high-quality digital images of a large sample of galaxies. Although bars are ubiquitous and contribute a significant fraction of a galaxy's total luminosity, the distribution of the bar light fractions, shapes, and sizes in galaxies ought to be predicted by theories of galaxy formation and evolution (Athanassoula & Misiriotis 2002). In 1985, Elmegreen & Elmegreen studied the blue and near-infrared surface photometry of 15 barred galaxies, they claim that the radial profile of early-type barred galaxies tend to be uniform along the bar length (i.e., they present a flat profile) while late-type bars show an exponential-like profile. This result was later confirmed by several observational studies (Baumgart & Peterson 1986; Ohta et al. 1990; Elmegreen et al. 1996) and also found an explanation from N-body simulations (Combes & Elmegreen 1993). Also Seigar & James (1998) found both types of bars in their sample of 45 spiral galaxies. However, they did not find the correlation between the profile and Hubble type. Only a few studies dedicated to a more detailed photometric decomposition of bar galaxies are present in the literature. In 2001, Prieto et al. proposed an iterative profile-fitting routine for the decomposition of galaxy surface-brightness with bars or other morphological features as lenses or ring. They found that half of the galaxies were well described by an elliptical profile (Freeman 1966) and the other half better modeled with a flat profile (Prieto et al. 1997). Even if in the recent years a lot of studies have used two-dimensional decomposition, these algorithms have been systematically applied only to bulge-disk decompositions (Byun & Freeman 1995; Möllenhoff & Heidt 2001; MacArthur et al. 2003; Méndez-Abreu et al. 2008). In 2004, Laurikainen et al. presented for the first time a two-dimensional photometric decomposition code including the presence of a bar. In a later paper Laurikainen et al. (2005) described the code in details, in which the bar component was modeled for the first time with a Ferrers profile and the code allowed for the presence of up to three non-axisymmetric components. The most recent attempt to recover the photometric properties of barred galaxies using a multi component two-dimensional decomposition was presented by Gadotti (2008). In this paper he described the new version of the code BUDDA v2.1 and its application to a sample of 17 nearby galaxies. The bar component is parameterized by a Sérsic profile and the galaxy model also include a central component to describe the presence of an AGN. All these recent papers have pointed out the necessity of including the bar component in the photometric decomposition codes. The effects of not including the bar have important consequences in deriving the structural parameters of bulges, in the B/T ratio (Aguerri et al. 2005; Laurikainen et al. 2007), and therefore in the interpretation of the results with respect to the Hubble type and to the calculation of the total mass budget of

the universe.

In this chapter we present an upgrade of the GASP2D code. In this new version (v2.0), the decomposition algorithm is allowed to fit a bar component parametrized either by a flat, elliptical or Ferrers profile. The code, as did its predecessor, works in an automatic way so the interaction with the user is minimal. This key feature makes the code unique and perfectly suitable to work with large galaxy samples in consrast to the codes now available. The photometric models of the bulge, disk, and bar components are described in Sect. 8.2. The technical procedure to search for the inital conditions is presented in Sect. 8.3. In Sect. 8.4 we test GASP2D v2.0 comparing the results obtained decomposing high and medium signal-to-noise galaxy images. We demonstrate the ability of the code to work with the data quality provided by the Sloan Digital Sky Survey (SDSS). Finally, the conclusions are given in Sect. 8.5.

8.2 Photometric model

In Chapter 2, we presented the first version of GASP2D and described the main characteristics of this code for the photometric decomposition of the surface-brightness distribution of galaxies. Here, we present an upgrade of this code, namely GASP2D v2.0, which allows us to fit a bar component. As in the previous version, the bulge surface-brightness distribution is described in GASP2D v2.0 by a Sérsic function (Sérsic 1968)

$$I_{\rm b}(x,y) = I_{\rm e} 10^{-b_n\left[(r_{\rm b}/r_{\rm e})^{1/n}-1\right]}, \tag{8.1}$$

where (x, y) are the Cartesian coordinates described in detail in Sect. 2.2 and $r_{\rm e}$, $I_{\rm e}$, and n are the effective (or half-light) radius, the surface-brightness at $r_{\rm e}$, and a shape parameter describing the curvature of the surface-brightness profile, respectively.

The disk surface-brightness profile is described by an exponential function (Freeman 1970)

$$I_{\rm d}(x,y) = I_0\, e^{-r_{\rm d}/h}, \tag{8.2}$$

where I_0 and h are the central surface-brightness and scale-length of the disk, respectively.

The main improvement of GASP2D v2.0 with respect to GASP2D is the inclusion of an ellipsoidal bar component to the describe the galaxy surface-brightness distribution. Several parametric profiles have been used in the literature in order to fit the surface-brightness distribution of bars. In GASP2D

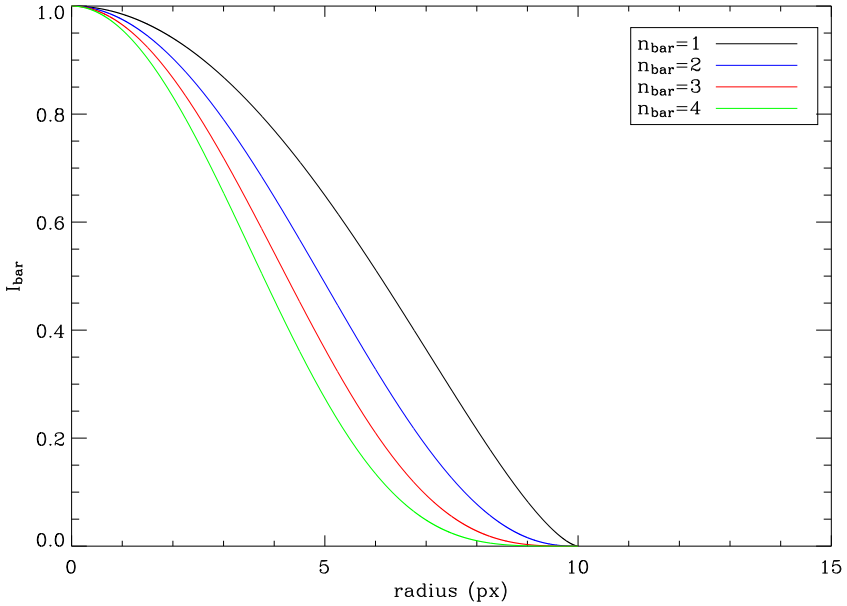

FIGURE 8.1— Surface-brightness profiles of a Ferrers bar. Different colors correspond to different values of the shape parameter ($n_{\rm bar=1,2,3,4}$). All the profiles have the same central surface-brightness ($I_{0,\rm bar}$) and the same bar length $a_{\rm bar}$=10 px.

v2.0 we modeled Ferrers bar ellipsoids (Laurikainen et al. 2005), flat bars (Prieto et al. 1997, 2001; Aguerri et al. 2003, 2005), and elliptical bars (Freeman 1966; Aguerri et al. 2005).

The projected surface density of a 3D Ferrers ellipsoid (Ferrers 1877) is given by:

$$I_{\rm bar}^{\rm Ferrers}(x,y) = I_{0,\rm bar}\left[1-\left(\frac{r_{\rm bar}}{a_{\rm bar}}\right)^2\right]^{n_{\rm bar}+0.5} \qquad r_{\rm bar} \leq a_{\rm bar}, \tag{8.3}$$

where $I_{0,\rm bar}$, $a_{\rm bar}$ and $n_{\rm bar}$ represent the central surface-brightness, length and shape parameter of the bar, respectively. All the bar models were built up in a frame of generalized ellipses (Athanassoula et al. 1990). Thus, the bar length is defined as:

$$\begin{aligned} r_{\rm bar} \;=\; & [(-(x-x_0)\sin{\rm PA_{bar}} + (y-y_0)\cos{\rm PA_{bar}})^c + \\ & - ((x-x_0)\cos{\rm PA_{bar}} + (y-y_0)\sin{\rm PA_{bar}})^c/q_{bar}^c]^{1/c}\,, \end{aligned} \tag{8.4}$$

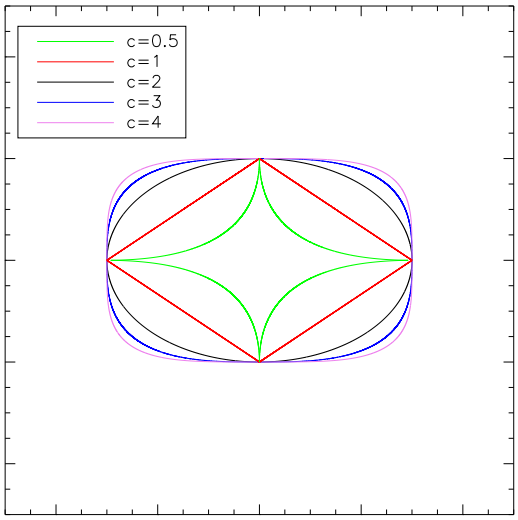

FIGURE 8.2— Ellipse shapes as a function of the c parameter. All the ellipses have the same axis ratio. The different colors correspond to different values of the c parameter.

where q_{bar} and PA_{bar} are the axis ratio and position angle of the bar, respectively. The parameter c controls the shape of the isophotes (see Fig. 8.2). The c parameter differs from the $\cos 4\theta$ Fourier coefficient. In fact, the latter applies to individual isophotes, while the former applies all the isophotes of a component. A value of $c = 2$ correspond to a perfect ellipse, $c > 2$ to a boxy shape and $c < 2$ to a disky shape.

To calculate the total luminosity associated with this profile we need to solve the following integral

$$L_{\mathrm{T,bar}}^{\mathrm{Ferrers}} = 2\pi I_{0,\mathrm{bar}} a_{\mathrm{bar}}^4 \int_0^\infty r(a_{\mathrm{bar}}^2 - r^2)^{n_{\mathrm{bar}}+0.5} dr. \tag{8.5}$$

Following Abramowitz & Stengun (1964) the general solution for this kind of integral takes the form

$$\int_0^a x^m \left(a^2 - x^2\right)^{n/2} dx \;=\; 1/2\, a^{m+n+1} \frac{\Gamma\left(\frac{m+1}{2}\right)\Gamma\left(\frac{n+2}{2}\right)}{\Gamma\left(\frac{m+n+3}{2}\right)}. \tag{8.6}$$

Due to the high degree of degeneracy that the n_{bar} parameter introduces during the fit, we decided to keep it as a fixed parameter during the fitting

process. The default value used by GASP2D v2.0 for this parameter was $n_{\rm bar} = 2$ (see also Laurikainen et al. 2005). In this particular case, the analytical expression for the total luminosity of the bar is given by

$$L_{\rm T,bar}^{\rm Ferrers} = \pi I_{0,\rm bar} a_{\rm bar}^2 \frac{\Gamma(7/2)}{\Gamma(9/2)} \frac{q_{\rm bar}}{R(c)}, \tag{8.7}$$

where $R(c)$ is a function that accounts for the area ratio between a perfect ellipse and a generalized ellipse of diskiness/boxiness parameter c. It is given by

$$R(c) = \frac{\pi(c-2)}{4\,\beta\left(\frac{1}{(c-2)}, 1+\frac{1}{(c-2)}\right)}, \tag{8.8}$$

where β is the beta function with two arguments (Abramowitz & Stengun 1964).

The surface-brightness profile corresponding to a flat bar is given by

$$I_{\rm bar}^{\rm flat}(x,y) = I_{0,\rm bar}\left[\frac{1}{1+e^{\frac{r_{\rm bar}-a_{\rm bar}}{r_{\rm s}}}}\right], \tag{8.9}$$

where $I_{0,\rm bar}$, $a_{\rm bar}$ are the central surface-brightness and length of the bar (Prieto et al. 2001; Aguerri et al. 2005). For radii larger than $a_{\rm bar}$ the surface-brightness profile falls off with a scale-length $r_{\rm s}$. The total luminosity of a flat bar is given by

$$L_{\rm T,bar}^{\rm flat} = -2\pi I_{0,\rm bar} r_{\rm s}^2 Li_2(-e^{a_{\rm bar}/r_{\rm s}}) \frac{q_{\rm bar}}{R(c)}, \tag{8.10}$$

where $Li_2(-e^{r_{\rm bar}/r_s})$ is the dilogarithm function, also known as the Jonquiere function (Abramowitz & Stengun 1964).

Finally, elliptical or Freeman bars are described by

$$I_{\rm bar}^{\rm ell}(x,y) = I_{0,\rm bar}\sqrt{1-\left(\frac{r_{\rm bar}}{a_{\rm bar}}\right)^2} \qquad r_{\rm bar} \leq a_{\rm bar}, \tag{8.11}$$

where $I_{0,\rm bar}$, $a_{\rm bar}$ are the central surface-brightness and length of the bar, respectively (Freeman 1966; Aguerri et al. 2005). The total luminosity associated with this profile is

$$L_{\rm T,bar}^{\rm ell} = \frac{2}{3}\pi I_{0,\rm bar} a_{\rm bar}^2 \frac{q_{\rm bar}}{R(c)}. \tag{8.12}$$

8.3 Technical procedure to the fit: initial conditions

As we explained in Sect. 2.6, GASP2D works automatically by minimizing the χ^2 merit function. This implies the necessity of looking for good initial estimates for all the free parameters to initialize the non-linear fit.

The number of free parameters to be fitted in the three-component model goes from 17 (Ferrers or elliptical bar) to 18 (flat bar). The search for the initial guesses for the bulge and disk parameters in GASP2D v2.0 was performed in the same way as in the previous version (see Sect. 2.6). Regarding the bar parameters, when a bar exists in the central region of a disk galaxy, the radial ellipticity profile shows a rise in the bar region and decays very sharply in the bar-disk region. In the position angle radial profile, the presence of the bar is indicated by a constant value of the position angle within the bar region. With these premises, the initial trial for the bar length was calculated using the method described in Sect. 7.3.1, which automatically measures the bar length using the position of the maximum in the ellipticity radial profile, the initial trial of the ellipticity and position angle were estimated using the algorithm presented in Sect. 7.3.1 too. The central surface-brightness of the bar was estimated simply by taking the value of the surface-brightness at the bar length. The bar model is considered, as initial input, isophotically as a pure elliptical component. This means that the shape parameter of the isophotes takes as initial trial the value $c = 2$. Finally, when the flat bar is used to perform the fit, another free parameter, the scale-length of the flat bar $r_{\rm s}$ needs to be initialized. This is implemented into GASP2D v2.0 in a purely empiral way. From the galaxy sample shown in Aguerri et al. (2005), we found that the ratio $r_{\rm s}/a_{\rm bar}$ goes from 0.05 to 0.2 with a mean value of 0.13. Therefore, the initial trial for $r_{\rm s}$ is obtained as $0.13 \times a_{\rm bar}$.

Once we have the initial guesses for all the free parameters involved in the fit, the two-dimensional non linear fit to the galaxy images is performed in the same way as in the previous version of GASP2D. A final output file with all the best fitted parameters for every galaxy is printed out. In addition, the reduced χ^2 of the fit and the luminosity ratios B/T, Bar/T, and D/T are also given.

8.4 Aplication to real galaxies

In order to test the reliability of GASP2D v2.0 in fitting bars, we analyzed the images of a subsample og galaxies studied by Aguerri et al. (2005). Their sample consist of SB0 galaxies with a smooth bar and no other components (such as spiral arms). In addition, their images were taken to have a high signal-to-noise in order to perform accurate measurements of the bar length.

A compilation of the main properties of these early-type barred galaxies is

TABLE 8.1— Parameters of the sample galaxies.

Galaxy	Type (RC3)	B_T (mag)	Distance (Mpc)
(1)	(2)	(3)	(4)
IC 874	SB0(rs)	13.60	34.7
NGC 364	(R)SB0(s):	15.61	65.1
NGC 936	$SB0^+$(rs)	11.16	14.7
NGC 2950	(R)SB0(r)	11.82	20.1
NGC 3941	SB0(s)	11.23	15.8
NGC 4340	$SB0^+$(r)	12.11	16.5

NOTE. The columns show the following: (1) galaxy name; (2) morphological classification from de Vaucouleurs et al. (1991, hereafter RC3); (3) total observed blue magnitude from Lyon Extragalactic Database (hereafter LEDA); (4) distance obtained as V_{CMB}/H_0 with $H_0 = 75$ km s^{-1} Mpc^{-1}.

given in Tab. 8.1. Details of the observations and data reduction are described in Aguerri et al. (2005). The galaxies were modeled as the sum of three component, using as model for the bar the three parametric functions described in Sect. 8.2 and following the prescription given in the previous section. The derived structural parameters, as well as those obtained by Aguerri et al. (2005) are shown in Tab. 8.2.

Aguerri et al. (2005) performed their photometric decomposition using as parametric model for the bar the flat profile. Our results obtained by GASP2D v2.0 are fully compatible with their results. When the flat profile is fitted by GASP2D, the mean differences in the bulge parameters r_e and n are $\sim$10% and $\sim$0.4, respectively, for the disk scale-length we obtain a mean difference of $\sim$16% and for the bar length and r_s the differences are $\sim$20% and $\sim$28%, respectively. When a different profile is chosen to fit the bar the differences in the bar length are $\sim$29% and $\sim$15% for the Ferrers and elliptical bars, respectively. This is an obvious result that comes from the different definition of the bar length given by the different parameterization of the bar profile. This is a common problem in dealing with the bar lenght even when non-parametric models are adopted (Michel-Dansac & Wozniak 2006).

Once the ability of GASP2D v2.0 to retrieve the right structural parameters for barred galaxies was demonstrated in high signal-to-noise images, the next step was to analyze medium signal-to-noise images retrieved from SDSS.

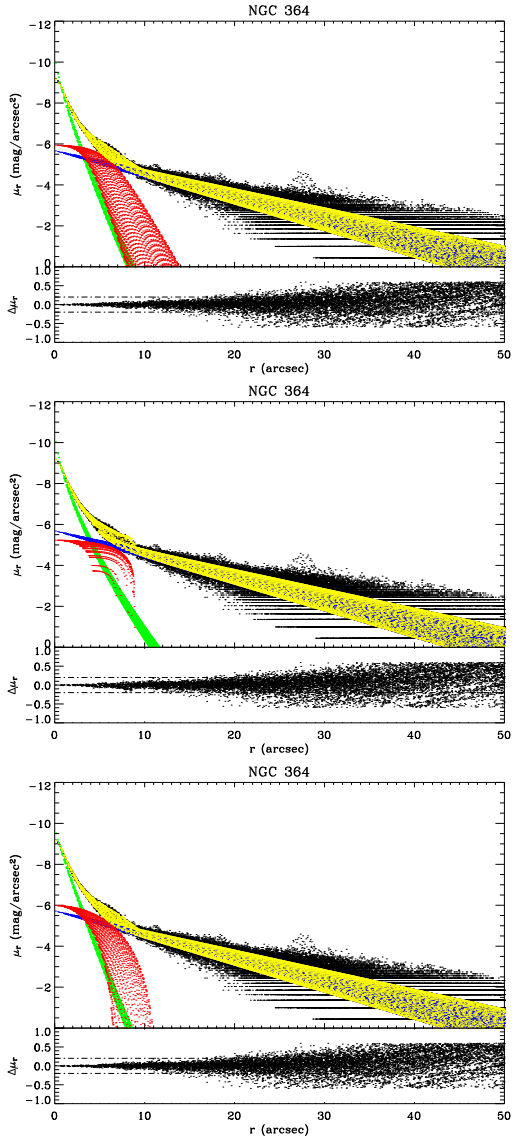

FIGURE 8.3— Result of the two-dimensional photometric decomposition of NGC 364 obtained from the SDSS $r-$band image using GASP2D v2.0. Upper panel: The black points represent the surface-brightness for every pixel in the galaxy image; the blue points represent the exponential disk surface-brightness; the green point represent the Sérsic bulge surface-brightness; the red point represent the surface-brightness of the flat bar profile and the yellow points represent the total surface-brightness of the best-fit model. The residuals of the fit for every pixel are show in the bottom panel. Middle panel: As in the upper panel but for the elliptical bar profile. Lower panel: As in the upper panel but for the Ferrers bar profile.

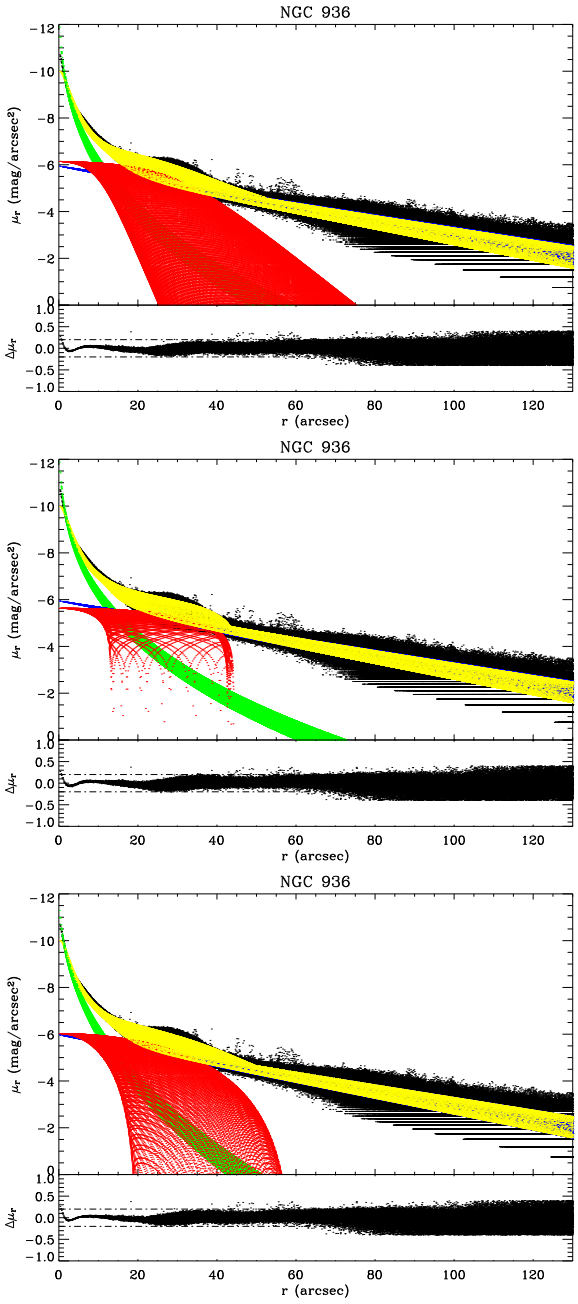

FIGURE 8.4— Result of the two-dimensional photometric decomposition of the NGC 936 obtained from the SDSS $r-$band image using GASP2D v2.0. Panels as in Fig. 8.3.

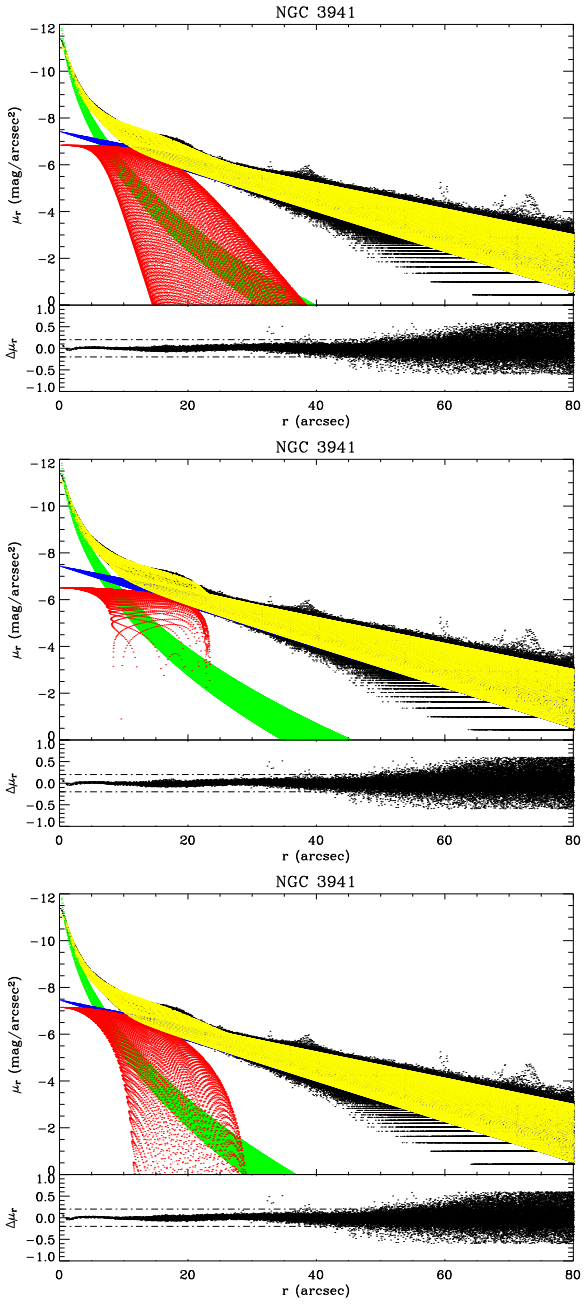

FIGURE 8.5— Result of the two-dimensional photometric decomposition of the NGC 3941 obtained from the SDSS $r-$band image using GASP2D v2.0. Panels as in Fig. 8.3.

TABLE 8.2— Photometric parameters of the sample galaxies.

Galaxy	Fit	r_e (arcsec)	n	q_b	PA_b (°)	h (arcsec)	q_d	PA_d (°)	a_{bar} (arcsec)	r_s (arcsec)	q_d	PA_{bar} (°)
(1)	(2)	(3)	(4)	(5)	(6)	(7)	(8)	(9)	(10)	(11)	(12)	(13)
IC 874	a	2.90	1.47	0.83	133.36	13.02	0.86	153.44	26.10	...	0.41	178.51
	b	3.07	1.54	0.84	139.23	12.59	0.84	161.57	18.99	...	0.38	178.83
	c	2.86	1.49	0.83	131.47	13.23	0.88	144.07	11.49	3.90	0.41	178.16
	d	2.40	1.28	...	...	14.70	...	...	15.00	3.53	...	...
NGC 364	a	2.21	1.45	0.88	48.45	15.88	0.74	31.01	16.17	...	0.55	88.11
	b	2.63	1.63	0.88	57.04	16.13	0.74	31.50	12.17	...	0.48	89.10
	c	2.15	1.40	0.88	48.77	16.18	0.73	30.14	8.24	2.10	0.56	87.74
	d	2.39	0.99	...	...	13.84	...	...	10.21	1.48	...	...
NGC 936	a	7.21	1.99	0.85	52.87	44.54	0.80	55.50	69.37	...	0.33	104.25
	b	8.15	2.13	0.87	59.39	44.33	0.81	59.36	48.42	...	0.30	104.70
	c	7.33	2.00	0.86	54.31	45.13	0.80	53.00	36.34	8.87	0.32	104.29
	d	8.36	1.40	...	...	63.72	...	...	46.20	6.62	...	...
NGC 2950	a	4.44	2.24	0.73	101.99	24.78	0.70	125.13	38.94	...	0.34	158.86
	b	4.62	2.29	0.74	103.80	23.29	0.69	131.23	28.43	...	0.30	159.75
	c	4.25	2.20	0.73	102.43	24.72	0.70	127.23	32.12	4.31	0.32	159.56
	d	8.16	3.06	...	...	35.61	...	...	32.20	2.38	...	...
NGC 3941	a	3.74	1.89	0.81	165.62	22.11	0.64	171.51	32.69	...	0.39	9.48
	b	4.20	2.00	0.80	169.44	22.12	0.63	172.46	25.75	...	0.36	9.77
	c	3.93	1.93	0.81	167.29	22.44	0.64	170.74	20.07	3.87	0.37	9.62
	d	4.24	1.70	...	...	17.70	...	...	23.63	0.96	...	...
NGC 4340	a	4.77	1.82	0.86	89.22	34.49	0.65	85.52	74.08	...	0.47	147.01
	b	4.92	1.86	0.85	90.60	33.07	0.67	89.70	51.05	...	0.46	149.85
	c	4.99	1.88	0.86	91.58	33.56	0.66	88.11	45.11	3.79	0.44	149.02
	d	5.32	1.27	...	...	33.38	...	...	61.51	2.88	...	...

NOTE. The columns show the following: (1) galaxy name; (2) type of fit performed. GASP2D three component fit assuming for the bar a Ferrers profile (a), an elliptical profile (b), a flat profile (c). The results obtained by Aguerri et al. (2005) are shown in (d) for the sake of comparison; (3) effective radius of the bulge; (4) shape parameter of the bulge; (5) axis ratio of the bulge; (6) position angle of the bulge; (7) scale-length of the disk; (8) axis ratio of the disk; (9) position angle of the disk; (10) bar length; (12) scale-length of the flat profile; (13) axis ratio of the bar; (14) position angle of the bar.

Unfortunately, only three galaxies in the subsample described above were also presents in the SDSS. The galaxy images in r-band were downloaded from the Data Archive Service (DAS) and the sky background was subtracted using the values present in the corresponding *TsField* file associated to each image. The seeing FWHMs calculated by fitting a Moffat function to the stars in each galaxy field were $1\farcs04$, $1\farcs14$ and $1\farcs08$ for NGC 364, NGC 3941 and NGC 936, respectively. A similar analysis to that on the images from Aguerri et al. (2005) was performed on the SDSS images obtaining similar results to the previous ones (see Tab. 8.3).

TABLE 8.3— Photometric parameters of the SDSS sample galaxies.

Galaxy	Fit	r_e (arcsec)	n	q_b	PA_b (°)	h (arcsec)	q_d	PA_d (°)	a_{bar} (arcsec)	r_s (arcsec)	q_d	PA_{bar} (°)
(1)	(2)	(3)	(4)	(5)	(6)	(7)	(8)	(9)	(10)	(11)	(12)	(13)
NGC 364	1	1.72	1.11	0.92	44.89	12.81	0.72	123.90	13.02	...	0.59	89.24
	2	1.92	1.50	0.90	57.76	12.96	0.72	124.49	9.84	...	0.50	88.18
	3	1.59	1.26	0.90	44.68	13.16	0.71	123.06	6.78	1.62	0.58	88.43
	4	2.39	0.99	...	...	13.84	...	...	10.21	1.48	...	...
NGC 936	1	6.18	2.24	0.82	47.11	45.70	0.79	38.24	67.33	...	0.33	101.55
	2	7.25	3.22	0.83	55.66	46.40	0.79	36.30	48.08	...	0.30	101.68
	3	5.98	2.92	0.80	46.55	46.90	0.78	40.00	32.61	9.18	0.33	101.30
	4	8.36	1.40	...	...	63.72	...	...	46.20	6.62	...	...
NGC 3941	1	3.60	2.22	0.78	165.84	21.96	0.64	102.81	33.97	...	0.39	10.05
	2	4.33	2.41	0.76	171.55	22.17	0.63	102.35	25.76	...	0.36	10.18
	3	3.87	2.27	0.77	168.17	22.21	0.64	103.24	19.51	3.78	0.37	10.19
	4	4.24	1.70	...	...	17.70	...	...	23.63	0.96	...	...

NOTE. Columns as in Tab. 8.2.

The mean differences in the fitted parameters between the fit performed in the Aguerri et al. sample and SDDS are ∼12%, ∼0.43, ∼7%, ∼7% for r_e, n, h and a_{bar}, respectively. It is important to notice that differences between the two kinds of images are due not only to their quality since effects such as the different band used (I-band and r-band for Aguerri et al. sample and SDSS, respectively) as well as variations in the seeing FWHM contributes to these differences. This confirms again the robustness and reliability of GASP2D.

8.5 Conclusions

We present the new version of the fitting algorithm GASP2D. In this upgraded version, the surface-brightness distribution of the galaxy was assumed to be the sum of the contribution of a Sérsic bulge, an exponential disk, and a realistic model of the bar light distribution. This can be modeled by an elliptical, a flat or a Ferrers profile. The bulge and disk components were characterized by elliptical and concentric isophotes with constant (but possibly different) ellipticity and position angles. The bar component was introduced using the generalized ellipse isophotes introduce by Athanassoula et al. 1990.

GASP2D v2.0 is optimized, as was the previous version, to deal with large image samples since it works automatically. In this chapter we have compared GASP2D with the one-dimensional decompositions performed by Aguerri et al. (2005). The results in the fitting parameter are in good agreement with errors of $\sim 20\%$ and $\sim 10\%$ in the bar length and bulge effective radius, respectively.

Moreover, we have demonstrated how the SDSS images of nearby galaxies are perfectly suitable to be decomposed with GASP2D, opening a new window to the study of the structural properties of bars.

Bibliography

Abramowitz, M., & Stengun, I. 1964, Handbook of Mathematical Functions (Dover, New York)
Aguerri, J. A. L., Debattista, V. P., & Corsini, E. M. 2003, MNRAS, 338, 465
Aguerri, J. A. L., Iglesias-Páramo, J., Vílchez, J. M., Muñoz-Tuñón, C., & Sánchez-Janssen, R. 2005, AJ, 130, 475
Athanassoula, E., & Misiriotis, A. 2002, MNRAS, 330, 35
Athanassoula, E., Morin, S., Wozniak, H., et al. 1990, MNRAS, 245, 130
Barazza, F. D., Jogee, S., & Marinova, I. 2008, ApJ, 675, 1194
Baumgart, C. W., & Peterson, C. J. 1986, PASP, 98, 56
Byun, Y. I., & Freeman, K. C. 1995, ApJ, 448, 563
Combes, F., & Elmegreen, B. G. 1993, A&A, 271, 391
Elmegreen, B. G., & Elmegreen, D. M. 1985, ApJ, 288, 438
Elmegreen, B. G., Elmegreen, D. M., Chromey, F. R., Hasselbacher, D. A., & Bissell, B. A. 1996, AJ, 111, 2233
Eskridge, P. B., Frogel, J. A., Pogge, R. W., et al. 2000, AJ, 119, 536
Freeman, K. C. 1966, MNRAS, 133, 47
Freeman, K. C. 1970, ApJ, 160, 811
Gadotti, D. A. 2008, MNRAS, 384, 420
Knapen, J. H., Shlosman, I., & Peletier, R. F. 2000, ApJ, 529, 93
Laurikainen, E., Salo, H., & Buta, R. 2004, ApJ, 607, 103
Laurikainen, E., Salo, H., & Buta, R. 2005, MNRAS, 362, 1319
Laurikainen, E., Salo, H., Buta, R., & Knapen, J. H. 2007, MNRAS, 381, 401
MacArthur, L. A., Courteau, S., & Holtzman, J. A. 2003, ApJ, 582, 689
Marinova, I., & Jogee, S. 2007, ApJ, 659, 1176
Méndez-Abreu, J., Aguerri, J. A. L., Corsini, E. M., & Simonneau, E. 2008, A&A, 478, 353
Menéndez-Delmestre, K., Sheth, K., Schinnerer, E., et al. 2007, ApJ, 657, 790
Michel-Dansac, L., & Wozniak, H. 2006, A&A, 452, 97
Möllenhoff, C., & Heidt, J. 2001, A&A, 368, 16
Ohta, K., Hamabe, M., & Wakamatsu, K.-I. 1990, ApJ, 357, 71
Prieto, M., Gottesman, S. T., Aguerri, J.-A. L., & Varela, A.-M. 1997, AJ, 114, 1413
Prieto, M., Aguerri, J. A. L., Varela, A. M., & Muñoz-Tuñón, C. 2001, A&A, 367, 405
Seigar, M. S., & James, P. A. 1998, MNRAS, 299, 672
Sérsic, J. L. 1968, Atlas de galaxias australes (Observatorio Astronomico, Cordoba)

9

Confirmation of a Kinematic Diagnostic for Face-On Box/Peanut-Shaped Bulges

Based on J. Méndez-Abreu, E. M. Corsini, Victor P. Debattista, S. De Rijcke, J. A. L. Aguerri and A. Pizzella, 2008, ApJ, 679, 73

We present the results of high resolution absorption-line spectroscopy of 3 face-on galaxies, NGC 98, NGC 600, and NGC 1703 with the aim of searching for box/peanut (B/P)-shaped bulges. These observations test and confirm, for the first time the prediction that face-on B/P-shaped bulges can be recognized by two minima in the profile along the bar's major axis of the fourth Gauss-Hermite moment h_4 of the line-of-sight velocity distribution (LOSVD). In NGC 98, a clear double minimum in h_4 is present along the major axis of the bar and before the end of the bar, as predicted. In contrast, in NGC 600, which is also a barred galaxy but lacks a substantial bulge, we do not find any significant kinematic signature for a B/P-shaped bulge. In NGC 1703, which is an unbarred control galaxy, we found no evidence of a B/P bulge. We also show directly that the LOSVD is broader at the location of the h_4 minimum in NGC 98 than elsewhere. This more direct method avoids possible artifacts associated with the degeneracy between the measurement of line-of-sight velocity dispersion and h_4.

9.1 Introduction

Roughly one-quarter of the visible light emitted by stars in the local universe comes out of the bulges of disk galaxies (Persic & Salucci 1992; Fukugita

et al. 1998). Understanding how bulges form is therefore of great importance in developing a complete picture of galaxy formation. The processes by which bulges form are still debated. On the one hand, the merger of dwarf-sized galactic subunits has been suggested as the main path for bulge formation (Kauffmann et al. 1993), which is supported by the relatively homogeneous bulge stellar populations of the Milky Way and M31 (Ferreras et al. 2003; Zoccali et al. 2003; Stephens et al. 2003). Bulges formed in such mergers are termed 'classical' bulges. Alternatively, bulges may form via internal 'secular' processes such as bar-driven gas inflows, bending instabilities, and clump instabilities (Combes & Sanders 1981; Pfenniger 1984; Combes et al. 1990; Pfenniger & Friedli 1991; Raha et al. 1991; Noguchi 1999; Immeli et al. 2004; Athanassoula 2005; Debattista et al. 2006). Moreover, the growth of the bulge out of disk material may also be externally trigggered by satellite accretion during minor merging events (Aguerri et al. 2001; Eliche-Moral et al. 2006) or also via external 'secular' processes. Evidence for secular bulge formation includes the near-exponential bulge light profiles (Andredakis & Sanders 1994; Andredakis et al. 1995; Courteau et al. 1996; de Jong 1996; Carollo et al. 1998; Prieto et al. 2001; Carollo et al. 2001; Carollo 1999; MacArthur et al. 2003; Erwin & Sparke 2003), a correlation between bulge and disk scale-lengths (de Jong 1996; MacArthur et al. 2003; Aguerri et al. 2005; Méndez-Abreu et al. 2008), the similar colors of bulges and inner disks (Terndrup et al. 1994; Peletier & Balcells 1996; Courteau et al. 1996; Erwin & Sparke 2003; Carollo et al. 2007), substantial bulge rotation (Kormendy 1993; Kormendy et al. 2002), and the presence of B/P-shaped bulges in $\sim 45\%$ of edge-on disk galaxies (Lütticke et al. 2000). A review of secular 'pseudo-bulge' formation and evidence for it can be found in Kormendy & Kennicutt (2004). Standard cold dark matter cosmology predicts that galaxies without classical bulges should be rare (D'Onghia & Burkert 2004). Not only are they not rare (e.g., Laurikainen et al. 2007), they are more prevalent among normal galaxies than classical bulges, exacerbating the disagreement between theory and observations (Debattista et al. 2006). It is therefore important to determine which bulges are of the classical, and which of the pseudo variety, and which are a mix of both.

N-body simulations show that barred galaxies have a tendency to develop B/P bulges (Combes & Sanders 1981; Combes et al. 1990; Pfenniger & Friedli 1991; Raha et al. 1991; Debattista et al. 2006). The fraction of edge-on galaxies with B/P bulges is comparable to the fraction of disk galaxies containing bars ($\sim 60\%$ Eskridge et al. 2000; Marinova & Jogee 2007) hinting that the two are related. The presence of bars in edge-on galaxies with B/P bulges has been established by the kinematics of gas and stars (Kuijken & Merrifield 1995; Merrifield & Kuijken 1999; Bureau & Freeman 1999; Bureau & Athanassoula

1999; Bureau & Athanassoula 2005; Vega Beltrán et al. 1997; Athanassoula & Bureau 1999; Chung & Bureau 2004). However, the degeneracy inherent in deprojecting edge-on galaxies makes it difficult to study other properties of the host galaxy. For example, simulations show that a bar can produce a B/P shape even if a massive classical bulge formed before the disk (Athanassoula & Misiriotis 2002; Debattista et al. 2005). Understanding the relative importance of classical and pseudo-bulges requires an attempt at a cleaner separation of bulges, bars and peanuts, which is easiest to accomplish in less inclined systems. In two cases, NGC 4442 (Bettoni & Galletta 1994) and NGC 7582 (Quillen et al. 1997), a B/P bulge can be recognized at inclination $i < 75^\circ$, which permits also a direct identification of the bar. No other such systems are known, however. Debattista et al. (2005) proposed a kinematic diagnostic of B/P bulges in face-on ($i < 30^\circ$) galaxies, namely a double minimum in the fourth moment, h_4, of the line-of-sight velocity distribution (LOSVD), along the major-axis of the bar. These minima occur because at the location of the B/P shape, the vertical density distribution of stars becomes broader, which leads to a double minimum in z_4, the fourth-order Gauss-Hermite moment of the vertical density distribution. The kinematic moment h_4 is then found to be an excellent proxy for the unobservable z_4. In contrast, the increase in the vertical scale-height does not produce any distinct signature of a B/P bulge and the vertical velocity dispersion, σ_z, is too strongly dependent on the radial density variation to provide a useful B/P bulge diagnostic. Debattista et al. (2006) showed that the diagnostic continues to hold even when gas is present since this sinks to a radius smaller than that of the B/P bulge.

In this chapter we present the first high resolution stellar kinematics of face-on galaxies with the goal of searching for B/P-shaped bulges and testing the diagnostic proposed by Debattista et al. (2005). In Sect. 9.2 we describe the observations of the sample and data reduction, while our results are presented in Sect. 9.3. Finally, the conclusions are given in Sect. 9.4.

9.2 Observations and data reduction

9.2.1 Sample selection

The barred galaxies NGC 98 and NGC 600 were selected as bright and undisturbed with low inclinations and resolved bars. The nearly face-on unbarred galaxy NGC 1703 was added as a control object. The main properties of the sample galaxies are given in Table 9.1.

TABLE 9.1— Parameters of the sample galaxies.

Object	Type	B_T	D_{25}	$M^0_{B_T}$	i	a_B
NGC 98	SBbc	13.4	$1\farcm7$	-22.4	$26°$	$14'' \pm 1''$
NGC 600	SBd	12.9	$3\farcm3$	-20.0	$21°$	$12'' \pm 1''$
NGC 1703	Sc	11.9	$3\farcm0$	-20.6	$15°$	

Hubble types, apparent magnitudes, and diameters are from the NASA/IPAC Extragalactic Database (NED). Absolute magnitudes are calculated from B^0_T (NED) with distance from $V_{\rm CMB}$ (NED) and $H_0 = 75$ km s^{-1} kpc^{-1}. Disk inclinations and bar semi-major axis lengths are from this chapter.

9.2.2 Long-slit spectroscopy

The spectroscopic observations were carried out in service mode at the Very Large Telescope (VLT) at the European Southern Observatory (ESO) on October 2-9 and November 2 2005. The Focal Reducer Low Dispersion Spectrograph 2 (FORS2) mounted the volume-phased holographic grism GRIS_1028z+29 with 1028 grooves mm^{-1} and the $0\farcs7 \times 6\farcm8$ slit. The detector was a mosaic of 2 MIT/LL CCDs, each with 2048×2068 pixels of 15×15 μm^2. The wavelength range from 7681 to 9423 Å was covered in the reduced spectra with a reciprocal dispersion of 0.858 Å pixel^{-1} and a spatial scale of $0\farcs250$ pixel^{-1} after a 2×2 pixel binning. The spectra were taken along the bar major-axis of NGC 98 (P.A. = $32\fdg2$) and NGC 600 (P.A. = $22\fdg1$) and along the disk major-axis of NGC 1703 (P.A. = $148\fdg8$). The P.A.'s were determined from ellipse fits to the Two-Micron All Sky Survey (2MASS) $J-$band archival images. The total integration time for each galaxy was 3 hours, in four exposures of 45 minutes each. Comparison lamp exposures obtained for each observing night ensured accurate wavelength calibrations. Spectra of G and K giant stars served as kinematic templates. The average seeing FWHM was $1\farcs3$ for NGC 98, $0\farcs9$ for NGC 600, and $0\farcs9$ for NGC 1703 as measured from the ESO Differential Imaging Meteo Monitor.

Using standard IRAF[1] routines, all the spectra were bias subtracted, flat-field corrected, cleaned of cosmic rays, corrected for bad pixels, and wavelength calibrated as in Debattista et al. (2002). The accuracy of the wavelength rebinning (≈ 1 km s^{-1}) was checked by measuring wavelengths of the brightest night-sky emission lines. The instrumental resolution was 1.84 ± 0.01 Å (FWHM) corresponding to $\sigma_{\rm inst} = 27$ km s^{-1} at 8552 Å. The spectra obtained

[1]IRAF is distributed by NOAO, which is operated by AURA Inc., under contract with the National Science Foundation.

for a given galaxy were co-added using the center of the stellar continuum as reference. In the resulting spectra the sky contribution was determined by interpolating along the outermost $\approx 30''$ at the edges of the slit and then subtracted.

9.2.3 Photometry

We analyzed the uncalibrated acquisition images from the VLT to derive the photometric properties of the sample galaxies. Isophote-fitting with ellipses, after masking foreground stars and bad pixels, was carried out using the IRAF task ELLIPSE. Under the assumption that the outer disks are circular, their inclination was determined by averaging the outer isophotes. All 3 galaxies have $i < 30^\circ$ (Table 9.1). The semi-major axis length, a_B, of the bars of NGC 98 and NGC 600 (Table 9.1) was measured from a Fourier decomposition as in Aguerri et al. (2000).

9.2.4 Kinematics

The stellar kinematics of the three galaxies were measured from the galaxy absorption features present in the wavelength range centered on the Ca II triplet ($\lambda\lambda$ 8498, 8542, 8662 Å) using the Penalized Pixel Fitting method (pPXF, Cappellari & Emsellem 2004). The spectra were rebinned along the dispersion direction to a logarithmic scale, and along the spatial direction to obtain a signal-to-noise ratio $S/N \gtrsim 40$ Å^{-1}, which decreases to $S/N = 20$ Å^{-1} at the outermost radii.

A linear combination of the template stellar spectra, convolved with the line-of-sight velocity distribution (LOSVD) described by the Gauss-Hermite expansion by van der Marel & Franx (1993) was fitted to each galaxy spectrum by χ^2 minimization in pixel space. This allowed us to derive profiles of the mean velocity ($v_{\rm los}$), velocity dispersion ($\sigma_{\rm los}$), third (h_3), and fourth-order (h_4) Gauss-Hermite moments. The uncertainties in the kinematic parameters were estimated by Monte Carlo simulations with photon, read out and sky noise. Extensive testing on simulated galaxy spectra was performed to provide an estimate of the biases of the pPXF method with the adopted instrumental setup and spectral sampling. The simulated spectra were obtained by convolving the template spectra with a LOSVD parametrized as a Gauss-Hermite series and measured as if they were real. No bias was found in the ranges of S/N and $\sigma_{\rm los}$ which characterize the spectra of the sample galaxies. The values of h_3 and h_4 measured for the simulated spectra differ from the intrinsic ones only within the measured errors (see also Emsellem et al. 2004).

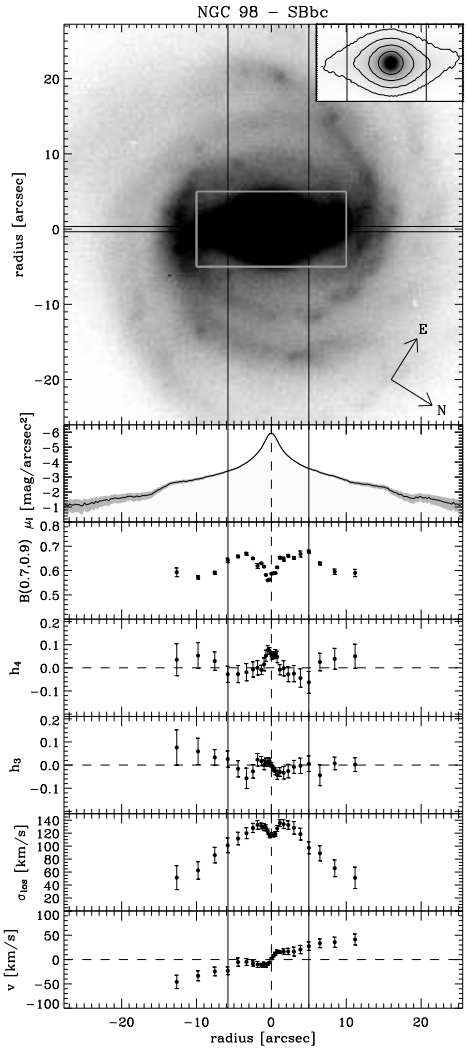

FIGURE 9.1— Morphology and stellar kinematics of NGC 98. The top panel shows the VLT/FORS2 $I-$band image. The slit position and image orientation are indicated. The inset shows the portion of the galaxy image marked with a white box. The gray scale and isophotes were chosen to enhance the features observed in the central regions. The remaining panels show from top to bottom the radial profiles of surface-brightness (extracted along the slit with an arbitrary zero point), $\mathcal{B}(0.7, 0.9)$, h_4, h_3, $\sigma_{\rm los}$, and velocity v (obtained by subtracting the systemic velocity from $v_{\rm los}$). The two vertical lines indicate the location of the h_4 minima in NGC 98.

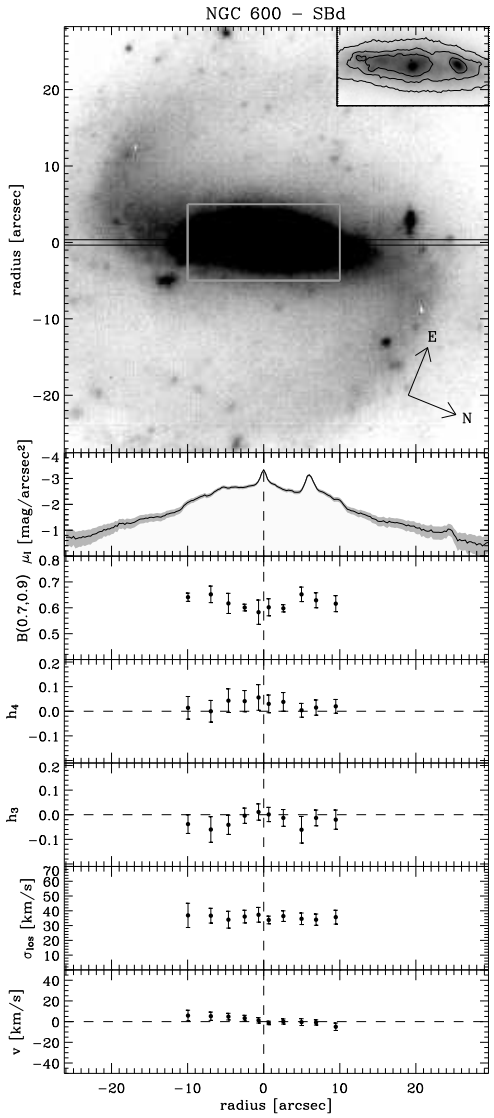

FIGURE 9.2— Morphology and stellar kinematics of NGC 600. Panels as in Fig. 9.1.

9.3 Results

The photometric and kinematic profiles of the sample of galaxies are shown in Figs. 9.1, 9.2, and 9.3. For the unbarred galaxy, NGC 1703, the h_4 profile shows no sign of a minimum. The same is true for the almost bulgeless, barred

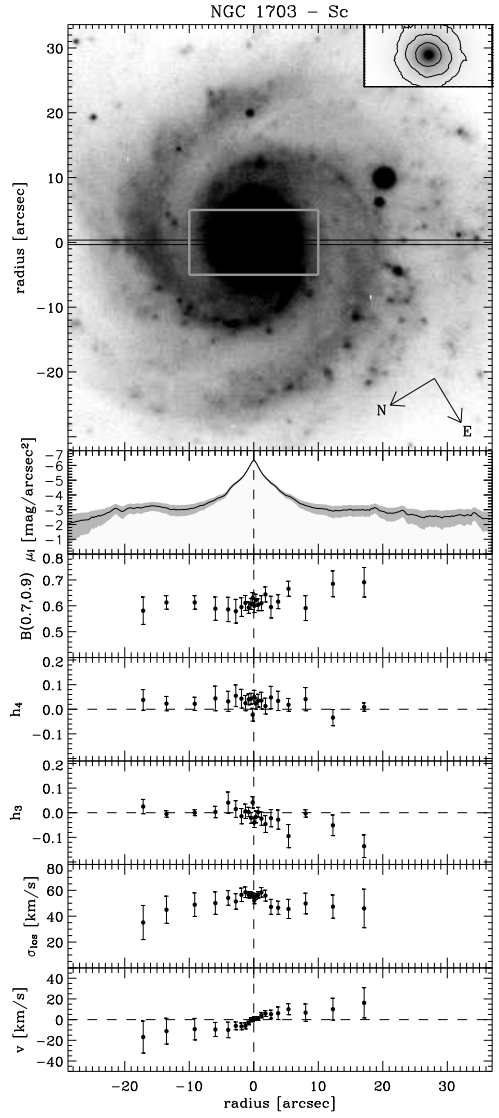

FIGURE 9.3— Morphology and stellar kinematics of NGC 1703. Panels as in Fig. 9.1.

NGC 600. In both these galaxies $\sigma > 30$ km s^{-1}, including within the bar in NGC 600. Thus, our failure to find an h_4 minimum cannot be ascribed to low spectral resolution. In NGC 98, instead, we find a double minimum in the h_4 profile. The two minima are symmetric with respect to the galaxy center

($|r| \approx 5''$). In the simulations of Debattista et al. (2005) the minima in h_4 are $\sim 0.05 - 0.1$ deep, comparable to the minima in the profile of NGC 98.

We confirmed that our kinematics, and minima in h_4 are not a result of details of the pPXF method by repeating the analysis using the Fourier Correlation Quotient (FCQ) method (Bender 1990) as in Pizzella et al. (2008). Nonetheless expansions in Gauss-Hermite moments are degenerate (Gerhard 1993; van der Marel & Franx 1993) since, for the even moments, it is possible to obtain comparably good fits by trading $\sigma_{\rm los}$ for h_4. In order to confirm that the signature of a B/P bulge obtained in NGC 98 is not due to a conspiracy of such degeneracies we introduced an LOSVD broadening measure defined for each radius as

$$\mathcal{B}(x_1, x_2) \equiv W(x_2)/W(x_1), \tag{9.1}$$

where

$$W(x) = \int_{v_{\rm los}^{\rm min}}^{v_{\rm los}^{\rm max}} F(v) dv, \tag{9.2}$$

with $F(v)$ the cumulative distribution of the LOSVD. The values of $v_{\rm los}^{\rm min}$ and $v_{\rm los}^{\rm max}$ correspond to $F(v_{\rm los}^{\rm min}) = 0.5\,(1-x)$ and $F(v_{\rm los}^{\rm max}) = 0.5\,(1+x)$, respectively. $\mathcal{B}(x_1, x_2)$ has the advantage of not being sensitive to the wings of the distribution (unlike the kurtosis), and is a non-parametric measure of the LOSVD shape. Experiments with N-body simulations, including those presented in Debattista et al. (2005), showed that $\mathcal{B}(0.7, 0.9)$ is a useful peanut diagnostic in the same spirit as h_4. Figs. 9.1, 9.2, and 9.3 plot $\mathcal{B}(0.7, 0.9)$. A clear peak in the broadening is apparent at $|r| \simeq 5''$ in NGC 98. We conclude that the evidence for a B/P-shaped bulge in NGC 98 is robust.

9.4 Conclusions

We have identified a B/P-shaped bulge in one galaxy from a sample of three face-on galaxies. In the unbarred control galaxy NGC 1703 we had not expected to find a B/P bulge. The failure to find a double-minimum in h_4 is therefore fully consistent with previous results (Chung & Bureau 2004). Of the two barred galaxies, NGC 98 has clear evidence of a B/P bulge while NGC 600 does not. The absence of a B/P shape in the latter galaxy is not surprising since it appears to not have a bulge and its bar has a lumpy structure.

If we identify the radius of the B/P bulge, $\rm R_{B/P}$, with the location of the minimum in h_4, as found in simulations (Debattista et al. 2005), then we find $\rm R_{B/P} \simeq 0.35 a_B$, where $\rm a_B$ is the bar semi-major axis. Similarly, (Kormendy & Kennicutt 2004) noted that the maximum radius of the boxy bulge is about one-third of the bar radius. Simulations also produce B/P-bulges which are generally smaller than the bar (Shen & Sellwood 2004; Debattista et al. 2005).

While observations have established the presence of bars in the majority of systems with B/P-bulges, the converse has not been established. (Debattista et al. 2005) demonstrate how the presence of a classical bulge can in some cases mask the presence of B/P bulge. Moreover, the ratio of radii of bulges and B/P bulges is determined by resonances. For these various reasons it would be very instructive to repeat measurements such as here for a sample of barred galaxies.

Bibliography

Aguerri, J. A. L., Muñoz-Tuñón, C., Varela, A. M., & Prieto, M. 2000, A&A, 361, 841
Aguerri, J. A. L., Balcells, M., & Peletier, R. F. 2001, A&A, 367, 428
Aguerri, J. A. L., Elias-Rosa, N., Corsini, E. M., & Muñoz-Tuñón, C. 2005, A&A, 434, 109
Andredakis, Y. C., & Sanders, R. H. 1994, MNRAS, 267, 283
Andredakis, Y. C., Peletier, R. F., & Balcells, M. 1995, MNRAS, 275, 874
Athanassoula, E. 2005, MNRAS, 358, 1477
Athanassoula, E., & Bureau, M. 1999, ApJ, 522, 699
Athanassoula, E., & Misiriotis, A. 2002, MNRAS, 330, 35
Bender, R. 1990, A&A, 229, 441
Bettoni, D., & Galletta, G. 1994, A&A, 281, 1
Bureau, M., & Athanassoula, E. 1999, ApJ, 522, 686
Bureau, M., & Athanassoula, E. 2005, ApJ, 626, 159
Bureau, M., & Freeman, K. C. 1999, AJ, 118, 126
Cappellari, M., & Emsellem, E. 2004, PASP, 116, 138
Carollo, C. M. 1999, ApJ, 523, 566
Carollo, C. M., Stiavelli, M., & Mack, J. 1998, AJ, 116, 68
Carollo, C. M., Stiavelli, M., de Zeeuw, P. T., Seigar, M., & Dejonghe, H. 2001, ApJ, 546, 216
Carollo, C. M., Scarlata, C., Stiavelli, M., Wyse, R. F. G., & Mayer, L. 2007, ApJ, 658, 960
Chung, A., & Bureau, M. 2004, AJ, 127, 3192
Combes, F., & Sanders, R. H. 1981, A&A, 96, 164
Combes, F., Debbasch, F., Friedli, D., & Pfenniger, D. 1990, A&A, 233, 82
Courteau, S., de Jong, R. S., & Broeils, A. H. 1996, ApJ, 457, L73
de Jong, R. S. 1996, A&A, 313, 45
Debattista, V. P., Corsini, E. M., & Aguerri, J. A. L. 2002, MNRAS, 332, 65
Debattista, V. P., Carollo, C. M., Mayer, L., & Moore, B. 2005, ApJ, 628, 678
Debattista, V. P., Mayer, L., Carollo, C. M., et al. 2006, ApJ, 645, 209
D'Onghia, E., & Burkert, A. 2004, ApJ, 612, L13
Eliche-Moral, M. C., Balcells, M., Aguerri, J. A. L., & González-García, A. C. 2006, A&A,457, 91
Emsellem, E., Cappellari, M., Peletier, R. F., et al. 2004, MNRAS, 352, 721
Erwin, P., Beltrán, J. C. V., Graham, A. W., & Beckman, J. E. 2003, ApJ, 597, 929
Eskridge, P. B., Frogel, J. A., Pogge, R. W., et al. 2000, AJ, 119, 536
Ferreras, I., Wyse, R. F. G., & Silk, J. 2003, MNRAS, 345, 1381
Fukugita, M., Hogan, C. J., & Peebles, P. J. E. 1998, ApJ, 503, 518
Gerhard, O. E. 1993, MNRAS, 265, 213

Immeli, A., Samland, M., Gerhard, O., & Westera, P. 2004, A&A, 413, 547
Kauffmann, G., White, S. D. M., & Guiderdoni, B. 1993, MNRAS, 264, 201
Kormendy, J. 1993, Galactic Bulges, ed. H. DeJonghe & H. J. Habing (Kluwer Academic Publishers, Dordrecht), 153, 209
Kormendy, J., & Kennicutt, R. C. 2004, ARA&A, 42, 603
Kormendy, J., Bender, R., & Bower, G. 2002, The Dynamics, Structure & History of Galaxies: A Workshop in Honour of Professor Ken Freeman, ed. G. S. Da Costa and H. Jerjen (ASP, San Francisco), 273, 29
Kuijken, K., & Merrifield, M. R. 1995, ApJ, 443, L13
Laurikainen, E., Salo, H., Buta, R., & Knapen, J. H. 2007, MNRAS, 381, 401
Lütticke, R., Dettmar, R.-J., & Pohlen, M. 2000, A&AS, 145, 405
MacArthur, L. A., Courteau, S., & Holtzman, J. A. 2003, ApJ, 582, 689
Marinova, I., & Jogee, S. 2007, ApJ, 659, 1176
Méndez-Abreu J., Aguerri J. A. L., Corsini E. M., & Simonneau E., 2008, A&A, 478, 353
Merrifield, M. R., & Kuijken, K. 1999, A&A, 345, L47
Noguchi, M. 1999, ApJ, 514, 77
Peletier, R. F., & Balcells, M. 1996, AJ, 111, 2238
Persic, M., & Salucci, P. 1992, MNRAS, 258, 14
Pfenniger, D. 1984, A&A, 134, 373
Pfenniger, D., & Friedli, D. 1991, A&A, 252, 75
Pizzella, A., Corsini, E. M., Sarzi, et al. 2008, MNRASin press (arXiv:0803.2689)
Prieto, M., Aguerri, J. A. L., Varela,A. M., & Muñoz-Tuñón, C. 2001, A&A, 367, 405
Quillen, A. C., Kuchinski, L. E., Frogel, J. A., & Depoy, D. L. 1997, ApJ, 481, 179
Raha, N., Sellwood, J. A., James, R. A., & Kahn, F. D. 1991, Nature, 352, 411
Shen, J., & Sellwood, J. A. 2004, ApJ, 604, 614
Stephens, A. W., et al. 2003, AJ, 125, 2473
Terndrup, D. M., Davies, R. L., Frogel, J. A., Depoy, D. L., & Wells, L. A. 1994, ApJ, 432, 518
van der Marel, R. P., & Franx, M. 1993, ApJ, 407, 525
Vega Beltrán J. C., Corsini E. M., Pizzella A., & Bertola F., 1997, A&A, 324, 485
Zoccali, M., Renzini, A., Ortolani, S., et al. 2003, A&A, 399, 931

10

Conclusions

The aim of this thesis was to shed some light on the formation and evolution scenarios for the bulges in disk galaxies proposed until now, i.e., monolithic collapse, hierarchical merger, and secular evolution. Througout this thesis, we have presented a series of new results spanning the most important issues in extragalactic astronomy of individual galaxies, i.e., their structure, stellar populations, and kinematics. The necessity, in the scientific comunity, for a new code to photometrically decompose galaxies with three components (bulge, disk, and bar) was our main concern when we started this thesis. To fill this gap, we developed a new quantitative morphological analysis based on the new code GASP2D. The power and utility of GASP2D has been proved throughout this thesis by using the code with different samples of nearby galaxies.

The conclusions of this thesis can be summarized in three main points: 1) The typical scaling relations for galaxies cannot be used alone to distinguish between the different formation scenarios proposed until now since different models are able nowdays to reproduce these relations. However, measuring the intrinsic structural properties represents an useful step forward in this field and sets new constraints that should be reproduce by simulations. 2) The kinematic and stellar population properties of the bulge give strong additional constraints on bulge formation. This information combined with the structural properties of the galaxies can help to obtain the more general picture of bulges needed to unveil their formation mechanism. 3) The link between bulges and bars appears to be fundamental to understand the formation of both components. The existence of boxy/peanut bulges and their relation with bars can be now investigated by a new kinematic diagnostic that can be applied in face-on galaxies.

This result opens a new line of research which will help to give a more general scheme of bulge formation and evolution.

10.1 Summary of the main results

10.1.1 GASP2D: A new two-dimensional photometric decomposition code (*Chapter 2 & Chapter 8*)

We presented a new fitting algorithm, GASP2D, to perform two-dimensional photometric decomposition of galaxy images. The surface-brightness distribution of the galaxy was assumed to be the sum of the contribution of a Sérsic bulge, an exponential disk and a bar component which can be modeled with a flat, an elliptical or a Ferrers profile. The bulge and disk components were characterized by elliptical and concentric isophotes with constant (but possibly different) ellipticity and position angles. The bar component was characterized in the same way but using the generalized ellipses introduce by Athanassoula et al. 1990.

GASP2D is optimized to deal with large image samples since it is implemented to work mainly in batch mode, and it adopts a robust Levenberg-Marquardt fitting algorithm in order to obtain reliable estimates of the galaxy structural parameters. We have sucessfully applied the code to very different sets of images demonstrating its versatility. In addition, we have shown how the Sloan Digital Sky Survey (SDSS) images of nearby galaxies are perfectly suitable to be decomposed with GASP2D, opening a new window on the study of the structural properties of galaxies using a three component (bulge, disk, and bar) photometric decomposition.

10.1.2 Scaling relations in disk galaxies (*Chapter 3*)

The $J-$band bulge and disk structural parameters of a magnitude-limited sample of 148 unbarred S0-Sb galaxies were investigated to constrain the dominant mechanism at the epoch of bulge assembly. These parameters were derived using the new code GASP2D.

The bulges of the sample galaxies follow the same fundamental plane, Faber-Jackson and photometric plane relationships found for elliptical galaxies, supporting the idea that bulges and ellipticals formed in the same way. However, tight correlations between the parameters of bulges and disks were found. In fact, the disk scale-lengths increase with both the central velocity dispersion and bulge effective radius. This link has been usually interpreted as an indication of the formation of bulges via secular evolution of their host disks. In addition, our measurements of the exponential scale-length of the bulge and disk as well as of bulge shape parameter are also fully consistent with numerical

simulations of the effects mergers on the mass distribution of the bulge and disk in galaxies formed in hierarchical clustering scenarios. Therefore, these results indicate that the above scaling relations alone are not enough to clearly distinguish between bulges formed by early dissipative collapse, merging or secular evolution.

10.1.3 The intrinsic shape of bulges (*Chapter 4*)

The probability distribution function (PDF) of the intrinsic equatorial ellipticity of the bulges described in chapter 3 was derived from the distribution of the observed ellipticities of bulges and their misalignments with disks. We have found that $\sim 80\%$ of bulges in unbarred lenticular and early-to-intermediate spiral galaxies are not oblate but triaxial ellipsoids. Their mean axial ratio in the equatorial plane is $\langle B/A \rangle = 0.85$. We did not find any significant dependence of the PDF on the galaxy morphology, light concentration, and luminosity of bulges. In addition, the derived PDF is independent of the possible presence of nuclear bars. The intrinsic structural properties of bulges represent a further constraint on their formation when comparing observations with numerical simulations.

10.1.4 Structure and stellar populations of nearby bulges (*Chapter 5*)

The structural parameters and properties of the stellar population of the bulges of sample of 14 S0 and spiral galaxies of the Fornax, Eridanus and Pegasus cluster, and NGC 7582 group were investigated to constrain the dominant mechanism at the epoch of their assembly. Correlations between Mg_2, $\langle \mathrm{Fe} \rangle$, H_β, and σ were found. According to the central age and metallicity, three classes of objects were identified. The youngest bulges have an average age of 2 Gyr. They are characterized by ongoing star formation. The stellar population of intermediate-age bulges is 4 to 8 Gyr old. It has solar metallicity ($[Z/\mathrm{H}] = 0.0$ dex). The older bulges have a narrow distribution in age around 10 Gyr and high metallicity ($[Z/\mathrm{H}] = 0.30$ dex). Most of the sample bulges display solar α/Fe ratios. A few have a central super-solar ratio ($[\alpha/\mathrm{Fe}] = 0.3$).

There is a correlation with the velocity dispersion. The more massive bulges of our sample galaxies are older, more metal rich and characterized by fast star formation. Since we did not find any correlation with galaxy morphology we exclude a strong interplay between the bulge and disk components.

Most of the sample galaxies show no gradient in age and a negative gradient of metallicity. The presence of a negative gradient in the metallicity radial profile favors a scenario with bulge formation via dissipative collapse. This

implies strong inside-out formation that should give rise to a negative gradient in the α/Fe ratio too (Ferreras & Silk 2002). But, no gradient was measured in the [α/Fe] radial profiles for any of the galaxies, except for NGC 1366 and NGC 7531. Moreover, the correlation between the central value and gradient of metallicity can not be caused by pure dissipative collapse (Bekki & Shioya 1999; Kobayashi & Arimoto 1999) and suggests that mergers or acquisition events need to be invoked during the bulge assembly.

The peculiar gradients observed for the stellar population of the bulges of NGC 1366 and NGC 7531 suggest they host a substructure. Very interestingly, in NGC 1366 we found the presence of a kinematically-decoupled component. It is younger than the host bulge and formed by enriched material probably acquired via interaction or minor merging.

According to the prescriptions by Kormendy & Kennicutt (2004) the bulge of NGC 1292 is a pseudobulge. The properties of its stellar population are consistent with a slow buildup within a scenario of secular evolution. Indeed, the bulge of NGC 1292 has a intermediate age (3 Gyr) and low metal content ([Z/H]$= -0.7$ dex). The α/Fe ratio is the lowest in our sample ([α/Fe]$= -0.12$ dex) suggesting a prolonged star formation history. The presence of emission lines in the spectrum is a signature of ongoing star formation.

10.1.5 Structure and dynamics of low surface-brightness galaxies (*Chapter 6*)

We have investigated the structural parameters and kinematic properties of 6 galaxies with low surface-brightness (LSB) disks. The presence of LSB disks in our sample galaxies was confirmed by carrying out a careful two-dimensional photometric bulge-disk decomposition using GASP2D. Our photometric analysis further revealed that our LSB galaxies have bulges that are well described by a Sérsic profile with an index $n \lesssim 2$, with a few of them displaying an apparent flattening rather similar to that of their surrounding disk. According to Kormendy & Kennicutt (2004), these disk-like features are the photometric signature of a pseudobulge.

In all targets, the depth of our data allowed us to measure the stellar and ionized-gas kinematics out to a surface-brightness level $\mu_R \approx 24$ mag arcsec^{-2}, comfortably reaching the outer disk regions where the rotation curve flattens.

We derived central values for the stellar velocity dispersion of σ_c and measured the circular velocity in the outskirts of our sample galaxy $V_{\rm c}$ by following the flat portion of the gas rotation curve.

Deviations from perfect circular gas motions are by no means limited to the minor-axis direction in our sample galaxies. Along the major-axes of our targets

(or the closest diagonal direction) the ionized-gas velocity curve is characterized by an higher degree of asymmetry and irregularity than the stellar curve. As a consequence, to derive the gas rotation curve it is often necessary to smooth the data over large radial bins before folding the gas velocities around the center of symmetry. This is not the case for the stars, since their velocities measured fold quite well and do not show sharp wiggles and bumps.

The main conclusion of this chapter is that the stellar kinematics of galaxies with LSB disks is less affected than the ionized-gas kinematics one by large-scale asymmetries and small-scale irregularities. The gas velocities have been found to deviate from the from the circular velocity in particular and more often in the inner regions of our sample galaxies. Unless the regularity of the ionized-gas motions can be establish with integral-field data, our findings strongly suggest that stars are more suitable to trace the mass distribution of galaxies with a LSB disk, in particular when the inner slope of the dark matter halo is the central question that one wishes to answer.

10.1.6 Properties of bars in the nearby universe (*Chapter 7*)

We have studied the fraction and properties of bars in a sample of $\sim$ 3000 galaxies extracted from the SDSS-DR5. This is a volume-limited sample of non-interacting galaxies in the redshift range $0.01 < z < 0.04$, with an absolute magnitude range $M_{\rm r} < -20$, and an inclination range $i < 60^{\circ}$. Our final sample consists of 30% of ellipticals, 26% of lenticulars, 18% of early-, and 25% of late-type spirals.

We derived the fraction of barred galaxies by analyzing the SDSS $r-$band images of the sample galaxies with the ellipse fitting and Fourier methods. The bar fraction derived depends strongly on the technique adopted for the analysis. By extensive testing on a large set of artificial galaxies, we concluded that the both methods are efficient in detecting the bars with sharp ends, such as the Ferrers and elliptical bars. On the contrary, the flat bars, which are characterized by a smooth transition to the disk, are more easily detected by the ellipse fitting method. For this reason, we decided to rely only onto the results obtained with the ellipse fitting method. We found that 45% of the disk galaxies in the sample host a bar in agreement with previous findings in optical wavebands (Marinova & Jogee 2007; Reese et al. 2007). The fraction of bars in the three different morphological bins is 32%, 55%, and 52% for lenticulars, early and late-type spirals, respectively.

The bar length was obtained by measuring the radius $r^{\epsilon}_{\rm bar}$ at which the maximum ellipticity was reached (e.g., Wozniak et al. 1995) or as the radius $r^{\rm PA}_{\rm bar}$ at which the PA changes by 5° with respect to the value corresponding

to the maximum ellipticity (e.g., Erwin & Sparke 2003). According to the analysis of the artificial galaxies, the bar length is underestimated when $r^{\epsilon}_{\rm bar}$ is used, as found by Michel-Dansac & Wozniak (2006) too. The bar length is underestimated when $r^{\rm PA}_{\rm bar}$ is used for the Ferrers bars, but is is overestimated for the flat and Freeman bars. Nevertheless, we found a a correlation between the bar length and galaxy size. This correlation is independent of the method used for measuring the bar length and of morphological type. The larger bars are located in larger galaxies, indicating an interplay between the bar and disk in the galaxy evolution.

The bar strength $f_{\rm bar}$ was estimated following the parameterization by Whyte et al. (2002) which requires the measurement of the bar ellipticity. The bars of lenticular galaxies were found to be weaker than those of host by spirals, as found by Laurikainen et al. (2007) too.

No difference between the local galaxy density was found between barred and non-barred galaxies in our sample. Thus, they share the same local environment. Moreover, neither the length nor strength of the bars are correlated with the local galaxy environment. These results indicate that formation and evolution of the bars studied depend mostly on internal galaxy processes rather than external ones.

A statistical significant difference between the central light concentration of barred and non-barred galaxies was found. The bars are mostly located in less concentrated galaxies. This difference could explain the lower fraction and strength of bars detected in S0 galaxies with respect to spirals.

Finally, bars are hosted by bluer galaxies. This is in agreement with previous results showing that the star formation is higher in barred galaxies (Martinet & Friedli 1997; Aguerri 1999).

10.1.7 Boxy/Peanuts bulges in Face-on galaxies (*Chapter 9*)

We have identified a B/P-shaped bulge in one galaxy from a sample of three face-on galaxies. In the unbarred control galaxy NGC 1703 we had not expected to find a B/P bulge. The failure to find a double-minimum in h_4, which the kinematic signature of the presence of a B/P structure, is therefore fully consistent with previous results (Chung & Bureau 2004). Of the two barred galaxies, NGC 98 has clear evidence of a B/P bulge while NGC 600 does not. The absence of a B/P shape in the latter galaxy is not surprising since it appears not to have a bulge and its bar has a lumpy structure.

If we identify the radius of the B/P bulge, $\rm R_{B/P}$, with the location of the minimum in h_4, as found in simulations (Debattista et al. 2005), then we find $\rm R_{B/P} \simeq 0.35 a_B$, where $\rm a_B$ is the bar semi-major axis. Similarly, Kormendy &

Kennicutt (2004) noted that the maximum radius of the boxy bulge is about one-third of the bar radius. Simulations also produce B/P-bulges which are generally smaller than the bar (Shen & Sellwood 2004; Debattista et al. 2005).

While observations have established the presence of bars in the majority of systems with B/P-bulges, the converse has not been established. Debattista et al. (2005) demonstrate how the presence of a classical bulge can in some cases mask the presence of B/P bulge. For these various reasons it would be very instructive to repeat measurements such as here for a sample of barred galaxies.

10.2 Future work

The analysis and results presented here have led to a series of shorten and long term projects which already started but were not ready to be included in this thesis:

10.2.1 Intrinsic shape of bulges

In Chapter 4, we demonstrated how bulges in disk galaxies are not oblate structures but mildly triaxial ellipsoids by calculating the probability distribution function of the intrinsic equatorial ellipticity. However, to fully characterize the three-dimensional structure of bulges, the intrinsic flattening must be calculated too. Unfortunately, the mathematical treatment of the intrinsic flattening is different from that of the intrinsic ellipticity since it is not possible to separate the observational and intrinsic parameters in a single equation. We have recently found the mathematical formalism to derive the intrinsic flattening for a single galaxy, that can be understand as the counterparts of the Sect. 4.4. The probability distribution function of the intrinsic flattening of bulges is ongoing work, which will give us an important piece of information for understanding the formation of bulges.

10.2.2 Photometric decomposition of barred galaxies

Since $\sim$ 40% of galaxies in the optical (Marinova & Jogee 2007; Barazza et al. 2008; Aguerri et al. 2008) and $\sim$ 60% in the near infrared (Eskridge et al. 2000; Menéndez-Delmestre et al. 2007) host a bar, reliable photometrical decompositions must include this component in their galaxy modeling. We plan to decompose photometrically the whole sample of galaxies presented in Chapter 7 using the GASP2D v2.0 code. Elliptical galaxies will be modeled with a single Sérsic profile for the spheroidal component, unbarred disk galaxies will be assumed to be well described by a Sérsic profile and an exponential profile for the bulge and disk, respectively, and barred disk galaxies will be modeled using the bar profiles allowed by GASP2D v2.0. With this huge database

(∼3000 galaxies) we plan to revise the scaling relations of disk galaxies, along the lines presented in Chapter 3. In addition, a larger statistic of the structural parameters of the bars will further contraint the possible formation scenarios of these galaxies.

10.2.3 Stellar populations in barred and unbarred galaxies

In Chapter 5, the study of the stellar populations for a limited sample of bulges was presented. This kind of studies provides an invaluable quantity of information that can help us to distinguish between different classes of bulges and different formation scenarios. In addition, in Chapters 7 and 9, we have shown how the presence of a bar inside a disk galaxy constitutes the most important factor causing the processes of secular evolution in the galaxy central regions. We are working on a project to study the differences in the central ages and metallicities for a statistically significant sample of barred and unbarred galaxies, to study the influence of bars in the galaxy stellar populations.

10.2.4 Unveiling peanut bulges in face-on barred galaxies

In Chapter 9, we show the first detection of a boxy/peanut (B/P) bulge in a face-on barred galaxy, this detection links unequivocally the B/P bulges with the presence of a bar. We have already observed another three galaxies where we plan to investigate the presence of the B/P structure. Actually, this represent the first part of a long-term programme to sistematically search for B/P objects. In order to obtain statistical information about their presence and position to compare them with the state-of-the-art in barred galaxy simulations.

Bibliography

Aguerri, J. A. L. 1999, A&A, 351, 43
Aguerri, J. A. L., Méndez-Abreu. J., & Corsini, E. M. 2008, A&A, submitted
Athanassoula, E., & Misiriotis, A. 2002, MNRAS, 330, 35
Athanassoula, E., Morin, S., Wozniak, H., et al. 1990, MNRAS, 245, 130
Barazza, F. D., Jogee, S., & Marinova, I. 2008, ApJ, 675, 1194
Bekki, K., & Shioya, Y. 1999, ApJ, 513, 108
Chung, A., & Bureau, M. 2004, AJ, 127, 3192
Debattista, V. P., Carollo, C. M., Mayer, L., & Moore, B. 2005, ApJ, 628, 678
Erwin, P., & Sparke, L. S. 2003, ApJS, 146, 299
Eskridge, P. B., Frogel, J. A., Pogge, R. W., et al. 2000, AJ, 119, 536
Ferreras, I., & Silk J. 2002, MNRAS, 336, 1181
Kobayashi, C., & Arimoto, N. 1999, ApJ, 527, 573
Kormendy, J., & Kennicutt, R. C. 2004, ARA&A, 42, 603
Laurikainen, E., Salo, H., Buta, R. & Knapen, J., 2007, MNRAS, 381, 401
Marinova, I., & Jogee, S. 2007, ApJ, 659, 1176
Martinet, L., & Friedli, D. 1997, A&A, 323, 363

Menéndez-Delmestre, K., Sheth, K., Schinnerer, E., Jarrett, T. H., & Scoville, N. Z. 2007, ApJ, 657, 790
Michel-Dansac, L., & Wozniak, H. 2006, A&A, 452, 97
Reese, A. S., Williams, T. B., Sellwood, J. A., Barnes, E. I., & Powell, B. A. 2007, AJ, 133, 2846
Shen, J., & Sellwood, J. A. 2004, ApJ, 604, 614
Whyte, L. F., Abraham, R. G., Merrifield, M. R., et al. 2002, MNRAS, 336, 1281
Wozniak, H., Friedli, D., Martinet, L., Martin, P., & Bratschi, P. 1995, A&AS, 111, 115